

**DENSITY FUNCTIONAL APPROACHES FOR THE
INTERACTION OF METAL OXIDES WITH SMALL
MOLECULES**

Adriel Domínguez García

DENSITY FUNCTIONAL APPROACHES FOR THE
INTERACTION OF METAL OXIDES WITH SMALL
MOLECULES

von

Adriel Domínguez García

Vom Zur Erlangung des akademischen Grades eines
DOKTORS DER NATURWISSENSCHAFTEN
(Dr. rer. nat.)

Dem Fachbereich für Physik und Elektrotechnik der Universität Bremen

1. Gutachter: Prof. Dr. rer. nat. Thomas Frauenheim
2. Gutachter: Prof. Dr. rer. nat. Thomas Heine

Datum des Kolloquiums: 07.05.2014

to my parents

Acknowledgements

This thesis would not have reached its final form without the invaluable help of several persons, whom I would like to thank. First, I would like to express my gratitude to Prof. Thomas Frauenheim, who gave me the opportunity to start an exciting route of research in his group, at the Bremen Center for Computational Material Science (BCCMS). For his permanent support and numerous discussions, I will be always indebted. My deepest gratitude also goes to Prof. Thomas Niehaus, who has supervised most of the present investigation. His guidance, valuable advices, constructive criticism and friendship are well appreciated. I am grateful for his warm hospitality offered during my visits to the University of Regensburg. Furthermore, I would like to thank him for his continual assistance and useful comments on this dissertation. Dr. Andreia L. da Rosa is greatly acknowledged for her supervision on the work concerning the study of zinc oxide. Her expertise on this metal oxide was exceptionally helpful and working under her guidance was rewarding. My most sincere appreciation also goes to Dr. Bálint Aradi, who has acted as an unofficial advisor for me. I have completely enjoyed all the fruitful discussions, and I am deeply grateful for his ingenious comments and suggestions and for his help with the DFTB+ code. I would like to thank the rest of colleagues at BCCMS, who have kept a collaborative atmosphere during all these years. Especially, Svea grosse Holthaus is hugely acknowledged for being an excellent officemate, coworker and friend. I have also had the opportunity to collaborate with current and former members of BCCMS such as Dr. Ney Moreira, Dr. Grygoriy Dolgonos, Dr. Michael Lorke and Dr. Jolla Kullgren. I would like to thank them for enjoyable and fruitful discussions. Dr. Dolgonos is particularly acknowledged for his assistance in the development and generation of the repulsive potentials involving titanium, employed in this work. Moreover, Vitalij Lutsker is acknowledged for the implementation of a FORTRAN code for the computation of the onsite parameters used in this thesis. My thanks also go to Prof. Detlef Bahnemann and Janna Freitag for supporting our theoretical predictions with experimental observations and for many productive discussions. Prof. Bahnemann is also acknowledged for accepting to be one of the examiners of this thesis. I am similarly grateful to Prof. Thomas Heine and Prof. Tim Wehling for agreeing to take part of the examining committee. I would like to express my gratitude to Dr. Fernando Guzmán, who proposed me as a doctoral candidate in Frauenheim's group. I am indebted for his support, encouragement and friendship during the last several years. I would like to thank the former and current members of the BCCMS secretariat Christine Frauenheim, Karin Schütte, Gabriela Berger, Marta Holowacz and Sandra Smit for their support with nonscientific tasks, yet indispensable for the unhindered development of this research project. I would like to thank all my friends from Bremen and Havana, who have shown genuine interest for the course of this investigation. Last, I would like to thank my family, both Cuban and German. Especially, I thank my beloved wife Kathi, in whom I have found a source of strength and stimulation. My achievements are also hers. I would not have made it without her support, understanding, inexhaustible love and endless patience. A very special acknowledgment goes to my parents, to whom this thesis is dedicated and who have been the foremost reason I have today completed this work. I will be eternally thankful for their education and dedication. My greatest achievement is to make them proud.

Abstract

Under ambient conditions, most metals are covered with an oxide layer. The interaction of these oxide surfaces with different molecules has been widely investigated as the formation of molecular-metal oxide complexes has found a broad range of applications in technology. Theoretical insights into the physics and chemistry of such hybrid interfaces are crucial for the growth of technological advancement. Approaches based on Density Functional Theory (DFT) constitute an efficient alternative to wavefunction-based methods and have gained a prominent role in the study of systems and processes of substantial complexity. The density functional tight binding (DFTB) approach and its time-dependent extension (TD-DFTB) combine the accuracy typical of first principles DFT with the efficiency representative of semiempirical methods. Despite their success, serious shortcomings of DFTB/TD-DFTB have been identified. Those include the inaccurate description of hydrogen bond interactions and $\sigma \rightarrow \pi^*$ electron transitions.

The DFTB and TD-DFTB methods are here extended in order to overcome the aforementioned deficiencies. The incorporation of one-center exchange-like terms in the expansion of multicenter integrals leads to a DFTB scheme in which the fluctuation of the dual density matrix is treated self-consistently. This formalism improves upon hydrogen bond energies of neutral, protonated and hydroxide water clusters as well as of methylimidazole-water complexes. An analogous correction for TD-DFTB leads to marked qualitative and quantitative improvements over the original method. Especially, the failure for the description of $\sigma \rightarrow \pi^*$ and $n \rightarrow \pi^*$ excitations is surmounted. Benchmark calculations on a large set of organic molecules also indicate a better description of triplet states. Overall, the accuracy of the revised TD-DFTB approach is found to be similar to that of *ab initio* TD-DFT calculations, at a highly reduced computational cost. Furthermore, TD-DFTB is generalized to account for fractional occupation and spin polarization.

DFTB and TD-DFTB are employed to investigate the structural and optical properties of titanium dioxide (TiO_2) complexed with two important environmental pollutants, namely, nitric oxide (NO) and acetaldehyde (CH_3CHO). The TiO_2 -NO systems are shown to absorb visible light by formation of charge-transfer (CT) complexes. In contrast, complexation with acetaldehyde does not lead to solar activation of TiO_2 . The CT complexes may act as visible light sensitizers which prompt the self-degradation of the contaminant. Our predictions are confirmed by experiments conducted in collaboration within the present work. We also explain the unexpected photo-decomposition of NO in the presence of aluminum oxide (Al_2O_3) under ultraviolet illumination.

Finally, the structural and electronic properties of the interfaces between zinc oxide (ZnO) and several organic molecules are investigated using DFT and DFTB. The influence of the ZnO surface coverage on the adsorption energies and geometries of the ligands is analyzed. Stable interfaces in the gas phase are found for carboxylic acids, thiols and phosphonates. We find that all these compounds prefer to bind dissociatively on the nonpolar surfaces of ZnO. Furthermore, glycine is found to bind to the (10 $\bar{1}$ 0) ZnO surface through either the carboxyl or the amino group with similar adsorption energies at full coverage. However, the electronic properties of the adduct depend on the orientation of the aminoacid. For lower coverages, glycine strongly adsorbs on the surface through both functional groups. We find that the presence of surface oxygen vacancies slightly strengthens the ligand-substrate interaction.

Contents

| | | |
|----------|---|-----------|
| 1 | INTRODUCTION | 17 |
| 1.1 | TiO ₂ Photocatalysis | 17 |
| 1.2 | Functionalization of ZnO with Organic Compounds | 20 |
| 1.3 | Theoretical Approach | 21 |
| 1.4 | Scope and Structure of the Thesis | 22 |
| 2 | A BRIEF REVIEW ON DENSITY FUNCTIONAL THEORY | 25 |
| 2.1 | The Hohenberg-Kohn Theorems | 25 |
| 2.2 | The Kohn-Sham Method | 26 |
| 2.3 | Exchange-Correlation Functionals | 27 |
| 2.3.1 | Local density approximation | 28 |
| 2.3.2 | Gradient correction | 28 |
| 2.3.3 | Hybrid Functionals | 29 |
| 2.4 | Time-Dependent Extension | 30 |
| 2.4.1 | Formal foundations | 30 |
| 2.4.2 | Linear Response | 32 |
| 3 | THE DENSITY FUNCTIONAL BASED TIGHT BINDING METHOD | 37 |
| 3.1 | Tight Binding meets DFT | 38 |
| 3.2 | The Standard DFTB Approach | 40 |
| 3.2.1 | Input density and basis set | 40 |
| 3.2.2 | Hamiltonian and overlap matrices | 41 |
| 3.2.3 | Repulsive potential | 42 |
| 3.3 | Second Order Corrections | 42 |
| 3.3.1 | Mulliken and monopole approximations | 43 |
| 3.4 | Density Matrix Formulation of DFTB | 45 |
| 3.5 | Beyond the Mulliken Approximation | 47 |

| | |
|---|------------|
| <i>CONTENTS</i> | 10 |
| 3.6 Onsite-corrected DFTB | 50 |
| 3.7 Onsite Correction in Practice. Onsite Parameters | 51 |
| 3.8 Hydrogen Bond Energies | 53 |
| 3.9 Summary | 58 |
| 4 THE TIME DEPENDENT DFTB METHOD | 61 |
| 4.1 Spin-unrestricted TD-DFTB | 62 |
| 4.2 Onsite Corrections in TD-DFTB | 63 |
| 4.2.1 Coupling matrix | 64 |
| 4.2.2 Dipole matrix | 65 |
| 4.3 Performance for Diatomic Systems | 66 |
| 4.4 Benchmarks | 69 |
| 4.4.1 Vertical transition energies | 70 |
| 4.4.2 Oscillator strengths | 77 |
| 4.4.3 Computational time | 78 |
| 4.5 Summary | 81 |
| 5 PHOTOCATALYTIC ACTIVITY OF TITANIUM DIOXIDE | 83 |
| 5.1 Ground State Properties of the Pollutant-TiO ₂ Complexes | 84 |
| 5.1.1 Validation of DFTB parameters | 84 |
| 5.2 Cluster Models and Absorption Spectra | 86 |
| 5.3 CT Complexes based on Alumina | 94 |
| 5.4 Comparison with Experimental Results | 95 |
| 5.5 Summary | 97 |
| 6 ORGANIC/ZINC OXIDE HYBRID INTERFACES | 99 |
| 6.1 Modification of (1210) ZnO Surfaces | 99 |
| 6.2 Modification of ZnO Nanowires | 103 |
| 6.3 Glycine Adsorption on (1010) ZnO Surfaces | 107 |
| 6.3.1 The effect of surface oxygen vacancies | 111 |
| 6.4 Summary | 113 |
| 7 CONCLUDING REMARKS | 115 |
| A PARAMETERS γ AND W | 119 |

| | | |
|----------|--|------------|
| B | OBTAINING ORIGINAL DFTB FORMALISM FROM ITS DENSITY MATRIX FORMULATION | 121 |
| C | VERTICAL EXCITATION ENERGIES OF BENCHMARK MOLECULES | 123 |
| C.1 | Singlet States | 123 |
| C.1.1 | Relative displacement of ω_1 with respect to ω_{KS} | 123 |
| C.1.2 | Vertical excitation energies and oscillator strengths | 128 |
| C.2 | Triplet States | 132 |
| C.2.1 | Relative displacement of ω_1 with respect to ω_{KS} | 132 |
| C.2.2 | Vertical excitation energies | 135 |

List of Figures

| | | |
|------|--|----|
| 1.1 | A collection of ZnO nanostructures. | 20 |
| 3.1 | Four water hexamers investigated in Table 3.2. | 55 |
| 3.2 | Five water hexadecamers investigated by Yoo <i>et al.</i> | 57 |
| 4.1 | Localization of σ and π^* <i>versus</i> π and π^* orbitals in the N ₂ molecule. | 64 |
| 4.2 | Absorption spectrum of nitric oxide as obtained with full TD-DFT, traditional TD-DFTB and TD-DFTB with on-site corrections | 68 |
| 4.3 | Thiel’s benchmark set of compounds. | 70 |
| 4.4 | Root mean square errors and mean signed deviation of S-T transition energies for a subset of Thiel’s benchmark with respect to experimental data. | 72 |
| 4.5 | Root mean square errors and mean signed deviation of S-T transition energies for Thiel’s benchmark set with respect to TBEs. | 72 |
| 4.6 | Root mean square errors and mean signed deviation of S-S transition energies for a subset of Thiel’s benchmark with respect to experimental data. | 73 |
| 4.7 | Root mean square errors and mean signed deviation of S-S transition energies for Thiel’s benchmark set with respect to TBEs. | 74 |
| 4.8 | Root mean square errors and mean signed deviation of S-S and S-T transition energies for a subset of Thiel’s benchmark with respect to experimental data. | 75 |
| 4.9 | Root mean square errors and mean signed deviation of S-S and S-T transition energies for Thiel’s benchmark set with respect to TBEs. | 76 |
| 4.10 | Total wall clock time for the computation of the first 15 singlet-singlet and singlet-triplet excitation energies of Thiel’s set of compounds. | 78 |
| 4.11 | Wall clock time for the computation of the first 20 singlet-singlet excitation energies of a macromolecule. | 79 |
| 4.12 | Low-lying absorption spectrum of a macromolecule as obtained with TD-DFT (PBE/TZP), traditional TD-DFTB and corrected TD-DFTB with and without constraints on the KS orbitals. | 80 |
| 5.1 | DFTB optimized structures of rutile (110) and anatase (001) surfaces of titania. | 83 |

| | | |
|------|--|-----|
| 5.2 | Side and top views of the optimized geometries of the rutile $\text{Ti}_{21}\text{O}_{68}\text{H}_{52}$ and anatase $\text{Ti}_{19}\text{O}_{57}\text{H}_{38}$ clusters. | 87 |
| 5.3 | UV-vis absorption spectrum for rutile and anatase TiO_2 clusters as obtained with TD-DFTB. | 88 |
| 5.4 | Optimized structure and density of electron states (DOS) of the NO adsorption on the neutral rutile cluster. | 89 |
| 5.5 | Absorption spectrum for the TiO_2 (rutile)-NO complex | 90 |
| 5.6 | Optimized geometries of the NO adsorption on the neutral anatase cluster. | 91 |
| 5.7 | Absorption spectra for the TiO_2 (anatase)-NO complexes | 91 |
| 5.8 | Charge density corresponding to the occupied and virtual Kohn-Sham states for the most dominant single-particle transition in the many-body wavefunction for the main CT peaks in the visible spectra of Fig. 5.7. | 92 |
| 5.9 | Optimized geometries of the adsorption of acetaldehyde on the rutile and anatase clusters. | 93 |
| 5.10 | Absorption spectrum for the TiO_2 -acetaldehyde complexes. | 94 |
| 5.11 | Optimized structure and the density of electron states (DOS) of the NO adsorption on the fully hydroxylated metal-terminated (0001) surface of $\alpha\text{-Al}_2\text{O}_3$ | 95 |
| 5.12 | Photonic efficiencies of different TiO_2 powders for the degradation of acetaldehyde and NO under visible-light and UV illumination. | 96 |
| 6.1 | First and second atom layers of the (10 $\bar{1}$ 0) and (1 $\bar{2}$ 10) ZnO surfaces. | 100 |
| 6.2 | Optimized geometries of the modified (1 $\bar{2}$ 10) ZnO surface using -SH, -COOH, -NH $_2$ and -OH functional groups. | 102 |
| 6.3 | Optimized geometries of the modified (1 $\bar{2}$ 10) ZnO surface using the -CN functional group. | 103 |
| 6.4 | Cross-sectional and side views of the optimized structure of the bare ZnO nanowire. | 104 |
| 6.5 | Cross-sectional and side views of the optimized structure of the CH_3COOH -modified ZnO nanowire. | 105 |
| 6.6 | Cross-sectional and side views of the optimized structure of the CH_3SH -modified ZnO nanowire. | 106 |
| 6.7 | Cross-sectional and side views of the optimized structure of the CH_3NH_2 -modified ZnO nanowire. | 106 |
| 6.8 | Cross-sectional and side views of the optimized structure of the $\text{CH}_3\text{PO}(\text{OH})_2$ -modified ZnO nanowire. | 107 |
| 6.9 | Optimized structures of the modified (10 $\bar{1}$ 0) ZnO surface using 1 ML of glycine molecules adsorbed through either the -COOH or the -NH $_2$ groups. | 109 |

| | | |
|------|---|-----|
| 6.10 | Optimized structures of the modified (10 $\bar{1}$ 0) ZnO surface using 0.5 ML of glycine molecules in different binding modes: -COOH bidentate bridging, -COOH bidentate chelating with dissociated -NH ₂ group and -COOH monodentate with nondissociated -NH ₂ group. | 110 |
| 6.11 | Optimized structures of glycine adsorbed on the defect-free and oxygen-reduced (10 $\bar{1}$ 0) ZnO surfaces for $\theta = 0.25$ | 110 |
| 6.12 | Total and projected density of states for the bare (10 $\bar{1}$ 0) ZnO surface and the modified surface using glycine adsorbed through the -COOH group and the -NH ₂ group for $\theta = 1$ | 111 |
| 6.13 | Electronic band structure for the 0.25 ML coverage of glycine molecules on the defect-free and oxygen-reduced (10 $\bar{1}$ 0) ZnO surfaces. | 112 |

List of Tables

| | | |
|-----|---|-----|
| 3.1 | Onsite parameters for some chemical elements calculated at the PBE level of theory. | 53 |
| 3.2 | Comparison of binding energies as obtained with the DFTB method at different levels of approximation and G3B3. | 54 |
| 3.3 | Comparison of binding energies of five water 16-mers as obtained with the DFTB method at different levels of approximation and CCSD(T). | 58 |
| 4.1 | Dipole parameters for some chemical elements calculated at the PBE level of theory. | 65 |
| 4.2 | Comparison of vertical excitation energies and oscillator strengths for TD-DFT, traditional TD-DFTB and TD-DFTB with onsite correction | 67 |
| 4.3 | Oscillator strengths for 9 $\pi \rightarrow \pi^*$ excitations to valence states. | 77 |
| 5.1 | Comparison between DFTB, PBE and experimental results concerning the properties of bulk rutile and anatase. | 85 |
| 5.2 | Comparison between DFTB and PBE in terms of optimized structures and energetics of the NO adsorption on TiO_2 | 86 |
| 6.1 | Adsorption energies of the substituted methane molecules $\text{CH}_3\text{-X}$ ($\text{X} = \text{CN}, \text{NH}_2, \text{OH}, \text{SH}$ and COOH) on $(1\bar{2}10)$ and $(10\bar{1}0)$ ZnO for both molecular and dissociative adsorptions. | 101 |
| 6.2 | DFTB adsorption energies and surface energy variations per (1×1) ZnO surface corresponding to the stable binding geometries of glycine on $(10\bar{1}0)$ ZnO. | 108 |
| C.1 | Singlet-singlet vertical excitation energies compared to energy difference of most dominant single particle transition for Group A. | 124 |
| C.2 | Singlet-singlet vertical excitation energies compared to energy difference of most dominant single particle transition for Group B. | 125 |
| C.3 | Singlet-singlet vertical excitation energies compared to energy difference of most dominant single particle transition for Group C. | 126 |
| C.4 | Singlet-singlet vertical excitation energies compared to energy difference of most dominant single particle transition for Group D. | 127 |

| | | |
|------|---|-----|
| C.5 | Singlet-singlet vertical excitation energies and oscillator strengths for Group A. . | 128 |
| C.6 | Singlet-singlet vertical excitation energies and oscillator strengths for Group B. . | 130 |
| C.7 | Singlet-singlet vertical excitation energies and oscillator strengths for Group C. . | 130 |
| C.8 | Singlet-singlet vertical excitation energies and oscillator strengths for Group D. . | 131 |
| C.9 | Singlet-triplet vertical excitation energies compared to energy difference of most dominant single particle transition for Group A. | 132 |
| C.10 | Singlet-triplet vertical excitation energies compared to energy difference of most dominant single particle transition for Group B. | 133 |
| C.11 | Singlet-triplet vertical excitation energies compared to energy difference of most dominant single particle transition for Group C. | 134 |
| C.12 | Singlet-triplet vertical excitation energies for Group A. | 135 |
| C.13 | Singlet-triplet vertical excitation energies for Group B. | 137 |
| C.14 | Singlet-triplet vertical excitation energies for Group C. | 138 |

Chapter 1

INTRODUCTION

The interaction between metal oxides and molecules is a ubiquitous phenomenon in nature. Due to exposure to atmospheric oxygen or water, all metals, except gold, undergo surface oxidation. These oxide surfaces then unavoidably interact with molecular constituents of the surrounding media. The study of these interactions is therefore crucial for the understanding of a wide range of processes occurring in our daily life. Furthermore, molecular/metal oxides interfaces have found a large number of applications in technology, such as catalysis, photocatalysis and gas sensing [1, 2].

An intensively investigated metal oxide is titanium dioxide (TiO_2), also known as titania. TiO_2 has been widely employed in industry as a white pigment, food coloring and sunscreen. It has been also successfully used in heterogeneous catalysis, dye-sensitized solar cells, gas sensors, electro-chromic devices and photocatalysis. The latter application has received increasing attention in the last few years as the global environmental pollution has been identified as a serious concern that needs to be addressed immediately. The study of the photocatalytic properties of TiO_2 is one of the main research targets within this thesis. The present work also deals with the properties of the modification of zinc oxide (ZnO) surfaces and nanostructures using small organic molecules. ZnO is another versatile metal oxide with several technological applications. In particular, the combination of different structures of ZnO with organic compounds has been the object of a large number of scientific publications. Along this introductory chapter, we will expand on these topics while exposing the motivations for this doctoral research as well as the state of the art of the concerned fields. The employed theoretical methodology will also be briefly motivated.

1.1 TiO_2 Photocatalysis

Photocatalysis has been recognized as a very efficient way to deal with air pollution, a serious problem that affects living beings across the globe. In a photocatalytic process, the generation of electron-hole pairs follows by absorption of light by a chosen semiconductor substrate (called the photocatalyst). The electron-hole pairs then generate free radicals which facilitate the occurrence of subsequent reactions (for example, degradation of unwanted species). Among the different semiconductor materials, titanium dioxide (TiO_2) is one of the most powerful photocatalysts [3–5], and is often used for the purpose of environmental purification due to its strong

oxidative ability, chemical inertness and nontoxicity [6]. TiO_2 can appear in nature in three different phases: rutile, anatase and brookite, the former being the most stable configuration. Rutile (110) is the most stable surface for this phase, whereas for anatase, (101) is found to be thermodynamically favorable. Nevertheless, the high reactivity of anatase nanoparticles has been often associated with the minority (001) surface [7].

Among the most harmful atmospheric pollutant gases emitted by combustion are the nitrogen oxides (NO_x), which are responsible for acid rains, smog, nitrogen pollution in water and greenhouse warming. NO_x also constitute a serious health hazard for the human respiratory system, causing or worsening diseases such as emphysema and bronchitis, and aggravating existing heart disorders [8]. There is, therefore, a great need for diminishing the concentration of these dangerous environmental pollutants. Removing dilute NO_x gas from the atmosphere presents a major difficulty. Therefore, the photocatalytic decomposition of these gases adsorbed on TiO_2 provides a practical way to deal with this problem. Under UV illumination, NO_x in contact with TiO_2 surfaces can be partially removed from air *via* their photo-degradation, leading to non-hazardous reaction products.

This promising application of TiO_2 photocatalysts has been widely studied from an experimental point of view, paying specific attention to nitric oxide (NO), as this gas is a major emission product of combustion [9]. Recent experiments conducted by Bahnemann's group at the University of Hanover returned results that contradict the traditional understanding of photocatalytic reactions. When studying the oxidation of NO on materials irradiated with a UV-A lamp, they unexpectedly observed degradation activity on alumina (Al_2O_3) films. This metal oxide is a strong insulator and the formation of electron-hole pairs is hence not viable. This indicates that the understanding of photoreactions on metal oxide surfaces is still in its infancy. Especially, these findings raise doubts about the generation of electron-hole pairs as the catalyzing mechanism governing the degradation of NO and other pollutants on TiO_2 . Theoretical simulations may play an important role in giving answers to this query and suggest new experiments that lead to a better insight into the nature of this phenomenon.

Despite the relevance of photocatalysis in environmental remediation, few theoretical works have addressed the decomposition of NO_x on TiO_2 . More importantly, those works are limited to the study of the ground state properties of the adduct. Excited state simulations, which are fundamental for a deep understanding of TiO_2 photocatalysis, are missing. This is due to the prohibitive computational cost incurred in performing accurate excited-state calculations for solid materials and its interaction with molecules. At the time of writing and to our knowledge, only one investigation reports on theoretical time-dependent calculations of small organic compounds adsorbed on anatase TiO_2 [10]. To circumvent the associated computational expense, the authors modeled the TiO_2 surface by employing a small cluster (Ti_6O_{12}) embedded in a classical field sampled with point charges. They found that, for phenol, the most important peak in the absorption spectra corresponds to an electron transfer from the molecule to the metal oxide surface. Charge transfer (CT) mechanisms in photocatalytic phenomena have attracted the attention of many researchers in the last few years. Especially, a photoinduced ligand-to-metal charge transfer (LMCT) process [11] has been suggested as an alternative to popular visible-light activation methods such as impurity doping and dye-sensitization (for a review on this topic see Ref. [12]).

Visible-light activation of TiO_2 -based hybrid systems whose separate parts do not absorb visible radiation has been generally attributed to the formation of LMCT complexes and has been

observed even for physisorbed systems [13–15]. Several pollutants, including NO_x , do not absorb visible light by themselves, nor does pure TiO_2 . However, the formation of pollutant- TiO_2 complexes may enable adsorption of visible irradiation *via* a LMCT mechanism. This represents an important advantage for addressing outdoor air pollution as the visible range is the major component of sunlight. Formation of CT complexes on TiO_2 has therefore a promising application in air cleaning when the surface ligand forming the complex is a pollutant. Absorption of visible light may then lead to self-degradation of the unwanted compound. Electron transfer from the ligand to the TiO_2 surface may undergo either direct oxidation of the former or reduction of O_2 molecules to form strongly oxidizing species, thus eventually leading to the oxidation of the pollutant. Theoretical simulations are crucial to confirm the prevalence of CT mechanisms on these systems and predict suitable anchors for the realization of LMCT complexes.

It has been traditionally argued that the photo-degradation of NO_x depends on the capacity of adsorption of the pollutants on the TiO_2 surface. The majority works on the topic investigate the structural properties and energetics of the adsorbate. Various studies have shown that nitrous oxide (N_2O) is a major product of the photo-decomposition of NO on rutile surfaces (NO reduction) [9, 16–18] whereas, on the anatase phase, the presence of species like nitrate (NO_3^-) and nitrite (NO_2^-) has been reported (NO oxidation) [19, 20].

Most theoretical studies so far has focused on the adsorption on the rutile phase. In 2000, Sorescu *et al.* investigated the adsorption properties of NO on the completely oxidized rutile TiO_2 (110) surface [21]. They found that NO adsorbs weakly and the most stable configuration corresponds to a tilted geometry in which the Nitrogen (N) atom is oriented towards the surface and bonded to the metal sites. Similar findings are reported in other theoretical studies [18, 22]. They also determined that a $\frac{1}{2}$ NO monolayer is energetically favorable over a 1 monolayer coverage. Furthermore, they observed a small modification of the NO bond length as well as small changes in the valence electron distribution which indicates the presence of a predominant physisorption mechanism. It has been shown that, for full coverages, the interaction between NO molecules leads to formation of N_2O_2 species that bind weakly to the surface.

In 2002, a similar theoretical investigation was conducted, this time considering a defective TiO_2 (110) surface [18]. It was shown that the adsorption properties of NO are strongly driven by the presence of oxygen vacancies (V_O) on the surface. The adsorption energies increase significantly when considering this kind of defect and new active sites become available (vacancy sites). The largest adsorption energies were obtained for bridge tilted configurations of NO between 4-fold coordinated Ti sites with no preferential orientation of the molecule. It was also suggested that the adsorption mechanism changes from physisorption to chemisorption when these defects are present. Moreover, the data obtained for various adsorption configurations reveal a weakening of the NO bond with the increase of the surface binding energy. This may favor the dissociation of the molecule and its reaction with other compounds. In 2001, Li and coworkers also found that when NO adsorbs on defective TiO_2 (110) surfaces the N-O bond is weakened, and the energy barrier for a NO decomposition reaction is reduced [23]. On the other hand, they demonstrated that the adsorption of N_2O_2 species, formed from NO - NO interactions, leads to an instability of the molecular structure and the formation of N_2O gas. In general, it could be stated that increasing the defect density on the surface leads to an increase in the NO reduction yield to N_2O and N_2 . N_2O is also an air pollutant and greenhouse gas, and a considerable effort has been undertaken to study its conversion to form N_2 on TiO_2 [24, 25].

Volatile organic compounds (VOCs) are also ubiquitous pollutants in the environment and indoors whose degradation has been pursued *via* TiO_2 photocatalysis. Acetaldehyde is an example of these chemicals and a major indoor air pollutant. Acute exposure to acetaldehyde can cause eye and skin irritation whereas chronic intoxication effects are similar to those of alcoholism [26]. Moreover, this pollutant is recognized as a potential human carcinogen [27]. The existent theoretical works addressing the acetaldehyde adsorption on TiO_2 are even fewer than for NO. A very recent investigation combines Fourier transform infrared (FTIR) spectroscopy and theoretical calculations to study the adsorption and condensation of this VOC on anatase [28]. The authors showed that the attachment of acetaldehyde on the majority (101) surface is dominated by a weak interaction between the carbonyl group and the Ti surface site. Similar binding properties were observed theoretically for the adsorption on (110) rutile [29].

1.2 Functionalization of ZnO with Organic Compounds

During the past several years, zinc oxide (ZnO) has captured the attention of many researchers due to its promising optical, optoelectronic, piezoelectric, catalytic and sensing properties. Thus, this semiconductor material has a number of potential applications in catalysis, light emitting diodes, solar cells, microelectronic devices and gas sensors. Another appealing attribute of ZnO is the ease of fabrication of a wide number of nanostructures. Novel electrical, chemical and optical properties are introduced with the synthesis of such low-dimensional ZnO materials, as the result of the surface and quantum confinement. Moreover, the large surface-to-volume ratios of nanostructures lead to a unique possibility of enhanced material sensitivity and selectivity. In this sense, a large variety of ZnO nanostructures have been grown and used in various nanodevices with a distinguished performance in electronics, optics and photonics [30,31](see Fig. 1.1).

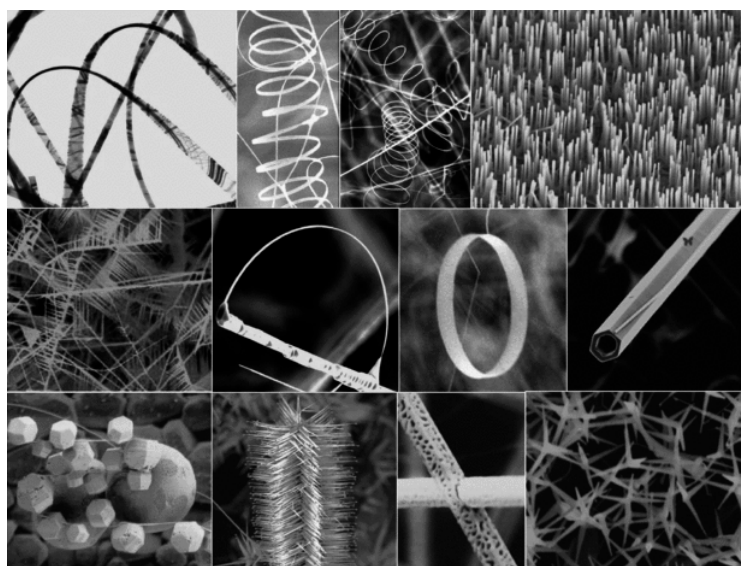


Figure 1.1: A collection of ZnO nanostructures. Adapted from Ref. [31].

Furthermore, the combination of organic matter with inorganic semiconductor nanostructures

has been of increasing interest in nanoscience and nanotechnology. Such hybrid materials are synthesized by coating the semiconductor surface with organic and bioorganic molecules. Organic/inorganic heterointerfaces offer the possibility of incorporation of specific functions, combination of molecular or biological and semiconducting features or enhancement of some properties of the pure semiconductor. These functionalized materials have promising applications in highly specific sensors, hybrid solar cells and multi-functional devices.

The functionalization of ZnO nanostructures and surfaces has been studied from an experimental and theoretical viewpoints, demonstrating the electrical, optoelectronic and sensing enhancement of devices fabricated on the basis of such materials [32, 32–37]. A very recent example of ZnO functionalization was carried out by Bach *et al.*. They showed that the dispersivity of ZnO nanoparticles is importantly enhanced *via* functionalization with polystyrene [38]. Other recent works include the functionalization of ZnO films with amines and thiols, which has been shown to induce ferromagnetism at room temperature [39, 40]. This behavior has been also reproduced for ZnO nanowires (NWs) and nanotubes (NTs) capped with thiol [41].

For the successful realization of hybrid organic-ZnO materials, a strong covalent attachment of the ligands on the semiconductor surface is required. Many anchor molecules have been investigated to determine which functional groups are the optimal ones to be covalently bound to the surface. Compounds which have been used as anchors include amines [42–44], carboxylic acids [45–53], phosphonic acids [54], thiols [43, 54–58] and silanes [45, 59–61]. There exist, however, some discrepancies regarding the success of some of these adsorbates for the functionalization of ZnO. Whereas some measurements suggest a favorable covalent binding of carboxylic acids on ZnO [45, 51, 52, 62], other studies indicate surface etching [57]. The experimental conditions seem to play a crucial role in the synthesis of the hybrid structures. Parameters such as the pH must be carefully controlled to prevent that the ZnO structures undergo unwanted reactions in the presence of anchor species. The chemisorption of amines on ZnO are, on the other hand, confirmed by X-ray photoelectron spectroscopy (XPS) and atomic force microscopy (AFM) measurements [39, 43] but other AFM studies indicate a rather weak adsorption of these compounds on (10 $\bar{1}$ 0) ZnO surfaces [57]. There is therefore a general demand of theoretical simulations that help get more insight into the chemistry and physics of organic/ZnO interfaces.

1.3 Theoretical Approach

The accurate description of molecular/metal oxide hybrid interfaces at the atomic scale entails the use of Quantum Mechanics (QM). In QM, solving the Schrödinger equation allows for the exact determination of the energy and wavefunction of a many-body system and hence, any property of such system. However, it turns out that the practical application of this equation is limited to very simple problems. For atomic systems, even within the Born-Oppenheimer approximation where the motion of the nuclei and the electrons are decoupled, the Schrödinger equation can only be solved exactly for hydrogen-like species. Fortunately, approximate solutions are provided *via* several quantum mechanical methods such as Hartree-Fock (HF). In HF, the stationary properties of atomic systems are obtained by invoking the energy variational principle, provided that the many-electron wavefunction is described by a single Slater determinant. To account for electron correlation, post-HF approaches were developed. Such methods include configuration interaction (CI) [63–65], Møller-Plesset perturbation theory (e.g.

MP2 [66], MP3, MP4 [67]), coupled cluster (CC) [68, 69] and quantum chemistry composite methods (e.g. G1 [70], G2 [71], G3 [72]). Although post-HF methods describe with high accuracy many chemical and physical properties, their applicability is rather limited to small systems due to their steep computational cost. A cheaper alternative to these approaches is provided by density functional theory (DFT), where the complex many-body wavefunction is replaced by the total electronic density as the basic variable.

DFT has been one of the most utilized tools during the last years for the description of ground-state properties of a wide variety of molecular systems that range from small molecules to large periodic materials. While it lacks the accuracy typical of correlated wavefunction-based methods, it goes beyond HF as electron correlation is incorporated in a self-consistent-field (SCF) fashion. Thus, DFT has turned out to be a good compromise between accuracy and computational cost; affordable to study hundreds-of-atoms systems on most current workstations with fairly good precision. The field of application of this method was subsequently extended to the study of excited states properties with the development of time-dependent density functional theory (TD-DFT) [73]. This method has become the *de facto* standard for the computation of optical properties for molecules with several tens of atoms. Also the limitations of TD-DFT are now well documented in the literature (see for example Refs [74–76]), which together with benchmark data [77–79], helps researchers judge *a priori* whether a certain class of density functionals is sufficient for the predictive simulation of the problem at hand.

With the increase of the dimension of the systems of interest or the need of longer simulation times for the description of a given phenomena, the field of application of *ab initio* methods, even DFT, gets quickly smaller. Approximate molecular orbital methods then appear as a useful tool to address highly demanding computational studies. Such approaches include Hückel theory [80–83] and semiempirical methods such as MINDO [84], AM1 [85] and PM3 [86–88]. Although during their early introduction computational resources were considerably scarce compared to present-day computing power, semiempirical approaches are, and will be, demanded due to the ever growing complexity of targeted problems in quantum chemistry and material science. The aforementioned semiempirical methods are based on HF theory. On the other hand, an approximate DFT-based formalism offers a unique opportunity for increased transferability due to explicit incorporation of correlation effects. Such approach is the density functional tight binding (DFTB) method [89, 90].

Since its early inception, DFTB has been continually extended in order to widen its field of application, address known limitations and improve its numerical accuracy. Especial mention deserves the development of time-dependent DFTB (TD-DFTB) [91], which is an approximation to linear-response TD-DFT. In DFTB and TD-DFTB additional approximations beyond the choice of a given exchange-correlation functional are accomplished to enhance the numerical efficiency. These are mostly the neglect, simplification and parametrization of two-electron integrals, thus circumventing their exact evaluation, considered as the main computational bottleneck of molecular orbital methods.

1.4 Scope and Structure of the Thesis

In the present work, density functional approaches are employed for the study of ground- and excited-state properties of molecules and their interaction with metal oxide surfaces and

nanostructures. In particular, the degradation of NO and acetaldehyde on TiO₂ under visible and UV irradiation is investigated *via* excited-state simulations. Rutile and anatase TiO₂ surfaces are considered in this investigation. To afford the use of sufficiently large models that allow a reliable description of these problems, we have employed TD-DFTB. The modification of ZnO surfaces and nanostructures using prototype organic molecules is also addressed within this thesis by using DFT and DFTB. Furthermore, special stress is laid upon the development and validation of new extensions within DFTB and TD-DFTB. Especially, a refinement is formulated in order to diminish the crude approximations originally made for the evaluation of the two-electron integrals. Thus, many of the neglected terms are brought back into the formalism at no substantial additional computational cost and complexity of the scheme. One of the TD-DFTB extensions, namely the generalization to treat spin-polarized systems, is crucial for the reliable description of the systems involving the radical NO and the study of ferromagnetic configurations of hydroxyl groups on TiO₂ surfaces. Other developments improve on the quantitative description of some particular systems. For example, the known poor description of $\sigma \rightarrow \pi^*$ and $n \rightarrow \pi^*$ transitions in many chromophores within TD-DFTB is overcome.

This thesis is organized as follows: Chapter 2 reviews DFT and TD-DFT. In Chapter 3, the DFTB method is presented in detail. The formulation followed there is, in essence, different from the original derivation. This clears away some ambiguities of the traditional formulation while paves the way for the introduction of the aforementioned refinement. The refined scheme is then tested along other approaches for the description of hydrogen bonded complexes, traditionally recognized as difficult systems for DFTB. Chapter 4 introduces TD-DFTB. The strategy employed for its derivation differs again from that originally conceived. This enables the direct inheritance of some features of the ground-state formalism such as fractional occupancy and spin polarization. Furthermore, the refinement of the two-electron integrals introduced in ground-state DFTB is translated into the time-dependent formalism. To highlight the qualitative improvement within the refined scheme, we report results for selected diatomic molecules. Additionally, a comparison between results obtained with the proposed formalism and the original TD-DFTB approach for a large set of benchmark molecules is presented. Our findings are further compared to TD-DFT, the best theoretical estimates from the literature and experimental observations. The results concerning the study of the photocatalytic degradation of NO and acetaldehyde are presented in Chapter 5. The formation of CT complexes is demonstrated for NO. Based on our observations, the unexpected experimental findings at Bahnemann's group are explained, and some aspects of TiO₂ photocatalysis are unveiled. In Chapter 6, the structural properties and energetics of ZnO nonpolar surfaces and nanowires modified with monofunctional organic ligands are reported. Furthermore, we investigate the electronic properties of fully-oxidized and oxygen-reduced ZnO surfaces covered with a bifunctional adsorbate. In Chapter 7, the conclusions of this work as well as some future prospects are drawn. At the end of Chapters 3, 4, 5 and 6, the main aspects and obtained results are summarized. This document also encloses a total of three appendices containing supporting material, including further theoretical aspects of the presented methodology as well as extensive tables with all our results.

Chapter 2

A BRIEF REVIEW ON DENSITY FUNCTIONAL THEORY

In this chapter we briefly review Density Functional Theory (DFT) and its time dependent extension, time-dependent density functional theory (TD-DFT). A more comprehensive review can be found for example in Ref. [92] for the ground state theory and in [93] for the time-dependent development. This will lay the foundations for the later introduction of an approximate DFT and TD-DFT formalism.

2.1 The Hohenberg-Kohn Theorems

The groundwork for DFT was laid by the model of Thomas and Fermi for the description of electrons in atoms, introduced in 1927 [94–98]. They were the first authors to write an explicit relation between the total kinetic energy of a many-electron system and its electron density, based on the consideration of a uniform distribution of noninteracting electrons in each small volume element of space. However, the modern era in DFT is initiated with the works by Hohenberg and Kohn, who generalized the approximate Thomas-Fermi (TF) model into an exact theory. The grounds of the formalism rely on two theorems. The first one states that *the external potential, V_{ext} , is determined, to within an additive constant, uniquely by the electron density $\rho(\mathbf{r})$* [99]. As integration of ρ yields the total number of electron, N , it follows that ρ also determines the ground-state wave function Ψ and hence, all ground-state properties of the system. Thus, such properties can be expressed as a functional of the density.

In particular, the total energy functional can be written as

$$E[\rho] = T[\rho] + V_{ee}[\rho] + \int V_{ext}(\mathbf{r})\rho(\mathbf{r})d\mathbf{r}, \quad (2.1)$$

where $T[\rho]$ is the kinetic energy and $V_{ee}[\rho]$ is the electron-electron repulsion. The latter consists of the coulomb interaction,

$$E_H[\rho] = \frac{1}{2} \iint \frac{\rho(\mathbf{r})\rho(\mathbf{r}')}{|\mathbf{r} - \mathbf{r}'|} d\mathbf{r}d\mathbf{r}', \quad (2.2)$$

and a nonclassical term. The sum $T[\rho] + V_{ee}[\rho]$ is independent of the external potential and is hence a universal functional of ρ , whereas the last term in Eq. (2.1) has a unique correspondence with ρ due to the first Hohenberg-Kohn (HK) theorem.

The second HK theorem serves an energy variational principle analogous to that for the wave functions. It enounces that *for a trial density $\tilde{\rho}(\mathbf{r})$, such that $\int \tilde{\rho}(\mathbf{r})d\mathbf{r} = N$ and $\tilde{\rho}(\mathbf{r}) \geq 0$, the energy functional evaluated at $\tilde{\rho}$, $E[\tilde{\rho}]$, is never smaller than the ground state energy.* In this way, the ground state energy in DFT is the minimum value of the energy functional, and this minimum value is obtained when the functional is evaluated at the ground state density.

Although the HK theorems were originally restricted to a nondegenerate closed-shell ground state, their validity was later demonstrated also for systems with degenerate ground-states [100]. Also, analogous theorems can be formulated for spin-dependent densities. Another issue is related to the fact that not every trial density $\tilde{\rho}$ yields an external potential V_{ext} . This *V-representability* problem is, however, easily circumvented by reformulating the theory so that the trial densities are simply subject to a *N-representability* condition, which is satisfied for any reasonable density [100, 101].

2.2 The Kohn-Sham Method

One problem still remains in the theory of Hohenberg and Kohn, and it is the difficulty associated to the calculation of $T[\rho]$ and the nonclassical part of $V_{\text{ee}}[\rho]$. In the TF model $V_{\text{ee}}[\rho]$ is simply replaced by the classical coulomb energy, $E_{\text{H}}[\rho]$, whereas the kinetic energy is taken from the theory of a noninteracting uniform electron gas. A next level of approximation to $V_{\text{ee}}[\rho]$ was introduced by Dirac few years later, by adding to $E_{\text{H}}[\rho]$ the exchange energy for a uniform electron gas [102]. Efforts to refine the approximation to $T[\rho]$ started with the work by Weizsäcker, who first considered the effects of the inhomogeneity of the electron density, which is particularly large in atoms and molecules [103]. Still, TF and related models lack accuracy. An alternative approach to the kinetic energy functional was developed by Kohn and Sham in 1965 [104], thereby turning DFT into a practical tool for accurate calculations. Nowadays, the Kohn-Sham (KS) method is the *de facto* standard for the calculation of ground-state properties of large molecules.

In the KS method the energy functional for a system of N electrons moving in the external potential V_{ext} is written as follows:

$$E[\rho] = T_{\text{s}}[\rho] + E_{\text{H}}[\rho] + E_{\text{xc}}[\rho] + \int V_{\text{ext}}(\mathbf{r})\rho(\mathbf{r})d\mathbf{r}, \quad (2.3)$$

where $T_{\text{s}}[\rho]$ is the exact ground-state kinetic energy of a fictitious system of N noninteracting electrons moving in the effective potential V_{s} and yielding the electronic density ρ :

$$T_{\text{s}}[\rho] = \sum_i n_i \int \psi_i^*(\mathbf{r}) \left(-\frac{1}{2}\nabla^2 \right) \psi_i(\mathbf{r})d\mathbf{r}. \quad (2.4)$$

ψ_i are the eigenfunctions resulting from solving the one-electron Schrödinger equation,

$$\hat{H}\psi_i(\mathbf{r}) = \left[-\frac{1}{2}\nabla^2 + V_{\text{s}}(\mathbf{r}) \right] \psi_i(\mathbf{r}) = \varepsilon_i\psi_i(\mathbf{r}), \quad (2.5)$$

and n_i are the corresponding occupation numbers. The electronic density of such noninteracting system is given by

$$\rho(\mathbf{r}) = \sum_i n_i |\psi_i(\mathbf{r})|^2. \quad (2.6)$$

The third term in Eq. (2.3) is called the exchange-correlation (XC) energy. It contains the difference between the kinetic energy of the actual system, $T[\rho]$, and $T_s[\rho]$, and the nonclassical component of $V_{ee}[\rho]$. The XC energy is the only functional in (2.3) with an unknown analytical form and so it must be approximated; otherwise the KS method is exact. Several approaches for the XC functionals have emerged; we will devote next section to this matter.

It is useful to write the KS energy functional in terms of the single-particle energies ε_i . To this end, we add and subtract in Eq. (2.3) the term $\sum_i n_i \int \psi_i^* V_s \psi_i d\mathbf{r}$ while employing (2.5) and (2.6), which results in

$$E[\rho] = \sum_i n_i \varepsilon_i + E_H[\rho] + E_{xc}[\rho] + \int V_{\text{ext}}(\mathbf{r})\rho(\mathbf{r})d\mathbf{r} - \int V_s(\mathbf{r})\rho(\mathbf{r})d\mathbf{r} \quad (2.7)$$

By applying the second HK theorem (variational principle) to the energy functional (2.7), one arrives at a set of equations (2.5), for which the effective potential V_s becomes

$$V_s[\rho_{\text{gs}}](\mathbf{r}) = V_{\text{ext}}(\mathbf{r}) + V_H[\rho_{\text{gs}}](\mathbf{r}) + V_{xc}[\rho_{\text{gs}}](\mathbf{r}), \quad (2.8)$$

where the so-called Hartree and XC potentials (V_H and V_{xc} , respectively) are defined as

$$V_H[\rho](\mathbf{r}) = \frac{\delta E_H[\rho]}{\delta \rho(\mathbf{r})} = \int \frac{\rho(\mathbf{r}')}{|\mathbf{r} - \mathbf{r}'|} d\mathbf{r}' \quad (2.9)$$

$$V_{xc}[\rho](\mathbf{r}) = \frac{\delta E_{xc}[\rho]}{\delta \rho(\mathbf{r})} \quad (2.10)$$

In Eq. (2.8) ρ_{gs} denotes the ground-state density of the many-body system. As V_s is a functional of the electron density, the set of equations (2.5) (known as the KS equations) are solved self-consistently. The procedure of finding its solutions usually starts with the assumption of the effective potential. The guessed V_s leads to a density ρ which is, in turn, used to evaluate V_s according to (2.8). This process is then repeated until the ground-state density is obtained within the desired accuracy. The eigenvalues, ε_i , and eigenfunctions, ψ_i , solution of the KS equations are known as KS energies and KS orbitals, respectively. Likewise, \hat{H} and V_s are respectively termed the KS Hamiltonian and the KS potential.

The ground-state energy is obtained by evaluating the energy functional (2.7) at ρ_{gs} . To this end, the KS potential $V_s[\rho_{\text{gs}}]$ [Eq. (2.8)] is substituted into Eq. (2.7), which leads to

$$E[\rho_{\text{gs}}] = \sum_i n_i \varepsilon_i - E_H[\rho_{\text{gs}}] + E_{xc}[\rho_{\text{gs}}] - \int V_{xc}[\rho_{\text{gs}}]\rho_{\text{gs}}(\mathbf{r})d\mathbf{r} \quad (2.11)$$

The first term of Eq. (2.11) contains the sum over the energies of all occupied KS orbitals, whereas the second, third and fourth terms are known as double-counting corrections.

2.3 Exchange-Correlation Functionals

The greatest challenge in KS DFT remains to be of how to accurately evaluate the XC functional. Today, a large variety of XC functionals are available and have been extensively benchmarked for the description of different ground-state properties. In this section we will review very briefly some of the most important contributions in the long trajectory of developments of this quantity.

2.3.1 Local density approximation

Kohn and Sham proposed the simplest existing approximation to the XC functional, the so-called local density approximation (LDA) [104]. It applies the uniform electron gas formula for the evaluation of E_{xc} , leading to

$$E_{xc}^{\text{LDA}}[\rho] = \int \rho(\mathbf{r})\varepsilon_{xc}(\rho)d\mathbf{r}, \quad (2.12)$$

ε_{xc} being the XC energy per particle of a homogeneous electron gas of density ρ . The XC potential then reads

$$V_{xc}^{\text{LDA}}(\mathbf{r}) = \frac{\delta E_{xc}^{\text{LDA}}[\rho]}{\delta \rho(\mathbf{r})} = \varepsilon_{xc}(\rho) + \rho(\mathbf{r})\frac{\delta \varepsilon_{xc}(\rho)}{\delta \rho}. \quad (2.13)$$

The exchange contribution of $\varepsilon_{xc} = \varepsilon_x + \varepsilon_c$ is given by the Dirac XC functional for the homogeneous electron gas [102],

$$\varepsilon_x(\rho) = -\frac{3}{4} \left(\frac{3}{\pi} \right)^{\frac{1}{3}} \rho(\mathbf{r})^{\frac{1}{3}}, \quad (2.14)$$

whereas the correlation part has no analytical expression, though accurate quantum Monte Carlo results [105] has been interpolated to provide various analytical forms [106–109].

The extension of LDA to spin-polarized densities is known as the local spin density approximation (LSDA). It turns out that a similar Density functional theory (known as spin(S)-DFT) can be built for those systems, leading to spin-polarized KS equations, where the kinetic energy is handled exactly whereas the XC functional is approximated. Within LSDA, the latter quantity reads

$$E_{xc}^{\text{LSDA}}[\rho_{\uparrow}, \rho_{\downarrow}] = \int \rho(\mathbf{r})\varepsilon_{xc}(\rho_{\uparrow}, \rho_{\downarrow})d\mathbf{r}, \quad (2.15)$$

where $\rho = \rho_{\uparrow} + \rho_{\downarrow}$ is the total density, consisting of the spin-up and -down densities. The form of the S-DFT exchange functional can be shown to be [110]

$$E_x[\rho_{\uparrow}, \rho_{\downarrow}] = \frac{1}{2} (E_x[2\rho_{\uparrow}] + E_x[2\rho_{\downarrow}]), \quad (2.16)$$

where for LSDA the functionals $E_x[2\rho_{\uparrow}]$ and $E_x[2\rho_{\downarrow}]$ are evaluated using (2.14). The correlation contribution to E_{xc}^{LSDA} has been constructed *via* interpolation of the known LDA forms for the paramagnetic ($\rho_{\uparrow} = \rho_{\downarrow}$) and ferromagnetic cases ($\rho = \rho_{\uparrow}$, $\rho_{\downarrow} = 0$) [106, 111].

Despite the crude consideration of a homogeneous electron gas for the description of atomic and molecular densities, LDA performs well in many cases. The main deficiencies within the approach are the presence of spurious self-interaction and the wrong long-range behavior of XC potentials.

2.3.2 Gradient correction

The LDA typically underestimates the exchange energy by about 10%. This is because the electron density in atomic and molecular systems is far from homogeneous. To account for this nonuniformity, corrections depending on the density gradient have been developed [112–115],

thus giving birth to the generalized gradient approximation (GGA). The GGA XC functional can be written in general terms as

$$E_{xc}^{\text{GGA}}[\rho_{\uparrow}, \rho_{\downarrow}] = \int f(\rho_{\uparrow}, \rho_{\downarrow}, \nabla\rho_{\uparrow}, \nabla\rho_{\downarrow})d\mathbf{r}, \quad (2.17)$$

where the functional f has been constructed in diversified manners. One of the most popular approaches for molecular systems is the BLYP method, which employs the asymptotically-corrected exchange functional of Becke [114] and the correlation functional of Lee, Yang and Parr [116]. Another prominent choice, especially in solid-state physics, is the Perdew-Burke-Ernzerhof (PBE) formalism [117, 118]. Unlike other GGA approaches, PBE improves upon LDA in every aspect, reducing to LDA in the limit of a uniform electron gas. However, GGA functionals do not heal the self-interaction error of local-density approaches. Corrections in GGA are local in the sense that they are applied to each point \mathbf{r} independently, but at the same time, they incorporate, to first order, information on the density in the infinitesimal neighborhood surrounding \mathbf{r} . GGA functionals are therefore called *semi-local*.

2.3.3 Hybrid Functionals

A notorious problem of local and semi-local functionals is the underestimation of the band gap of semiconductor and insulator materials. For ZnO, for example, GGA returns a band gap of 0.7 eV, with a relative error of roughly 80% with respect to the experimental value of 3.4 eV. In 1993, Becke stated that, for further improvement upon GGA methods, exact-exchange information had to be included in the XC functionals [119, 120]. Admixing a fraction of nonlocal HF exchange alleviates the self-interaction error present in conventional DFT methods. The resulting hybrid functionals can be expressed in the following form [121]:

$$E_{xc}^{\text{Hyb}}[\rho] = \alpha E_x^{\text{HF}} + (1 - \alpha)E_x^{\text{DFT}}[\rho] + E_c^{\text{DFT}}[\rho] \quad (2.18)$$

The parameter α controls the amount of exact exchange, E_x^{HF} , being included in the XC functional. For PBE0 (a popular hybrid functional) α is fixed to 0.25, whereas the DFT exchange and correlation are taken at the PBE level of theory [122–124]. The chosen ratio of exact and PBE exchange seems to work satisfactorily and surpass the GGA description of structural, thermochemical and electronic properties of solids [125]. However, as it has been pointed out [122, 124], this ratio is not universally optimal. Another widely employed hybrid functional is B3LYP, which makes use of parameters fitted to experimental data [119].

The use of hybrid functionals carries an additional computational workload compared to typical DFT approaches. This can be alleviated if the long-range exchange interaction is limited to short distances. Thereby the exchange functional is separated into two components, a short-range part containing a fraction of HF exchange and a long-range contribution consisting solely of the pure DFT exchange. The Heyd-Scuseria-Ernzerhof (HSE) functional is a popular example of such range-separated hybrid functionals [126, 127]. It uses PBE0 and PBE for the short- and long-range sections of the exchange interaction, respectively.

Another kind of range-separated functionals are the so-called long-range corrected (LC) hybrids, CAM-B3LYP being one of the most representative examples [128]. This functional combines the hybrid B3LYP scheme with the long-range correction formalism of Hirao and co-workers [129]. While retaining the good quality of atomization energies yield by B3LYP, CAM-B3LYP

has been shown to overcome the inaccurate description of charge transfer excitations of the conventional hybrid method [130–132]. Therefore, CAM-B3LYP finds particular applicability in non-stationary problems. An extension of DFT to time-dependent investigations is reviewed in the next section.

2.4 Time-Dependent Extension

DFT has doubtlessly become the first-choice tool to efficiently address an ample range of stationary problems. For time-dependent phenomena, a Δ SCF scheme has found some applicability. However, this method can be only justified under certain assumptions on the excited states. Also, the need to perform SCF calculations for each excited state, along with other practical difficulties, result in a cumbersome formalism. An alternative consists of extending DFT into the time domain.

2.4.1 Formal foundations

Significant efforts to bring the Hohenberg-Kohn-Sham formalism to non-stationary problems were accomplished by adapting the HK theorems to the description of electrons moving in a time-dependent external potential [133–135]. However, it was not until the seminal paper of Runge and Gross in 1984 [73], that the desired analogy with the ground-state scheme was proven for any¹ arbitrary non-stationary situation. Runge and Gross formulated two HK-like theorems that set the basis for the development of TD-DFT.

The first Runge-Gross (RG) theorem (analogous to the first HK theorem) states that *the time-dependent external potential, $V_{ext}(\mathbf{r}t)$, is determined, to within an additive function of time, uniquely by the time-dependent electron density, $\rho(\mathbf{r}t)$* . Thus, $\rho(\mathbf{r}t)$ determines the time-dependent Hamiltonian, $\hat{H}(t)$, and the wavefunction, $\Psi[\rho](t)$, up to a time-dependent phase factor. It follows then that the expectation value of any operator that does not contain time derivatives is a functional of the time-dependent density.

The second RG theorem² introduces a variational principle (or, more precisely, a principle of stationary action) in TD-DFT for the determination of $\rho(\mathbf{r}t)$. It states that *the action*

$$A[\rho] = \int_{t_0}^{t_1} \langle \Psi[\rho](t) | i \frac{\partial}{\partial t} - \hat{H}(t) | \Psi[\rho](t) \rangle dt \quad (2.19)$$

is, up to an additive constant³, a unique functional of the density and is stationary about the true density of the system. Thus, $\rho(\mathbf{r}t)$ can be calculated from the Euler equation,

$$\frac{\delta A[\rho]}{\delta \rho(\mathbf{r}t)} = 0 \quad (2.20)$$

¹The only restriction in the theory of Runge and Gross is that the external potential must be t -analytic around the initial time, $t = t_0$.

²The Runge-Gross paper [73] actually contains four theorems. The second one proposes a hydrodynamical formulation of TD-DFT and the third one, the action theorem, is the one we here refer to as the second.

³Note that the action defined in (2.19) contains indeed the expectation value of an operator including a time derivative. This quantity is hence not a unique functional of ρ as the wavefunction may have an arbitrary time-dependent phase factor for a given density which does not cancel out. However, it is easy to show that the existence of the phase factor simply adds an arbitrary constant to A .

The stationary action principle (2.20) yields the so-called time-dependent KS (TDKS) equations,

$$\hat{H}\psi_j(\mathbf{r}t) = \left[-\frac{1}{2}\nabla^2 + V_s(\mathbf{r}t) \right] \psi_j(\mathbf{r}t) = i\frac{\partial\psi_j(\mathbf{r}t)}{\partial t}, \quad (2.21)$$

where $\psi_j(\mathbf{r}t)$ are the TDKS orbitals producing the time-dependent density,

$$\rho(\mathbf{r}t) = \sum_j n_j |\psi_j(\mathbf{r}t)|^2, \quad (2.22)$$

and the TDKS potential $V_s(\mathbf{r}t)$ is expressed as

$$V_s(\mathbf{r}t) = V_{\text{ext}}(\mathbf{r}t) + \int \frac{\rho(\mathbf{r}'t)}{|\mathbf{r} - \mathbf{r}'|} d\mathbf{r}' + V_{\text{xc}}(\mathbf{r}t), \quad (2.23)$$

where the second term is the time-dependent Hartree potential and $V_{\text{xc}} = \delta A_{\text{xc}}/\delta\rho$. The functional A_{xc} is unknown but it can be subject to a local approximation in time:

$$A_{\text{xc}} = \int_{t_0}^{t_1} E_{\text{xc}}[\rho_t] dt, \quad (2.24)$$

where ρ_t is the instantaneous density at time t . This is the case of an external potential varying infinitely slowly in time and is known in TD-DFT as the adiabatic approximation. Within this approach the first derivative of A_{xc} reads

$$V_{\text{xc}}[\rho](\mathbf{r}t) = \frac{\delta A_{\text{xc}}[\rho]}{\delta\rho(\mathbf{r}t)} \cong \frac{\delta E_{\text{xc}}[\rho_t]}{\delta\rho_t(\mathbf{r})} = V_{\text{xc}}[\rho_t](\mathbf{r}), \quad (2.25)$$

that is, it amounts to the XC potential (2.10) evaluated at the electron density at a particular time, but it does not contain any information on the history of the density. This means that memory effects on the XC potential are completely disregarded. This can be directly seen from the second derivative of A_{xc} (the so-called XC kernel) which gives the response of the XC potential to a density fluctuation,

$$\frac{\delta A_{\text{xc}}[\rho]}{\delta\rho(\mathbf{r}t)\delta\rho(\mathbf{r}'t')} = \frac{\delta V_{\text{xc}}[\rho](\mathbf{r}t)}{\delta\rho(\mathbf{r}'t')} \cong \delta(t - t') \frac{\delta V_{\text{xc}}[\rho_t](\mathbf{r}')}{\delta\rho_t(\mathbf{r})}. \quad (2.26)$$

The Hartree kernel is, on the other hand, inherently local in time and so is given exactly within the adiabatic approximation. The adiabatic approximation brings considerable simplicity to the scheme and works satisfactorily in many cases. However, this approach finds its limits for the description of charge-transfer and Rydberg excited states [136, 137] or states dominated by double excitations [138, 139] as well as in cases of conical intersections [140, 141], to just mention a few critical shortcomings. Many schemes have been designed to go beyond or circumvent the adiabatic approximation. For a review on these formalisms see Ref. [74].

The RG formalism is limited to applied electric fields. As the effects of magnetic fields are often smaller than those of electric fields in experimental investigations of molecular properties, this is in many cases sufficient. To suppress this restraint, Ghosh and Dhara developed the TD current DFT method [142] which is a more general formalism, accounting also for time-dependent magnetic fields. This thesis is, however, not concerned with magnetic fields and so this formalism will not be developed here.

2.4.2 Linear Response

There are two main routes to solve the TDKS equations, namely, the real-time propagation of the KS wavefunction and using linear response techniques. The latter is a perturbative approach and is therefore limited to weak fields. Excitation energies can be extracted within this method since the linear response function of a finite interacting system has discrete poles at these energies. This thesis is only concerned with linear-response TD-DFT, which was first developed by Casida in 1995 [143]. In the following, we will derive the linear response equation and its transformation into an eigenvalue problem. The derivation will be consistent with a general spin-unrestricted scheme with possible fractional occupation of the KS states. Greek letters σ and τ stand for the spin variables. We employ the usual nomenclature of MOs throughout, that is, labels i, j, k, l denote occupied orbitals, a, b, c, d denote virtual orbitals and s, t, u, v denote general orbitals. However, as we allow for fractional occupation and spin polarization, coupled indexes $i\sigma$ and $a\sigma$ (or $j\tau$ and $b\tau$) will stand more generally for KS orbitals such that $n_{i\sigma} > n_{a\sigma}$ (or $n_{j\sigma} > n_{b\sigma}$). For more detail on the derivation of linear-response TD-DFT the reader is referred to Refs. [143, 144].

For a system initially in the ground state the perturbation introduced into the KS Hamiltonian due to an external perturbation δV_{ext} is, to linear order,

$$\delta \hat{H}^\sigma(\mathbf{r}t) = \delta V_s^\sigma(\mathbf{r}t) = \delta V_{\text{ext}}^\sigma(\mathbf{r}t) + \delta V_{\text{hxc}}^\sigma(\mathbf{r}t), \quad (2.27)$$

where $\delta V_{\text{hxc}}^\sigma = \delta V_{\text{H}}^\sigma + \delta V_{\text{xc}}^\sigma$ is the linear response of the Hartree-XC potential due to the change in the electron density:

$$\delta V_{\text{hxc}}^\sigma(\mathbf{r}t) = \sum_{\tau} \int \int f_{\text{hxc}}^{\sigma\tau}[\rho_{\text{gs}}](\mathbf{r}t, \mathbf{r}'t') \delta \rho_{\tau}(\mathbf{r}'t') d\mathbf{r}' dt'. \quad (2.28)$$

$f_{\text{hxc}}^{\sigma\tau}[\rho_{\text{gs}}]$ is the sum of the Hartree and XC kernels evaluated at the ground-state density, which in the adiabatic approximation reads

$$\begin{aligned} f_{\text{hxc}}^{\sigma\tau}[\rho_{\text{gs}}](\mathbf{r}t, \mathbf{r}'t') &= \delta(t-t') \left(\frac{1}{|\mathbf{r}-\mathbf{r}'|} + \left. \frac{\delta V_{\text{xc}}^\sigma[\rho_{t,\uparrow}, \rho_{t,\downarrow}](\mathbf{r}')}{\delta \rho_{t,\tau}(\mathbf{r})} \right|_{\rho_{\text{gs}}} \right) \\ &= \delta(t-t') f_{\text{hxc}}^{\sigma\tau}[\rho_{\text{gs}}](\mathbf{r}, \mathbf{r}'). \end{aligned} \quad (2.29)$$

Now, we turn our attention to the change in the charge density, $\delta \rho_{\sigma}$. According to the first RG theorem, there is a one-to-one mapping between the time-dependent density and the external potential. Thus, to first order, the density fluctuation is given by the linear density response to the external perturbation, characterized by the nonlocal susceptibility χ of the many-body system at the ground-state density:

$$\delta \rho_{\sigma}(\mathbf{r}t) = \sum_{\tau} \int \int \chi^{\sigma\tau}[\rho_{\text{gs}}](\mathbf{r}t, \mathbf{r}'t') \delta V_{\text{ext}}(\mathbf{r}'t') d\mathbf{r}' dt' \quad (2.30)$$

On the other side, the linear density response equals that of the KS system due to the perturbation of the KS Hamiltonian and we hence can write,

$$\delta \rho_{\sigma}(\mathbf{r}t) = \sum_{\tau} \int \int \chi_s^{\sigma\tau}[\rho_{\text{gs}}](\mathbf{r}t, \mathbf{r}'t') \delta V_s^\tau(\mathbf{r}'t') d\mathbf{r}' dt', \quad (2.31)$$

where χ_s is the KS susceptibility, that is, the response function of a system of noninteracting particles with unperturbed density ρ_{gs} . We can thereby substitute Eq. (2.27) into (2.31) and equate with Eq. (2.30), which leads to a Dyson-like equation for the true χ of the system [144]:

$$\begin{aligned} \chi^{\sigma\tau}(\mathbf{r}t, \mathbf{r}'t') &= \chi_s^{\sigma\tau}(\mathbf{r}t, \mathbf{r}'t') \\ &+ \sum_{\sigma'\tau'} \int \int \int \int \chi_s^{\sigma\sigma'}(\mathbf{r}t, \mathbf{r}t) f_{\text{hxc}}^{\sigma'\tau'}(\mathbf{r}t, \mathbf{r}'t') \chi^{\tau'\tau}(\mathbf{r}'t', \mathbf{r}'t') d\mathbf{r}d\mathbf{r}'dt dt' \end{aligned} \quad (2.32)$$

This is the central equation of linear-response TD-DFT. The KS susceptibility can be easily calculated from time-dependent perturbation theory. The susceptibility of the real interacting system contains valuable information. Their poles are the excitation energies of the system. Furthermore, response properties such as the dynamic polarizability can be determined; oscillator strengths are then found as the residues of the mean polarizability.

The poles of χ can be determined as the solution to an eigenvalue problem as pointed out by Casida [143]. To this end, we now move to a matrix representation. This implies to set, for example, $\delta\rho_\sigma = \sum_{st} \psi_{s\sigma}\psi_{t\sigma}\delta P_{st}^\sigma$ and $\delta V_s^\sigma = \sum_{st} \delta V_{st}^s P_{st}^\sigma$, where $P_{st}^\sigma = \langle \Psi | \hat{a}_{t\sigma}^\dagger \hat{a}_{s\sigma} | \Psi \rangle$ are the elements of the KS density matrix. Next, changing to the frequency domain by Fourier transforming in time, one can write the linear response of the KS density matrix to the applied field as

$$\delta P_{st}^\sigma(\omega) = \sum_{uv\tau} \chi_{st\sigma,uv,\tau}^s(\omega) \delta V_{uv\tau}^s(\omega) = \frac{n_{s\sigma} - n_{t\sigma}}{\omega_{st} - \omega} \delta V_{st\sigma}^s(\omega), \quad (2.33)$$

where $\omega_{st\sigma} = \varepsilon_{s\sigma} - \varepsilon_{t\sigma}$ is the KS energy difference relative to states s and t , solutions of the stationary KS equation. The energies $\omega_{st\sigma}$ are the poles of the KS susceptibility. It should be noted that δP_{st}^σ vanishes when the KS orbitals $\psi_{s\sigma}$ and $\psi_{t\sigma}$ have equal occupations, that is, only elements of the type δP_{ia}^σ and δP_{ai}^σ are nonzero. This means, in turn, that only KS matrix elements of the type $\delta V_{ia\sigma}^s$ and $\delta V_{ai\sigma}^s$ contribute to the density matrix response. Thereby, the linear density response can be expressed as

$$\delta\rho_\sigma(\omega) = \sum_{ia} (\psi_{i\sigma}\psi_{a\sigma} X_{ia}^\sigma(\omega) + \psi_{i\sigma}\psi_{a\sigma} Y_{ia}^\sigma(\omega)), \quad (2.34)$$

where $X_{ia}^\sigma = \delta P_{ia}^\sigma$ and $Y_{ia}^\sigma = \delta P_{ai}^\sigma$. The matrix elements $\delta V_{ia\sigma}^s$ and $\delta V_{ai\sigma}^s$ depend, in turn, on the response of the density matrix through the Hartree-XC component,

$$\begin{aligned} \delta V_{ia\sigma}^{\text{hxc}}(\omega) &= \sum_{uv\tau} K_{ia\sigma,uv\tau}(\omega) \delta P_{uv}^\tau(\omega) \\ &= \sum_{jb\tau} (K_{ia\sigma,jb\tau}(\omega) X_{jb}^\tau(\omega) + K_{ia\sigma,bj\tau}(\omega) Y_{jb}^\tau(\omega)), \end{aligned} \quad (2.35)$$

and an identical relation holds for the matrix elements $\delta V_{ai\sigma}^{\text{hxc}}$. The elements of the coupling matrix \mathbf{K} are generally defined as the derivative of the unperturbed KS Hamiltonian with respect to the density matrix elements. In the adiabatic approximation this leads to

$$\begin{aligned} K_{ia\sigma,jb\tau} &= \frac{\partial H_{ia\sigma}}{\partial P_{jb}^\tau} = \frac{\partial V_{ia\sigma}^{\text{hxc}}}{\partial P_{jb}^\tau} \\ &\cong \int \int \psi_{i\sigma}(\mathbf{r}) \psi_{a\sigma}(\mathbf{r}) f_{\text{hxc}}^{\sigma\tau}[\rho_{gs}](\mathbf{r}, \mathbf{r}') \psi_{j\tau}(\mathbf{r}') \psi_{b\tau}(\mathbf{r}') d\mathbf{r}d\mathbf{r}'. \end{aligned} \quad (2.36)$$

It should be noticed that the dependence of \mathbf{K} upon the frequency vanishes within the adiabatic approximation. An important feature of the coupling matrix for local or semi-local XC functionals is its invariance with respect to the permutation of any connected (real orbital) indices (for instance, $K_{ia\sigma,jb\tau} = K_{ia\sigma,bj\tau} = K_{ai\sigma,jb\tau}$). This symmetry does not hold for functionals involving Hartree-Fock exchange [143].

Substituting Eq. (2.35) and (2.27) into (2.33) while setting $\delta V_{\text{ext}} = 0$ (condition for a system excitation) yields two coupled equations (one for $\delta V_{ia\sigma}^s$ and one for $\delta V_{ai\sigma}^s$) for the determination of the excitation energies, ω_I , which can be written as a single matrix equation,

$$\begin{pmatrix} \mathbf{A} & \mathbf{B} \\ \mathbf{B} & \mathbf{A} \end{pmatrix} \begin{pmatrix} \mathbf{X}_I \\ \mathbf{Y}_I \end{pmatrix} = \omega_I \begin{pmatrix} \mathbf{C} & 0 \\ 0 & -\mathbf{C} \end{pmatrix} \begin{pmatrix} \mathbf{X}_I \\ \mathbf{Y}_I \end{pmatrix}, \quad (2.37)$$

where the matrices \mathbf{A} , \mathbf{B} and \mathbf{C} are defined according to

$$\begin{aligned} A_{ia\sigma,jb\tau} &= \frac{\delta_{ij}\delta_{ab}\delta_{\sigma\tau}\omega_{jb\tau}}{n_{j\tau} - n_{b\tau}} + K_{ia\sigma,jb\tau} \\ B_{ia\sigma,jb\tau} &= K_{ia\sigma,bj\tau} \\ C_{ia\sigma,jb\tau} &= \frac{\delta_{ij}\delta_{ab}\delta_{\sigma\tau}}{n_{j\tau} - n_{b\tau}}. \end{aligned} \quad (2.38)$$

The dimension of the eigenproblem (2.37) can be reduced by half *via* a suitable unitary transformation:

$$(\mathbf{A} - \mathbf{B})(\mathbf{A} + \mathbf{B})|\mathbf{X}_I + \mathbf{Y}_I\rangle = \omega_I^2 \mathbf{C}^2 |\mathbf{X}_I + \mathbf{Y}_I\rangle. \quad (2.39)$$

Next, provided that the orbital rotation Hessian $(\mathbf{A} - \mathbf{B})$ is positive definitive, Eq. (2.39) can be further transformed to finally yield the so-called Casida equation:

$$\mathbf{\Omega} \mathbf{F}_I = \omega_I^2 \mathbf{F}_I, \quad (2.40)$$

where the response matrix $\mathbf{\Omega}$ is defined as

$$\mathbf{\Omega} = \mathbf{S}^{-1/2} (\mathbf{A} + \mathbf{B}) \mathbf{S}^{-1/2} \quad (2.41)$$

$$\mathbf{S} = -\mathbf{C} (\mathbf{A} - \mathbf{B})^{-1} \mathbf{C}. \quad (2.42)$$

Due to the symmetry of the coupling matrix, $(\mathbf{A} - \mathbf{B})$ becomes strictly diagonal. Thus, the expression for the response matrix elements acquires the following simplified form:

$$\Omega_{ia\sigma,jb\tau} = \delta_{ij}\delta_{ab}\delta_{\sigma\tau}\omega_{jb\tau}^2 + 2\sqrt{(n_{i\sigma} - n_{a\sigma})\omega_{ia\sigma}} K_{ia\sigma,jb\tau} \sqrt{(n_{j\tau} - n_{b\tau})\omega_{jb\tau}}. \quad (2.43)$$

For closed shell systems the problem can be further simplified after a unitary transformation of the response matrix into a diagonal block matrix,

$$\tilde{\mathbf{\Omega}} = \mathbf{U}^{-1} \mathbf{\Omega} \mathbf{U} = \begin{pmatrix} \mathbf{\Omega}^S & 0 \\ 0 & \mathbf{\Omega}^T \end{pmatrix}, \quad (2.44)$$

where the singlet (S) and triplet (T) response submatrices are

$$\Omega_{ia,jb}^{S/T} = \omega_{jb}^2 \delta_{ij} \delta_{ab} + 2\sqrt{(n_i - n_a)\omega_{ia}} K_{ia,jb}^{S/T} \sqrt{(n_j - n_b)\omega_{jb}}, \quad (2.45)$$

with

$$\begin{aligned} K_{ia,jb}^S &= K_{ia\uparrow,jb\uparrow} + K_{ia\uparrow,jb\downarrow} \\ K_{ia,jb}^T &= K_{ia\uparrow,jb\uparrow} - K_{ia\uparrow,jb\downarrow}. \end{aligned} \quad (2.46)$$

In this way the dimension of the eigenvalue problem is again reduced, and the singlet-triplet and singlet-singlet excitations can be independently computed.

Once the excitation vectors, \mathbf{F}_I , are obtained, the oscillator strength related to excitation I can be calculated as

$$f^I = \frac{2}{3} \sum_{k=1}^3 \left| \sum_{ia\sigma} d_{ia\sigma}^k \sqrt{(n_{i\sigma} - n_{a\sigma}) \omega_{ia\sigma}} F_{ia\sigma}^I \right|^2, \quad (2.47)$$

where $d_{ia\sigma}^k = \langle \psi_{i\sigma} | \hat{r}_k | \psi_{a\sigma} \rangle$ is the k -th component of the dipole matrix element $\mathbf{d}_{ia\sigma}$, with \hat{r}_k denoting the k -th component of the position operator, $\hat{\mathbf{r}}$.

A very basic simplification of TD-DFT is carried out within the single-pole approximation (SPA) [144–147], which consists of truncating $\mathbf{\Omega}$ to a 1×1 matrix. It works surprisingly well in several cases. However, the most important fact about this approach is not its often accurate performance, but the fact that it provides with a simple model for the qualitative understanding of TD-DFT results. Within the SPA, the excitation energies can be directly evaluated from the KS energy difference and the corresponding diagonal coupling matrix element as follows:

$$\omega_{I(ia\sigma)} \approx \omega_{ia\sigma} + (n_{i\sigma} - n_{a\sigma}) K_{ia\sigma,ia\sigma}. \quad (2.48)$$

From Eq. (2.48) one can see that the coupling matrix plays a fundamental role in the scheme. It has the effect of shifting the true excitation energies away from the transition energies of the KS noninteracting system. On the other hand, oscillator strengths are not corrected within the SPA, that is, they keep their KS values,

$$f_{I(ia\sigma)} = \frac{2}{3} (n_{i\sigma} - n_{a\sigma}) \omega_{ia\sigma} \sum_{k=1}^3 |d_{ia\sigma}^k|^2. \quad (2.49)$$

The SPA fails for systems with important collective effects. A more advance approach is the double-pole approximation (DPA), which accounts for pairs of strongly coupled KS transitions [148].

Chapter 3

THE DENSITY FUNCTIONAL BASED TIGHT BINDING METHOD

There exist several quantum mechanical approaches for the calculation of energies and interatomic forces in solids. Among them, DFT-based methods have become increasingly popular due to their accuracy and efficiency. However, there are still many problems that escape from the scope of DFT due to their demanding computational requirements. Less accurate approaches have emerged to address, at least qualitatively, interatomic interaction in solid-state physics. Those schemes include models described by Kim-Gordon theory [149], pseudopotential perturbation methods [150] or the semiempirical tight-binding (TB) approach. Although the latter was first intended for the study of periodic solids only [151], it has been subsequently generalized to an atomistic total-energy method.

In the simplest TB model, the total electronic energy is written as

$$E = \sum_i n_i \varepsilon_i + \frac{1}{2} \sum_{\substack{A \neq B \\ AB}} U(|\mathbf{R}_A - \mathbf{R}_B|), \quad (3.1)$$

where ε_i are the solution of a non-self-consistent Schrödinger equation,

$$\hat{H}\psi_i(\mathbf{r}) = \left[-\frac{1}{2}\nabla^2 + V(\mathbf{r}) \right] \psi_i(\mathbf{r}) = \varepsilon_i \psi_i(\mathbf{r}), \quad (3.2)$$

and $U(|\mathbf{R}_A - \mathbf{R}_B|)$ is a short-range pairwise potential between atoms A and B which is usually fitted to experiment. Application of the variational principle to (3.1) and consequent expansion of the eigenfunctions ψ_i in a basis of atomiclike orbitals, $\{\phi_\alpha\}$, leads to a secular equation,

$$|\mathbf{H} - \varepsilon \mathbf{S}| = 0, \quad (3.3)$$

where $H_{\alpha\beta} = \langle \phi_\alpha | \hat{H} | \phi_\beta \rangle$ and $S_{\alpha\beta} = \langle \phi_\alpha | \phi_\beta \rangle$. The basis functions are often chosen to be orthogonal which results in $\mathbf{S} = \mathbf{I}$, whereas the Hamiltonian matrix elements are treated as parameters fitted to the band structure of a reference system.

Although the TB approach has been applied with some success [152–155], critical limitations have been acknowledged [156, 157]. Issues arise due to the limited transferability of the derived parameters. While they are designed to reproduce properties of the reference system, they

fail to cover a wide range of different problems. The poor transferability of the parameters is mainly given, on the one hand, because they lack physical meaning. On the other hand, it has been shown that orthogonality of the basis functions often hinders transferability [158]. These problems might be then remediated by adopting a nonorthogonal basis set and calculating the parameters directly from a more fundamental theory. Approaches in this direction include the linear muffin-tin orbitals (LMTO) TB scheme of Andersen and Jepsen [159], a Hartree Fock-based TB [160] and the density functional-based TB method (DFTB) [89, 90], to which this chapter is devoted.

The formulation of DFTB presented here differs from its original derivation as we express the energy functional and Hamiltonian in terms of the density matrix fluctuation and not in terms of net Mulliken charges as it is traditionally done. The final expressions for the energy and Hamiltonian are obtained after applying the Mulliken approximation for the evaluation of two-electrons integrals. Mulliken charges then appear naturally and unambiguously and not as one choice for the electron density partition. This formulation is appropriate for a following extension of DFTB that goes beyond the Mulliken approach.

3.1 Tight Binding meets DFT

A connection between DFT and TB total energy expressions is not straightforward as that would suppose that the double-counting energy in Eq. (2.11) can be represented by the sum of short-range pair potentials. Another contrasting aspect rests on the self-consistent nature of the KS equations *versus* the non-self-consistency in TB. Foulkes and Haydock, based on the work by Harris [161], were the first to relate this two theories [162]. They stated that the DFT energy functional at a given density ρ , close to the ground state density, can be written as¹

$$E[\rho] = \sum_i n_i \varepsilon_i + E_H[\rho] + E_{xc}[\rho] - \int V_H[\rho_0] \rho(\mathbf{r}) d\mathbf{r} - \int V_{xc}[\rho_0] \rho(\mathbf{r}) d\mathbf{r}, \quad (3.4)$$

where ρ_0 is such that the eigenfunctions ψ_i of the Hamiltonian $\hat{H}^0 = -\frac{1}{2}\nabla^2 + V_s[\rho_0]$ describe a noninteracting electron gas with density $\rho(\mathbf{r}) = \sum_i n_i |\psi_i(\mathbf{r})|^2$ and ε_i are the eigenvalues of \hat{H}^0 . ρ_0 can be then understood as a guessed ground-state density from which the input Hamiltonian \hat{H}^0 is constructed, whose eigenfunctions, in turn, lead to the output density ρ , at which the functional is to be evaluated. Eq. (3.4) is obtained by taking $V_s[\rho_0] = V_{\text{ext}} + V_H[\rho_0] + V_{xc}[\rho_0]$ in Eq. (2.7), that is, having the form of the self-consistent potential $V_s[\rho_{\text{gs}}]$, Eq. (2.8). This is justified on the basis of ρ being a good guess of the ground-state density and hence, $V_s[\rho_0]$ being close to $V_s[\rho_{\text{gs}}]$.

Expansion of $E[\rho]$ about ρ_0 yields

$$E[\rho] = \mathcal{E}[\rho_0] + \frac{1}{2} \iint f_{\text{hxc}}[\rho_0](\mathbf{r}, \mathbf{r}') \Delta\rho(\mathbf{r}) \Delta\rho(\mathbf{r}') d\mathbf{r} d\mathbf{r}' + \dots, \quad (3.5)$$

¹In Ref. [162] ρ and ρ_0 are termed n_{out} and n_{in} , respectively.

where $\Delta\rho = \rho - \rho_0$ and $f_{\text{hxc}} = f_{\text{H}} + f_{\text{xc}}$ with

$$\begin{aligned} f_{\text{H}}(\mathbf{r}, \mathbf{r}') &= \frac{\delta^2 E_{\text{H}}[\rho]}{\delta\rho(\mathbf{r})\delta\rho(\mathbf{r}')} = \frac{1}{|\mathbf{r} - \mathbf{r}'|} \\ f_{\text{xc}}[\rho](\mathbf{r}, \mathbf{r}') &= \frac{\delta^2 E_{\text{xc}}[\rho]}{\delta\rho(\mathbf{r})\delta\rho(\mathbf{r}')}. \end{aligned} \quad (3.6)$$

The quantity \mathcal{E} is sometimes called the Harris functional and is defined as follows:

$$\mathcal{E}[\rho] = \sum_i n_i \varepsilon_i - E_{\text{H}}[\rho] + E_{\text{xc}}[\rho] - \int V_{\text{xc}}[\rho]\rho(\mathbf{r})d\mathbf{r}. \quad (3.7)$$

This functional has an important meaning. It coincides with $E[\rho]$ at the ground-state density (see Eq. (2.11)) and is also stationary about this density. \mathcal{E} is, however, not strictly variational as a small fluctuation around its ground-state value, $\delta\mathcal{E} = \mathcal{E}[\rho_{\text{gs}} + \delta\rho] - \mathcal{E}[\rho_{\text{gs}}]$, may be either positive or negative. Its advantage with respect to $E[\rho]$ relies on the fact that it does not depend explicitly on the output density ρ , and the eigenvalues ε_i are the solution of a non-self-consistent Schrödinger equation where the effective potential depends on ρ_0 only. Thus, the problem of finding the stationary solution of \mathcal{E} is equivalent to (and much simpler than) solving the KS equations, whereas the error of $\mathcal{E}[\rho_0]$ with respect to the actual ground-state energy are second order in the error of the guessed density.

Now, it only remains to choose the input density ρ_0 . Foulkes and Haydock stressed that there are many ways to define ρ_0 and that some choices may work better for some materials than others do [162]. To keep the scheme simple, the obvious option is to take ρ_0 as the superposition of spherical atomiclike densities,

$$\rho_0(\mathbf{r}) = \sum_A \rho_A(\mathbf{r}). \quad (3.8)$$

Evaluation of the Harris functional at this input density leads to

$$\mathcal{E}[\rho_0] = \sum_i n_i \varepsilon_i - \sum_A E_{\text{H}}[\rho_A] - \frac{1}{2} \sum_{A \neq B} \iint \frac{\rho_A(\mathbf{r})\rho_B(\mathbf{r}')}{|\mathbf{r} - \mathbf{r}'|} d\mathbf{r}d\mathbf{r}' + \mathcal{E}_{\text{xc}} \left[\sum_A \rho_A \right], \quad (3.9)$$

where \mathcal{E}_{xc} is the exchange-correlation contribution (third and fourth terms in (3.7)) to \mathcal{E} and $E_{\text{H}}[\rho_A]$ is the intra-atomic Hartree energy of atom A . Due to the spherical symmetry of the atomic densities ρ_A , the third term in (3.9) is given exactly by the sum of strictly pairwise potentials. If in addition the atomic densities are subject to the constraint, $\int \rho_A(\mathbf{r})d\mathbf{r} = Z_A$, and we explicitly include the nucleus-nucleus repulsion energy, E_{NN} , the resulting two-body potentials become also short-range, since at large interatomic distances the electron-electron and nucleus-nucleus interactions are canceled. Unlike E_{H} , \mathcal{E}_{xc} is not separable into pair potentials because of the nonlinearity of exchange-correlation functionals, but it is possible to expand it in a cluster series as

$$\mathcal{E}_{\text{xc}} \left[\sum_A \rho_A \right] = \sum_A \mathcal{E}_{\text{xc}}[\rho_A] + \frac{1}{2} \sum_{A \neq B} (\mathcal{E}_{\text{xc}}[\rho_A + \rho_B] - \mathcal{E}_{\text{xc}}[\rho_A] - \mathcal{E}_{\text{xc}}[\rho_B]) + \dots, \quad (3.10)$$

and truncate the expansion after the two center term by arguing that the overlap of densities from three or more atoms is negligible [162]. This argument also relies on the screening of

electron-electron and nucleus-nucleus interaction of the chosen neutral atomic charges. Thus, the Harris functional can be finally written in a TB form²:

$$\mathcal{E}[\rho_0] = \sum_i n_i \varepsilon_i + \sum_A (\mathcal{E}_{\text{xc}}[\rho_A] - E_{\text{H}}[\rho_A]) + \frac{1}{2} \sum_{\substack{A \neq B \\ AB}} U_{AB} (|\mathbf{R}_A - \mathbf{R}_B|). \quad (3.11)$$

The repulsive potentials U_{AB} include the Hartree and XC pairwise contributions. These potentials can be easily evaluated from a dimer calculation and are by concept completely transferable. The eigenvalues ε_i are obtained from the one-electron Schrödinger equation,

$$\hat{H}^0 \psi_i(\mathbf{r}) = \left[-\frac{1}{2} \nabla^2 + \sum_A V_A(\mathbf{r}) + U(\mathbf{r}) \right] \psi_i(\mathbf{r}) = \varepsilon_i \psi_i(\mathbf{r}), \quad (3.12)$$

where $V_A = V_{\text{ext},A} + V_{\text{H}}[\rho_A] + V_{\text{xc}}[\rho_A]$ and U is a small additional potential due to the nonlinearity of the exchange-correlation functional, $U = V_{\text{xc}}[\sum_A \rho_A] - \sum_A V_{\text{xc}}[\rho_A]$. As \hat{H}^0 is not self-consistent, the eigenvalues ε_i can be easily obtained after reducing (3.12) to a secular equation (3.3). For this, a suitable basis of nonorthogonal atomiclike functions has to be defined, and the Hamiltonian and overlap matrices have to be evaluated.

3.2 The Standard DFTB Approach

The DFTB method is an example of how one could employ the theory described above in practice. The formalism follows as a series of approximations and considerations made to the scheme of Foulkes and Haydock.

3.2.1 Input density and basis set

First, it is desirable to define a proper atomiclike densities ρ_A , which superposed conform the input density ρ_0 . This is a very important step as a well guessed density will greatly determine the success of the method. A natural choice is to obtain the density of the corresponding isolated atom *via* a self-consistent DFT atomic calculation. However, free-atom densities are diffuse, and their superposition does not represent properly the density of a compound system. To simulate the effect of neighboring atoms on the atomic density, they are calculated using a modified KS equation,

$$\left[-\frac{1}{2} \nabla^2 + V_{\text{s}}[\rho_A] + \left(\frac{r}{r_0} \right)^2 \right] \phi_\nu(\mathbf{r}) = \varepsilon_\nu \phi_\nu(\mathbf{r}), \quad (3.13)$$

where an extra parabolic³ potential, $(r/r_0)^2$, is introduced for confinement purposes. The resulting densities are compressed with respect to the free-atom densities and are therefore a

² $E_{\text{H}}[\rho_A]$ and $E_{\text{xc}}[\rho_A]$ depend only on the chosen ρ_A densities and so they are just constant contributions to the total energy for any atomic configuration of a given system.

³In principle, the exponent of the confinement potential can be considered an adjustable parameter and indeed, it was originally set to 4 [163]. Later on, it was shown that this parameter has rather small influence on the results [164] and it is nowadays usually taken as 2. However, see Ref. [165] for a recent parametrization scheme where values ranging from 2 to 16.8 are used. See also Refs. [166, 167] for suggested alternative form of the confinement potential for the calculation of pseudoatomic orbitals.

more suitable choice for the description of a wide variety of molecules and condensed systems. The confinement radius, r_0 , is chosen for the given element to yield an optimal transferability in different reference systems.

Another important aspect of the method deals with the employed basis set. In DFTB a minimal set of compressed AO is used. There are two possible routes for their computation. The first one uses Eq. (3.13) to obtain self-consistently both the density and the atomic functions for the *pseudo-atom* [164]. The second way considers the calculation of the atomic density and orbitals in separate steps, where different confinement radii are employed. While the former scheme intends to keep a low number of parameters to be handled, the latter offers the possibility to improve DFTB results by individual optimization of the basis set. The confinement radius used for the AO has been shown to have an optimal value of about $1.85 r_{\text{cov}}$, where r_{cov} is the covalent radius of the corresponding element. The value of r_0 for the calculation of the densities is usually taken larger and may vary strongly from element to element. The pseudo-atomic wave functions are constructed by the linear combination of Slater-type orbitals (STO),

$$\phi_\mu(\mathbf{r}) = \sum_{i=1}^{n_i} \sum_{j=0}^{n_j} a_{ij} r^{l+j} e^{-\alpha_i r} Y_{lm} \left(\frac{\mathbf{r}}{r} \right), \quad (3.14)$$

and characterized by their angular momentum l and magnetic quantum number m . All functions are centered at the corresponding atom. Orbitals corresponding to the same atom are therefore orthogonal.

3.2.2 Hamiltonian and overlap matrices

Once the atomic orbitals ϕ_ν and densities ρ_A are obtained, the Hamiltonian and overlap matrices can be determined as

$$H_{\mu\nu}^0 = \langle \phi_\mu | -\frac{1}{2} \nabla^2 + V_s \left[\sum_A \rho_A \right] | \phi_\nu \rangle, \quad S_{\mu\nu} = \langle \phi_\mu | \phi_\nu \rangle. \quad (3.15)$$

Although in DFTB the effective potential V_s was initially decomposed into atomiclike contributions as in (3.12), today it is an established practice to evaluate V_s at the superposed atomic densities⁴. In this way, the nonlinearity of the XC functional is accounted. In practice, the potential is not evaluated at the sum of all atomic densities. Even considering the sum of densities of first neighbor atoms would complicate the scheme considerably. Instead, the evaluation of V_s in the matrix element $H_{\mu\nu}^0$ contemplates only the contributions from those atoms at which the orbitals ϕ_μ and ϕ_ν are located. If we consider $\mu \in A$ and $\nu \in B$, with $A \neq B$ the Hamiltonian matrix elements read

$$H_{\mu\nu}^0 = \langle \phi_\mu | -\frac{1}{2} \nabla^2 + V_s[\rho_A + \rho_B] | \phi_\nu \rangle. \quad (3.16)$$

In this way, three-center or higher terms are completely neglected within DFTB. The atomic blocks of the Hamiltonian matrix are described by a diagonal matrix, $H_{\mu\nu} = \delta_{\mu\nu} \varepsilon_\mu$, where ε_μ are the eigenvalues of the Hamiltonian for an isolated atom, which ensures the correct limit for a dissociated system. The energies ε_μ are obtained *via* SCF DFT calculations for a single

⁴However, in a very recent DFTB parametrization scheme [165] the authors obtain better band structure energies and curvatures when superposing the potentials than when employing a density superposition.

atom. The Hamiltonian and overlap matrix elements are then determined with respect to the distance of the atom pairs and are tabulated. Thus, no integral evaluation is required during geometry optimizations or MD runs.

3.2.3 Repulsive potential

For the evaluation of the Harris functional, Eq. (3.11), it only remains to evaluate the one and two-body potentials. To ensure that at large distances the repulsive energy goes to zero, all monomer (constant) contributions are ignored. The pairwise potentials are not calculated by its direct evaluation at ρ_0 , but fitted to *ab initio* results for a reference system. They are then represented by a polynomial or spline for every pair of elements up to a limit interatomic distance R_c (see, for example, Refs. [168, 169]). This cutoff distance is usually chosen between 1.5 to 2 times the equilibrium bond length.

The DFTB total energy can be finally written as

$$E = \mathcal{E}[\rho_0] = \sum_i n_i \varepsilon_i + E_{\text{rep}}, \quad (3.17)$$

where the repulsive energy, E_{rep} , comprises the sum of the fitted pairwise potentials.

3.3 Second Order Corrections

Numerous systems and materials have been successfully investigated within the DFTB approach [89, 170–176]. But not for every case the chosen input density is satisfactory. For systems with considerably charged atoms the error introduced by the assumed neutral density becomes appreciable. Such problematic systems include heteronuclear molecules and polar semiconductors. A systematic extension of the method is accomplished by including up to the second term of the energy functional (3.5), that is, the second-order in the density difference $\Delta\rho$. This leads to a self-consistent scheme with the iterative update of the electron density until convergence is reached. Such an extension is called self-consistent-charge DFTB (SCC-DFTB).

In the following we will consider a spin-unrestricted scheme [177]. This generalization implies to write the second-order contribution to the energy as

$$E^{(2)} = \frac{1}{2} \sum_{\sigma\tau} \iint \Delta\rho_\sigma(\mathbf{r}) f_{\text{hxc}}^{\sigma\tau}[\rho_0](\mathbf{r}, \mathbf{r}') \Delta\rho_\tau(\mathbf{r}') d\mathbf{r}d\mathbf{r}', \quad (3.18)$$

where the sum runs over the spin variables $\sigma = \uparrow, \downarrow$, and $\Delta\rho_\sigma = \rho_\sigma - \rho_{0,\sigma}$. The input density $\rho_0 = [\rho_{0,\uparrow}, \rho_{0,\downarrow}]$ is chosen spin-unpolarized ($\rho_{0,\uparrow}(\mathbf{r}) - \rho_{0,\downarrow}(\mathbf{r}) = 0, \forall \mathbf{r}$). The exchange-correlation component of f_{hxc} now depends on the spin-dependent electron density,

$$f_{\text{xc}}^{\sigma\tau}[\rho](\mathbf{r}, \mathbf{r}') = \frac{\delta^2 E_{\text{xc}}[\rho]}{\delta\rho_\sigma(\mathbf{r})\delta\rho_\tau(\mathbf{r}')}. \quad (3.19)$$

For the succeeding formulation, the Greek indices $\mu, \nu, \kappa, \lambda$ will denote atomic orbitals (AO). Let us also abbreviate a general two-point integral over a kernel $g(\mathbf{r}, \mathbf{r}')$ in the following form:

$$(f|g|h) = \iint f(\mathbf{r})g(\mathbf{r}, \mathbf{r}')h(\mathbf{r}') d\mathbf{r}d\mathbf{r}'. \quad (3.20)$$

For atomic orbital products $f(\mathbf{r}) = \phi_\mu(\mathbf{r})\phi_\nu(\mathbf{r})$ and $h(\mathbf{r}') = \phi_\kappa(\mathbf{r}')\phi_\lambda(\mathbf{r}')$ the shorthand $(\mu\nu|g|\kappa\lambda)$ will be also used. Expanding the KS orbitals into the AO set, $\psi_{s\sigma} = \sum_\mu c_{\mu s}^\sigma \phi_\mu$, $E^{(2)}$ can be written as

$$E^{(2)} = \frac{1}{2} \sum_{\sigma\tau} \sum_{\mu\nu\kappa\lambda} \Delta P_{\mu\nu}^\sigma (\mu\nu|f_{\text{hxc}}^{\sigma\tau}[\rho_0]|\kappa\lambda) \Delta P_{\kappa\lambda}^\tau, \quad (3.21)$$

where $\Delta P_{\mu\nu}^\sigma = P_{\mu\nu}^\sigma - P_{\mu\nu}^{0,\sigma}$ denotes the AO density matrix of the difference density $\Delta\rho_\sigma(\mathbf{r})$, with

$$P_{\mu\nu}^\sigma = \sum_{st} c_{\mu s}^\sigma c_{\nu t}^\sigma P_{st}^\sigma, \quad P_{\mu\nu}^{0,\sigma} = \sum_{st} c_{\mu s}^\sigma c_{\nu t}^\sigma P_{st}^{0,\sigma}. \quad (3.22)$$

Here $P_{st}^\sigma = \langle \Psi | \hat{a}_{t\sigma}^\dagger \hat{a}_{s\sigma} | \Psi \rangle$ are the MO density matrix elements, Ψ being the ground state KS determinant. This leads to $P_{st}^\sigma = n_{s\sigma} \delta_{st}$ for the orthogonal KS functions $\psi_{s\sigma}$. The term $P_{st}^{0,\sigma}$ designates the MO density matrix of the reference system.

By applying the variational principle to the modified energy functional, $E = \mathcal{E}[\rho_0] + E^{(2)}$, we obtain the secular equation (3.3) with a modified DFTB Hamiltonian, $H_{\mu\nu} = H_{\mu\nu}^0 + H_{\mu\nu}^1$, where

$$H_{\mu\nu}^1 = \sum_{\tau} \sum_{\kappa\lambda} (\mu\nu|f_{\text{hxc}}^{\sigma\tau}[\rho_0]|\kappa\lambda) \Delta P_{\kappa\lambda}^\tau. \quad (3.23)$$

Thus, second-order corrections due to charge fluctuations leads to a KS Hamiltonian which includes up to first-order corrections. The Hamiltonian is now self-consistent and so the secular equations are solved iteratively.

3.3.1 Mulliken and monopole approximations

So far the SCC formalism has been described exactly. Next, two important approximations will be applied for the evaluation of the multicenter integrals appearing in (3.21) and (3.23), which will simplify considerably the scheme. First, the Mulliken approximation is applied. This amounts to set $\phi_\mu\phi_\nu \approx \frac{1}{2}S_{\mu\nu}(|\phi_\mu|^2 + |\phi_\nu|^2)$, using the known AO overlap integrals $S_{\mu\nu}$. Thus, the general four-center integrals are written in terms of two-center integrals,

$$(\mu\nu|f_{\text{hxc}}^{\sigma\tau}[\rho_0]|\kappa\lambda) \approx \frac{1}{4}S_{\mu\nu}S_{\kappa\lambda} \sum_{\alpha \in \{\mu,\nu\}} \sum_{\beta \in \{\kappa,\lambda\}} (\alpha\alpha|f_{\text{hxc}}^{\sigma\tau}[\rho_0]|\beta\beta). \quad (3.24)$$

By substituting Eq. (3.24) into (3.21), the second order contribution to the energy reads,

$$E^{(2)} = \frac{1}{2} \sum_{\sigma\tau} \sum_{\mu\nu} \Delta \tilde{P}_{\mu\mu}^\sigma (\mu\mu|f_{\text{hxc}}^{\sigma\tau}[\rho_0]|\nu\nu) \Delta \tilde{P}_{\nu\nu}^\tau, \quad (3.25)$$

where $\tilde{P}_{\mu\nu}^\sigma$ are the elements of the dual density matrix defined as

$$\tilde{\mathbf{P}}^\sigma = \frac{1}{2} (\mathbf{P}^\sigma \cdot \mathbf{S} + \mathbf{S} \cdot \mathbf{P}^\sigma). \quad (3.26)$$

The concept of dual representation of the density matrix was introduced by Han and coworkers in their implementation of the LDA+U method [178]. The authors show that for a nonorthogonal orbital basis this matrix satisfies exactly the sum rule, $\sum_\sigma \text{Tr}(\tilde{\mathbf{P}}^\sigma) = N_e$, where N_e is the

total number of electrons. They also pointed out, that the use of the dual density matrix is consistent with the Mulliken population analysis. Thus, for example, the trace of the atom- A block of $\tilde{\mathbf{P}}^\sigma$ returns the Mulliken population for that atom:

$$q_A^\sigma = \sum_{\mu \in A} \tilde{\mathbf{P}}^\sigma = \sum_s n_{s\sigma} \sum_{\mu \in A} \sum_\nu c_{\mu s}^\sigma c_{\nu s}^\sigma S_{\mu\nu}. \quad (3.27)$$

A further simplification to Eq. (3.25) is obtained by spherical averaging over AO products. Such monopole approximation ensures that the final total energy expression is invariant with respect to arbitrary rotations of the molecular frame. To this end, the functions F_{Al} are introduced:

$$F_{Al}(|\mathbf{r} - \mathbf{R}_A|) = \frac{1}{2l+1} \sum_{m=-l}^{m=l} |\phi_\mu(\mathbf{r} - \mathbf{R}_A)|^2, \quad (3.28)$$

where l and m denote the angular momentum and magnetic quantum number of AO ϕ_μ , centered on atom A . We then have for $\mu = \{Alm\}$, $\nu = \{Bl'm'\}$:

$$(\mu\mu|f_{\text{hxc}}^{\sigma\tau}[\rho_0]|\nu\nu) \approx (F_{Al}|f_{\text{hxc}}^{\sigma\tau}[\rho_0]|F_{Bl'}) = \Gamma_{Al,Bl'}^{\sigma\tau} \quad (3.29)$$

introducing the shorthand notation Γ . Thus, the second-order energy can be expressed as

$$E^{(2)} = \frac{1}{2} \sum_{\sigma\tau} \sum_{AB,l'l'} \Delta q_{Al}^\sigma \Gamma_{Al,Bl'}^{\sigma\tau} \Delta q_{Bl'}^\tau, \quad (3.30)$$

where q_{Al}^σ is the Mulliken population for atom A , angular momentum l and spin σ .

In practice, rather than working with spin-dependent charge fluctuations, it is preferred to evaluate the net charge and spin populations during the self-consistent process. This is achieved after transformation from the set $\{\rho_\uparrow, \rho_\downarrow\}$ to the total density $\rho = \rho_\uparrow + \rho_\downarrow$ and magnetization $m = \rho_\uparrow - \rho_\downarrow$. By this change of variables, the XC kernel can be split and one arrives at (see Appendix A)

$$\Gamma_{Al,Bl'}^{\sigma\tau} = \gamma_{Al,Bl'} + \delta_\sigma \delta_\tau \delta_{AB} W_{Al,l'}, \quad (3.31)$$

where $\delta_\sigma = 2\delta_{\sigma\uparrow} - 1$ and the parameters

$$\gamma_{Al,Bl'} = (F_{Al}|f_{\text{hxc}}[\rho_0]|F_{Bl'}) \quad (3.32)$$

$$W_{Al,l'} = \left(F_{Al} \left| \frac{\delta^2 E_{xc}[\rho, m]}{\delta m(\mathbf{r}) \delta m(\mathbf{r}')} \right|_{\rho_0, 0} \right| F_{Al'} \right). \quad (3.33)$$

The constants $W_{Al,l'}$ depend only on the XC kernel, but not on the long-range Coulomb interaction. Moreover, as the reference density ρ_0 is built from neutral spin-unpolarized atomic densities and the XC functional is an even functional in m , there are no integrals that involve mixed derivatives of the XC energy with respect to both the density and magnetization. The parameters $\gamma_{Al,Bl'}$ and $W_{Al,l'}$ are known in DFTB as the γ -functional and spin coupling constants, respectively [179]. The latter are treated as strictly on-site parameters, whereas $\gamma_{Al,Bl'}$ is calculated for every atom pair using an interpolation formula, that depends on the distance R_{AB} between the atoms A and B and the atomic Hubbard-like parameters $\gamma_{Al,Al}$ and $\gamma_{Bl',Bl'}$:

$$\gamma_{Al,Bl'} = \frac{1}{R_{AB}} - S(R_{AB}, \gamma_{Al,Al}, \gamma_{Bl',Bl'}). \quad (3.34)$$

S is a short-range function ensuring the correct convergence at $R_{AB} = 0$ and the correct R^{-1} behavior at large interatomic distances.

Traditionally, the Hubbard parameters are not computed directly from the integrals (3.32), but from total energy derivatives according to $\gamma_{Al,Al} = \delta^2 E / \delta n^2$, where E denotes the DFT total energy of atom A and n refers to the occupation of the shell with angular momentum l . The derivative is evaluated numerically by full self-consistent field calculations at perturbed occupations. Due to orbital relaxation, Hubbard parameters obtained in this way are roughly 10-20 % smaller than the ones from a direct integral evaluation. It has been pointed out that use of a low-quality basis set leads to overestimated Hubbard parameters as the *missing* basis functions would otherwise screen its value [180]. Thus, the approximation used for determining $\gamma_{Al,Al}$ in DFTB partly compensates for the error introduced by the employed minimal basis. In part because of this error compensation, DFTB often returns better results than DFT itself when employing a minimal basis set.

By substituting Eq. (3.31) into (3.30), the second-order energy term finally reads

$$E^{(2)} = \frac{1}{2} \sum_{AB, ll'} \Delta q_{Al} \gamma_{Al, B l'} \Delta q_{B l'} + \frac{1}{2} \sum_{A, ll'} \Delta m_{Al} W_{Al, l'} \Delta m_{B l'}, \quad (3.35)$$

where $q_{Al} = q_{Al}^{\uparrow} + q_{Al}^{\downarrow}$ and $m_{Al} = q_{Al}^{\uparrow} - q_{Al}^{\downarrow}$ are the Mulliken net charge and spin population of shell l on atom A . Likewise, by applying the Mulliken (3.24) and monopole (3.29) approximations to Eq. (3.23), one arrives at

$$\begin{aligned} H_{\mu\nu\sigma}^1 &= \frac{1}{2} S_{\mu\nu} \sum_{\tau} \sum_{\gamma} [(\mu\mu | f_{\text{hxc}}^{\sigma\tau}[\rho_0] | \gamma\gamma) + (\nu\nu | f_{\text{hxc}}^{\sigma\tau}[\rho_0] | \gamma\gamma)] \Delta \tilde{P}_{\gamma\tau} \\ &= \frac{1}{2} S_{\mu\nu} \sum_{\tau} \sum_{C l''} (\Gamma_{Al, C l''}^{\sigma\tau} + \Gamma_{B l', C l''}^{\sigma\tau}) \Delta q_{C l''}^{\tau} \\ &= \frac{1}{2} S_{\mu\nu} \sum_{C l''} (\gamma_{Al, C l''} + \gamma_{B l', C l''}) \Delta q_{C l''} \\ &\quad + \frac{1}{2} \delta_{\sigma} S_{\mu\nu} \sum_{l''} (W_{Al, l''} \Delta m_{A l''} + W_{B l', l''} \Delta m_{B l''}). \end{aligned} \quad (3.36)$$

It should be noted that atomic blocks of the Hamiltonian matrix are diagonal due to the orthogonality of the AO centered at the same atom. In the SCC scheme, the repulsive potentials are determined as a function of the distance by taking the difference between DFT cohesive energies and the corresponding SCC-DFTB electronic energies, $\sum_i n_i \varepsilon_i + E^{(2)}$, for suitable reference systems. SCC-DFTB has been applied to large biological systems, atomic clusters and solids with great success [181–184]. Nowadays, the use of non-self-consistent DFTB has been diminished in favor of its SCC variant, for which the term DFTB will stand in the following.

3.4 Density Matrix Formulation of DFTB

In this section we propose a more general formulation of DFTB, where the KS Hamiltonian and the total energy are expressed in terms of the KS density matrix fluctuations. This formulation is especially suitable for a linear response extension as the coupling matrix could be obtained directly. Such extension will be addressed in the next chapter.

First, let us express the dual density matrix, $\tilde{\mathbf{P}}^\sigma$, with respect to the MO density matrix elements. Using the definitions (3.22) and (3.26), we obtain,

$$\tilde{P}_{\mu\nu}^\sigma = \sum_{st} \tilde{P}_{\mu\nu}^{st\sigma} P_{st}^\sigma, \quad (3.37)$$

where the matrix $\tilde{\mathbf{P}}^{st\sigma}$ is defined as

$$\tilde{P}_{\mu\nu}^{st\sigma} = \frac{1}{4} (c_{\mu s}^\sigma \tilde{c}_{\nu t}^\sigma + c_{\mu t}^\sigma \tilde{c}_{\nu s}^\sigma + c_{\nu s}^\sigma \tilde{c}_{\mu t}^\sigma + c_{\nu t}^\sigma \tilde{c}_{\mu s}^\sigma), \quad \tilde{\mathbf{c}}_s = \mathbf{c}_s \cdot \mathbf{S}. \quad (3.38)$$

Next, we substitute Eq. (3.37) in the expression of the second-order energy, (3.25). Using the definition of the Γ functional, (3.29), $E^{(2)}$ can be then expressed as

$$E^{(2)} = \frac{1}{2} \sum_{\sigma\tau} \sum_{stuv} \sum_{ABll'} \Delta P_{st}^\sigma q_{Al}^{st\sigma} \Gamma_{Al,Bl'}^{\sigma\tau} q_{Bl'}^{uv\tau} \Delta P_{uv}^\tau, \quad (3.39)$$

where $\Delta P_{st}^\sigma = P_{st}^\sigma - P_{st}^{0,\sigma}$. The quantity $q_{Al}^{st\sigma} = \sum_{\mu \in A,l} \tilde{P}_{\mu\mu}^{st\sigma}$ is the trace of the angular-momentum block of the matrix $\tilde{\mathbf{P}}^{st\sigma}$, corresponding to atom A and momentum l and its importance will be revealed in section 4.1. Also for a later reference, we now define a matrix $\bar{\mathbf{K}}$,

$$\bar{K}_{st\sigma,uv\tau} = \sum_{ABll'} q_{Al}^{st\sigma} \Gamma_{Al,Bl'}^{\sigma\tau} q_{Bl'}^{uv\tau}. \quad (3.40)$$

Using this abbreviation, the DFTB total energy can be written in the following simple form,

$$E = \sum_{\sigma} \sum_{st} H_{st\sigma}^0 P_{st}^\sigma + \frac{1}{2} \sum_{\sigma\tau} \sum_{stuv} \Delta P_{st}^\sigma \bar{K}_{st\sigma,uv\tau} \Delta P_{uv}^\tau + E_{\text{rep}}, \quad (3.41)$$

The DFTB KS equations are obtained after applying the variational principle to the energy functional,

$$H_{st\sigma} - \epsilon_{s\sigma} \delta_{st} = 0, \quad \forall s, t, \sigma, \quad (3.42)$$

where the KS Hamiltonian is expressed as

$$H_{st\sigma} = \frac{\partial E}{\partial P_{st}^\sigma} = H_{st\sigma}^0 + \sum_{\tau} \sum_{uv} \bar{K}_{st\sigma,uv\tau} \Delta P_{uv}^\tau. \quad (3.43)$$

This expression can be recognized as a Taylor expansion of the DFT Hamiltonian up to the first order in the density matrix, around the reference density. $\bar{\mathbf{K}}$ is then identified as the first derivative of the DFT Hamiltonian with respect to the density matrix, evaluated at ρ_0 , within the Mulliken and monopole approximations.

The standard expression for the DFTB Hamiltonian can be retrieved in a straightforward way. First, the KS orbitals are expanded into the AO basis. Then, we employ the expression for the converged ground state density, $P_{st}^\sigma = n_{s\sigma} \delta_{st}$, and the identity $\sum_{st} c_{\mu s}^\sigma P_{st}^{0,\sigma} c_{\nu t}^\sigma = n_{\mu\sigma}^0 \delta_{\mu\nu}$ ($\forall \mu, \nu, \sigma$), $n_{\mu\sigma}^0$ being the occupation numbers for the reference atoms. For details, we refer the reader to Appendix B.

3.5 Beyond the Mulliken Approximation

The original DFTB approach had limitations regarding the description of some molecular systems with an electronic density different from the mere superposition of neutral atomic contributions. The method was significantly improved with the SCC extension, thus addressing in a self-consistent fashion charge transfer between atoms. Afterwards, DFTB has been gradually extended in numerous directions. It was importantly augmented to allow for spin-unrestricted calculations [177,184], which widens the type of systems and properties that can be targeted within the approach. DFTB parameters have also received considerable attention. Witek *et al.*, for example, introduced relativistic effects on the parametrization process, thus broadening the number of chemical elements to be covered by this formalism [166]. The conquest of the periodic table has especially been a longed goal in the DFTB community. Concerning this, a LDA+U-like approach was developed to allow for the correct description of compounds containing elements with strongly localized electrons, such as rare earths and transition metals [185,186]. Very recently, a semiautomatic parametrization scheme for the electronic part of DFTB that covers the periodic table was developed [165]. Other contributions include empirical corrections for dispersion interaction [187,188] as well as implementations for hybrid QM/MM simulations [189,190], just to name a few.

One of the most recent efforts to improve DFTB is based on a third-order expansion of the total energy [191–194]. This appears to be the obvious sequential step to reach a new level of approximation. A higher degree of self-consistency, and hence accuracy, can be obtained with such scheme. This extension becomes particularly important for highly charged molecules and combined with an empirical correction to the γ functional [192] it has been shown to improve the parameter transferability to reproduce hydrogen bonding energies and proton affinities [193]. At this point, an important query may arise: Is there no room left for second-order extensions within DFTB? In second-order DFTB, two main approaches should be recognized: the monopole approximation of the density fluctuations and the Mulliken approach for the evaluation of the multicenter integrals. Possible corrections to these approaches have, however, not been fully exploited. Only for the former, a refinement has been proposed recently, where dipole-monopole interactions are considered [195]. In this section, we address the sophistication of the Mulliken approximation. We will propose a more accurate evaluation of multicenter integrals which does not imply additional computational effort.

The Mulliken approximation has enjoyed considerable popularity amongst chemical physicists for the evaluation of multicenter integrals over atomic basis functions, recognized as one of the most critical bottlenecks in early quantum chemistry. Although the growing computing power of modern workstations allows now for their numerical integration, an approximate treatment of such integrals remains advantageous for the study of large systems. Such is the case of DFTB, where the numerical calculation of those integrals would substantially increase the computational requirements of the method. It should be also mentioned that the analytical evaluation of three- and four-center Coulomb integrals over STOs is neither possible.

The Mulliken approach simplifies the computational scheme considerably as it considers only one- and two-center interactions. While in general, this approximation accounts, at least approximately, for the differential overlap of atomic orbitals, there is an important exception. If orbitals ϕ_μ and ϕ_ν with $\mu \neq \nu$ reside on the same atom, their product vanishes as for every atom sub-block the overlap matrix reduces to the identity due to the orthogonality of basis

functions at a common center. In other words, monoatomic differential overlaps (i.e. overlaps involving orbitals centered at the same atom) are subject to a zero-differential overlap (ZDO) approximation within DFTB. This implies that many three-, two-, and more importantly, one-center integrals are completely neglected even though some of the latter may be fairly large. Visible consequences of this approximation for the calculation of the absorption spectra of some molecules will be shown in the next chapter.

A next level of approximation demands the evaluation of every one-center integral of the exchange type, i.e., $(\mu\nu|f_{\rho_\sigma\rho_\tau}^{\text{hxc}}[\rho_0]|\mu\nu)$ with $\mu \neq \nu$. This resembles how Pople *et al.* proceeded in the development of the intermediate neglect of differential overlap model (INDO) [196] to overcome the deficiencies encountered within the complete neglect of differential overlap method (CNDO) [197]. Unlike the INDO model, where the one-center two-electron integrals are fitted to atomic spectroscopic data, in DFTB the corresponding onsite integrals are calculated by numerical integration. Another difference between the present procedure and that followed in INDO is related to the process of inclusion of the additional terms. Both CNDO and INDO are based on a ZDO approximation and in consequence, all three- and four-center integrals are set to zero. Hence, the direct inclusion of the one-center exchange-like terms in the Fock matrix elements does not introduce any inconsistency in the formalism. DFTB operates in a different way. All multicenter integrals are subject to the same approximation and this leads to neglect of some of them. A refinement of this approach should then consider in an equal manner integrals involving different number of atomic centers. Therefore, we include here up to exchange-like onsite terms in the expansion of every multicenter integral. This ensures that three- and two-center integrals are also refined at the same level of approximation as for one-center terms.⁵

To illustrate this, we follow a derivation that stems from Rüdberg demonstration of Mulliken formula [198]. Let $\{\phi_\alpha\}$ and $\{\phi_\beta\}$ be a complete set of orthonormalized real orbitals centered at atom A and B , respectively. Let also $\mu \in A$, $\nu \in B$, $\kappa \in C$ and $\lambda \in D$ unless otherwise specified. Then, the orbitals ϕ_μ and ϕ_ν can be expanded as

$$\phi_\mu(\mathbf{r}) = \sum_{\beta \in B} S_{\beta\mu} \phi_\beta(\mathbf{r}), \quad \phi_\nu(\mathbf{r}) = \sum_{\alpha \in A} S_{\alpha\nu} \phi_\alpha(\mathbf{r}), \quad (3.44)$$

and the differential overlap of these two orbitals can be expressed as

$$\phi_\mu(\mathbf{r})\phi_\nu(\mathbf{r}) = \frac{1}{2} \left(\sum_{\alpha \in A} S_{\alpha\nu} \phi_\alpha(\mathbf{r})\phi_\mu(\mathbf{r}) + \sum_{\beta \in B} S_{\beta\mu} \phi_\beta(\mathbf{r})\phi_\nu(\mathbf{r}) \right), \quad (3.45)$$

or more conveniently as

$$\begin{aligned} \phi_\mu(\mathbf{r})\phi_\nu(\mathbf{r}) &= \frac{1}{2} S_{\mu\nu} (|\phi_\mu(\mathbf{r})|^2 + |\phi_\nu(\mathbf{r})|^2) \\ &+ \frac{1}{2} \left(\sum_{\alpha \in A}^{\alpha \neq \mu} S_{\alpha\nu} \phi_\alpha(\mathbf{r})\phi_\mu(\mathbf{r}) + \sum_{\beta \in B}^{\beta \neq \nu} S_{\beta\mu} \phi_\beta(\mathbf{r})\phi_\nu(\mathbf{r}) \right), \end{aligned} \quad (3.46)$$

where the first term accounts for the Mulliken approach. Let us now denote with $(\mu\nu|\kappa\lambda)$, a two-electron integral with an arbitrary local or semi-local kernel. Using (3.46), $(\mu\nu|\kappa\lambda)$ can be

⁵Below we show that our refinement does not affect four-center integrals. However, the fact that all multicenter integrals (also four-center) are equally treated ensures consistency throughout the scheme.

expanded as follows:

$$\begin{aligned}
(\mu\nu|\kappa\lambda) &= \frac{1}{4}S_{\mu\nu}S_{\kappa\lambda} [(\mu\mu|\kappa\kappa) + (\mu\mu|\lambda\lambda) + (\nu\nu|\kappa\kappa) + (\nu\nu|\lambda\lambda)] \\
&+ \frac{1}{4}S_{\mu\nu} \left(\sum_{\gamma \in C}^{\gamma \neq \kappa} S_{\gamma\lambda} [(\mu\mu|\kappa\gamma) + (\nu\nu|\kappa\gamma)] + \sum_{\delta \in D}^{\delta \neq \lambda} S_{\delta\kappa} [(\mu\mu|\delta\lambda) + (\nu\nu|\delta\lambda)] \right) \\
&+ \frac{1}{4}S_{\kappa\lambda} \left(\sum_{\alpha \in A}^{\alpha \neq \mu} S_{\alpha\nu} [(\mu\alpha|\kappa\kappa) + (\mu\alpha|\lambda\lambda)] + \sum_{\beta \in B}^{\beta \neq \nu} S_{\beta\mu} [(\beta\nu|\kappa\kappa) + (\beta\nu|\lambda\lambda)] \right) \\
&+ \frac{1}{4} \left(\sum_{\alpha \in A}^{\alpha \neq \mu} \sum_{\gamma \in C}^{\gamma \neq \kappa} S_{\alpha\nu} S_{\gamma\lambda} (\mu\alpha|\kappa\gamma) + \sum_{\alpha \in A}^{\alpha \neq \mu} \sum_{\delta \in D}^{\delta \neq \lambda} S_{\alpha\nu} S_{\delta\kappa} (\mu\alpha|\delta\lambda) \right) \\
&+ \frac{1}{4} \left(\sum_{\beta \in B}^{\beta \neq \nu} \sum_{\gamma \in C}^{\gamma \neq \kappa} S_{\beta\mu} S_{\gamma\lambda} (\beta\nu|\kappa\gamma) + \sum_{\beta \in B}^{\beta \neq \nu} \sum_{\delta \in D}^{\delta \neq \lambda} S_{\beta\mu} S_{\delta\kappa} (\beta\nu|\delta\lambda) \right). \tag{3.47}
\end{aligned}$$

Note that expression (3.47) is exact as long as the AO sets $\{\phi_\alpha\}$, $\{\phi_\beta\}$, $\{\phi_\gamma\}$ and $\{\phi_\delta\}$ are complete. The first line in Eq. (3.47) contains the leading terms, which include Coulomb-like integrals. Truncation of the expansion up to the first line accounts for the Mulliken approximation of multicenter integrals. A next level of approximation demands the further inclusion of every fully-onsite exchange-like integral, i.e., $(\mu\nu|\mu\nu)$, with $\mu, \nu \in A$ and $\mu \neq \nu$. At this level of theory the multicenter integrals can be expressed as

$$(\mu\nu|\kappa\lambda) \approx (\mu\nu|\kappa\lambda)^{\text{mull}} + (\mu\nu|\kappa\lambda)^{\text{ons}}, \tag{3.48}$$

where

$$(\mu\nu|\kappa\lambda)^{\text{mull}} = \frac{1}{4}S_{\mu\nu}S_{\kappa\lambda} [(\mu\mu|\kappa\kappa) + (\mu\mu|\lambda\lambda) + (\nu\nu|\kappa\kappa) + (\nu\nu|\lambda\lambda)], \tag{3.49}$$

and

$$\begin{aligned}
(\mu\nu|\kappa\lambda)^{\text{ons}} &= \frac{1}{4} \sum_{\alpha \in A}^{\alpha \neq \mu} S_{\alpha\nu} S_{\alpha\lambda} (\mu\alpha|\mu\alpha) \delta_{\mu\kappa} + \frac{1}{4} \sum_{\alpha \in A}^{\alpha \neq \mu} S_{\alpha\nu} S_{\alpha\kappa} (\mu\alpha|\mu\alpha) \delta_{\mu\lambda} \\
&+ \frac{1}{4} \sum_{\beta \in B}^{\beta \neq \nu} S_{\beta\mu} S_{\beta\lambda} (\beta\nu|\beta\nu) \delta_{\nu\kappa} + \frac{1}{4} \sum_{\beta \in B}^{\beta \neq \nu} S_{\beta\mu} S_{\beta\kappa} (\beta\nu|\beta\nu) \delta_{\nu\lambda} \\
&+ \frac{1}{4} S_{\kappa\nu} S_{\mu\lambda} (\mu\kappa|\mu\kappa) \delta_{AC} (1 - \delta_{\mu\kappa}) + \frac{1}{4} S_{\lambda\nu} S_{\mu\kappa} (\mu\lambda|\mu\lambda) \delta_{AD} (1 - \delta_{\mu\lambda}) \\
&+ \frac{1}{4} S_{\kappa\mu} S_{\nu\lambda} (\nu\kappa|\nu\kappa) \delta_{BC} (1 - \delta_{\nu\kappa}) + \frac{1}{4} S_{\lambda\mu} S_{\nu\kappa} (\nu\lambda|\nu\lambda) \delta_{BD} (1 - \delta_{\nu\lambda}) \tag{3.50}
\end{aligned}$$

It should be noted that for nonzero $(\mu\nu|\kappa\lambda)^{\text{ons}}$, at least two of the four orbitals have to belong to a common center, which means that this refinement strictly excludes four-center integrals. Moreover, as it should be expected, integrals of the type $(\mu\mu|\nu\nu)$, which are given exactly within the Mulliken approach, are not affected by this correction.

3.6 Onsite-corrected DFTB

The refinement of the expression for the multicenter integrals, Eq. (3.48), will be hereafter referred to as the onsite correction. After substituting this formula into (3.21) and doing some lengthy but straightforward algebra, it is possible to obtain a refined expression for the DFTB second-order energy,

$$\begin{aligned}
 E^{(2)} &= \frac{1}{2} \sum_{\sigma\tau} \sum_{\mu\nu} \Delta\tilde{P}_{\mu\mu}^{\sigma} (\mu\mu|f_{\text{hxc}}^{\sigma\tau}[\rho_0]|\nu\nu) \Delta\tilde{P}_{\nu\nu}^{\tau} \\
 &+ \sum_{\sigma\tau} \sum_A \sum_{\mu\nu \in A}^{\mu \neq \nu} \Delta\tilde{P}_{\mu\nu}^{\sigma} (\mu\nu|f_{\text{hxc}}^{\sigma\tau}[\rho_0]|\mu\nu) \Delta\tilde{P}_{\mu\nu}^{\tau}.
 \end{aligned} \tag{3.51}$$

Eq. (3.51) differs from the traditional formula (3.25) in the additional second term, which depends on the fluctuations of the off-diagonal elements of the dual density matrix, $\tilde{P}_{\mu\nu}^{\sigma}$, connecting orbitals ϕ_{μ} and ϕ_{ν} placed at the same atom.

In a similar manner, by substituting (3.48) into (3.23) it is possible to obtain a refined Hamiltonian $\mathbf{H}^{\text{new}} = \mathbf{H}^{\text{old}} + \mathbf{H}^{\text{ons}}$, where \mathbf{H}^{old} is given by Eq. (3.36) and \mathbf{H}^{ons} is given by

$$H_{\mu\nu\sigma}^{\text{ons}} = \sum_{\tau} \sum_{\alpha \in A}^{\alpha \neq \mu} S_{\alpha\nu} (\mu\alpha|f_{\text{hxc}}^{\sigma\tau}[\rho_0]|\mu\alpha) \Delta\tilde{P}_{\mu\alpha}^{\tau} + \sum_{\tau} \sum_{\beta \in B}^{\beta \neq \nu} S_{\beta\mu} (\beta\nu|f_{\text{hxc}}^{\sigma\tau}[\rho_0]|\beta\nu) \Delta\tilde{P}_{\beta\nu}^{\tau}. \tag{3.52}$$

Unlike one might deceptively think, the onsite contribution to the Hamiltonian has nonzero off-site elements, that is, our correction affects also matrix elements, $H_{\mu\nu\sigma}$, with orbitals ϕ_{μ} and ϕ_{ν} placed at different atoms. The major effect relies, however, on the atomic blocks of the Hamiltonian matrix. Important differences from the previous scheme should be noted for these quantities. To see this in details let us write the DFTB Hamiltonian for an arbitrary atom A under the onsite correction:

$$\begin{aligned}
 H_{\mu\nu\sigma} &= \delta_{\mu\nu} \left(\varepsilon_{\mu} + \sum_{\tau} \sum_{\gamma} (\mu\mu|f_{\text{hxc}}^{\sigma\tau}[\rho_0]|\gamma\gamma) \Delta\tilde{P}_{\gamma\gamma}^{\tau} \right) \\
 &+ 2(1 - \delta_{\mu\nu}) \sum_{\tau} (\mu\nu|f_{\text{hxc}}^{\sigma\tau}[\rho_0]|\mu\nu) \Delta\tilde{P}_{\mu\nu}^{\tau}, \quad \forall \mu, \nu \in A.
 \end{aligned} \tag{3.53}$$

As can be seen from this formula, the onsite-correction term (last term) incorporate nonzero off-diagonal elements to the traditional strictly diagonal matrix. Within the new formalism, the Hamiltonian is thus self-consistent in terms of the whole dual density matrix and not only of its diagonal elements (Mulliken population). Within the onsite-corrected DFTB, convergence is reached when a converged dual density matrix is obtained. As this represents a somewhat heavier convergence criterion, our correction is in principle expected to moderately prolong the computational time with respect to the previous scheme. In the dissociation limit, the dual density matrix is restored to its free-atom value and hence, the Hamiltonian recovers its diagonal form.

3.7 Onsite Correction in Practice. Onsite Parameters

In standard DFTB, the first term of Eq. (3.51) is subject to a monopolar approximation as described in (3.30). However, with inclusion of the exchange integrals, the spherical averaging over AO products will in general not lead to an expression that is invariant under a rotation of the molecular frame. A similar issue is met for the INDO model. A detailed discussion on the rotational invariance (RI) in INDO has been addressed by Figeys *et al.* [199]. The authors state that, for instance, for two orbitals with angular momentum p centered at the same atom A , the following identity must hold to preserve RI:

$$(pp|f_{\text{hxc}}^{\sigma\tau}[\rho_0]|pp) - (pp|f_{\text{hxc}}^{\sigma\tau}[\rho_0]|p'p') = 2(pp'|f_{\text{hxc}}^{\sigma\tau}[\rho_0]|pp'), \quad \forall p, p' \in A. \quad (3.54)$$

In the original DFTB formulation this requirement is fulfilled, as both integrals on the left-hand side of Eq. (3.54) are approximated to have the same value, $\Gamma_{Ap,Ap}^{\sigma\tau}$, while the integral on the right-hand side is neglected. To retain RI within the present scheme, one could evaluate all onsite integrals exactly so that (3.54) holds automatically. Off-site integrals are exempt from this issue and can be approximated as usual using (3.29). Splitting the first term of Eq. (3.51) into onsite and off-site contributions while applying (3.29) for the off-site component, one obtains

$$\begin{aligned} E^{(2)} &= \frac{1}{2} \sum_{\sigma\tau} \sum_A \sum_{\mu\nu \in A} \Delta \tilde{P}_{\mu\mu}^{\sigma} (\mu\mu|f_{\text{hxc}}^{\sigma\tau}[\rho_0]|\nu\nu) \Delta \tilde{P}_{\nu\nu}^{\tau} \\ &+ \sum_{\sigma\tau} \sum_A \sum_{\mu\nu \in A}^{\mu \neq \nu} \Delta \tilde{P}_{\mu\nu}^{\sigma} (\mu\nu|f_{\text{hxc}}^{\sigma\tau}[\rho_0]|\mu\nu) \Delta \tilde{P}_{\mu\nu}^{\tau} \\ &+ \frac{1}{2} \sum_{\sigma\tau} \sum_{AB} \sum_{l'}^{A \neq B} \Delta q_{Al}^{\sigma} \Gamma_{Al,Bl'}^{\sigma\tau} \Delta q_{Bl'}^{\tau}. \end{aligned} \quad (3.55)$$

In section 3.3 we stressed the importance of using the screened parameters $\gamma_{Al,Al}$ to counter-vail the poor quality of the basis set employed in DFTB. Accordingly, only the exchange-like integrals are in practice obtained directly from the wavefunctions whereas the coulomb-like integrals, $(pp|f_{\rho\sigma\rho\tau}^{\text{hxc}}[\rho_0]|pp)$ and $(pp|f_{\rho\sigma\rho\tau}^{\text{hxc}}[\rho_0]|p'p')$, are evaluated using the identity (3.54) and the known (approximate) values of the Hubbard-like parameters:

$$\begin{aligned} (pp|f_{\rho\sigma\rho\tau}^{\text{hxc}}[\rho_0]|pp) &= \Gamma_{Ap,Ap}^{\sigma\tau} + \frac{4}{3}(pp'|f_{\rho\sigma\rho\tau}^{\text{hxc}}[\rho_0]|pp') \\ (pp|f_{\rho\sigma\rho\tau}^{\text{hxc}}[\rho_0]|p'p') &= \Gamma_{Ap,Ap}^{\sigma\tau} - \frac{2}{3}(pp'|f_{\rho\sigma\rho\tau}^{\text{hxc}}[\rho_0]|pp'). \end{aligned} \quad (3.56)$$

Apart from the improved accuracy, the use of the traditional Γ -parameters keeps the modifications of the original method as small as possible, while RI is still exactly preserved. Additionally, in this way the simplicity of the scheme is not destroyed and the number of parameters to add is reduced.

As discussed by Figeys and coworkers, integrals involving d -orbitals need to be set to their averaged value for RI fulfillment. In this case a similar identity holds:

$$(dd|f_{\text{hxc}}^{\sigma\tau}[\rho_0]|dd) - (dd|f_{\text{hxc}}^{\sigma\tau}[\rho_0]|d'd') = 2(dd'|f_{\text{hxc}}^{\sigma\tau}[\rho_0]|dd'), \quad (3.57)$$

where $(dd|f_{\text{hxc}}^{\sigma\tau}[\rho_0]|d'd')$ and $(dd'|f_{\text{hxc}}^{\sigma\tau}[\rho_0]|dd')$ stand for the mean value of every possible combination (ten in total) of orbitals d and d' , with $d \neq d'$. Using (3.57) and the definition (3.29), one obtains

$$\begin{aligned} (dd|f_{\text{hxc}}^{\sigma\tau}[\rho_0]|dd) &= \Gamma_{Ad,Ad}^{\sigma\tau} + \frac{8}{5}(dd'|f_{\text{hxc}}^{\sigma\tau}[\rho_0]|dd') \\ (dd|f_{\text{hxc}}^{\sigma\tau}[\rho_0]|d'd') &= \Gamma_{Ad,Ad}^{\sigma\tau} - \frac{2}{5}(dd'|f_{\text{hxc}}^{\sigma\tau}[\rho_0]|dd'). \end{aligned} \quad (3.58)$$

As a last requirement for a basis set containing up to d functions, it is necessary to set also every $(pp|f_{\text{hxc}}^{\sigma\tau}[\rho_0]|dd)$ integral to its averaged value, which is given by the exact $\Gamma_{Ap,Ad}$. However, RI fulfillment does not depend on the value of this quantity and so the usual screened Hubbard is also employed in this case. Thus, by substituting Eqs. (3.56) and (3.58) into (3.55), the second-order energy reads

$$\begin{aligned} E^{(2)} &= \frac{1}{2} \sum_{\sigma\tau} \sum_{AB, ll'} \Delta q_{Al}^{\sigma} \Gamma_{Al, Bl'}^{\sigma\tau} \Delta q_{Bl'}^{\tau} \\ &+ \sum_{\sigma\tau} \sum_{A, ll'} \sum_{\substack{\mu \neq \nu \\ \mu \in A, l \\ \nu \in A, l'}} \Delta \tilde{P}_{\mu\nu}^{\sigma} \Lambda_{Al, Al'}^{\sigma\tau} \Delta \tilde{P}_{\mu\nu}^{\tau} \\ &+ \frac{1}{3} \sum_{\sigma\tau} \sum_A \sum_{\mu\nu \in A, p} (3\delta_{\mu\nu} - 1) \Delta \tilde{P}_{\mu\mu}^{\sigma} \Lambda_{Ap, Ap'}^{\sigma\tau} \Delta \tilde{P}_{\nu\nu}^{\tau} \\ &+ \frac{1}{5} \sum_{\sigma\tau} \sum_A \sum_{\mu\nu \in A, d} (5\delta_{\mu\nu} - 1) \Delta \tilde{P}_{\mu\mu}^{\sigma} \Lambda_{Ad, Ad'}^{\sigma\tau} \Delta \tilde{P}_{\nu\nu}^{\tau}, \end{aligned} \quad (3.59)$$

where the shorthand $\Lambda_{Al, Al'}^{\sigma\tau} = (ll'|f_{\text{hxc}}^{\sigma\tau}[\rho_0]|ll')$ is used. The first term in Eq. (3.59) accounts for the noncorrected energy (3.30). The second term corrects partly for the employed Mulliken approximation in the first term. It accounts for the interaction of the fluctuations of off-diagonal dual density matrix elements. Finally, third and fourth terms correct for the RI loss due to the concurrent application of the monopolar approximation in the first term and the onsite correction (second term).

It is worth stressing that RI is satisfied using (3.59) but regardless of the employed Γ and Λ parameters. The latter (which will be referred to as the onsite parameters) are in our model neither freely adjustable nor fitted to experiments. Instead, they are computed numerically at the PBE level (see Ref. [200] for details on their evaluation). Due to symmetry, only ten onsite parameters per element are needed for angular momenta up to $l = 2$:

$$\Lambda_{As, Ap}^{\uparrow\uparrow}, \Lambda_{As, Ap}^{\uparrow\downarrow}, \Lambda_{Ap, Ap'}^{\uparrow\uparrow}, \Lambda_{Ap, Ap'}^{\uparrow\downarrow}, \Lambda_{As, Ad}^{\uparrow\uparrow}, \Lambda_{As, Ad}^{\uparrow\downarrow}, \Lambda_{Ap, Ad}^{\uparrow\uparrow}, \Lambda_{Ap, Ad}^{\uparrow\downarrow}, \Lambda_{Ad, Ad'}^{\uparrow\uparrow}, \Lambda_{Ad, Ad'}^{\uparrow\downarrow} \quad (3.60)$$

These integrals are calculated for every atom type, stored in a file and read during the calculation. Table 3.1 shows some calculated onsite parameters. Hydrogen has vanishing Λ -parameters because the employed basis set contains only s -functions residing on this element. Therefore, no onsite correction applies for hydrogen atoms. The present DFTB scheme has been implemented in a development version of the DFTB+ code [201].

| Element | $sp(\uparrow\uparrow)$ | $pp'(\uparrow\uparrow)$ | $sd(\uparrow\uparrow)$ | $pd(\uparrow\uparrow)$ | $dd'(\uparrow\uparrow)$ |
|---------|--------------------------|---------------------------|--------------------------|--------------------------|---------------------------|
| | $sp(\uparrow\downarrow)$ | $pp'(\uparrow\downarrow)$ | $sd(\uparrow\downarrow)$ | $pd(\uparrow\downarrow)$ | $dd'(\uparrow\downarrow)$ |
| H | 0.00000 | 0.00000 | 0.00000 | 0.00000 | 0.00000 |
| | 0.00000 | 0.00000 | 0.00000 | 0.00000 | 0.00000 |
| C | 0.04973 | -0.01203 | 0.00000 | 0.00000 | 0.00000 |
| | 0.10512 | 0.02643 | 0.00000 | 0.00000 | 0.00000 |
| N | 0.06816 | -0.00879 | 0.00000 | 0.00000 | 0.00000 |
| | 0.12770 | 0.03246 | 0.00000 | 0.00000 | 0.00000 |
| O | 0.08672 | -0.00523 | 0.00000 | 0.00000 | 0.00000 |
| | 0.14969 | 0.03834 | 0.00000 | 0.00000 | 0.00000 |
| S | 0.07501 | 0.00310 | 0.00398 | 0.01100 | -0.01792 |
| | 0.11653 | 0.03058 | 0.03915 | 0.04979 | 0.01582 |
| Ti | 0.02659 | -0.01297 | -0.00587 | -0.00523 | -0.00750 |
| | 0.06881 | 0.01640 | 0.01239 | 0.01144 | 0.02604 |
| Au | 0.03752 | -0.00505 | 0.00073 | -0.00002 | 0.00531 |
| | 0.06928 | 0.01677 | 0.01339 | 0.01228 | 0.02519 |

Table 3.1: Onsite parameters for some chemical elements calculated at the PBE level of theory.

3.8 Hydrogen Bond Energies

Despite the outstanding success of DFTB in many fields, serious shortcomings have been disclosed for some applications. Especial mention deserves the inaccurate description of hydrogen bonded complexes. In particular, DFTB has been shown to poorly reproduce bulk water and water clusters properties partly due to underestimation of the strength of hydrogen bonding interaction [202–205]. This issue was partly overcome with the introduction of a purely empirical short-range correction to the γ functionals involving hydrogen [192] (the modified functions will be denoted γ^h in the following). Within this correction the short-range contribution, S , to the functional $\gamma_{Al,B'}$ (Eq. 3.34) is damped by the factor

$$\exp \left[- \left(\frac{\gamma_{Al,Al} + \gamma_{B',B'}}{2} \right)^\xi R_{AB}^2 \right], \quad (3.61)$$

if at least one of atoms A and B is a hydrogen-like species. The parameter ξ is fitted to reproduce a desired property, generally binding energies and/or proton affinities of hydrogen-bonded complexes. The combination of this correction with a third order energy expansion (the so-called DFTB3 method) has been shown to further improve hydrogen bond energies [193]. In DFTB3, apart from the empirical ξ , one additional parameter per atom type is required, namely, the derivative of the Hubbard-like functions with respect to the atomic occupation. These parameters can be either calculated numerically or fitted to higher-level results. In this section we assess the performance of the onsite-corrected DFTB method for the description of hydrogen bonds. To this end, we calculated the binding energies of 22 small systems containing

water, including neutral, protonated and deprotonated water clusters. This benchmark set has been employed earlier for the validation of different variants of DFTB3 [192, 193].

| System | DFTB | DFTB | DFTB | DFTB | | DFTB3 | | G3B3 |
|---|-------|--------|--------------|----------|------------|-------|-------|-------|
| | (ons) | (3ord) | (ons + 3ord) | γ | γ^h | calc | fit | |
| (H ₂ O) ₂ | 0.2 | 1.5 | 0.3 | 1.6 | 0.0 | 0.0 | 0.0 | -4.9 |
| (H ₂ O) ₃ | -0.4 | 5.4 | 0.0 | 5.5 | -0.6 | -0.3 | -0.01 | -15.1 |
| (H ₂ O) ₄ | -1.4 | 9.4 | -1.1 | 9.7 | 0.6 | 0.8 | 1.1 | -27.4 |
| (H ₂ O) ₅ | -1.4 | 12.5 | -1.5 | 13.3 | 1.4 | 1.3 | 1.7 | -36.3 |
| H ⁺ (H ₂ O) ₂ | -4.2 | 5.9 | -2.3 | 4.5 | -2.0 | 0.9 | 2.1 | -33.9 |
| H ⁺ (H ₂ O) ₃ | -2.4 | 11.6 | 0.1 | 10.4 | -0.1 | 3.7 | 5.3 | -57.3 |
| H ⁺ (H ₂ O) ₄ | -1.0 | 15.0 | 1.9 | 13.9 | 1.1 | 5.0 | 6.7 | -77.2 |
| H ⁺ (H ₂ O) ₅ | 0.0 | 19.7 | 3.7 | 18.3 | 1.8 | 6.2 | 8.1 | -91.9 |
| OH ⁻ (H ₂ O) | -10.4 | 1.5 | -2.3 | -5.1 | -12.8 | -5.9 | -3.2 | -27.4 |
| OH ⁻ (H ₂ O) ₂ | -8.7 | 5.3 | -0.4 | -2.6 | -17.0 | -8.4 | -5.3 | -48.6 |
| OH ⁻ (H ₂ O) ₃ | -10.5 | 9.0 | -0.2 | 0.3 | -17.5 | -7.2 | -3.5 | -66.7 |
| OH ⁻ (H ₂ O) ₄ | -9.2 | 14.2 | 0.8 | 6.1 | -18.2 | -7.8 | -4.7 | -86.3 |
| NH ₃ (H ₂ O) | 1.8 | 3.1 | 1.7 | 3.2 | 2.1 | 2.1 | 2.1 | -6.6 |
| NH ₄ ⁺ (H ₂ O) | -4.6 | 1.4 | -3.4 | 0.6 | -3.4 | -1.3 | -0.9 | -20.4 |
| (H ₂ O) ₆ [book] | -1.3 | 16.5 | -0.7 | 16.7 | 1.2 | 1.7 | 2.2 | -45.8 |
| (H ₂ O) ₆ [cage] | -0.8 | 17.6 | 0.5 | 17.2 | 0.3 | 1.5 | 1.8 | -46.6 |
| (H ₂ O) ₆ [prism] | 0.0 | 18.0 | 1.1 | 17.6 | 0.0 | 1.3 | 1.7 | -47.2 |
| (H ₂ O) ₆ [ring] | -1.6 | 15.3 | -2.1 | 16.5 | 1.8 | 1.5 | 2.1 | -44.7 |
| methylimidazole(-H ⁺)(H ₂ O) | -0.6 | 3.2 | -1.9 | 4.1 | 2.0 | 1.2 | 1.1 | -15.9 |
| methylimidazole(H ₂ O) [donor] | 1.2 | 2.6 | 1.7 | 2.4 | 1.4 | 1.9 | 2.0 | -6.2 |
| methylimidazole(H ₂ O) [acceptor] | 1.4 | 2.8 | 0.5 | 3.5 | 2.6 | 1.9 | 1.9 | -8.2 |
| methylimidazole H ⁺ (H ₂ O) | -0.4 | 3.9 | 0.5 | 3.3 | 1.2 | 2.3 | 2.5 | -16.0 |
| MUD | 2.9 | 8.9 | 1.3 | 8.0 | 4.0 | 2.9 | 2.7 | |
| MSD | -2.5 | 8.9 | -0.1 | 7.3 | -2.5 | 0.1 | 1.1 | |
| MAX | 10.5 | 19.7 | 3.7 | 18.3 | 18.2 | 8.4 | 8.1 | |

Table 3.2: Comparison of binding energies as obtained with the DFTB method at different levels of approximation and G3B3. For all DFTB variants, the reported values are the deviations from the G3B3 results. (H₂O)_n, H⁺(H₂O)_n and OH⁻(H₂O)_n denote a neutral, protonated and deprotonated (hydroxide) water *n*-mer, respectively. The structures of the four water hexamers are depicted in Fig. 3.1. Methylimidazole(H⁺)(H₂O) and methylimidazole(-H⁺)(H₂O) denote, respectively, a protonated and deprotonated methylimidazole complexed with water, whereas methylimidazole(H₂O) [donor] ([acceptor]) stand for the neutral methylimidazole complexed with water as a hydrogen-bond donor (acceptor). All energies are expressed in kcal/mol.

In Table 3.2 the aforementioned binding energies are reported as obtained with different DFTB approaches. These approaches include the original second-order scheme using the standard γ functions [DFTB(γ)] and the modified parameters for hydrogen [DFTB(γ^h)] as well as using third order corrections [DFTB(3ord)] and the proposed onsite refinement [DFTB(ons)]. Additionally, the combination of both onsite and third order corrections [DFTB(ons + 3ord)] is tested. Finally, we also compare our results to DFTB3 findings using Hubbard derivatives either obtained from PBE calculations [DFTB3(calc)] or fitted to reproduce binding energies and proton affinities for a large set of molecules [DFTB3(fit)]. For DFTB3(calc) the parameter ξ is fitted to reproduce the binding energy of the neutral water dimer whereas it is fitted to

an extended data set for DFTB3(fit). As a reference data, we employed previously obtained results [193] using the quantum chemistry composite method G3B3 [206], which is a variant of the G3 formalism in which geometries and zero point vibrational energies are calculated at the B3LYP/6-31G(d) level. Except for the onsite corrected schemes, DFTB(ons) and DFTB(ons + 3ord), the binding energies were taken from reference [193]. Geometries were also extracted from the mentioned work, which are optimized at the B3LYP/6-31G(d) level of theory. All binding energies are defined as the energy difference between the complex and the isolated molecules, so that a negative value designates a bonded system. For all DFTB variants the deviation with respect to G3B3 results is reported, where the DFTB energies are taken as the minuend, that is, a positive value indicates an underestimation of the absolute value of the binding energy (and hence, an underestimation of the strength of the hydrogen bonding interaction). At the bottom of the table, the mean unsigned and signed deviation or error (MUD and MSD, respectively) as well as the maximum deviation from G3B3 results (MAX) are given for every tested method.

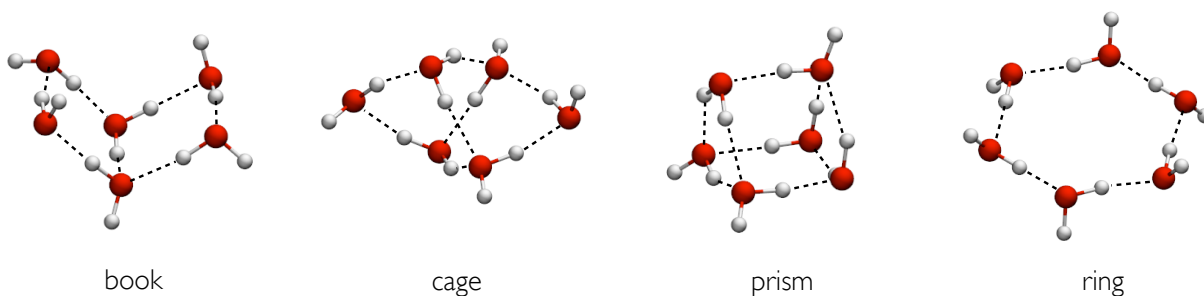


Figure 3.1: Four water hexamers investigated in Table 3.2.

As shown in Table 3.2, the standard DFTB method generally underestimates the strength of hydrogen bonding interaction with an error of about 2-4 kcal/mol per hydrogen bond. The only exceptions are the deprotonated water clusters. In this case, the tetramer and pentamer exhibit a rather small underestimation of this interaction whereas for the water dimer and trimer an overestimation is observed. For the protonated water clusters and protonated water-methylimidazole complex, errors are especially large. Use of the empirical γ^h functions substantially improves upon binding energies for the neutral and protonated clusters but worsens the description of the deprotonated ones with a remarkable overestimation of the strength of the hydrogen bonding interaction. On the other hand, third order corrections in combination with the standard γ parameters does not improve the results overall. However, the DFTB3 schemes retain the good results obtained with DFTB(γ^h) while systematically improve the description of the deprotonated systems. The overall enhancement of DFTB3 over the traditional scheme should be, however, mainly attributed to the empirical correction for hydrogen and only in part to the combined application of this modification and the third-order extension.

With the application of the onsite correction a global improvement is perceived, resulting in a MUD (2.9 kcal/mol) similar to that obtained with the DFTB3 method. In this case, there is a clear tendency to overestimation of the hydrogen bonding interaction, in contrast to the global underestimation within the standard formalism and the scattered DFTB3 values around G3B3 results. This overestimation is especially important for the hydroxide water clusters. The associated errors are smaller than those of the DFTB(γ^h) variant but considerably larger

than for the standard approach. Particularly outstanding is, in contrast, the description of the water hexamers and methylimidazole-water complexes, with errors under 2 kcal/mol per hydrogen bond. When combining the onsite correction with the third-order extension the obtained energies are even better. The MUD is in this case reduced to only 1.3 kcal/mol with a maximum individual deviation of 3.7 kcal/mol. The MSD is also substantially small (-0.1 kcal/mol) which indicates that the obtained values are scattered around the reference data. Among all tested DFTB variants, the DFTB(ons + 3ord) scheme is the only one for which the errors for the hydroxide water clusters are really consistent with those of the neutral and positive charged systems. This indicates that a high parameter transferability is achieved within such a formalism. More importantly, both DFTB (ons) and DFTB (ons+3ord) methods are totally free of empirical or semiempirical parameters, which is a desired feature in DFTB.

Although the use of the fitted γ^h functions in DFTB seems to work well for the small systems considered above, results are not longer satisfactory when studying larger water clusters. This has been shown in a recent benchmark by the group of Truhlar for the description of water nanoparticles [203]. They tested the accuracy of 85 DFT and semiempirical methods to reproduce the binding energies of five water hexadecamers (16-mers) [see Fig. 3.2], obtained by Yoo and coworkers [207] using coupled cluster theory with quasiperturbative triplet excitations [CCSD(T)] [68, 69]. The geometries of the water nanoparticles and monomer were optimized at the MP2/aug-cc-pVTZ level. As shown in that work, DFTB(γ)⁶ highly underestimate the strength of the hydrogen bonding interaction with a mean binding energy error of 68 kcal/mol. This issue is importantly alleviated with DFTB(γ^h), although absolute values of the binding energy are still substantially underestimated.

Furthermore, Truhlar and coworkers assessed the accuracy of the methods in terms of relative energies of the water 16-mers. For this property, the tested DFTB variants perform well, with MUD of 1.2 and 1.7 kcal/mol when employing the standard and modified γ , respectively. In order to assess quantitatively the ability of the investigated approaches to reproduce both relative energies and absolute binding energies, Truhlar *et al.* defined a characteristic error (CE) as follows:

$$\text{CE} = 0.5 \left(\frac{\text{MUD}_{\text{BE}}^{\text{X}}}{\text{MUD}_{\text{BE}}^{\text{med}}} \right) + 0.5 \left(\frac{\text{MUD}_{\text{RE}}^{\text{X}}}{\text{MUD}_{\text{RE}}^{\text{med}}} \right). \quad (3.62)$$

$\text{MUD}_{\text{BE}}^{\text{X}}$ and $\text{MUD}_{\text{RE}}^{\text{X}}$ are, respectively, the mean unsigned errors in the five binding energies and ten relative energies as computed with method X. $\text{MUD}_{\text{BE}}^{\text{med}} = 19.9$ kcal/mol and $\text{MUD}_{\text{RE}}^{\text{med}} = 2.0$ kcal/mol are the median of all of the $\text{MUD}_{\text{BE}}^{\text{X}}$ and $\text{MUD}_{\text{RE}}^{\text{X}}$ values, respectively. Whether or not the errors for the binding and relative energies should have the same weight in the calculation of the CE might be a matter of debate. However, it seems adequate for a very general assessment to avoid a possible bias towards one of these properties and so we would like to assess the new DFTB formalism based on this indicator. Table 8 of Ref. [203] shows all 85 tested methods sorted by their CE. The authors consider as satisfactory those approaches with a CE well below 1.0 whereas those with CE values close to or greater than 1.0 are disapproved. DFTB(γ) belongs to the latter group of approaches with a CE = 2.02. If the empirical γ^h function is employed, the value decreases to 1.31 but the use of the method is still discouraged.

Table 3.3 shows the binding energies for the five water 16-mers obtained by DFTB(ons), DFTB(3ord), DFTB(ons+3ord) and both DFTB3(cal) and DFTB3(fit). The same MP2 ge-

⁶In Ref. [203] standard self-consistent-charge DFTB [DFTB(γ)] is termed SCC-DFTB whereas DFTB(γ^h) is referred to as SCC-DFTB- γ^h .

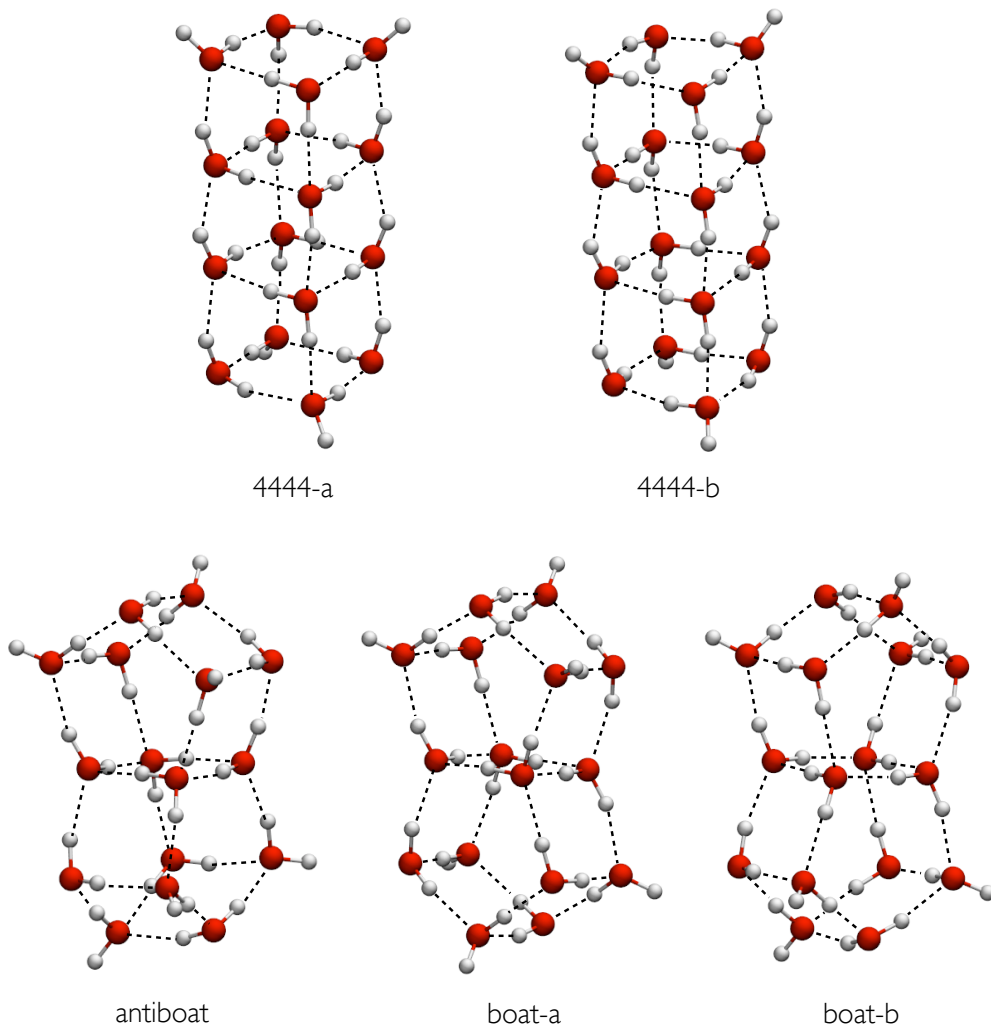


Figure 3.2: Five water hexadecamers investigated by Yoo *et al.* [207].

ometries for the water 16-mer and monomer employed in Ref. [203] are used throughout. We also include the results for $\text{DFTB}(\gamma)$ and $\text{DFTB}(\gamma^h)$ as well as the reference CCSD(T) energies from Ref. [203]. At the bottom of the table we provide the MUD_{BE} , MUD_{RE} and Truhlar’s CE for every DFTB variant. Our results reveal that inclusion of onsite corrections cures the problem of standard DFTB for the description of these systems. $\text{DFTB}(\text{ons})$ and $\text{DFTB}(\text{ons}+3\text{ord})$ exhibit MUD_{BE} of only 10.5 and 14.0 kcal/mol, respectively. Third-order corrections alone does not improve the performance of standard DFTB. However, DFTB3 does return binding energies in better agreement with CCSD(T) findings. $\text{DFTB}(\text{ons})$ also keeps a low MUD_{RE} and as a result it exhibits a Truhlar’s CE of 0.56. With this result, our method would occupy the sixteenth place in Truhlar’s table, above DFT approaches such as PBE (CE = 0.77) and hybrid schemes such as HSE06 (CE = 0.70) and PBE0 (CE = 0.79). DFTB3 would also obtain a distinguished position in the table, with a CE of 0.61 when using third-order parameters computed by DFT. Combination of third-order and onsite corrections apparently is not a good formula here; such formalism scores a CE close to 1.0 and would be considered as an “average” method by Truhlar and co-workers.

| Structure | DFTB | DFTB | DFTB | DFTB | | DFTB3 | | CCSD(T) |
|-------------------|-------|--------|--------------|----------|------------|-------|-------|---------|
| | (ons) | (3ord) | (ons + 3ord) | γ | γ^h | calc | fit | |
| 4444-a | 12.01 | 68.26 | 16.58 | 67.03 | 33.99 | 13.63 | 14.92 | -171.06 |
| 4444-b | 10.97 | 68.20 | 15.67 | 66.90 | 33.45 | 12.99 | 14.26 | -170.52 |
| antiboat | 9.50 | 67.82 | 12.22 | 68.14 | 35.80 | 14.22 | 15.86 | -170.55 |
| boat-a | 9.91 | 68.73 | 12.61 | 69.04 | 36.48 | 14.86 | 16.48 | -170.80 |
| boat-b | 10.10 | 68.67 | 12.77 | 68.98 | 36.46 | 14.93 | 16.55 | -170.64 |
| MUD _{BE} | 10.5 | 68.3 | 14.0 | 68.0 | 35.2 | 14.1 | 15.6 | |
| MUD _{RE} | 1.2 | 0.5 | 2.4 | 1.2 | 1.7 | 1.0 | 1.2 | |
| CE | 0.56 | 1.83 | 0.95 | 2.02 | 1.31 | 0.61 | 0.70 | |

Table 3.3: Comparison of binding energies of five water 16-mers as obtained with the DFTB method at different levels of approximation and CCSD(T). For all DFTB variants, the reported values are the deviations from the CCSD(T) results. The five water configurations are depicted in Fig. 3.2. At the bottom of the table, we provide the mean unsigned errors in the five binding energies (MUD_{BE}) as well as the mean unsigned errors in the ten relative energies of every combination pair (MUD_{RE}). Truhlar’s characteristic error (CE) is also given for every DFTB variant. All energies are expressed in kcal/mol.

As a final check, we computed the binding energies for the two water heptadecamers studied in Ref. [203] using DFTB(ons) and DFTB3(cal). Both methods also perform fairly well in this case, with MUD_{BE} of 10.1 and 15.6 kcal/mol and relative energy errors of 0.26 and 0.27 kcal/mol, respectively. These results suggest that both the onsite-corrected DFTB and DFTB3 method may be reliably employed for the study of some properties of neutral bulk water at a little computational cost.

3.9 Summary

The density functional based tight binding (DFTB) approach is an approximate DFT method which is parametrized as in TB theory. Due to important simplifications of the scheme, such as the employment of a minimal basis set and neglect of three and higher center interactions, together with the elusion of on-the-fly integral evaluations, DFTB has emerged as a very efficient tool. After the original formulation, the formalism has been extended in a wide variety of ways. Second-order corrections account for interatomic charge transfer in a self-consistent fashion. For this extension, two main approximations are employed, namely, the so-called Mulliken approximation and the truncation up to the monopolar term of a multipole expansion of the square of the basis functions. This chapter has been primarily dedicated to the refinement of the Mulliken approximation. Following the ideas yielding the INDO method, we incorporate the disregarded one-center exchange-like integrals into the formalism. This leads to a scheme which treats in a self-consistent way the fluctuations of the whole dual density matrix, and not only its diagonal elements (charges). This scheme substantially improves upon hydrogen bond energies for a set of 22 water-containing systems. The overall accuracy is comparable to that obtained with the DFTB3 method, which employs empirical parameters fitted to reproduce

this property. If, in addition, a third order extension is combined with our correction, hydrogen bond energies are further improved. Within such a scheme, the transferability to treat different charge states in hydrogen bonded systems clearly surpasses that of DFTB3 whereas no empirical parameters are necessary. The description of larger neutral water clusters is also improved with respect to standard DFTB results when employing onsite corrections. In this case, however, the combination of third-order extensions with our refinement does not outperform the onsite-corrected DFTB. We additionally showed that DFTB3 also describe these systems accurately. The onsite correction has again the advantage of requiring no fitted parameters.

Chapter 4

THE TIME DEPENDENT DFTB METHOD

Although Casidas' TD-DFT has demonstrated to be highly efficient, there are still many applications in photochemistry and nanophysics out of the scope of the method. Quantum molecular dynamics in the excited state, for example, require the evaluation of energies and forces at a large number of points along the trajectory. Also, the investigation of extended nanostructures with intrinsic defects or surface modifications can not be reliably performed with small models. These kind of problems might be addressed with an approximate TD-DFT formalism. Such a scheme is the time-dependent density functional based tight-binding method (TD-DFTB).

The development of TD-DFTB dates back to the year 2001 when Niehaus and coworkers, prompted by the good performance of ground-state DFTB, decided to extend the method to account for excited state properties [91]. The idea behind was simple. In density functional response theory, aside from the KS eigenpairs one needs to evaluate the coupling matrix. This matrix can be expressed as a sum of multicenter integrals by expanding the KS orbitals into the AO basis set. Next, it is straightforward to apply the same techniques for the evaluation of multicenter integrals that were earlier employed for second-order DFTB, namely, the Mulliken approximation and the monopole truncation of a MO multipole expansion. These approaches grant TD-DFTB users with the same advantages they savor with DFTB, that is, avoiding expensive integrations on the fly in favor of using pre-calculated two-center parameters. This results in a numerically efficient tool giving fast, yet fairly accurate results for demanding calculations.

The method was originally referred to as the γ approximation. The introduced parameters are very similar to the so-called γ and W constants. The only difference rests on that the new parameters are based on the actual electron density whereas γ and W are computed using neutral spin-unpolarized atoms. As the KS density is not known *a priori*, the new set of parameters would need to be determined during the calculation and the main asset of TD-DFTB would be lost. It was claimed, however, that the dependence of these quantities on the atomic net charges is negligible at least for systems with small charge transfer. Accordingly, TD-DFTB employs the known γ and W constants.

After the original implementation [91], TD-DFTB was extended in a number of different directions. The derivation of analytical excited state gradients [208] allows for the calculation of adiabatic transition energies and excited states geometries. Also, a real time propagation

of KS orbitals using order-N algorithms has been derived [209]. Other extensions include non-adiabatic molecular dynamics simulations in the Ehrenfest [210] or surface hopping [211, 212] approach as well as a TD-DFTB approach for open boundary conditions in the field of quantum transport [213]. A recent detailed review on the advantages and limitations of the method has been provided by Niehaus *et al.* [214].

In this chapter, we will follow a different strategy for the derivation of TD-DFTB. The coupling matrix will be obtained directly from the ground state theory. It will be shown that no additional approximation or neglect is required for a linear response treatment within DFTB. The following derivation will also clearly justify the employment of the ground-state DFTB parameters in TD-DFTB. Additionally, the method will be extended to account for spin-polarized systems and fractional occupation of the KS orbitals. It will be also shown that onsite corrections in TD-DFTB lead to important improvements over the traditional formalism.

4.1 Spin-unrestricted TD-DFTB

In section 3.4 we introduced a new formulation of DFTB, where the energy functional and KS Hamiltonian are expressed in terms of the KS density matrix fluctuations. This formalism is especially suitable for the derivation of a TD-DFTB scheme as the derivative of the KS Hamiltonian with respect to the density matrix elements (namely, the coupling matrix) is obtained straightforwardly. Thus, the coupling matrix is in this case a subblock¹ of the matrix $\bar{\mathbf{K}}$ defined in Eq. (3.40):

$$K_{ia\sigma,jb\tau} := \frac{\partial H_{ia\sigma}}{\partial P_{jb}^\tau} = \bar{K}_{ia\sigma,jb\tau}. \quad (4.1)$$

This quantity depends on the γ and W parameters, as well as on $q_{Al}^{st\sigma}$, introduced earlier in Eq. (3.39). In this case, for which $s = i$ and $t = a$, the quantities, $q_{Al}^{ia\sigma}$, are called Mulliken transition charges [91] and the matrix $\tilde{\mathbf{P}}^{ia\sigma}$, defined in Eq. (3.38), represents the dual KS transition density for an excitation from orbital i to a . It should be then clear that in TD-DFTB no further approximations are needed, other than those already introduced in DFTB.

From Eq. (3.38), it should be noted that the dual transition density matrix is invariant with respect to the permutation of the indices i and a , that is, $\tilde{\mathbf{P}}^{ia\sigma} = \tilde{\mathbf{P}}^{ai\sigma}$. This implies that in TD-DFTB the coupling matrix is symmetric. This is, indeed, an expected property as typical DFTB is derived as an approximation to local or semi-local DFT². Due to this symmetry, the expression for the response matrix elements can be simplified as in Eq. (2.43). Note that the coupling matrix, Eq. (4.1), was derived from a spin-unrestricted formalism which, additionally, allows for occupancies such that $0 \leq n_{s\sigma} \leq 1$, and hence, this generality is automatically transferred to the time-dependend scheme.

It is worth formulating the method for closed shell systems as a particular case, in order to make contact with the original derivation of TD-DFTB. In this special case the Mulliken transition charges have the property $q_{Al}^{ia\uparrow} = q_{Al}^{ia\downarrow} = q_{Al}^{ia}$. If, in addition, the dependence of the γ -functional

¹Recall that the coupling matrix is defined only for those elements $K_{ia\sigma,jb\tau}$ such that $n_{i\sigma} > n_{a\sigma}$ and $n_{j\tau} > n_{b\tau}$ whereas $\bar{\mathbf{K}}$ is a more general matrix with no restriction or constraint on the orbitals.

²See Ref. [215] for an extension of DFTB to general hybrid functionals.

and W constants on the angular momentum is neglected, the coupling matrix simplifies to

$$K_{ia\sigma,jb\tau} = \sum_{AB} q_A^{ia} (\gamma_{AB} + \delta_\sigma \delta_\tau \delta_{AB} W_A) q_B^{jb}, \quad (4.2)$$

with $q_A^{ia} = \sum_l q_{Al}^{ia}$. This expression is in full agreement³ with that derived previously for spin-unpolarized densities [91].

The singlet and triplet coupling submatrices are then expressed as

$$\begin{aligned} K_{ia,jb}^S &= K_{ia\uparrow,jb\uparrow} + K_{ia\uparrow,jb\downarrow} = \sum_{AB} q_A^{ia} q_B^{jb} \gamma_{AB} \\ K_{ia,jb}^T &= K_{ia\uparrow,jb\uparrow} - K_{ia\uparrow,jb\downarrow} = \sum_A q_A^{ia} q_A^{jb} W_A \end{aligned} \quad (4.3)$$

Once the excitation vectors, $F_{ia\sigma}^I$, are obtained within TD-DFTB, the oscillator strengths can be computed from (2.47). The transition dipole matrix is then conveniently subject to a Mulliken approximation,

$$\mathbf{d}_{ia\sigma} \approx \sum_A \mathbf{R}_A q_A^{ia\sigma}, \quad (4.4)$$

where \mathbf{R}_A is the position of atom A .

4.2 Onsite Corrections in TD-DFTB

In the previous chapter we addressed the limitations of the Mulliken approximation and showed that refinements accounting for the interaction of electrons at the same atom improve the description of some ground-state properties. In TD-DFTB, an important outcome of this approach is related to the evaluation of the transition charges $q_{Al}^{ia\sigma}$, and hence, the coupling matrix. The Mulliken approximation returns correct values for these quantities as long as the states i and a are localized on different centers or when their projection on a same center happens on the same orbital. On the contrary, if i and a have components $c_{\mu i}$ and $c_{\nu a}$ at different AO ϕ_μ and ϕ_ν , with $\mu, \nu \in A$, the Mulliken transition charges $q_{Al}^{ia\sigma}$ are underestimated or even vanish identically for some critical cases.

These critical cases occur for systems with high symmetry, especially, for diatomic molecules. Let us see this case in details. Let the z -axis be along the line connecting the atoms 1 and 2 of the molecule. Consider first a transition from the bonding orbital $\pi = c_{p_{1x}\pi} p_x^{(1)} + c_{p_{2x}\pi} p_x^{(2)}$ to the antibonding orbital $\pi^* = c_{p_{1x}\pi^*} p_x^{(1)} - c_{p_{2x}\pi^*} p_x^{(2)}$ (see Fig. 4.1). The corresponding Mulliken transition charge for atom 1, for example, is $q_1^{\pi\pi^*} = \frac{1}{2}(c_{p_{1x}\pi} c_{p_{1x}\pi^*} S_{p_{1x}p_{1x}} - c_{p_{1x}\pi} c_{p_{2x}\pi^*} S_{p_{1x}p_{2x}})$. The overlap matrix element $S_{p_{1x}p_{1x}}$ is equal to 1 whereas $S_{p_{1x}p_{2x}}$ is nonzero as the atomic functions $p_x^{(1)}$ and $p_x^{(2)}$ are nonorthogonal. As a result, the coupling matrix has nonzero elements involving $\pi \rightarrow \pi^*$ transitions and so the Mulliken approach accounts approximately for this kind of excitation. Consider now a transition from the bonding orbital $\sigma = c_{p_{1z}\pi} p_z^{(1)} + c_{p_{2z}\pi} p_z^{(2)}$ to the same virtual orbital π^* . In this case the transition charge amounts to $q_1^{\sigma\pi^*} = \frac{1}{2}(c_{p_{1z}\sigma} c_{p_{1x}\pi^*} S_{p_{1z}p_{1x}} - c_{p_{1z}\sigma} c_{p_{2x}\pi^*} S_{p_{1z}p_{2x}})$. $S_{p_{1z}p_{1x}}$ is zero due to the orthogonality of the atomic functions located at

³The parameter W is termed M in Ref. [91]

the same center, whereas $S_{p_{1z}p_{2x}}$ vanishes because p_{1z} and p_{2x} are orthogonal for the diatomic system. This leads to $q_1^{\sigma\pi^*} = 0$ and in a similar manner, $q_2^{\sigma\pi^*} = 0$. This in turn means that the coupling matrix elements $K_{\sigma\pi^*,jb}$ ($\forall j, b$) vanish and hence, no correction of the KS energy difference occurs in the linear response treatment. As an important outcome, the triplet-singlet gap is zero for such transitions. More importantly, singlet-singlet excitations appears as electric-dipole forbidden as they show vanishing oscillator strengths.

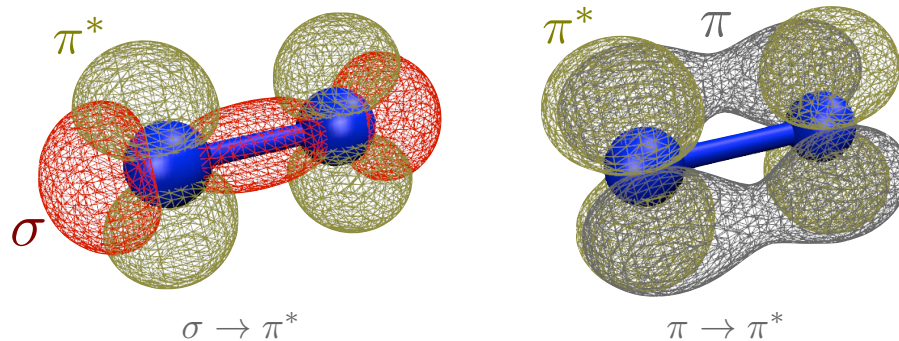


Figure 4.1: Localization of σ and π^* (left) *versus* π and π^* (right) orbitals in the N_2 molecule. In the former case the orbitals have projections on different atomic functions and hence, no coupling is accounted within the Mulliken approximation.

To overcome these limitations we apply the onsite correction for the evaluation of the coupling and dipole matrices.

4.2.1 Coupling matrix

The refinement of the coupling matrix can be obtained straightforwardly from the ground-state theory. The idea is to arrange the expression for the corrected energy functional (3.55) to look like in (3.41), with $\bar{\mathbf{K}}$ being a refined matrix. This is done by substituting Eq. (3.37) in (3.55). Thus, the corrected coupling matrix is expressed as

$$\begin{aligned}
 K_{ia\sigma,jb\tau} &= \sum_A \sum_{\mu\nu \in A} \tilde{P}_{\mu\mu}^{ia\sigma} (\mu\mu | f_{\text{hxc}}^{\sigma\tau}[\rho_0] | \nu\nu) \tilde{P}_{\nu\nu}^{jb\tau} \\
 &+ 2 \sum_A \sum_{\substack{\mu \neq \nu \\ \mu\nu \in A}} \tilde{P}_{\mu\nu}^{ia\sigma} (\mu\nu | f_{\text{hxc}}^{\sigma\tau}[\rho_0] | \mu\nu) \tilde{P}_{\mu\nu}^{jb\tau} \\
 &+ \sum_{\substack{A \neq B \\ ABll'}} q_{Al}^{ia\sigma} \Gamma_{Al,Bl'}^{\sigma\tau} q_{Bl'}^{jb\tau}.
 \end{aligned} \tag{4.5}$$

The one-center integrals in the first and second terms are evaluated in terms of the parameters Γ and Λ as explained in section 3.7.

4.2.2 Dipole matrix

In a similar manner, the approximation for the transition dipole matrix [Eq. (4.4)], and hence the oscillator strengths, can be improved by including all nonvanishing one-center dipole integrals. Consider the expansion of the KS orbitals into a set of localized atom-centered AO, $\psi_{s\sigma} = \sum_{\mu} c_{\mu s}^{\sigma} \phi_{\mu}$. Thus, the elements of the transition dipole matrix read

$$\mathbf{d}_{ia\sigma} = \sum_{\mu\nu} c_{\mu i}^{\sigma} c_{\nu a}^{\sigma} \langle \mu | \hat{\mathbf{r}} | \nu \rangle \quad (4.6)$$

Let $\mu \in A$ and $\nu \in B$ unless otherwise indicated. Using the orbital product expansion (3.46), the AO dipole matrix elements, $\langle \mu | \hat{\mathbf{r}} | \nu \rangle$, can be expressed as follows,

$$\langle \mu | \hat{\mathbf{r}} | \nu \rangle = \frac{1}{2} S_{\mu\nu} (\mathbf{R}_A + \mathbf{R}_B) + \frac{1}{2} \left(\sum_{\alpha \in A}^{\alpha \neq \mu} S_{\alpha\nu} \langle \alpha | \hat{\mathbf{r}} | \mu \rangle + \sum_{\beta \in B}^{\beta \neq \nu} S_{\beta\mu} \langle \beta | \hat{\mathbf{r}} | \nu \rangle \right), \quad (4.7)$$

where $\mathbf{R}_A = \langle \mu | \hat{\mathbf{r}} | \mu \rangle$ and $\mathbf{R}_B = \langle \nu | \hat{\mathbf{r}} | \nu \rangle$ denote the positions of centers A and B, respectively. After substituting Eq. (4.7) in (4.6), we finally have

$$\mathbf{d}_{ia\sigma} = \sum_A \mathbf{R}_A q_A^{ia\sigma} + \sum_A \sum_{\mu\nu \in A}^{\mu \neq \nu} \tilde{P}_{\mu\nu}^{ia\sigma} \langle \mu | \hat{\mathbf{r}} | \nu \rangle, \quad (4.8)$$

where the definition (3.38) was additionally employed.

| Element | D_{sp} | D_{pd} | D'_{pd} | D''_{pd} |
|---------|----------|----------|-----------|------------|
| H | 0.00000 | 0.00000 | 0.00000 | 0.00000 |
| C | 0.76346 | 0.00000 | 0.00000 | 0.00000 |
| N | 0.64604 | 0.00000 | 0.00000 | 0.00000 |
| O | 0.60175 | 0.00000 | 0.00000 | 0.00000 |
| S | 0.46427 | 0.39975 | -0.23079 | 0.46159 |
| Au | 0.76444 | 0.25369 | -0.14647 | 0.29293 |
| Ti | 0.73030 | 0.21775 | -0.12572 | 0.25143 |

Table 4.1: Dipole parameters for some chemical elements calculated at the PBE level of theory.

According to the dipole selection rules only s - p and p - d dipole integrals are non-zero. Among the s - p integrals, only those of the type $D_{sp} = \langle s | r_k | p_k \rangle$ do not vanish, all of them being equal. With regards to the p - d integrals, eleven of them are non-vanishing:

$$\begin{aligned} D_{pd} &= \langle p_y | x | d_{xy} \rangle = \langle p_x | y | d_{xy} \rangle = \langle p_y | z | d_{yz} \rangle = \langle p_z | y | d_{yz} \rangle = \langle p_z | x | d_{xz} \rangle = \langle p_x | z | d_{xz} \rangle \\ &= \langle p_x | x | d_{x^2-y^2} \rangle = -\langle p_y | y | d_{x^2-y^2} \rangle \\ D'_{pd} &= \langle p_y | y | d_{z^2} \rangle = \langle p_x | x | d_{z^2} \rangle \\ D''_{pd} &= \langle p_z | z | d_{z^2} \rangle. \end{aligned} \quad (4.9)$$

These integrals are also calculated numerically at the PBE level for every atom type and read during the calculation. In table 4.1 we report the dipole parameters for some elements. For hydrogen, all parameters are zero as only s functions are employed for this species. For the second-row elements C, N and O only the integrals D_{sp} are nonzero because the basis set is sampled with s and p orbitals only.

4.3 Performance for Diatomic Systems

The downsides of the traditional TD-DFTB approach were already acknowledged in the original article [91]. A minor attention has been given to this issue because $\pi \rightarrow \pi^*$ transitions usually dominate the absorption spectrum. Indeed, $\sigma \rightarrow \pi^*$ and $n \rightarrow \pi^*$ excitations are generally found to have a rather small oscillator strength. However, these excitations play a significant role in the absorption spectra of some species. Furthermore, they may be crucial for the luminescence properties of some compounds, which are of key importance in many technological applications. In this section, it is shown that the inaccurate description of $\sigma \rightarrow \pi^*$ transitions is surpassed within the refined formalism. Three diatomic molecules, NO, N₂ and O₂, were chosen to better illustrate the performance of the new method in this regard.

Table 4.2 shows the low-lying vertical excitation energies of the investigated molecules calculated within both the corrected and the original formulation of TD-DFTB. It should be noted that only valence excited states can be treated within TD-DFTB due to the employed minimal basis set. For NO and O₂, spin-unrestricted TD-DFTB calculations have been performed, where the doublet $X^2\Pi$ and the triplet $X^3\Sigma_g^-$ ground states have been considered, respectively. To identify the excited state multiplicity of the open-shell systems, we evaluate the expectation value of the square of the total spin operator, $\langle S^2 \rangle$, by using the expression II.83 in Ref. [216]⁴. In Table 4.2, a multiplicity is only assigned to those excited states with low spin contamination. This covers the most important excitations in the absorption spectrum.

As a reference, we computed vertical excitation energies to valence states of these compounds by using TD-DFT as implemented in the TURBOMOLE package [218]. The PBE XC functional as well as triple-zeta plus polarization (TZP) basis set has been used. All ground state geometries were previously optimized at the corresponding level of theory. Some experimental findings taken from the literature [219, 220] are also included for comparison. The oscillator strength for each excitation is indicated to the right of the corresponding excitation energy, and in the first column of the table the symmetry and type of the transition are specified.

These molecules have as a common feature that they all exhibit low-lying $\sigma \rightarrow \pi^*$ excitations playing an important role in their absorption spectra. As stated above, a wrong description of these transitions is a known issue in original TD-DFTB. In the following discussion, we also identify a failure in the description of some $\pi \rightarrow \pi^*$ transitions of these compounds.

⁴This expression is in accordance with the simplified characterization of the many body excited state in terms of singly excited Slater determinants given by Casida [143]. A more rigorous formula for $\langle S^2 \rangle$ can be found in Ref. [217]. However, for a roughly assignment of the multiplicity and detection of spin-contaminated states, the former expression is sufficient.

| Molecule/Trans. | TD-DFT | | | TD-DFTB | | | | | Exp. |
|--|------------|-------|---------------|-------------------------|--------------------|-------------------------|--------------------|---------------|---------|
| | ω_I | f_I | ω_{KS} | ω_I^{new} | f_I^{new} | ω_I^{old} | f_I^{old} | ω_{KS} | |
| NO | | | | | | | | | |
| Σ^+ ($\pi \rightarrow \pi^*$) | 6.46 | <0.01 | 8.36 | 7.22 | <0.01 | 7.49 | <0.01 | 8.53 | |
| Π ($\sigma \rightarrow \pi^*$) | 6.49 | <0.01 | 7.23 | 7.29 | <0.01 | 7.77 | 0.00 | 7.80/7.77 | |
| Δ ($\pi \rightarrow \pi^*$) | 7.26 | 0.00 | 8.36 | 7.74 | 0.00 | 8.53 | 0.00 | 8.64/8.53 | |
| Σ^- ($\pi \rightarrow \pi^*$) | 8.36 | 0.00 | 8.36 | 8.53 | 0.00 | 8.53 | 0.00 | 8.53 | |
| $^2\Pi$ ($\sigma \rightarrow \pi^*$) | 8.61 | 0.02 | 7.84 | 8.33 | 0.01 | 7.80 | 0.00 | 7.77/7.80 | |
| Σ^- ($\pi \rightarrow \pi^*$) | 8.74 | 0.00 | 8.74 | 8.64 | 0.00 | 8.64 | 0.00 | 8.64 | |
| $^2\Delta$ ($\pi \rightarrow \pi^*$) | 9.11 | 0.00 | 8.74 | 9.09 | 0.00 | 8.64 | 0.00 | 8.64 | |
| Π ($\sigma^* \rightarrow \pi^*$) | 11.64 | <0.01 | 12.45 | 12.68 | <0.01 | 13.19 | 0.00 | 13.19 | |
| $^2\Sigma^+$ ($\pi \rightarrow \pi^*$) | 14.00 | 0.35 | 8.47 | 11.90 | 0.63 | 11.65 | 0.50 | 8.64 | |
| $^2\Pi$ ($\sigma^* \rightarrow \pi^*$) | 14.82 | 0.38 | 12.87 | 14.64 | 0.24 | 13.23 | 0.00 | 13.23 | |
| N ₂ | | | | | | | | | |
| $^3\Pi_g$ ($\sigma_g \rightarrow \pi_g$) | 7.30 | | 8.20 | 7.48 | | 8.12 | | 8.12 | 8.04 |
| $^3\Sigma_u^+$ ($\pi_u \rightarrow \pi_g$) | 7.42 | | 9.60 | 6.91 | | 7.36 | | 9.01 | 7.75 |
| $^3\Delta_u$ ($\pi_u \rightarrow \pi_g$) | 8.24 | | 9.60 | 7.76 | | 9.01 | | 9.01 | 8.88 |
| $^3\Sigma_u^-$ ($\pi_u \rightarrow \pi_g$) | 9.60 | | 9.60 | 9.01 | | 9.01 | | 9.01 | 9.67 |
| $^3\Pi_u$ ($\sigma_u \rightarrow \pi_g$) | 10.37 | | 11.49 | 11.30 | | 12.06 | | 12.06 | 11.19 |
| $^1\Pi_g$ ($\sigma_g \rightarrow \pi_g$) | 9.05 | 0.00 | 8.20 | 8.71 | 0.00 | 8.12 | 0.00 | 8.12 | 9.31 |
| $^1\Sigma_u^-$ ($\pi_u \rightarrow \pi_g$) | 9.60 | 0.00 | 9.60 | 9.01 | 0.00 | 9.01 | 0.00 | 9.01 | 9.92 |
| $^1\Delta_u$ ($\pi_u \rightarrow \pi_g$) | 10.03 | 0.00 | 9.60 | 9.66 | 0.00 | 9.01 | 0.00 | 9.01 | 10.27 |
| $^1\Pi_u$ ($\sigma_u \rightarrow \pi_g$) | 13.53 | 0.42 | 11.49 | 13.82 | 0.33 | 12.06 | 0.00 | 12.06 | 12.78 |
| $^1\Sigma_u^+$ ($\pi_u \rightarrow \pi_g$) | 14.84 | 0.77 | 9.60 | 13.02 | 0.98 | 12.75 | 0.80 | 9.01 | 12.96 |
| O ₂ | | | | | | | | | |
| $^3\Delta_u$ ($\pi_u \rightarrow \pi_g$) | 6.39 | 0.00 | 6.90 | 6.21 | 0.00 | 6.35 | 0.00 | 6.35 | 6.0-6.2 |
| $^3\Sigma_u^-$ ($\pi_u \rightarrow \pi_g$) | 6.90 | 0.00 | 6.90 | 6.35 | 0.00 | 6.35 | 0.00 | 6.35 | 6.3-6.5 |
| $^3\Pi_g$ ($\sigma_g \rightarrow \pi_g$) | 7.84 | 0.00 | 7.91 | 6.80 | 0.00 | 6.79 | 0.00 | 6.79 | |
| $^3\Sigma_u^+$ ($\pi_u \rightarrow \pi_g$) | 9.00 | 0.18 | 6.90 | 8.36 | 0.32 | 8.21 | 0.24 | 6.35 | ~8.6 |
| $^3\Pi_u$ ($\sigma_u \rightarrow \pi_g$) | 14.85 | 0.18 | 14.16 | 15.35 | 0.18 | 14.52 | 0.00 | 14.52 | |

Table 4.2: Comparison of vertical excitation energies ω_I and oscillator strengths f_I for TD-DFT with TZP basis set, the traditional TD-DFTB method (old) and TD-DFTB with onsite correction (new). The PBE functional is used throughout. ω_{KS} denotes the KS orbital energy difference corresponding to the most dominant single particle transition in the many body wavefunction, as discussed by Casida in Ref. [143]. Experimental data for N₂ and O₂ were taken from Ref. [219] and inferred from the potential energy curves in Ref. [220], respectively. Oscillator strengths are only provided for excitations that are not trivially spin-forbidden. All energies are expressed in eV.

NO

NO belongs to the symmetry point group $C_{\infty v}$ for which Π and Σ^+ transitions are electric dipole allowed. However, TD-DFTB describes the former as forbidden. This is due to the mentioned vanishing of the corresponding transition charge which leads to an equality of the KS energy difference ω_{KS} and the excited state energy ω_I . Within the refined formulation this failure is successfully overcome as shown in Table 4.2. This improvement is specially important for the second and fourth Π transitions with oscillator strengths of 0.01 and 0.24, respectively, which are in agreement with the TD-DFT values of 0.02 and 0.38. Our correction is in this case, essential for providing qualitatively correct oscillator strengths in the absorption spectrum (see Fig. 4.2) where traditional TD-DFTB is able to describe only the Σ^+ peak.

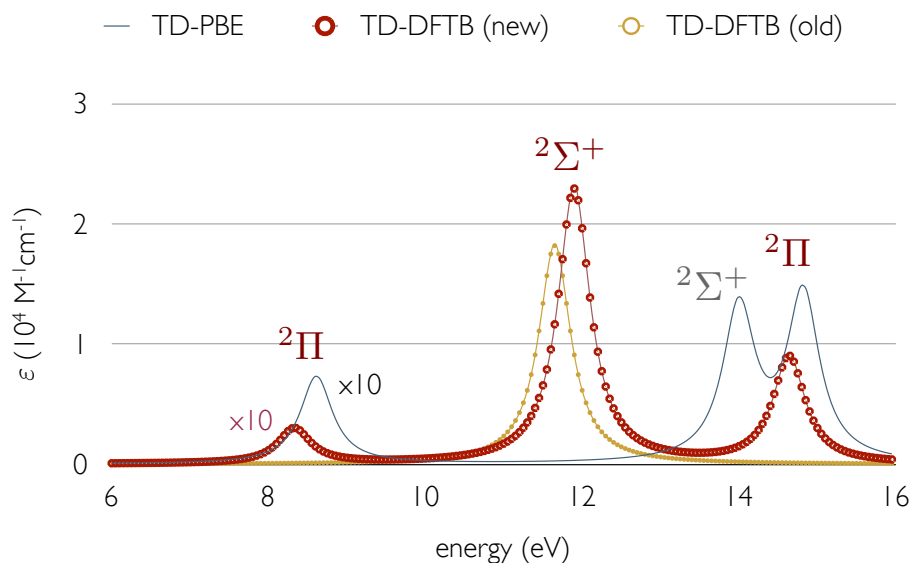


Figure 4.2: Absorption spectrum of nitric oxide as obtained with full TD-DFT (PBE/TZP), traditional TD-DFTB (old) and TD-DFTB with on-site corrections (new). The y -axis represents the molar extinction coefficient, $\varepsilon = \sum_I \varepsilon_I$. For its calculation we use the relationship, $f_I = C \int \varepsilon_I(\omega) d\omega$ [221], where f_I is the oscillator strength related to excitation I , $C = 3.5 \times 10^{-5}$ M cm/eV and the energy, ω , is given in eV. By using Lorentzian functions for the spectral broadening, the extinction coefficient can then be written as $\varepsilon(\omega) = \sum_I \frac{f_I}{C\pi} \frac{\Gamma/2}{(\omega - \omega_I)^2 + (\Gamma/2)^2}$. The full width at half maximum (FWHM), Γ , was set to 0.5 eV.

The onsite correction also improves the description of Π transitions quantitatively. For example, the first Π excitation energy is clearly overestimated with respect to first-principle results. When using the correction the overestimation is reduced by almost 0.5 eV. Oppositely, the second Π excitation energy is strongly underestimated within traditional TD-DFTB whereas the corrected calculations return a value (8.33 eV) close to that from TD-DFT (8.61 eV). The Σ^+ ($\pi \rightarrow \pi^*$) transitions are also found to be better described within the onsite correction, although the first (second) Σ^+ excitation energy is still significantly overestimated (underestimated).

Unlike $\sigma \rightarrow \pi^*$ and $n \rightarrow \pi^*$, $\pi \rightarrow \pi^*$ excitations has been shown to be correctly described within TD-DFTB. There is however a critical exception for NO and other diatomic species (see below N_2 and O_2 molecules, for instance). It should be noted in Table 4.2 that for the

forbidden transitions Σ^- and Δ , no energy displacement with respect to the KS energy difference happens within the original TD-DFTB. For Σ^- excitations, this is in correspondence with ab-initio observations, and the corrected and traditional results are in this case identical. However, first-principle findings do indicate an energy shift for Δ transitions. The wrong degeneracy of Σ^- and Δ excitations of diatomic molecules should be identified as another important failure of traditional TD-DFTB. The onsite correction also rectifies this problem as can be seen in Table 4.2.

As a final minor enhancement, it should be mentioned that the spin contamination of the doublet ${}^2\Pi$ states are reduced within the onsite-corrected formalism (data not shown).

N₂ and O₂

The electric-dipole-allowed transitions ${}^1\Pi_u$ and ${}^3\Pi_u$ of the homonuclear molecules N₂ and O₂ (point group $D_{\infty h}$), respectively, are neither correctly described by traditional TD-DFTB as shown in Table 4.2. When applying the onsite correction, these excitations become allowed with oscillator strengths in agreement with ab-initio results. However, it is necessary to indicate that the O₂ ${}^3\Pi_u$ excitation energy is somewhat overestimated, being in better agreement within the non-corrected formalism. In contrast, the onsite correction greatly improves the correspondence of the excitation energy of N₂ ${}^1\Pi_u$ with the TD-DFT result. This transition and the ${}^3\Pi_u$ state are degenerate according to traditional results whereas such degeneracy is broken at the corrected TD-DFTB level. This degeneracy breaking is in total accordance with the results obtained at a higher level of theory.

The original formalism also predicts the degeneracy of the singlet and triplet Σ_u^- and Δ_u states of N₂ with excitation energy equal to 9.01 eV. This is however only partially confirmed by the ab-initio results and in total disagreement with the experimental findings. According to TD-DFT, the triplet and singlet Σ_u^- states are degenerate with excitation energy of 9.60 eV but the triplet and singlet Δ_u degeneracy is not observed. On the other hand, experiments report nearly degenerate Σ_u^- states with excitation energies of 9.67 and 9.92 eV for the triplet and singlet states, respectively, in contrast with the TD-DFT findings. This apparent failure of TD-DFT has been noticed before [222, 223]. In a recent letter, it was shown that excited states like Σ_u^- of N₂ cannot be described by linear-response TD-DFT as their corresponding excitation energies do not correspond to poles of the response function [224]. TD-DFTB as an approximation to TD-DFT unavoidably inherits this issue and our correction is unable to fix it. However, it does break the wrong degeneracy of the triplet and singlet Δ_u states. For O₂, a similar degeneracy breaking of the transitions Σ_u^- and Δ_u within the corrected TD-DFTB can be observed. This is again in total agreement with first-principle results.

4.4 Benchmarks

In this section we intend to give a more general assessment of the performance and efficiency of the presented formalism by comparing it to the old scheme and different TD-DFT variants in terms of vertical transition energies, oscillator strengths and employed computational time. A statistical analysis for an extensive sample data is pursued but not always possible. As a reference, both high-level theoretical results and experimental observations are used. For both TD-DFTB scheme, the same set of parameters (except, of course, the newly introduced onsite

and dipole parameters) are employed throughout. Also, calculations with either methods are subject to the same convergence criteria in every case. In all reported MSD, the excitation energies and oscillator strengths of the assessed method are taken as the minuend, that is, a positive MSD denotes an overestimation with respect to the reference method.

4.4.1 Vertical transition energies

To assess the general performance of the corrected TD-DFTB method in terms of vertical excitation energies we have employed a large benchmark set defined by the group of Thiel [225]. This set has been largely used during the last few years to test several density functionals [77–79, 226–230] and DFT-based methods [229–232]. In particular, it has been recently used for the validation of TD-DFTB [232]. It covers $\pi \rightarrow \pi^*$, $n \rightarrow \pi^*$ and $\sigma \rightarrow \pi^*$ excitations of 28 organic compounds, intending to embrace the most important chromophores in organic photochemistry. Thiel's set is divided into 4 groups according to the nature of the compounds (Fig. 4.3): unsaturated aliphatic hydrocarbons (group A), aromatic hydrocarbons and heterocycles (group B), carbonyl compounds (group C) and nucleobases (group D).

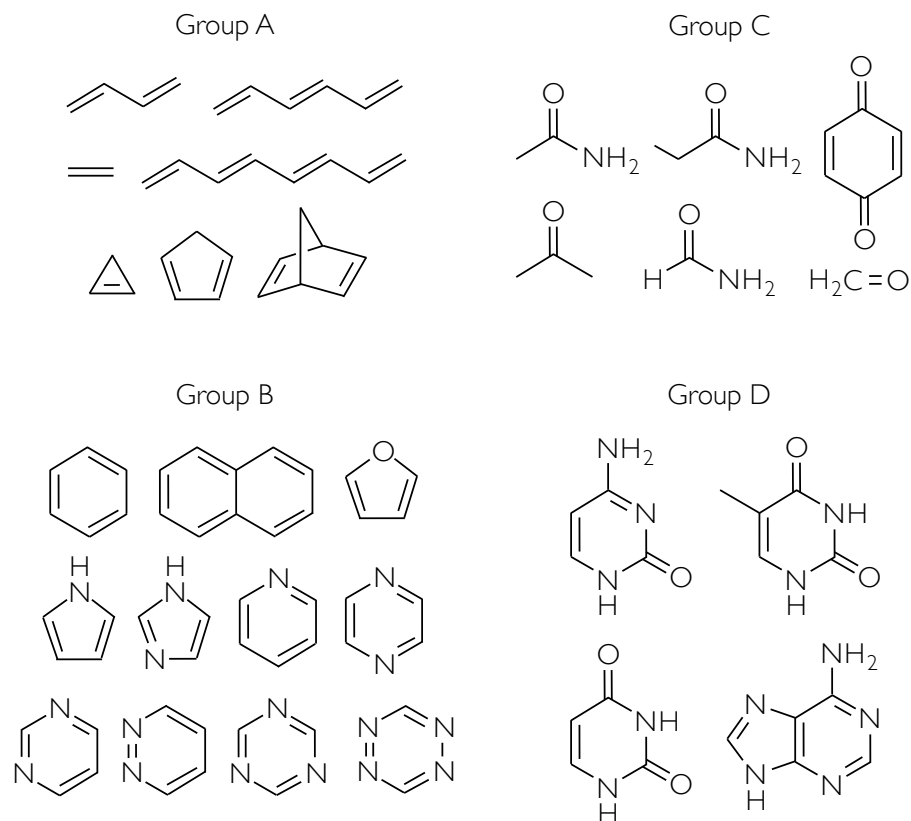


Figure 4.3: Thiel's benchmark set of compounds.

For comparison we have calculated singlet and triplet vertical excitation energies at the TD-DFT level, employing three types of density functionals: pure, hybrid and long-range corrected (LC) ones. PBE is chosen as the pure functional, which allows for assessment of TD-DFTB as an approximation. PBE has been shown, however, to not be the most suitable functional to

compute vertical excitation energies and, therefore, the benchmark has been enriched with employment of the global hybrid PBE0 [123,124] and the LC functional CAM-B3LYP [128]. PBE0 and CAM-B3LYP have been extensively benchmarked, resulting in ones of the best tested functional in reproducing theoretical best estimates (TBE) and experimental findings [77,233–236]. For the PBE and PBE0 cases, a TZP basis set was employed whereas we used 6-311G** basis functions for the LC functional calculations. Given the known poor description of singlet-triplet (S-T) transition energies by TD-DFT due to triplet instabilities in the ground states [237–239], we have also performed CAM-B3LYP/6-311G** calculations in the Tamm-Dancoff approximation (TDA) [238]. The significant improvement of triplet states under the TDA was simultaneously shown by the groups of Tozer [240,241] and Brédas [242]. The TURBOMOLE package was used for those calculations involving the conventional functionals, whereas NWChem [243] was employed for CAM-B3LYP in both TD-DFT and TDA calculations. To detach the accuracy of TD-DFTB as an approximation to TD-DFT from the quality of DFTB ground state geometries, the same optimized structures were used along the benchmark. These geometries were previously obtained at the MP2 level [225]. Nevertheless, it has been shown that TD-DFTB results for Thiel’s set are not too sensitive to employment of either MP2 or DFTB geometries [232].

In Appendix C, all our calculation results can be consulted. In sections C.1.1 and C.2.1 we include the KS energy difference of the corresponding dominant single-particle transition, which is useful for the analysis of the relative displacement of the excitation energies with respect to the KS energy difference as compared to ab-initio TD-DFT at the PBE level (TD-PBE). Oscillator strengths are also given as another useful information. For further comparison, we also provide the TBEs for this benchmark set, calculated at the CASPT2 level and reported by Thiel’s group [225]. Experimental values for some vertical excitation energies are additionally given. At the bottom of Tables C.5 - C.8 and C.12 - C.14 a statistical analysis of the collected data is presented. The MSD and the root-mean-square (RMS) deviation of the TD-DFTB excitation energies with respect to the experiment, the TBE and TD-PBE are reported for each group of compounds. Statistics on TD-DFT results are also provided to indicate its degree of correspondence with a higher level of theory and experiment.

To assess the validity of our approximation, we focus on the comparison with the TD-PBE data set. It is important to recall that TD-DFTB parameters are calculated at this level of theory and the main aim of our approach is to improve its agreement with respect to the TD-DFT description. Since TD-DFT at the PBE level is of course an approximation itself, we are also interested in examining the accuracy of our method compared to a higher level of theory and experiment. In this case, we can benchmark both the traditional and corrected formalisms side by side with different TD-DFT approaches. It is worth mentioning that the subset of S-T excitations for which experimental observations are provided is around 50% smaller than the original set, but we consider it still suitable to perform a statistical analysis. The TBEs are, on the other hand, available for the complete benchmark set and they are fairly close to their corresponding experimental values, with a RMS error of 0.24 eV for triplet states and 0.38 eV for singlet states. On average, both singlet and triplet TBEs are slightly overestimated (MSD = 0.15 eV and 0.20 eV, respectively). This should be borne in mind for the further analysis.

Consistent with earlier studies [77,78], TD-DFT excitation energies at the PBE level appear to be somewhat underestimated with regard to experimental findings as a general trend (MSD = -0.28 eV and -0.27 eV for singlet and triplet states, respectively). Opposed to this, with the incorporation of a fraction of exact exchange, singlet-singlet (S-S) excitation energies become

overestimated, being in closer agreement with the TBEs. Especially, the PBE0 functional agrees significantly with a MSD = 0.00 and RMS error of only 0.31 eV for S-S transitions. The TDA, on the other hand, shows a high overestimation of singlet energies, whereas returns the expected good accordance with TBEs and experiment for S-T excitations.

Triplet States

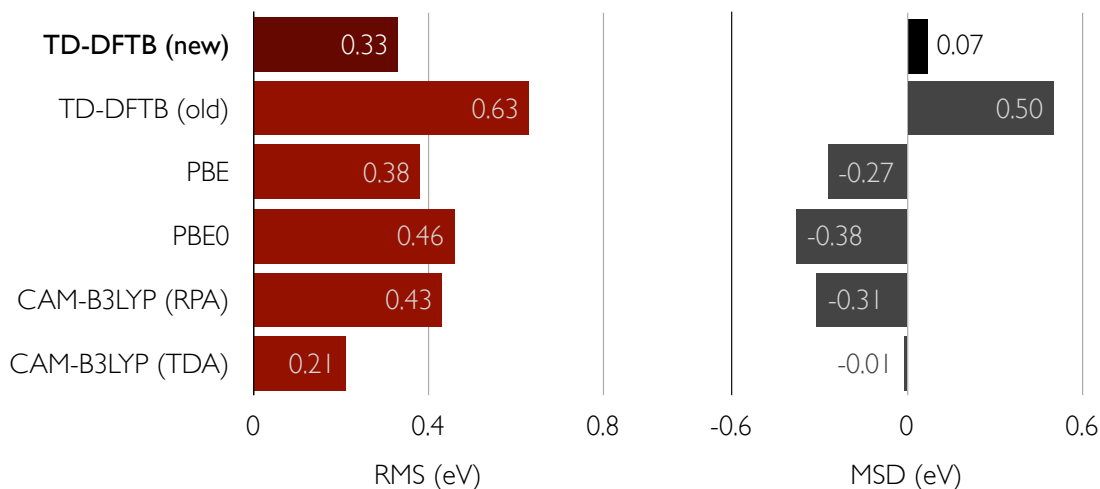


Figure 4.4: Root mean square errors and mean signed deviation of S-T transition energies for a subset of Thiel's benchmark with respect to experimental data.

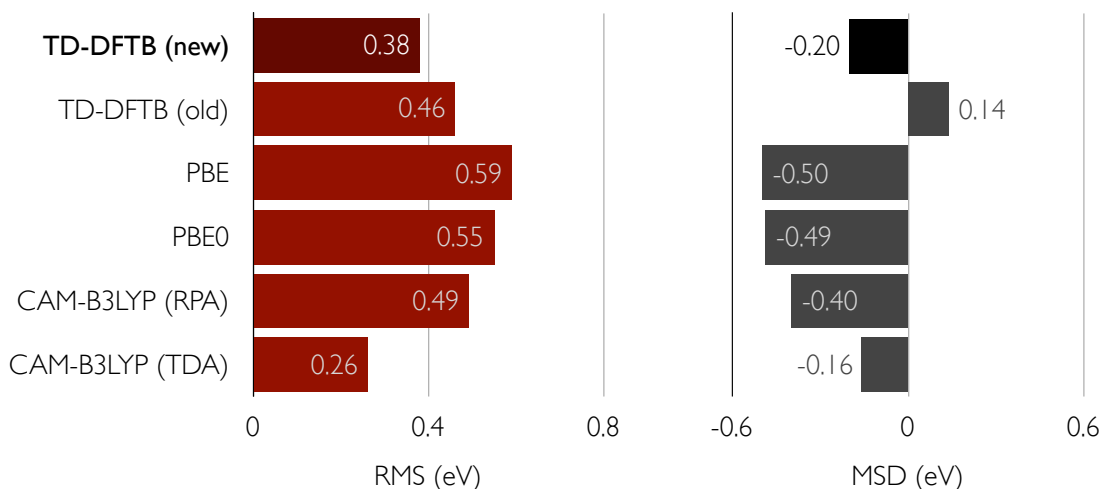


Figure 4.5: Root mean square errors and mean signed deviation of S-T transition energies for Thiel's benchmark set with respect to TBEs.

Fig. 4.4 and 4.5 show the MSD and RMS deviations of S-T energies from experiment and the TBEs, respectively, for the investigated methods. As should be seen from the former Figure,

triplet state energies are significantly overestimated compared to experiment ($\text{MSD} = 0.50$ eV) within traditional TD-DFTB. One of the main effects of our correction is indeed the significant improvement of S-T excitation energies taking TD-PBE and experimental values as a reference. Within the refined formulation, the RMS error for this kind of transition is reduced by 0.3 eV with respect to both TD-PBE and experiment. More importantly, the RMS error with respect to the latter (0.33 eV) is slightly lower than that for TD-PBE itself (0.38 eV). This difference is yet increased if the functionals PBE0 (0.46 eV) and CAM-B3LYP (0.43 eV) are employed, and if the TBEs are taken as the reference, the RMS deviations for TD-DFT S-T energies are even larger. Only the TDA clearly outperforms our method in this case. A similar accuracy for both TD-PBE and refined TD-DFTB can be seen for the first two groups of compounds whereas, for the third group, the agreement with experimental data is somewhat better for our method (see Appendix C). In addition, whereas Tables C.12 - C.14 still indicate some overestimation of the corrected TD-DFTB results with respect to TD-PBE, the MSD of our refined approach compared to experiment becomes very small, which shows that the corrected S-T excitation energies are scattered around the experimental values. Specifically, in the group of aromatic hydrocarbons and heterocycles, transition energies are overestimated whereas there is some underestimation for the carbonyl compounds. Only with regard to TBE, the refined excitation energies appear to be underestimated for every group of compounds (see Appendix C).

Singlet States

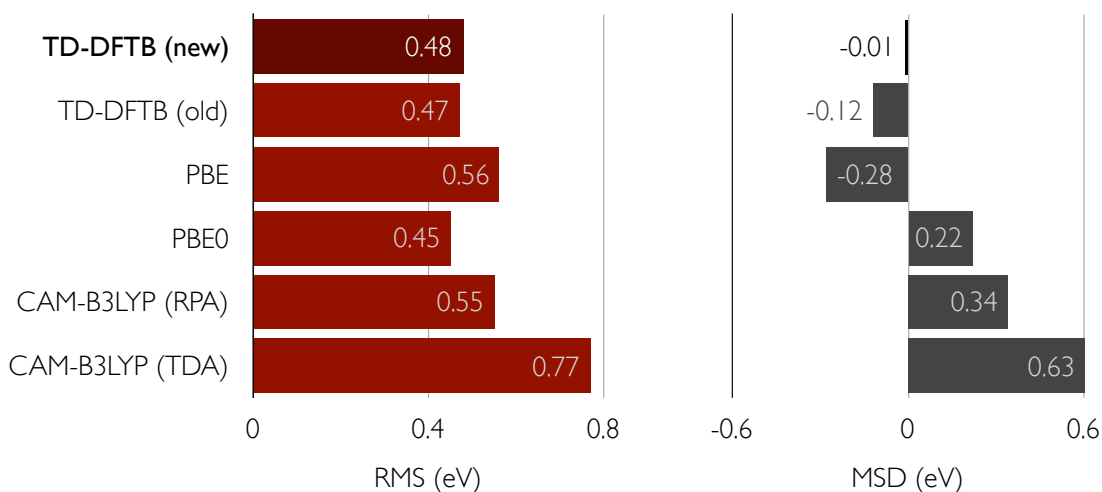


Figure 4.6: Root mean square errors and mean signed deviation of S-S transition energies for a subset of Thiel’s benchmark with respect to experimental data.

In contrast to the observations for S-T transitions, the traditional TD-DFTB method is, on average, in slightly better agreement with TD-PBE for the description of S-S excitations, compared to the new formulation. The RMS deviations of the corrected and non-corrected transition energies from TD-PBE values are in this case 0.57 eV and 0.50 eV, respectively. On the other hand, regarding the experimental references and the TBEs, both approaches perform with similar accuracy for this kind of transition (see Figs. 4.6 and 4.7). The refined formalism returns overestimated S-S excitation energies according to TD-PBE results, although with

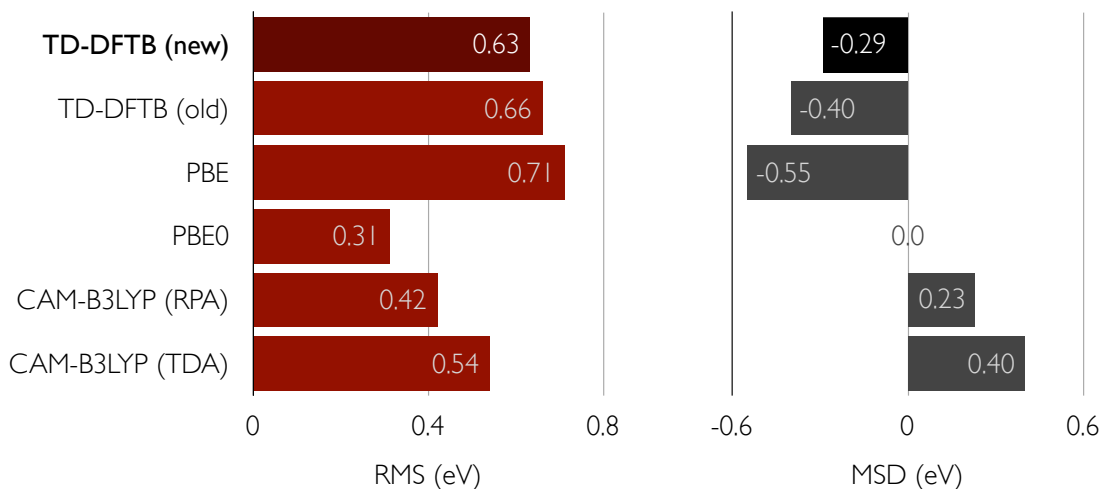


Figure 4.7: Root mean square errors and mean signed deviation of S-S transition energies for Thiel’s benchmark set with respect to TBEs.

respect to experiment they are again spread around the reference values as can be seen from Fig. 4.6. In this case, the overestimation for the second group of compounds is compensated with the underestimation for the aliphatic hydrocarbons and the nucleobases, thus leading to an almost vanishing MSD (-0.01 eV). The results for the latter mentioned group of compounds are the least overestimated with respect to TD-PBE, with a MSD of only 0.09 eV. By contrast, the underestimation with respect to experiment is significant (MSD = -0.37 eV) and increases even more by taking the TBEs as the reference, for which the MSD amounts to -0.75 eV. For this group, the RMS error of TD-DFTB for singlet states with respect to TBEs is remarkably high (0.91 eV and 0.96 eV for the corrected and non-corrected approaches, respectively). The limited agreement between the TD-DFTB excitation energies of the nucleobases and their TBE counterparts has been already pointed out by Trani and co-workers [232]. However, it is necessary to notice that this failure should be rather attributed to TD-PBE itself and not to TD-DFTB as an approximation. In fact, the worst agreement between TD-PBE and TBE along the benchmark set is found for the carbonyl compounds and the nucleobases, with RMS errors of 0.96 eV and 0.89 eV, respectively. A very recent study by Foster and Wong indeed shows that conventional semi-local functionals fail in the description of the optical properties of nucleobases while tuned range-separated functionals offer significant improvements [244]. This is evidenced by the good performance of CAM-B3LYP (see Appendix C), whose RMS deviation from TBE is lowered to 0.30 eV. It should be indicated, however, that the best agreement with both experiment and TBEs is for the global hybrid functional PBE0, with RMS errors of 0.30 eV and only 0.11 eV, respectively. The enhancement of PBE0 over long-range corrected functionals for the description of these compounds has been previously pointed out by Jacquemin and co-workers [77].

Overall Performance

The overall analysis (accounting excitations to both singlet and triplet states) leads to somewhat smaller RMS errors for corrected TD-DFTB compared to the non-corrected formalism, as can

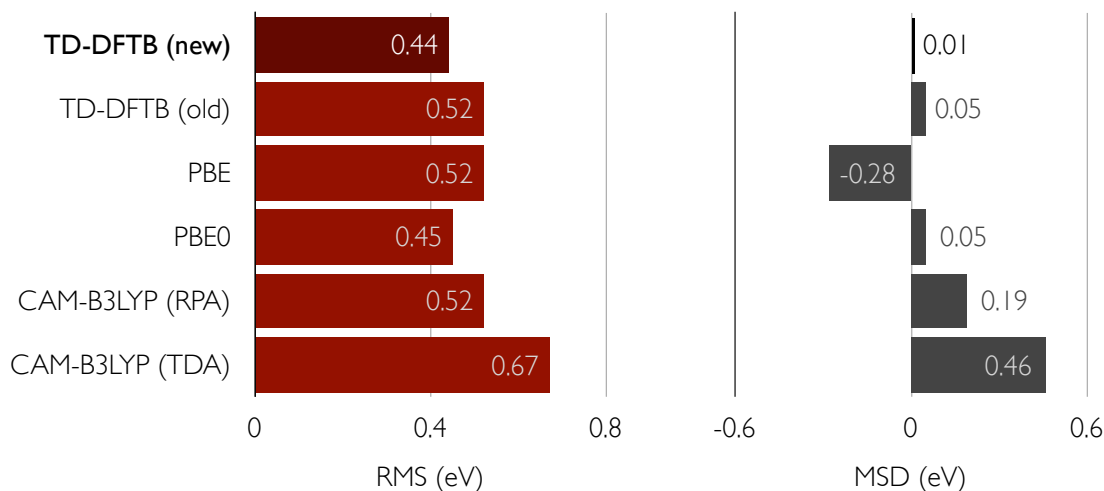


Figure 4.8: Root mean square errors and mean signed deviation of S-S and S-T transition energies for a subset of Thiel's benchmark with respect to experimental data.

be seen from Figs. 4.8 and 4.9. It should be indicated that, despite the important improvements for the triplet states within the corrected formulation, the benchmark set for S-S excitations is comparatively larger, conceding more importance to this kind of transitions within the total balance. As a general behavior, it can be stated that TD-DFTB singlet excited states are shifted up in energy when the onsite correction is switched on. At the same time, the correction shifts triplet states down.

Let us investigate this trend in more detail. For local functionals, the TD-DFT coupling matrix leads to an upward shift of excitation energies with respect to Kohn-Sham energy differences for singlets and a downward shift for triplets. Ground state DFTB generally overestimates KS energy differences with respect to TD-PBE, due to the employed minimal basis set. In the original TD-DFTB, this error is partially compensated for singlet states, because the coupling matrix is underestimated with respect to first principles results. For triplet states the aforementioned errors do not compensate, but sum up, leading to strongly overestimated S-T energies. In the new approach, the underestimation of the coupling correction to KS energies is reduced, which leads to a widening of the singlet-triplet gap. Whereas S-T energies are now in much better accord with the TD-PBE reference, S-S energies are slightly overestimated. Given the fact that TD-PBE systematically underestimates S-S energies with respect to the experiment, the new formalism performs well for both S-S and S-T energies in this comparison.

Let us now turn our attention to the overall accuracy of the singlet-triplet energy gap within the onsite correction. By inspection of Figs. 4.4 to 4.7, it should be noticed that with respect to both reference data, MSDs for the corrected singlet and triplet states are similar. For instance, with respect to the TBEs, S-T and S-S energies are underestimated by 0.20 and 0.29 eV, respectively. This indicates that corrected TD-DFTB returns a mean singlet-triplet gap in agreement with *ab initio* and experimental results. This is not the case for original TD-DFTB, where for the most critical case (taking experimental data as reference) it gives a large positive MSD for triplet states whereas returns a negative value for S-S transitions, thus strongly underestimating the mean singlet-triplet gap.

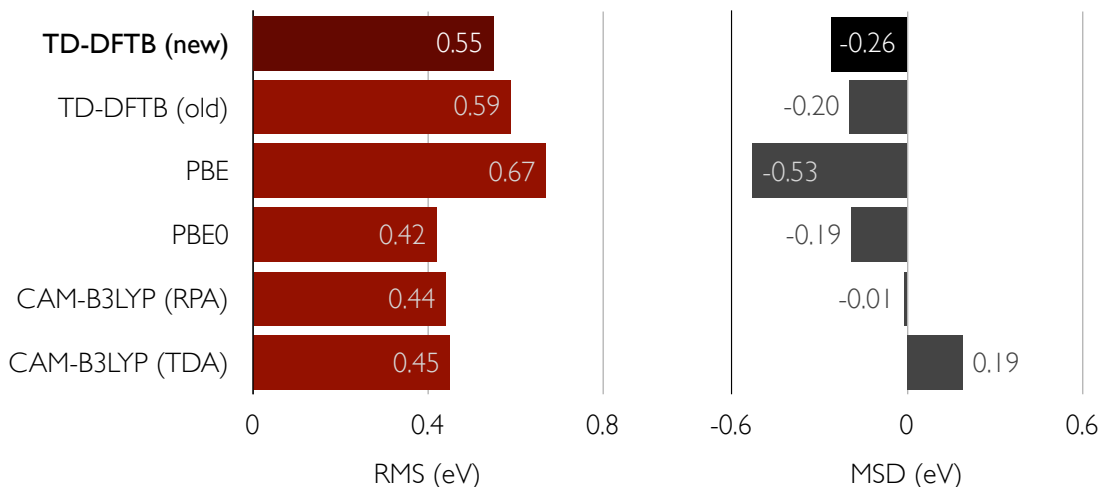


Figure 4.9: Root mean square errors and mean signed deviation of S-S and S-T transition energies for Thiel’s benchmark set with respect to TBEs.

The singlet-triplet gap broadening under the onsite correction is particularly noticeable for $n \rightarrow \pi^*$ and $\sigma \rightarrow \pi^*$ excitations. The excitation energies for these transitions are either identically equal or (for few cases) very close to their corresponding KS energy differences at the non-corrected TD-DFTB level, resulting in degenerate or nearly-degenerate singlet and triplet states (see Appendix C). The only exception are the triplet B_{1u} states of tetrazine, for which an energy displacement occurs also for traditional TD-DFTB, although clearly underestimated with respect to the TD-PBE results. Within the onsite correction the excitation energies are either shifted down for triplets or shifted up for singlets with respect to the KS energy difference, leading to a singlet-triplet gap in accordance with the observations at the TD-DFT level. A similar degeneracy breaking was shown earlier for N_2 . Also in terms of oscillator strengths these transitions are flawed in original TD-DFTB as they appear to be forbidden, in contradiction with the TD-DFT and TBE findings. The proposed correction returns nonzero oscillator strengths in agreement with more sophisticated calculations.

Considering only $n \rightarrow \pi^*$ and $\sigma \rightarrow \pi^*$ transitions, the RMS error of S-T excitation energies at the corrected and non-corrected TD-DFTB level as compared to TD-PBE are, respectively, 0.58 and 0.82 eV. This kind of excitations are evidently difficult cases for the traditional formalism, and an important improvement is obtained with the onsite correction, although the major quantitative enhancement of the latter approach is for S-T $\pi \rightarrow \pi^*$ transitions. Indeed, $n \rightarrow \pi^*$ and $\sigma \rightarrow \pi^*$ excitation energies are still strongly overestimated at the corrected TD-DFTB level with respect to TD-PBE, with MSD of 0.49 and 0.32 eV for triplet and singlet states, respectively. However, if we compare our findings with the TBEs, those are by contrast, significantly underestimated (MSD = -0.21 and -0.40 eV for S-T and S-S transitions, respectively) and the RMS deviations for both corrected and non-corrected formalisms are similar.

4.4.2 Oscillator strengths

The most important effect of the onsite correction on TD-DFTB oscillator strengths is perceived for $n \rightarrow \pi^*$ and $\sigma \rightarrow \pi^*$ transitions. In the benchmark set of Thiel, most of these excitations appear as forbidden within the traditional formalism, which does not concur with TD-DFT results (see Tables C.5 - C.8). Within the refined scheme, the allowed transitions recover their nonvanishing oscillator strengths. The majority of them exhibit rather small values of this quantity. The only exception is for the A_2' state of triazine with an oscillator strength of 0.01 according to corrected TD-DFTB, which is in agreement with the TD-DFT findings. Although the correct qualitative description of $n \rightarrow \pi^*$ and $\sigma \rightarrow \pi^*$ excitations constitutes the main asset of corrected TD-DFTB, it is of interest to assess its general accuracy for the evaluation of $\pi \rightarrow \pi^*$ oscillator strengths. Opposed to the existing situation for vertical excitation energies, there is no standard, well established benchmark for oscillator strengths. Moreover, there are considerably fewer works addressing the assessment of TD-DFT for the description of this magnitude than there are for transition energies. Also, they generally consider a reduced number of compounds/transitions for the statistical analysis. Some authors have found that range separated and global hybrids have the best performance among some tested functionals [129, 245, 246]. Coupled cluster (CC) models have been repeatedly employed as a reference method [230, 245–247], whereas comparison to experiment is troublesome due to overlapping and broadening of the spectral lines.

| Molecule / Trans. | TD-DFTB | | PBE | PBE0 | CAM-B3LYP | EOM-CCSD |
|-------------------------------------|---------|-------|------|------|-----------|----------|
| | new | old | | | | |
| Ethene | | | | | | |
| ${}^1B_{1u}(\pi \rightarrow \pi^*)$ | 0.37 | 0.27 | 0.33 | 0.37 | 0.38 | 0.35 |
| Butadiene | | | | | | |
| ${}^1B_u(\pi \rightarrow \pi^*)$ | 0.65 | 0.52 | 0.61 | 0.69 | 0.70 | 0.62 |
| Pyridine | | | | | | |
| ${}^1B_2(\pi \rightarrow \pi^*)$ | 0.03 | 0.02 | 0.03 | 0.04 | 0.04 | 0.03 |
| ${}^1A_1(\pi \rightarrow \pi^*)$ | 0.02 | 0.01 | 0.01 | 0.02 | 0.02 | 0.01 |
| Pyrazine | | | | | | |
| ${}^1B_{2u}(\pi \rightarrow \pi^*)$ | 0.09 | 0.07 | 0.07 | 0.10 | 0.09 | 0.08 |
| ${}^1B_{1u}(\pi \rightarrow \pi^*)$ | 0.06 | 0.03 | 0.05 | 0.06 | 0.07 | 0.05 |
| Pyrimidine | | | | | | |
| ${}^1B_2(\pi \rightarrow \pi^*)$ | 0.03 | 0.03 | 0.03 | 0.04 | 0.03 | 0.03 |
| ${}^1A_1(\pi \rightarrow \pi^*)$ | 0.03 | 0.02 | 0.04 | 0.04 | 0.04 | 0.02 |
| Pyridazine | | | | | | |
| ${}^1A_1(\pi \rightarrow \pi^*)$ | 0.03 | 0.02 | 0.02 | 0.02 | 0.02 | 0.02 |
| RMS | 0.01 | 0.04 | 0.01 | 0.02 | 0.03 | |
| MSD | 0.01 | -0.02 | 0.00 | 0.02 | 0.02 | |

Table 4.3: Oscillator strengths for 9 $\pi \rightarrow \pi^*$ excitations to valence states.

Caricato’s benchmark is possibly the most extensive and significant one among those in the literature [246]. They tested 28 XC functionals using a set of 11 small organic molecules

against equation-of-motion CC singles and double (EOM-CCSD) [248, 249] results. Ground-state geometries were optimized at the MP2/6-311G(p,d) level whereas a 6-311(3+,3+)G(p,d) basis set was employed for the evaluation of the oscillator strengths. They show that the best agreement with EOM-CCSD is achieved at the CAM-B3LYP level. However, it should be borne in mind that, in TD-DFT, oscillator strengths are not only sensitive to the employed functional but also to variation of the basis set. Table 4.3 shows the oscillator strength of 9 $\pi \rightarrow \pi^*$ excitations as obtained with the methods tested in the previous subsection except the TDA. Those have been extracted from Caricato’s set by considering the most important transitions (with oscillator strengths ≥ 0.01) to valence states only. For comparison, the EOM-CCSD results reported by Caricato and coworkers are also provided. A visible consequence of our correction is the systematic increase of the oscillator strength values. This is also observed for Thiel’s set in Appendix C. As suggested by the reference data in Table 4.3, this is indeed a desired feature. Traditional results appear to be underestimated not only with respect to EOM-CCSD but also to the investigated TD-DFT variants. On the other hand, the agreement of refined TD-DFTB with the reference data is satisfactory, with a RMS deviation of only 0.01. The onsite correction apparently returns slightly overestimated values, although TD-DFT results are even more overestimated when the hybrid functionals are employed.

4.4.3 Computational time

Figure 4.10 shows the total elapsed (wall clock) time employed for the calculation of the low-lying excitation energies and oscillator strengths of the 28 compounds of Thiel. All calculations were performed on a workstation with an Intel Xeon processor E3-1225 at 3.10 GHz and a memory of 8 Gb. The first 15 S-S and S-T excitation energies of every compound were computed for each case. As can be seen from Fig. 4.10, the real time employed by both TD-DFTB variants is significantly shorter than for any of the TD-DFT methods.

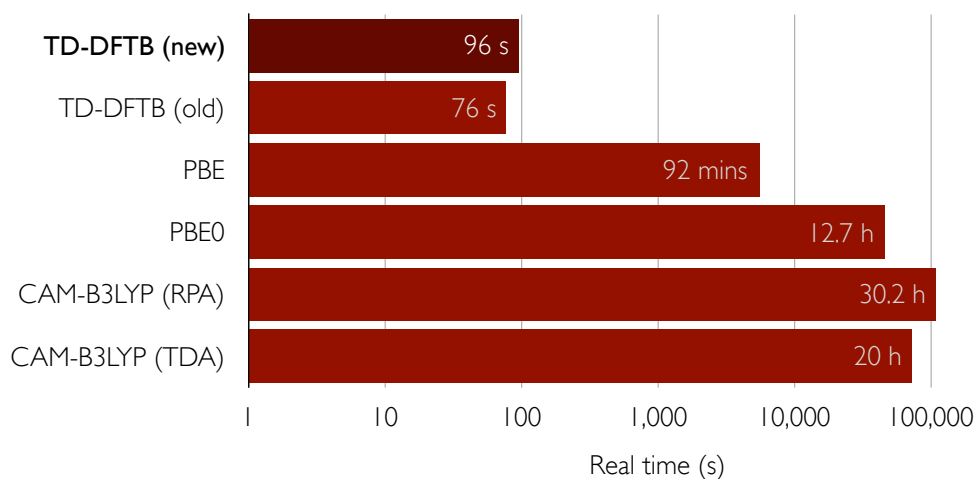


Figure 4.10: Total wall clock time for the computation of the first 15 singlet-singlet and singlet-triplet excitation energies of Thiel’s set of compounds.

Small molecules are not the usual target of TD-DFTB, whose efficiency makes it especially useful for the study of large systems. It is therefore of interest to benchmark the computational

time in a more realistic applicability of the method. Thus, as a second test we calculated the first 20 S-S energies of a large molecule ($C_{66}O_{10}N_4H_{44}$). The real time employed by traditional and corrected TD-DFTB, as well as by TD-PBE as calculated with TURBOMOLE are shown in Fig. 4.11. For TD-PBE a TZP basis set was used. For the tight-binding approaches, we additionally truncated the set of KS states to reduce the dimension of the linear-response eigenproblem and hence, shorten the computational time. In Fig. 4.11 we show both the results for the *full* calculation (with no cut-off) and the one using the aforementioned restriction. The latter are indicated with a star (see Figure).

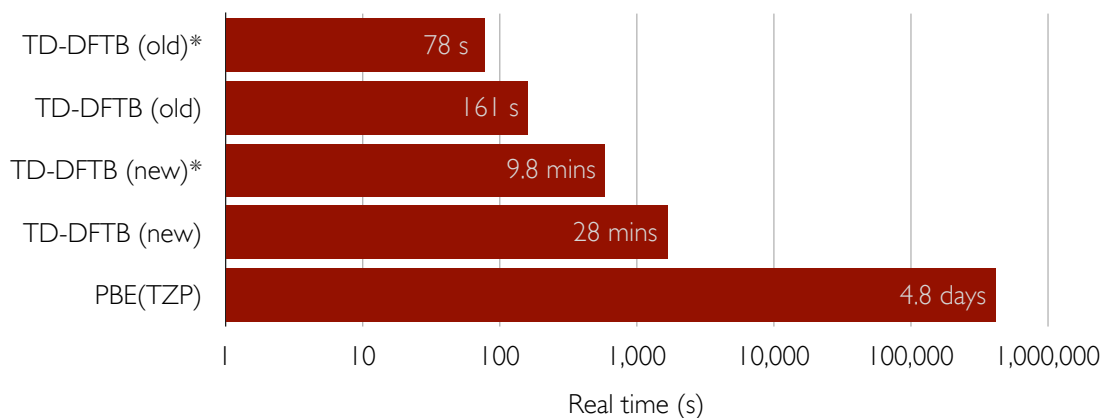


Figure 4.11: Wall clock time for the computation of the first 20 singlet-singlet excitation energies of a macromolecule.

There are many ways to establish the constraints of the KS orbitals entering the calculation. For investigations with *a priori* knowledge of the localization of the states involved in the important transitions, a constraint of the orbitals based on their Mulliken population on selected atoms has been used [250]. This is for instance the case of molecules in solution, for which excitations involving the solvent are usually of minor interest. This constraint is therefore intended for very specific purposes. We chose to restrict the orbitals by their energies rather than by their spatial location. Instead of defining subsets of occupied and virtual orbitals independently, we set a KS energy difference threshold to which all single-particle transitions are subject. That is, we include every orbital pair, ψ_i and ψ_a , such that $\omega_{ia} \leq \omega^{thres}$, where ω^{thres} must be greater than the upper boundary of the energetic region of interest, ω^{max} . An appropriate value for ω^{thres} depends on the optical properties of the system. For systems with transitions with a marked collective character, the defined energy window needs to be large. Conversely, for systems featuring single-particle excitations, ω^{thres} may be chosen fairly close to the maximum energy of the region of interest and yet obtain accurate transition energies.

The requirements for returning accurate oscillator strengths are, in contrast, generally higher. Contrary to the transition energies, these quantities are specially sensitive to even small off-diagonal elements of the response matrix [251]. This means that even a weak transition coupling affects the oscillator strengths and to a significantly lesser extent, the excitation energies. Thus, the correct description of the former magnitude usually demands a greater threshold energy difference.

There is, however, a more efficient way of setting an orbital constraint that accounts for both

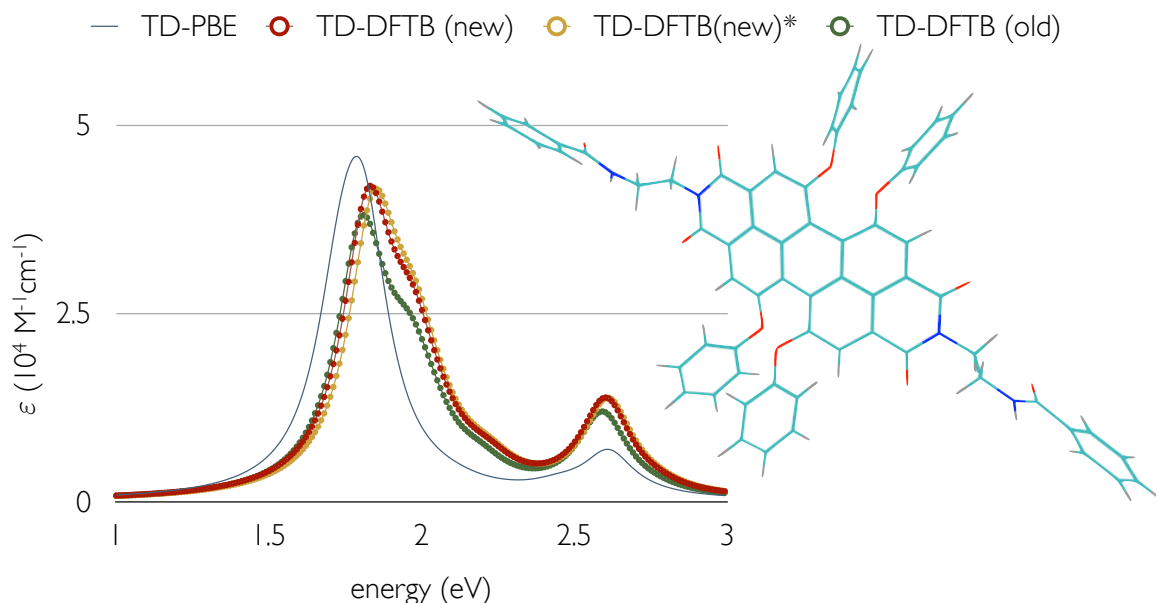


Figure 4.12: Low-lying absorption spectrum of a macromolecule (displayed to the right) as obtained with TD-DFT (PBE/TZP), traditional TD-DFTB (old) and corrected TD-DFTB with (new) and without (new)* constraints on the KS orbitals. See Fig. 4.2 for details on the calculation of ϵ . The Lorentzian FWHM was set to 0.2 eV.

accurate energies and oscillator strengths, that is, a constraint giving a smaller orbital subset than that obtained with a mere restriction on the energy, while yielding the same accuracy. Oscillator strengths depend, apart from the response vector \mathbf{F}^I , on the dipole matrix \mathbf{d} and the KS energy difference as expressed in Eq. (2.47). This formula indicates that this quantity has important contributions from $\{i, a\}$ pairs for which the matrix elements d_{ia} and ω_{ia} are significant. In this sense, a truncation of the transitions based on their SPA oscillator strengths might be more effective for the calculation of oscillator strengths. Our experience shows that the combination of an energy window with a cutoff in SPA oscillator strengths reduces the dimension of the orbital subset compared to a truncation based only on energetic considerations, for a given accuracy. On the other hand, the former restriction usually slows down convergence of the Lanczos algorithm for the diagonalization of the response matrix. This altogether leads to similar CPU times for both approaches. The results shown in Fig. 4.11 correspond to an energy cutoff of $\omega^{max} + 2.72$ eV and an oscillator strength cutoff of 10^{-3} . ω^{max} is in this case about 2.7 eV. As can be seen from the Figure, the enforced constraints reduce the wall time in up to 65% with respect to the full TD-DFTB calculation. In Fig. 4.12, the absorption spectrum of the molecule is shown. It should be noted that, despite the constraints, both TD-DFTB (new) and TD-DFTB (new)* give very similar spectra. The same holds for traditional TD-DFTB (spectrum for TD-DFTB (old)* not shown). Further restrictions start compromising the accuracy of the method. This is because some of the low-lying KS transitions are coupled to higher ones and hence, the latter have to be included within the energy window in order to obtain correct results. Our orbital constraints are obviously more promising for systems displaying excitations with a low collective character. This is the case of TiO_2 surfaces, for which restricted TD-DFTB calculations were up to 700% faster at no additional loss of accuracy.

These systems will be studied in the next chapter.

4.5 Summary

In this chapter, we generalized the TD-DFTB method to account for spin-polarized densities and fractional occupation of the KS orbitals. Although a spin-unrestricted TD-DFTB scheme has been already implemented [232], our method is fully consistent with the use of local XC functionals, in total contrast to the previous formulation. The present formalism was obtained *via* a linear response treatment of ground-state DFTB, which leads without ambiguities to the original formulation for closed-shell systems. The coupling matrix is thus extracted from a more general matrix $\bar{\mathbf{K}}$, which accounts for second-order corrections in DFTB. Any extension or further improvement of the DFTB second-order energy can be straightforwardly translated into the time depended scheme. An example of this practice is the onsite correction for the ground-state theory, from which it is possible to obtain a refined coupling matrix. This leads to improved excitation energies and vectors. Following a similar idea, the transition dipole matrix can be enhanced by taking the AO product expansion beyond a Mulliken approximation. Thus, oscillator strengths are improved *via* a refinement of both the excitation vectors and the transition dipole matrix.

The onsite corrections to the coupling and dipole matrices improve especially upon the description of $n \rightarrow \pi^*$ and $\sigma \rightarrow \pi^*$ transitions. The inaccurate characterization of these excitations has been one of the acknowledged limitations of traditional TD-DFTB. They often appear as electric-dipole forbidden even though more sophisticated methods predict strong associated peaks in the absorption spectra of some systems. With our formalism, we have been able to surpass this failure, returning oscillator strengths in agreement with *ab initio* observations. In particular, for diatomic molecules the refined scheme is essential to obtain a qualitatively correct spectra. Moreover, for closed-shell systems the erroneous $\sigma \rightarrow \pi^*$ and $n \rightarrow \pi^*$ triplet-singlet degeneracy is overcome within the refined formalism.

Another shortcoming of non-corrected TD-DFTB for the description of diatomic systems was uncovered. $\pi \rightarrow \pi^*$ transitions with irreducible representations Σ^- and Δ appear as degenerate, which contradicts *ab initio* and experimental findings. The new formulation delivers the correct behavior compared to TD-DFT results. An overall numerical correspondence with TD-DFT results can also be recognized for the diatomic species N_2 , NO and O_2 .

We employed a set of 28 compounds (Thiel’s set) to benchmark the new formalism in terms of vertical excitation energies, oscillator strengths and computational time. With respect to TD-PBE, traditional TD-DFTB performs better for singlet-singlet (S-S) than for singlet-triplet (S-T) excitations. It should be pointed out, however, that S-T excitation energies are in better agreement with theoretical best estimates (TBE) than S-S energies. Nevertheless, compared to some collected experimental findings, S-S energies appear again to be more accurate than S-T energies, which are strongly overestimated. Our correction successfully heals this overestimation, returning singlet-triplet excitation energies in agreement with TBE and experiment. In this regard, the refined formalism also outperforms TD-DFT at the PBE, PBE0 and CAM-B3LYP level, which give underestimated S-T energies. On the other side, corrected S-S energies have the same overall quality as in the traditional scheme. In this case, both TD-DFTB formalisms slightly outperform TD-DFT at the PBE level. The quality of the refined TD-DFTB

approach is nonetheless accomplished at a considerably smaller computational effort. The total elapsed time required by our formalism for the computation of the low-lying transition energies of Thiel's compounds was roughly 60 times shorter than that needed using TD-PBE. For large systems this factor is increased to circa 250. We finally discussed the implementation of orbital constraints within TD-DFTB to further reduce the computational time. The calculation of low-lying excitation energies with marked collective character using orbital constraints was roughly three times faster than for the unrestricted scheme, at no additional loss of accuracy. For systems displaying single-particle excitations, restricted calculations can be further sped up by a factor of 7.

Chapter 5

PHOTOCATALYTIC ACTIVITY OF TITANIUM DIOXIDE

In this chapter we investigate the photocatalytic degradation of nitric oxide and acetaldehyde on TiO_2 under UV and visible illumination. We consider two titania surfaces, namely, rutile (110) and anatase (001). The rutile (110) surface consists of alternating rows of fivefold coordinated (5c) Ti and twofold coordinated (2c) O atoms (see Fig. 5.1). This surface is not only the most investigated single-crystal TiO_2 surface but has also become the prototypical metal oxide surface for fundamental studies [252]. However, for the purpose of photocatalysis the anatase phase of titania enjoys more relevance due to its generally higher photocatalytic activity [253–256]. The (001) facet of anatase is well known by its high reactivity [257,258]. This surface is structurally simpler than rutile (110), with every Ti atom on the surface being pentacoordinated (Fig. 5.1). Although (101) is the naturally dominant facet of anatase, different techniques have emerged for the synthesis of TiO_2 structures with exposed $\{001\}$ crystal facets in order to enhance their photocatalytic properties [256,259–261].

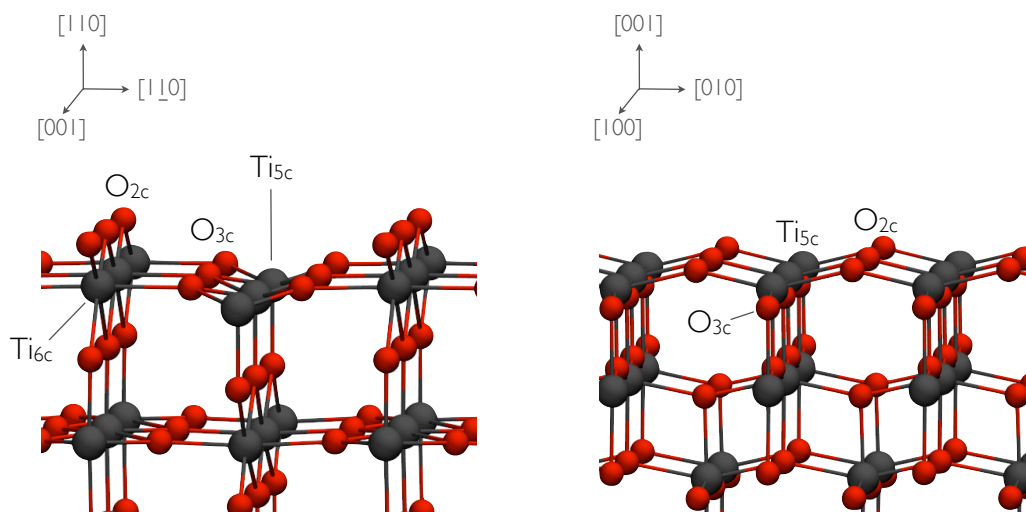


Figure 5.1: DFTB optimized structures of rutile (110) (left) and anatase (001) (right) surfaces of titania.

The TD-DFTB approach is employed for the computation of the excitation energies and oscillator strengths of the pollutant-TiO₂ complexes. PBE and HSE calculations are performed for the validation of DFTB for the description of the ground-state properties of the systems under investigation. We finally compare our predictions to experimental results.

5.1 Ground State Properties of the Pollutant-TiO₂ Complexes

The study of the excited-state properties of ligand adsorption on TiO₂ surfaces is currently not feasible within a first-principle methodology without compromising the accuracy of the results with the use of oversimplified models. The utilization of small clusters to describe a periodic material introduces a significant error amounting to sampling the Brillouin zone with a single k -point. This error is alleviated by increasing the model size, thus decreasing the dimensions in the reciprocal space. To afford the use of reliable models for the ambitious computational assignment we employ TD-DFTB. For the accurate description of the systems under investigation, a proper parametrization set has to be defined. In this section we test the suitability of DFTB parameters for the description of the ground-state properties of TiO₂ and its interaction with NO. This represents an important step towards the appropriate characterization of the photocatalytic properties of titania.

5.1.1 Validation of DFTB parameters

For the study of TiO₂ surfaces and its interaction with NO and acetaldehyde, we have modified the set of DFTB parameters *tiorg* [262]. Pure TiO₂ surfaces interact weakly with the investigated ligands, which physisorb at rather large distances (over 2 Å) from the surface. We have improved the Ti-O and Ti-N repulsive potentials, laying special emphasis on the function tail in order to reproduce interatomic distances and adsorption energies of the adsorbates.

As reference systems we employed NO attached to the Ti_{5c} atom of rutile (110) and anatase (001) surfaces. We considered both orientation of the molecule, that is, either O or N pointing towards the metal site. Additionally, the oxygen-reduced rutile (110) surface was employed to explore a different interatomic distance regime. The defective surfaces were modeled by removing a bridging O_{2c} atom per each (2×1) surface unit cell. Furthermore, we compare bulk properties of both considered morphologies of titania with DFT and experimental findings.

Reference calculations were performed at the PBE level of theory as implemented in the Vienna *ab initio* Simulation Package (VASP) [263–266]. Plane wave basis set with an energy cutoff of 420 eV as well as the projector augmented-wave (PAW) method [267, 268] have been used. For the surface systems periodic calculations were performed according to the slab approach, where a fairly large vacuum region is created along the normal to the surface in the supercell, thus avoiding spurious interaction between the periodically repeated slabs. For Brillouin zone integrations, k -point meshes were sampled using a (8×8×4) and (8×8×8) Monkhorst-Pack (MP) [269, 270] grids for bulk anatase and rutile, respectively. For rutile (110) and anatase (001) surfaces, (8×8×1) MP grids were employed. During the geometry optimization, all atoms were allowed to move till the interatomic forces were smaller than 10⁻³ eV/Å for bulk

calculations and 10^{-2} eV/Å for surface calculations. Spin polarized calculations were performed for those systems involving NO.

Similar supercells were employed for the DFTB calculations where the supercell dimensions were re-optimized. The Brillouin zone was sampled with a $(4 \times 4 \times 8)$ and $(4 \times 4 \times 2)$ MP grids for bulk rutile and anatase, respectively, whereas for surface calculations, $(3 \times 1 \times 3)$ and $(4 \times 4 \times 1)$ MP grids were respectively used for rutile (110) and anatase (001). For the optimization of the geometries, every atomic position was relaxed till the interatomic forces were smaller than 5×10^{-4} eV/Å for bulk and 5×10^{-3} eV/Å for the pristine and modified TiO₂ surfaces. Single-point calculations were conducted using VASP optimized geometries and then varying the Ti_{5c}-molecule distance in a vertical configuration (that is, N-O bond oriented along the surface normal) with a step of 0.1 Å. Analogue VASP single-point calculations were also performed with the aim of construction of the repulsive potentials.

The cohesive energies and lattice constants of anatase and rutile as calculated with the modified tiorg set are given in Table 5.1. We further provide PBE and experimental values for comparison. DFTB results are overall in line with the *ab initio* and experimental findings with some tendency of underestimation of the cohesive energies and overestimation of the lattice constants. The calculated band gaps are 3.1 eV and 3.2 eV for bulk rutile and anatase, respectively, which agree well with the experimental values of 3.0 eV for rutile [271] and 3.2 eV for anatase [272]. More remarkably, they are in better agreement with experiment than the typically underestimated values obtained within DFT using local or semi-local XC functionals [273–275] or the overestimated values obtained with hybrid functionals [262, 273]. This originates from a fortunate error compensation within the method.

| Property | DFTB | PBE | Exp. |
|-----------------------|-------|-------|-------|
| <i>anatase</i> | | | |
| a (Å) | 3.90 | 3.79 | 3.78 |
| c (Å) | 9.49 | 9.74 | 9.52 |
| c/a | 2.43 | 2.57 | 2.51 |
| E _{coh} (eV) | 18.88 | 21.54 | 19.73 |
| <i>rutile</i> | | | |
| a (Å) | 4.72 | 4.63 | 4.59 |
| c (Å) | 3.00 | 2.96 | 2.96 |
| c/a | 0.64 | 0.64 | 0.64 |
| E _{coh} (eV) | 19.16 | 21.44 | 19.79 |

Table 5.1: Comparison between DFTB, PBE and experimental results concerning the properties of bulk rutile and anatase.

The adsorption properties of NO on rutile and anatase surfaces are summarized in Table 5.2. The adsorption energies were calculated as

$$E_{\text{ads}} = \frac{1}{n}(E_{\text{T}} - E_{\text{bare}} - n E_{\text{NO}}), \quad (5.1)$$

where E_T is the total energy of the complex, E_{bare} is the total energy of the bare TiO₂ surface, E_{NO} is the energy of an isolated NO molecule in the gas phase and n is the number of NO molecules adsorbed on the surface. To determine the most stable ground-state structure of the ligand-TiO₂ complexes several molecular orientations and binding sites were considered. According to our findings, NO adsorbs favorably on the perfect (110) surface in a tilted configuration with the N atom oriented towards the surface and bonded to the Ti_{5c} atom. The distance from the N atom to the metal site is 2.56 Å. These results are in line with previous theoretical predictions [18, 21, 22] and our PBE results. For the adsorption through the oxygen atom the O-Ti_{5c} distance (2.80 Å) also compares well to our PBE findings, which returned an optimized distance of 2.75 Å. For the oxygen-reduced surface the N-Ti_{5c} and O-Ti_{5c} distances are shortened to 1.95 and 1.83 Å, respectively. In the case of adsorption on the anatase (001) surface, ligand-substrate distances are also in agreement with PBE. In terms of adsorption energies, the correspondence of DFTB with higher-level theory is also remarkable with absolute errors equal or smaller than 0.08 eV.

| Configuration | Property | DFTB | PBE |
|---|------------------|-------|-------|
| <i>rutile (110)</i> | | | |
| on perfect surface <i>via</i> N-Ti _{5c} | N-Ti distance | 2.56 | 2.55 |
| | E _{ads} | -0.25 | -0.27 |
| on perfect surface <i>via</i> O-Ti _{5c} | O-Ti distance | 2.80 | 2.75 |
| | E _{ads} | -0.15 | -0.14 |
| on O _{2c} -reduced surface <i>via</i> N-Ti _{5c} | N-Ti distance | 1.95 | 1.87 |
| | E _{ads} | -0.89 | -0.86 |
| on O _{2c} -reduced surface <i>via</i> O-Ti _{5c} | O-Ti distance | 1.83 | 1.99 |
| | E _{ads} | -0.29 | -0.34 |
| <i>anatase (001)</i> | | | |
| on perfect surface <i>via</i> N-Ti _{5c} | N-Ti distance | 2.25 | 2.26 |
| | E _{ads} | -0.47 | -0.35 |
| on perfect surface <i>via</i> O-Ti _{5c} | E _{ads} | -0.11 | -0.16 |

Table 5.2: Comparison between DFTB and PBE in terms of optimized structures and energetics of the NO adsorption on TiO₂. Distances are given in Å and energies in eV.

5.2 Cluster Models and Absorption Spectra

We have built reasonably large TiO₂ clusters to model the anatase and rutile surfaces (Fig. 5.2), which still make possible the computation of the absorption spectra at the TD-DFTB level. The peripheral oxygen atoms not belonging to the surface were saturated with hydrogen atoms in such way that the clusters are neutral. Rutile (110) and anatase (001) surfaces are represented by a Ti₂₁O₆₈H₅₂ and Ti₁₉O₅₇H₃₈ clusters, respectively. To determine the optimized ground-state structure of the rutile cluster, all atomic positions were allowed to relax within DFTB

until the interatomic forces were smaller than 2.5×10^{-2} eV/Å. For the anatase cluster the peripheral oxygens were kept fixed during the geometry optimizations as the structure otherwise undergoes large deformations. For those systems involving NO, spin-unrestricted calculations were performed.

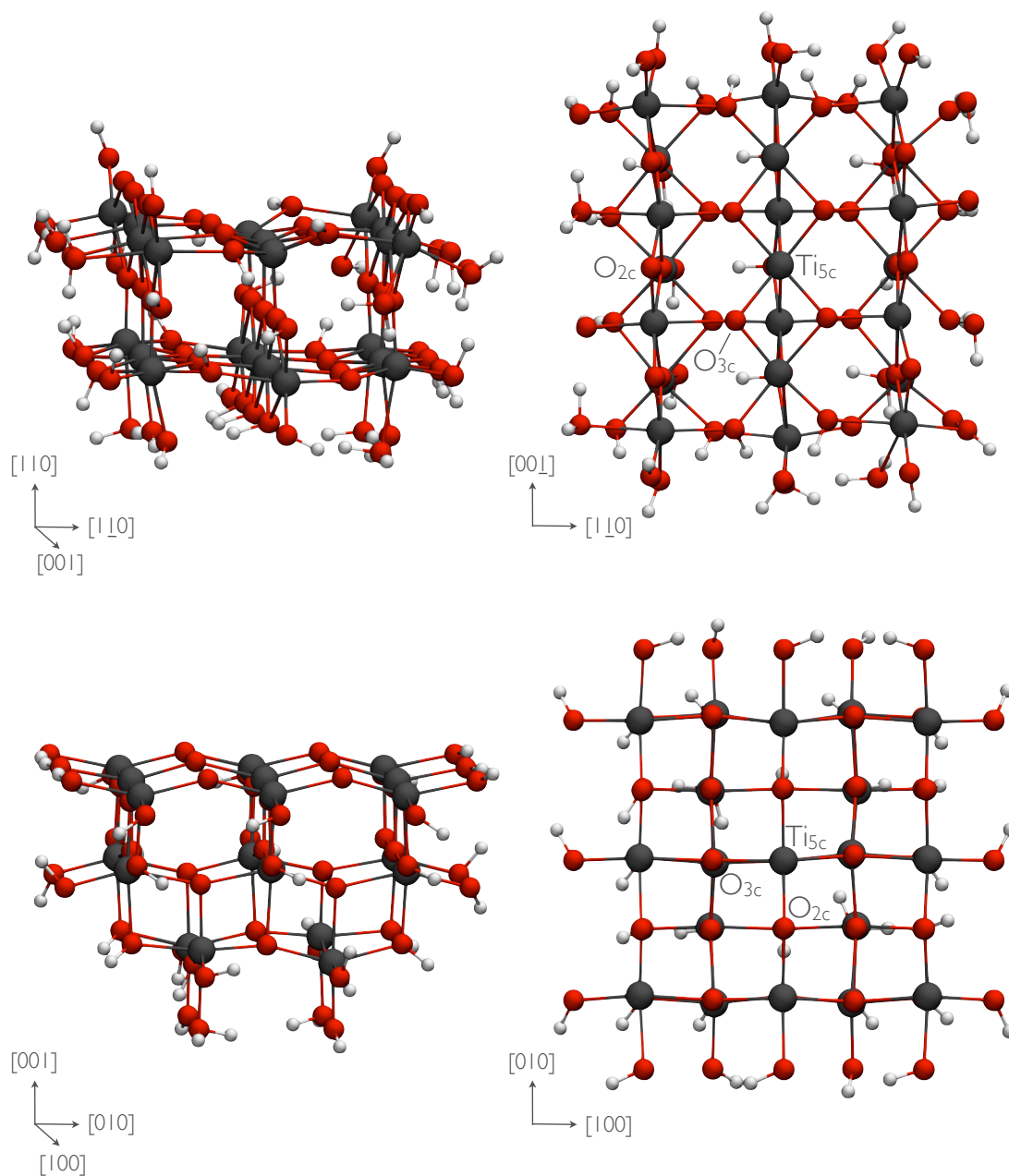


Figure 5.2: Side (left) and top (right) views of the optimized geometries of the rutile $\text{Ti}_{21}\text{O}_{68}\text{H}_{52}$ (top) and anatase $\text{Ti}_{19}\text{O}_{57}\text{H}_{38}$ (bottom) clusters.

To test the validity of the employed models, we first compare the DFTB structural and electronic properties of the clusters with first-principle results. Surface $\text{Ti}_{5c}\text{-O}_{2c}$ and $\text{Ti}_{5c}\text{-O}_{3c}$ bond lengths are in correspondence with those found at the PBE level. The interatomic distance

between the central pentacoordinated Ti and the adjacent O_{3c} atoms on the rutile cluster is 2.00 Å which agrees with the PBE value of 1.95 Å for the periodic system. In the anatase case, Ti_{5c}-O_{2c} and Ti_{5c}-O_{3c} interatomic distances are 1.89 and 1.96 Å, respectively, compared to the PBE values of 1.75 and 1.95 Å. Band gaps are also accurately described. DFTB yields a HOMO-LUMO gap of 2.98 eV for the rutile cluster and 3.05 eV for the anatase cluster. The UV-vis absorption spectra for both TiO₂ clusters are shown in Fig. 5.3. These findings are in agreement with very recent room-temperature optical absorption measurements, reproducing the relative steepness degree of the absorbance curves for rutile and anatase at the vis-UV frontier [276].

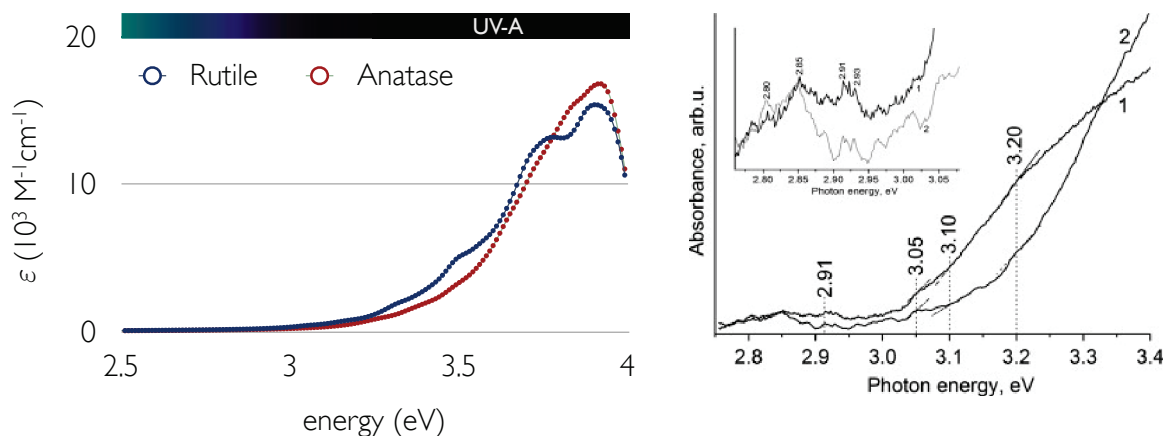


Figure 5.3: Left panel: UV-vis absorption spectrum for rutile and anatase TiO₂ clusters as obtained with TD-DFTB. See Fig. 4.2 for details on the calculation of ϵ . The Lorentzian FWHM was set to 0.1 eV. Right panel: experimental UV-vis absorption spectrum for rutile (1) and anatase (2) TiO₂ nanocrystalline powders. Reprinted from [276]. Copyright 2014, with permission from Elsevier.

The most stable configuration of the NO adsorption on the rutile cluster is depicted in Fig. 5.4. The pollutant binds to the Ti_{5c} site in a tilted configuration *via* N with a N-Ti_{5c} interatomic distance of 2.55 Å, in total agreement with the PBE findings reported above (see Table 5.2). The adsorption configuration through the O atom also resembles that found at a higher level of theory with a O-Ti_{5c} distance of 2.75 Å.

In order to assess the suitability of our cluster models in terms of electronic structure of the TiO₂-NO compound system, we employed the range-separated hybrid scheme HSE as the reference method. Periodic single-point calculations were performed using the PBE optimized geometry. The Brillouin zone was sampled with a (3×1×3) MP grid. The highest occupied molecular orbital (HOMO) of an isolated NO molecule is a degenerate antibonding π^* orbital (π^*) which is singly occupied in one spin component (say spin-up). The two degenerate π^* states with spin down are the lowest unoccupied molecular orbitals (LUMO). When the molecule adsorbs on the TiO₂ surface, the system loses its symmetry and the orbital degeneracy is broken. Thereby one of the former spin-up degenerate states turns into the LUMO. Our HSE results indicate that the HOMO lies in the band gap of rutile TiO₂ at 0.8 eV above the valence band maximum (VBM) with marked localization on the molecule. The LUMO lies in the conduction band edge and is more delocalized. Besides, the two unoccupied π^* orbitals of the spin-down

channel are also inserted close to the conduction band minimum (CBM) of the semiconductor (see Fig. 5.4 right). DFTB results agree about the insertion of the NO levels in the energy gap region, although their positions differ from the HSE findings. Within HSE the HOMO lies deeper in the band gap compared to DFTB results. Moreover, the HOMO-LUMO energy difference amounts to only 0.3 eV according to DFTB whereas HSE yields a value of approximately 2.6 eV. More importantly for the study of CT excitations is however the position of the HOMO with respect to the CBM. DFTB underestimate the HOMO-CBM energy difference by about 0.8 eV taking HSE results as reference. However, as mentioned above, hybrid DFT approaches generally overestimate the band gap of TiO_2 . In the present case HSE yields a, too large, value of approximately 3.4 eV. All this should be borne in mind for the subsequent analysis of the absorption spectra. The fact that NO also introduces unoccupied KS states in the band gap is indeed remarkable as this might enable a CT mechanism which is generally not regarded, that is, a metal-to-ligand charge transfer (MLCT) process.

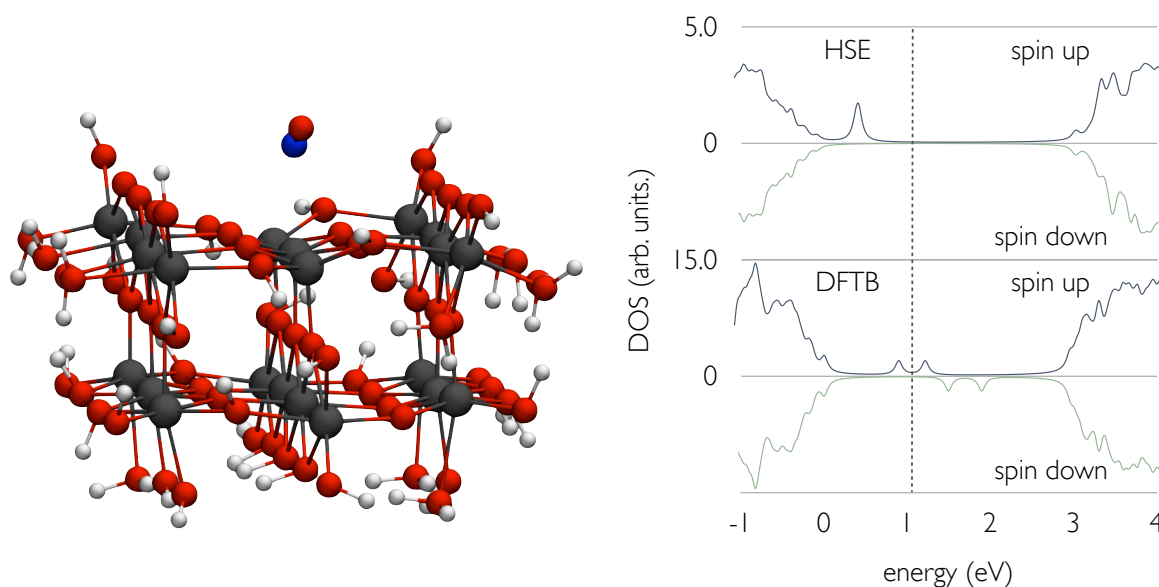


Figure 5.4: Optimized structure (left) and density of electron states (DOS) (right) of the NO adsorption on the neutral rutile cluster. Oxygen, titanium, nitrogen and hydrogen atoms are represented by red, dark gray, blue and white spheres, respectively. In the DOS plot the zero of energy is set to the valence band maximum and the dashed line indicates the Fermi level position.

To compute the absorption spectra in the region of interest (up to about 4 eV), the first 1200 excitation energies and oscillator strengths for the TiO_2 -NO complexes were obtained. We used expression II.83 in Ref. [216] to evaluate the expectation value of the square of the total spin operator, $\langle S^2 \rangle$, of the excited states for the open-shell systems (those involving NO) (see section 4.3). For computing the absorption spectra we considered only those states with a $\langle S^2 \rangle$ contamination of less than 0.5. The set of KS transitions entering the calculations were truncated by a cutoff KS energy difference of roughly 30 eV. This constraint leads to similar results as for the TD-DFTB calculation without any restriction for the investigated systems whereas the computational time is reduced by a factor of up to 7.

The UV-vis absorption spectrum corresponding to the NO adsorption on rutile is shown in Fig. 5.5. We observe weak absorption bands in the visible region of the spectrum corresponding to CT from both the molecule to the surface and the surface to the molecule. Specifically, the electron is transferred from the singly occupied π^* orbital of NO to $3d$ orbitals of the Ti atoms of the substrate for the LMCT mechanism. In the case of a MLCT process the electron is promoted from the O- $2p$ states of TiO₂ to a virtual π^* molecular orbital. The most intense LMCT peak is assigned to a transition to d states of surface Ti_{5c} and subsurface Ti_{6c} atoms. It is important to stress that the CT peaks may be red-shifted with respect to the actual behavior as suggested by the HSE results. Additionally, CT excitation energies are commonly underestimated by TD-DFT calculations using conventional XC functionals [277, 278]. In particular, the MLCT component may be completely displaced to the UV-A region of the spectrum. In this region, a band-to-band excitation leading to the generation of an electron-hole pair is much more likely to occur as indicated in Fig. 5.5.

Absorption of visible radiation by the TiO₂-NO complex may lead to formation of nitrosonium ions (NO⁺), which may in turn react with water to form nitrous acid,



thus fulfilling the first step in the oxidation reaction of NO. As pointed out above, our results suggest that under illumination with UV light, NO is likely to oxidize *via* reaction with oxidizing species formed from the interaction with the photoinduced electron or hole.

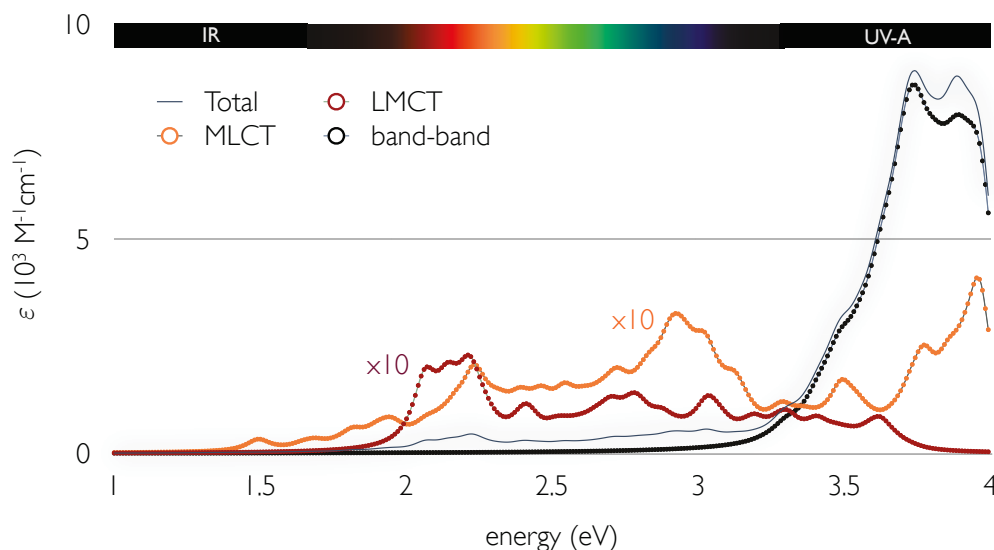


Figure 5.5: Absorption spectrum for the TiO₂(rutile)-NO complex depicted in Fig. 5.4. The spectrum has been projected onto three different components: the red dotted line denotes ligand-to-metal charge transfer excitations, the orange dotted line metal-to-ligand charge transfer excitations and the black dotted line band-to-band excitations.

Let us now investigate the photodegradation of NO on anatase TiO₂. The most stable configuration for the NO adsorption on the anatase cluster is shown in Fig. 5.6 (right). The binding on the Ti_{5c} site weakens one of the adjacent O_{2c}-Ti_{5c} bonds, eventually leading to its division.

This results in the formation of reactive Ti_{4c} and O_{1c} surface sites. Within DFTB, this configuration is circa 1 eV more stable than that depicted in Fig. 5.6 (left) where no bond breaking is observed. Let us denote the most stable adsorption mode configuration B and that featuring no bond breaking configuration A. For a 1 ML coverage of NO the surface Ti-O bond is not disturbed and NO attaches to the surface as in Fig. 5.6 (left). In both cases the distance from the molecular N atom to the metal site is 2.25 Å. The bond breaking at a low-coverage regime was confirmed by periodic PBE calculations where a tetragonal supercell with a (2×3) surface unit cell and a single NO molecule were considered. PBE yields a N- Ti_{4c} distance of 2.24 Å and a N- O_{1c} distance of 1.94 Å. The latter compares well to the value of 2.01 Å obtained with DFTB. The adsorption energy is -0.65 eV at the PBE level, whereas DFTB yields a value of -1.47 eV. The transition from configuration A to B occurs barrierless at low NO concentrations within both DFTB and PBE approaches.

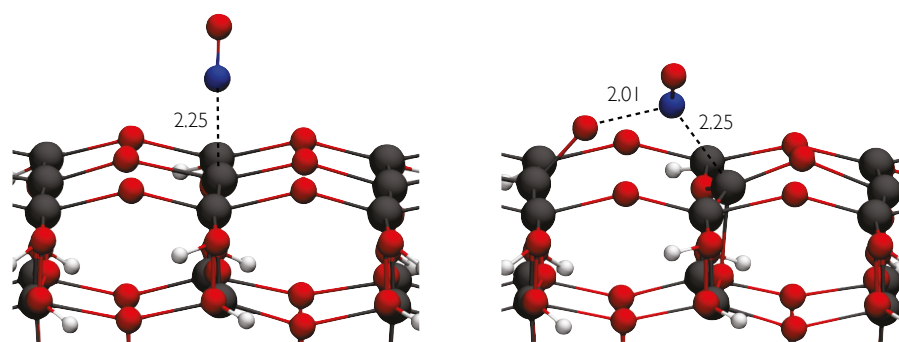


Figure 5.6: Optimized geometries of the NO adsorption on the neutral anatase cluster. The color code is that employed in Fig. 5.4.

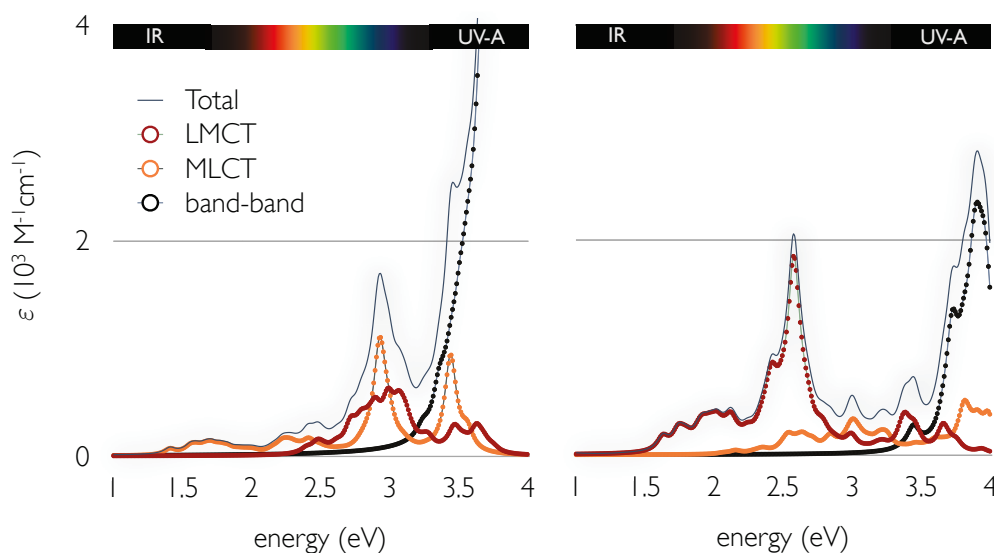


Figure 5.7: Absorption spectra for the $\text{TiO}_2(\text{anatase})\text{-NO}$ complexes depicted in Fig. 5.6. See Fig. 5.5 for information.

Fig. 5.7 shows the absorption spectra corresponding to both configurations. Both spectra indicate vis-light activation of the CT complexes. The CT excitation energies for the 1 ML-like configuration are in general blue-shifted with respect to those for the low-coverage adsorption. The main distinctive feature among both spectra is however the enhanced LMCT absorbance for the low-coverage case. Also, the probability of occurrence of a MLCT process is diminished for configuration B whereas this type of transition has a higher relevance for configuration A. The most dominant sp transitions of the CT excitations corresponding to the highest peaks of Fig. 5.7 are depicted in Fig. 5.8. The occupied and virtual KS orbitals are represented with blue and orange wireframes, respectively. For the structure A, the transition takes place mainly from threefold coordinated O-2p orbitals to the unoccupied π^* state of NO. On the other hand, configuration B is the only adsorption mode with clear indication of a covalent bond between NO and the TiO_2 surface with the HOMO having a strong component onto the N-Ti_{4c} bonding orbital.

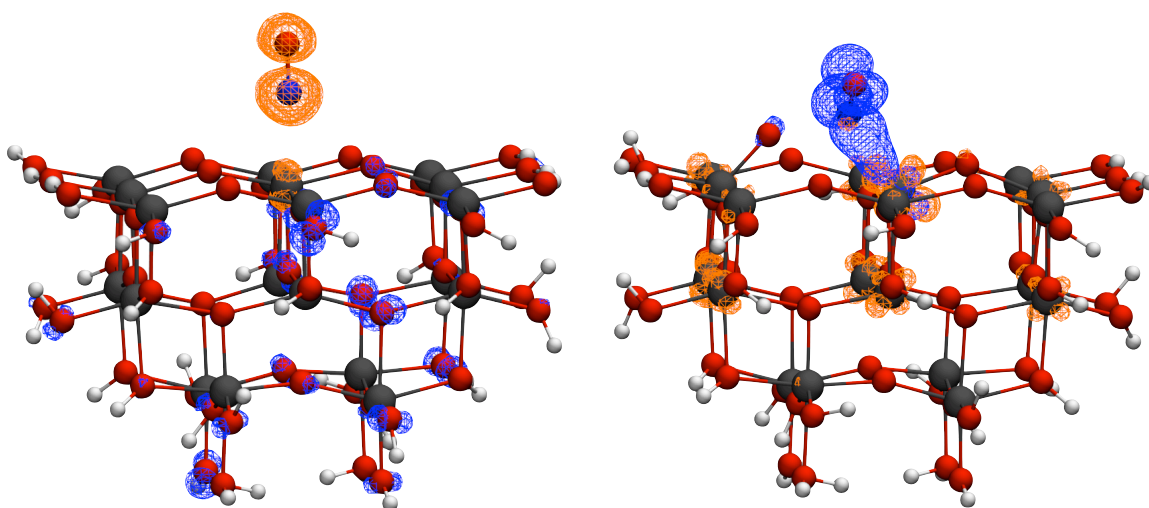


Figure 5.8: Charge density corresponding to the occupied (blue) and virtual (orange) Kohn-Sham states for the most dominant single-particle transition in the many-body wavefunction for the main CT peaks in the visible spectra of Fig. 5.7.

The adsorption mode for low NO concentrations suggests that the direct interaction of the pollutant with the surface could lead to formation of nitrite or nitrate species. The photoinduced transfer of the unpaired electron from NO to the substrate may provoke the weakening of the N-Ti_{5c} bond as the corresponding molecular orbital shows a Ti-O bonding character. In addition, this orbital has a small component on the O_{1c}-Ti_{5c} bond and so a promotion of this state to the conduction band of the semiconductor may also weaken this bond, thus leading to the oxidation of the pollutant. In a DFT study, Minot *et al.* suggested that the formation of nitrite or nitrate would be possible if monocoordinated surface O atoms react with NO [279]. They proposed a model of the (001) facet with the presence of terminal O_{1c} atoms. They observed an improved reactivity of the surface (the NO adsorption energy went from 0.4 eV for the regular (001) surface to 2.96 eV for the O-terminated one). According to our findings, the existence of this less stable surface termination would not be required as NO can itself evoke the formation of such reactive O_{1c} atoms at the conventional surface.

We now turn to the adsorption of acetaldehyde on the surfaces of TiO₂. The most stable binding configuration on the rutile and anatase clusters are depicted in Fig. 5.9. Acetaldehyde favorably attaches to the rutile surface through the carbonyl O atom at the Ti_{5c} site with the H atom of the -CHO group oriented towards and adjacent bridging O_{2c} atom. A dissociative adsorption where a proton is transferred from the ligand to the substrate was found to be unstable. The O-Ti_{5c} interatomic distance obtained within DFTB is 2.73, which is larger than the value (2.16 Å) reported in a recent GGA investigation [29]. In the anatase case, acetaldehyde binds through the carbonyl group onto the undercoordinated metal site whereas the H atom relaxes to a position between two neighboring O_{2c} atoms. The O-Ti_{5c} interatomic distance is identical as for the rutile case. Unlike NO, the adsorption of the volatile compound was not found to cause Ti-O bond breaking at the surface.

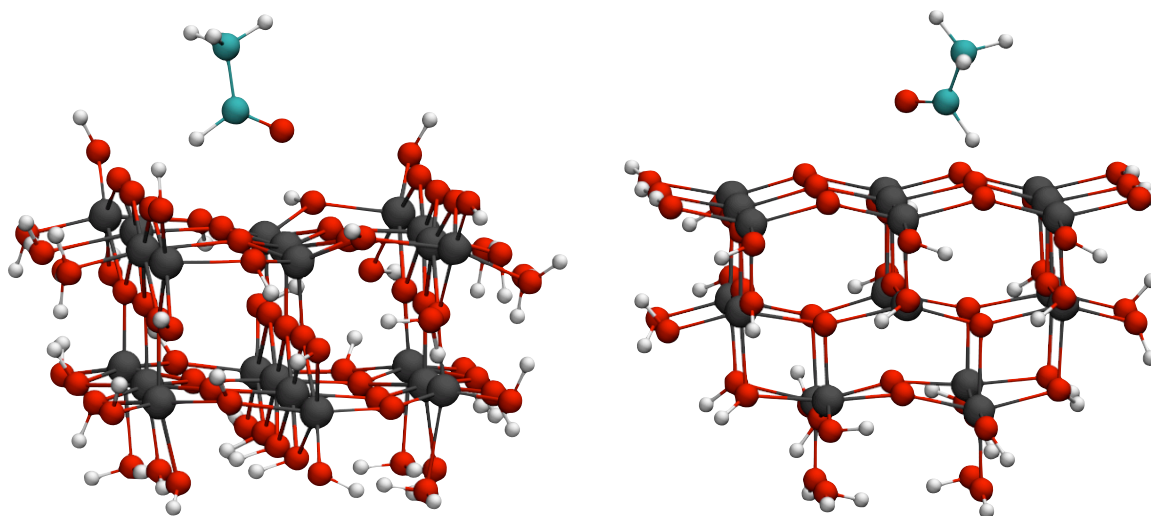


Figure 5.9: Optimized geometries of the adsorption of acetaldehyde on the rutile (left) and anatase (right) clusters. The color code is that employed in Fig. 5.4. Additionally, cyan spheres represent carbon atoms.

Unlike NO, the HOMO of acetaldehyde lies in the valence band of TiO₂ and the LUMO is located in the conduction band. The electronic structure of TiO₂ is hence not substantially modified upon adsorption of the pollutant organic compound. The absorption spectra of the complex is neither expected to change considerably from that of the bare surfaces of titania. To plot the absorption spectra in the UV(A)-vis region, the computation of the first 415 S-S excitation energies and oscillator strengths of the modified TiO₂ clusters was required. The same KS orbital constraint as for the NO based complexes was employed. The resulting spectra are given in Fig. 5.10. As expected from the electronic structure analysis, no vis-light activation is observed for the acetaldehyde case. Furthermore, the absorption profiles for rutile and anatase systems resemble those of the clean TiO₂ surfaces (Fig. 5.3).

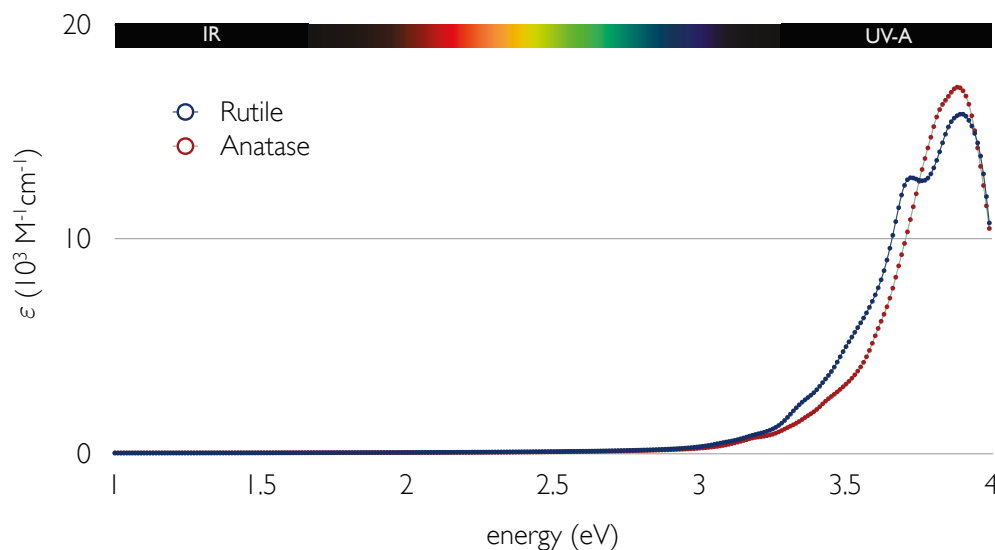


Figure 5.10: Absorption spectrum for the TiO_2 -acetaldehyde complexes depicted in Fig. 5.9.

5.3 CT Complexes based on Alumina

In a similar manner as the solar activation of a wide-gap semiconductor can be achieved by CT complexation with a suitable ligand, the absorption of UV-A light by an insulator material may be enabled by photoinduced electron transfer from the adsorbate to the insulator surface. This might explain the unexpected photocatalytic activity of alumina for the decomposition of NO. To confirm this, we investigate the electronic properties of NO adsorption on the (0001) surface of $\alpha\text{-Al}_2\text{O}_3$. The Al-terminated (0001) surface has been shown to be the most stable bulk termination experimentally [280–282] and theoretically [283–286]. Furthermore, it is known that this surface easily undergoes hydroxylation [280, 284, 286–291] even in the presence of water vapor at low pressure [292]. To model this surface we replaced each surface Al atom by three H atoms as proposed in Refs. [287, 288]. Periodic spin-polarized DFT calculations were conducted at the PBE level of theory for the geometry optimization of the system using the PAW method as implemented in VASP. The wavefunctions were expanded into a plane-wave basis set with an energy cutoff of 420 eV. The supercell consists of a Al_2O_3 slab containing 6 alumina layers and one NO molecule initially placed vertically with the N atom oriented to the surface. This configuration has been found to be favorable in a recent theoretical study [293]. The position of all atoms were allowed to relax till the change in the total energy was smaller than 10^{-3} eV.

After relaxation, one of the onsite -OH groups is oriented parallel to the surface plane whereas the other two point almost vertically along the normal to the surface. This is in agreement with previous theoretical observations [286, 290, 293]. The system exhibited large surface relaxations similarly as observed previously in other investigations [280, 288, 293–295]. The NO molecule adsorbs in a tilted mode as shown in Fig. 5.11.

For the computation of the electronic structure, single-point HSE calculations were performed at the optimized geometry. The Brillouin zone was sampled with a $(3 \times 3 \times 1)$ MP grid. The

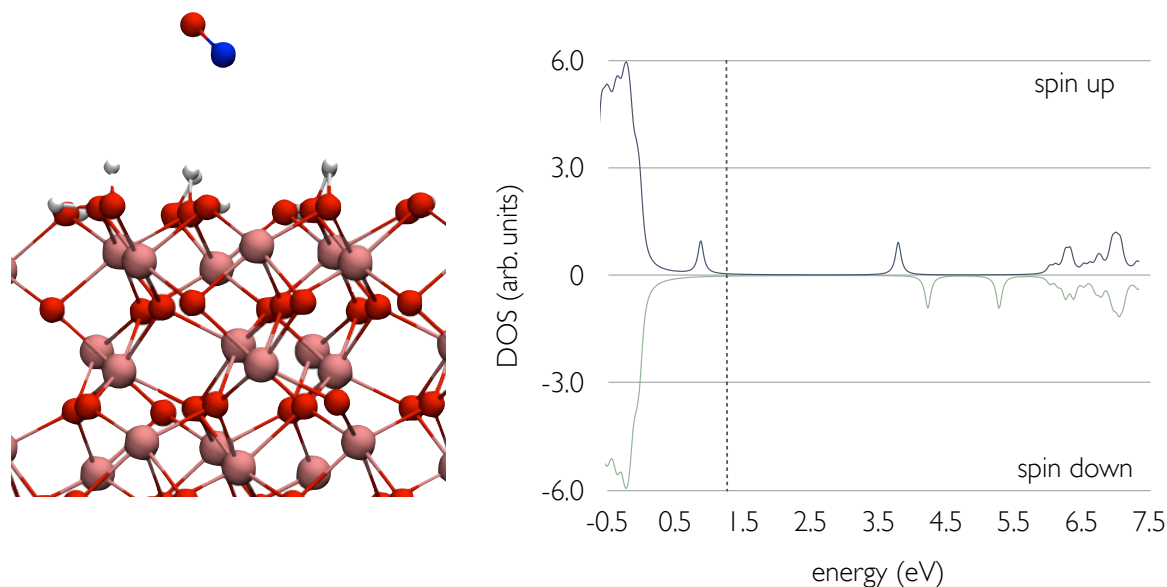


Figure 5.11: Optimized structure (left) and the density of electron states (DOS) (right) of the NO adsorption on the fully hydroxylated metal-terminated (0001) surface of α -Al₂O₃. Blue, red, pink and white spheres denote nitrogen, oxygen, aluminum and hydrogen atoms, respectively. In the DOS plot the zero of energy is set to the valence band maximum and the dashed line indicates the Fermi level position.

corresponding DOS is shown in Fig. 5.11. HSE calculations yield a Al₂O₃ band gap of 6.02 eV, which is notably greater than that obtained at the PBE level (4.7 eV) and in better agreement with experiment. The insertion of NO levels in the gap region is also observed for the insulator material as can be seen from the figure. The HOMO lies at 0.87 eV above the VBM and the LUMO at 3.78 eV. This suggests the possibility of a CT process under UV illumination. However, the large HOMO-CBM energy difference (5.15 eV) indicate that a LMCT excitation might not be possible under UV-A radiation. In contrast, a MLCT process appears to be more plausible.

5.4 Comparison with Experimental Results

In close collaboration within this research, the aforementioned group of Prof. Bahnemann has conducted experimental studies to support our findings. In this section we would like to summarize their main observations. The photodegradation of NO and acetaldehyde on powders of TiO₂ were investigated under UV and visible illumination. To remove residual organic compounds at the surface, the samples were pretreated under UV radiation. As light source they employed a UV-A lamp with a maximum wavelength $\lambda_{max} = 365$ nm. This corresponds roughly to the region from 3.4 to 3.9 eV in the computed absorption spectra shown in section 5.2. Additionally, they employed a light-emitting diode (LED) lamp with $\lambda = 455$ nm (~ 2.7 eV) for the analysis of the vis-light activity of TiO₂. The pollutants were exposed to irradiation for two hours after the concentration of NO (acetaldehyde) were equilibrated to 1 (5) ppm. A relative

humidity of 50 % was employed. After the lamps were deactivated, the concentration of the pollutants were followed under dark conditions till it reached its initial value. To evaluate the activity of titania, the photonic efficiency, ξ , was calculated. This quantity is defined as

$$\xi = \frac{\dot{V} \cdot p \cdot (c_d - c_i)}{J \cdot A \cdot R \cdot T}, \quad (5.3)$$

where \dot{V} stands for the volume flux, p is the pressure, c_i and c_d are the pollutant concentrations under illumination and dark conditions, respectively, J denote the photon flux, A the irradiation area, R the gas constant and T the absolute temperature. The obtained photonic efficiencies for different TiO₂ samples under vis and UV irradiation are given in Fig. 5.12 for NO and acetaldehyde degradation. The employed TiO₂ photocatalysts are Degussa P25, Kronoclean vlp 7000, Hombikat UV 100, PP10 and Rutile. UV 100 and Rutile are composed of 100% anatase and rutile TiO₂ respectively. Degussa P25 is a mixture of 80% anatase and 20% rutile whereas vlp 7000 and PP10 are anatase TiO₂ modified with impurities to enable absorption of visible light.

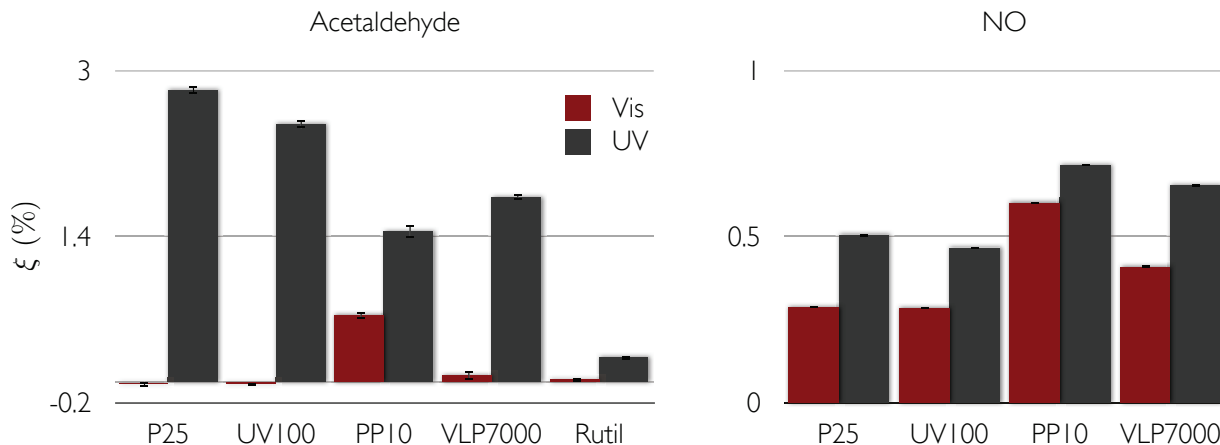


Figure 5.12: Photonic efficiencies (ξ) of different TiO₂ powders for the degradation of acetaldehyde (left) and NO (right) under visible-light (red bars) and UV (gray bars) illumination.

As seen from Fig. 5.12 the degradation of acetaldehyde occurs under UV irradiation for all investigated photocatalysts. The maximum photonic efficiency is achieved by the P25 sample, followed closely by the pure-anatase UV100 powders. The lowest efficiency is obtained for rutile, which exhibits a value of only 0.24 %. Under visible light, only the modified anatase powders show nonzero degradation activity within the experimental error. This is in line with our theoretical findings, which indicate no visible-light absorption of the acetaldehyde molecule complexed with either pure rutile or anatase (see Fig. 5.10). In contrast to these observations, all TiO₂-NO systems exhibit nonvanishing photonic efficiencies under illumination with both UV and visible light (Fig. 5.12 right). The absorption in the visible spectrum by the TiO₂-NO complexes were also predicted by our theoretical results (Fig. 5.5 and 5.7).

5.5 Summary

In this chapter we studied the optical properties of TiO₂ complexed with acetaldehyde and nitric oxide (NO) by means of the DFTB/TD-DFTB approach. Both defect-free rutile (110) and anatase (001) surfaces were investigated. The complexes were modeled by finite rutile and anatase clusters and a single pollutant molecule. The structural, electronic and optical properties of the TiO₂ models were validated by periodic calculations using a higher level of theory and experiment. The adsorption properties of the pollutants on the TiO₂ clusters were also found to be in agreement with more sophisticated theoretical methods.

NO favorably adsorbs on either surfaces with the N atom oriented towards the Ti_{5c} surface site. We found that adsorption on the anatase surface leads to surface Ti_{5c}-O_{2c} bond destabilization and eventually to the presence of highly undercoordinated Ti_{4c} and O_{1c} atoms on the oxide surface. Analysis of the charge density of the highest occupied molecular orbital indicates the presence of a covalent bond between NO and the Ti_{4c} surface site. This effect is however not observed for a full surface coverage of NO molecules, in which case the TiO₂ surface does not undergo any reconstruction. The availability of singly coordinated surface oxygens might facilitate the photo-oxidation of NO *via* a direct reaction of the pollutant with the substrate. In the case of acetaldehyde, the molecule binds to the pentacoordinated metal site *via* its carbonyl group and through hydrogen bonds with neighboring O_{2c} atoms. No surface bond destabilization was seen in this case.

The calculated UV-vis absorption spectra for the TiO₂-NO systems reveal the creation of visible absorption bands by formation of CT complexes. In contrast, no vis-light activation occurs by complexation between acetaldehyde and TiO₂. This is in agreement with experimental measurements of the photonic efficiency of various TiO₂ samples for the degradation of the investigated pollutants. Under vis-light illumination, pure TiO₂ powders show vanishing photonic efficiency for the acetaldehyde degradation whereas for the photocatalytic oxidation of NO the photonic efficiencies are nonzero. Apart from a ligand-to-metal CT (LMCT) mechanism our results suggest the possibility of electron transfer from the substrate valence band to the molecule unoccupied orbitals, although, for moderately low concentrations of NO on anatase (001), a LMCT process is expected to predominate. According to our findings, the photocatalytic degradation of the pollutants under UV irradiation is governed by band-to-band excitations leading to photogenerated electron-hole pairs.

UV activation of alumina is also expected by CT complexation with NO as indicated by the insertion of NO electron levels in the band gap of the insulator material. However, in this case the charge transfer mechanism may only occur from the metal oxide to the molecule under illumination with UV-A light. The formation of Al₂O₃-NO CT complexes explains the experimentally observed photocatalytic activity of the wide-band gap insulator for the NO degradation.

Chapter 6

ORGANIC/ZINC OXIDE HYBRID INTERFACES

In this chapter we employ DFT to investigate the structural properties and energetics of the modification of nonpolar ZnO surfaces and NWs using different functional groups. To this end, we employ prototype molecules of the form $\text{CH}_3\text{-X}$, where -X is the anchor group of interest. Namely, the investigated moieties are -COOH , -NH_2 , -OH , -SH , -CN and -PO(OH)_2 . Additionally, we study the structural and electronic properties of a bifunctional compound, namely, glycine ($\text{NH}_2\text{-CH}_2\text{-COOH}$), which is the simplest α aminoacid and serves as a prototypical biomolecule. Moreover, glycine contains two of the most investigated anchor groups on ZnO: the -NH_2 and -COOH groups. Due to the extra complexity associated to the investigation of a bifunctional ligand (increase of degrees of freedom in the adsorption mode) the, more efficient, DFTB method is employed in this case.

6.1 Modification of ($\underline{1}\underline{2}\underline{10}$) ZnO Surfaces

An important characteristic of wurtzite ZnO is the presence of polar low-index (0001) planes, which leads to positively charged Zn- and negatively charge O-terminated surfaces. Polar surfaces in ZnO are surprisingly stable and can be observed as atomically flat, unreconstructed facets of ZnO nanoparticles. The other two usually detected facets of ZnO are the nonpolar $\{10\underline{10}\}$ and $\{\underline{1}\underline{2}\underline{10}\}$. They have lower formation energies than their polar counterparts and, therefore, appear as the majority surfaces of synthesized ZnO nanoparticles. Nonpolar surfaces are mixed-terminated, that is, they consist of pairs of Zn and O atoms. Among the two nonpolar surfaces, $(10\underline{10})$ is the energetically most favorable. The unreconstructed surface consists of periodically repeated threefold coordinated Zn-O pairs as depicted in Fig. 6.1. These surface atoms exhibit dangling bonds, which are responsible for the attachment of the target adsorbate. The $(10\underline{10})$ ZnO surface has been widely studied, and its structure and properties are known with high detail. Wöll compares the knowledge about this surface with that gained on (110) TiO_2 , considered the best understood metal oxide surface [296]. In contrast, the number of studies on the $(\underline{1}\underline{2}\underline{10})$ surface is significantly smaller. In particular, few investigations have addressed the functionalization of this surface with organic molecules.

In this section we report on DFT calculations of the structural properties and energetics of

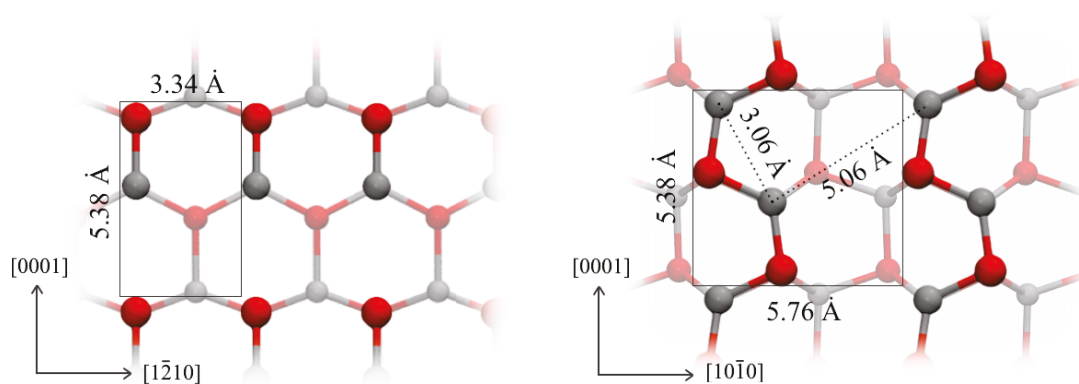


Figure 6.1: First and second atom layers of the $(10\bar{1}0)$ (left) and $(1\bar{2}10)$ (right) ZnO surfaces. The surface unit cell has been enclosed by a rectangle. To create depth perception and ease of identification, the first-layer atoms have been represented with more vivid colors. Oxygen and zinc atoms are represented by red and silver spheres, respectively.

the interaction between the $(1\bar{2}10)$ ZnO surface and amino ($-\text{NH}_2$), hydroxyl ($-\text{OH}$), thiol ($-\text{SH}$), carboxyl ($-\text{COOH}$) and nitrile ($-\text{CN}$) functional groups. The choice was based on the availability of electron lone pairs, which make possible the formation of covalent or ion-dipole bonds with the Zn binding sites. The ZnO surfaces were modeled using a tetragonal supercell consisting of a ZnO slab containing 16 atomic Zn-O layers and a vacuum region of 50 \AA along the $[1\bar{2}10]$ direction. This region is thus sufficiently large to avoid spurious interaction between periodically repeated slabs. Periodic DFT calculations were performed at the PBE level as implemented in the SIESTA package [297]. An optimized set of double-zeta plus polarization (DZP) functions as well as norm-conservative Troullier-Martins pseudopotentials [298] were employed. A $(4 \times 1 \times 4)$ MP grid was used for the k -point samplings. During the calculation, all atomic positions were allowed to change till every interatomic force was smaller than 10^{-2} eV/\AA .

The $(1\bar{2}10)$ surface also exhibits threefold coordinated Zn and O atoms arranged in pairs. However, in this case the number of Zn-O pairs per surface unit cell increases to two (see Fig. 6.1). At the same time, the area of the unit cell is almost twice greater than that of the $(10\bar{1}0)$ surface, which results in an averaged Zn-O dimer density of 0.065 Zn-O/\AA^2 , similar to that for the most favorable nonpolar surface (0.056 Zn-O/\AA^2) [299]. As surface Zn-O pairs can be translated into potentially available binding sites, it is therefore expected that similar adsorption properties be observed for both nonpolar surfaces.

Let us define the ligand coverage, θ , as the number of adsorbate molecules per surface Zn-O pairs. We investigate the cases $\theta = 1$ and $\theta = 0.5$ (by considering two and one ligand per surface unit cell, respectively) for each anchor group. To study the interaction between the ligands and the ZnO surfaces, several configurations of the adduct were considered. To have a quantitative measure of the strength of the ligand-substrate interaction, we calculated the adsorption energy per adsorbate, E_{ads} , for every tested configuration. This quantity is defined as

$$E_{\text{ads}} = \frac{1}{n}(E_{\text{T}} - E_{\text{bare}} - n E_{\text{lig}}), \quad (6.1)$$

where E_T is the total energy of the modified surface, E_{bare} is the total energy of the bare surface, E_{lig} is the energy of an isolated neutral ligand in the gas phase and n is the number of ligands absorbed on the surface. The obtained adsorption energies for the most stable configurations are summarized in Table 6.1. For comparison we also show the adsorption energies concerning the (1010) surface, taken from Ref. [299]. As expected, the same adsorption trend as for the (1010) surface is observed: -COOH is the most energetically favorable anchor group whereas the aprotic -CN group attaches weakly to the surface. Moreover, in all cases ligand-substrate interactions are stronger for $\theta = 0.5$. This can be partly explained in terms of molecule-molecule repulsion interaction, whose strength increases with the ligand coverage.

Two general binding modes should be identified in Table 6.1. The dissociative mode involves a proton transfer from the molecule to the surface O atom. In contrast to the findings for the (1010) surface, only one adsorption regime was found for each investigated moiety on the (1210) surface. Non-dissociative adsorptions are favored for -OH, -CN and -NH₂, whereas -SH and -COOH groups adsorb dissociatively. This resembles the behavior found for the (1010) surface.

| group | mode | (1210) | | (1010) | |
|------------------|----------|----------------|--------------|----------------|--------------|
| | | $\theta = 0.5$ | $\theta = 1$ | $\theta = 0.5$ | $\theta = 1$ |
| -CN | diss. | - | - | - | - |
| | nondiss. | -0.65 | -0.50 | -0.80 | -0.48 |
| -NH ₂ | diss. | - | - | -0.94 | -0.18 |
| | nondiss. | -1.36 | -1.15 | -1.35 | -0.88 |
| -OH | diss. | - | - | -1.06 | -0.75 |
| | nondiss. | -1.06 | -1.02 | -1.30 | -1.02 |
| -SH | diss. | -1.38 | -1.28 | -1.79 | -1.03 |
| | nondiss. | - | - | -0.82 | - |
| -COOH | diss. | -1.79 | -1.36 | -2.07 | -1.39 |
| | nondiss. | - | - | - | - |

Table 6.1: Adsorption energies (in eV) of the substituted methane molecules CH₃-X (X = CN, NH₂, OH, SH and COOH) on (1210) and (1010) ZnO for both molecular (nondiss.) and dissociative (diss.) adsorptions.

Discrepancies between the adsorption energies and adduct geometries for the two nonpolar surfaces in some cases can be explained by pointing out some dissimilarities between both surface structures. Although both surfaces have similar Zn-O dimer densities, their atomic arrangements differ significantly (see Fig. 6.1). For the most stable nonpolar surface, the Zn-O dimers are disposed homogeneously, in contrast to the configuration for the (1210) surface. The distance between two neighboring surface Zn atoms is 3.34 Å and 3.06 Å for the (1010) and (1210) surfaces, respectively. However, for the former, dangling bonds are practically oriented along the surface normal with a small component onto the [0001] direction and so a bidentate bridging adsorption becomes favorable for low-covered regimes. Such is the case of -SH and -COOH [299]. On the contrary, for the (1210) surface, dangling bond orientations do not favor this binding mode and so -SH adsorbs in a monodentate fashion for $\theta = 0.5$, despite

the similarities of both surfaces regarding Zn-Zn distances (see Fig. 6.2). Thus, the weaker adsorption of this ligand on the (1210) surface can be explained on the basis of its denticity reduction. For this surface, a -COOH bidentate bridging adsorption is however possible if second nearest-neighbors are considered as binding sites. In this case, the orientation of the dangling bonds favors this mode for low coverages. The second nearest-neighbor distance is rather large (5.06 Å) for the bare (1210) surface but decreases to 4.48 Å when the surface is covered with a one-half monolayer of carboxylic acid (Fig. 6.2). This stabilization mechanism involves a significant surface relaxation which partly explains the adsorption energy decrease with respect to the (1010) case.

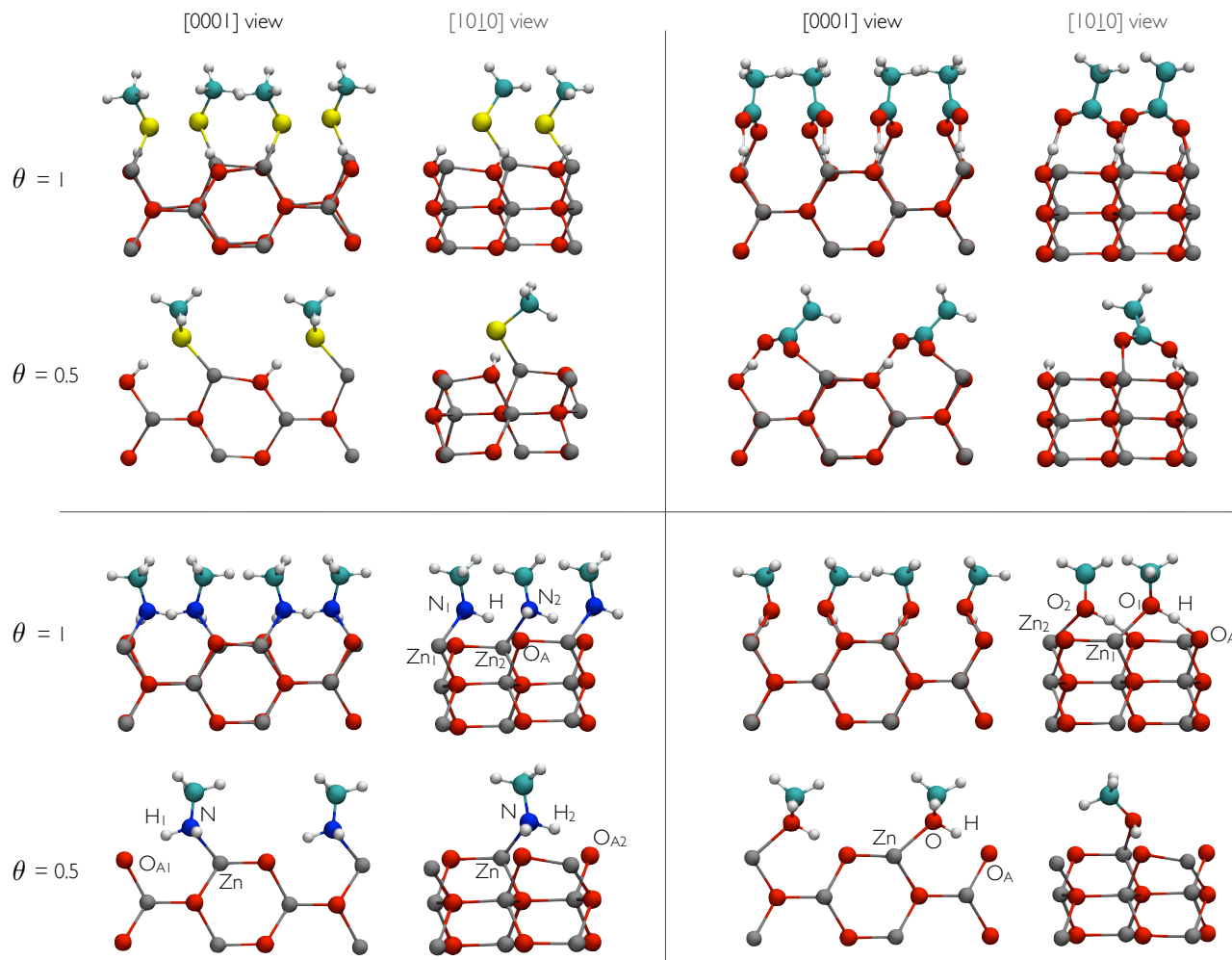


Figure 6.2: Optimized geometries of the modified (1210) ZnO surface using -SH (top left), -COOH (top right), -NH₂ (bottom left) and -OH (bottom right) functional groups. Only the three topmost Zn-O layers are shown.

The -OH and -NH₂ functional groups attach in a similar way as on the (1010) surface. We have found monodentate geometries for these moieties with interatomic distances $d_{\text{Zn-O}} = 2.17$ Å and $d_{\text{Zn-N}} = 2.10$ Å for $\theta = 0.5$, and $d_{\text{Zn}_1\text{-O}_1} = 2.15$ Å, $d_{\text{Zn}_2\text{-O}_2} = 2.13$ Å and $d_{\text{Zn}_1\text{-N}_1} = d_{\text{Zn}_2\text{-N}_2} = 2.13$ Å for $\theta = 1$ (Fig. 6.2). Hydrogen bonds with surface oxygens have lengths $d_{\text{H}\cdots\text{O}_A} = 1.42$ Å and $d_{\text{H}\cdots\text{O}_A} = 1.74$ Å at full coverage for -OH and -NH₂, respectively. For $\theta = 0.5$, $d_{\text{H}\cdots\text{O}_A}$

= 1.59 Å in the case of -OH surface modification whereas for -NH₂ both hydrogen atoms form hydrogen bonds with lengths $d_{\text{H}_1 \dots \text{O}_{\text{A}1}} = 1.96$ Å and $d_{\text{H}_2 \dots \text{O}_{\text{A}2}} = 1.92$ Å.

For the -CN group, the formation of a covalent C-O bond is not favorable for $\theta = 0.5$ and the molecule retains its linear structure (Fig. 6.3). This differs from the findings concerning the (10 $\bar{1}$ 0) surface for which the functional group is found to adsorb *via* formation of C-O and N-Zn bonds [299]. However, for $\theta = 1$, we find that one of the two ligands per surface unit cell does preferentially bind in a bidentate mode, resembling that for the most stable ZnO surface (see Fig. 6.3 top). In this case a bond length of $d_{\text{C-O}_\text{A}} = 1.45$ Å was found.

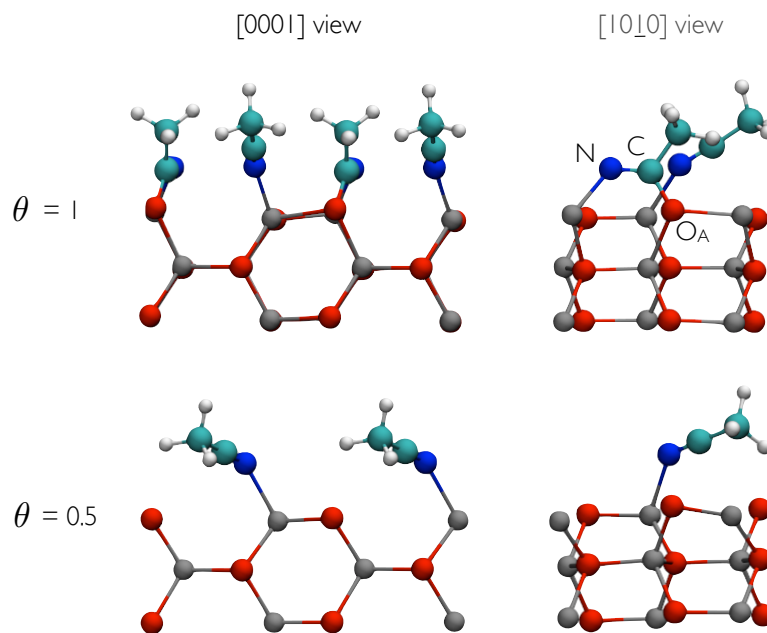


Figure 6.3: Optimized geometries of the modified (1 $\bar{2}$ 10) ZnO surface using the -CN functional group.

6.2 Modification of ZnO Nanowires

In this section we investigate the adsorption of monofunctional compounds on ZnO NWs. The bare NW has been modeled by cutting a hexagonal prism out of a ZnO wurtzite structure in such a way that its growth direction is oriented along the *c*-axis, and it exhibits nonpolar {10 $\bar{1}$ 0} and {1 $\bar{2}$ 10} facets. It has been shown that ZnO NWs typically grow in this way [300,301] and similar models have been employed in other theoretical studies [302]. Fig. 6.4 depicts the lateral and cross-sectional view of the bare NW. We considered a tetragonal supercell with a dimension of $30 \times 30 \times 5.41$ Å³ containing 48 atoms. Large vacuum regions along the [10 $\bar{1}$ 0] and [1 $\bar{2}$ 10] directions avert spurious interaction of the NW with the supercell images. The lattice parameter *c* was optimized for the bare system and kept fixed in the following.

For the coated NW, the previously investigated -COOH, -NH₂ and -SH moieties were employed. The -OH and -CN groups were disregarded due to their relative weak interaction with the non-polar ZnO surfaces. On the other side, methylphosphonic acid (MPA, formula CH₃PO(OH)₂)

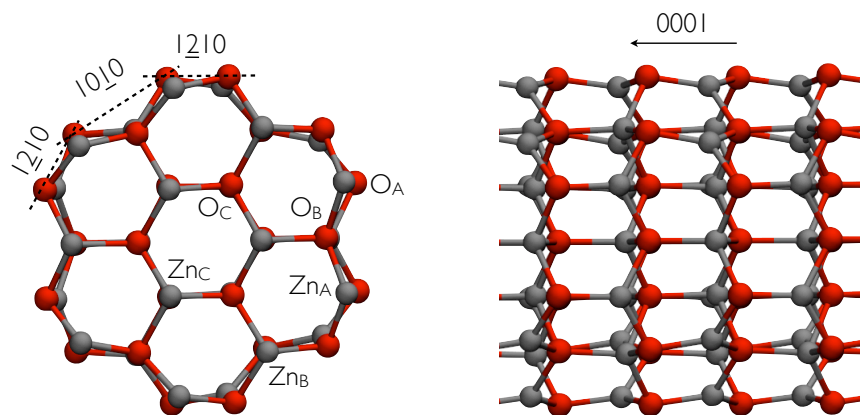


Figure 6.4: Cross-sectional (left) and side (right) views of the optimized structure of the bare ZnO nanowire.

is added here to the set of investigated ligands. The $-\text{PO}(\text{OH})_2$ functional group has been shown to chemisorb onto the ZnO $(10\bar{1}0)$ surface in a recent theoretical investigation [303]. We considered the adsorption of one ligand per surface Zn-O pair ($\theta = 1$) for the systems involving $-\text{COOH}$, $-\text{NH}_2$ and $-\text{SH}$ groups. This amounts to 12 molecules per supercell. This surface coverage has been demonstrated to be favored on nonpolar ZnO surfaces under ligand-rich conditions [299]. By contrast, MPA has been found to adsorb preferentially in a bidentate bridging mode, that is, *via* two O-Zn bonds as depicted in Fig. 6.8. Hence, for this particular case $\theta = 0.5$ (six molecules per supercell).

The preferred molecular configurations obtained in the previous section were regarded as initial guess for the geometry optimization of the modified NWs. For MPA, a double dissociated structure (that is, a structure for which the two hydrogen atoms are transferred from the $-\text{PO}(\text{OH})_2$ group to the nanowire surface) was assumed as initial geometry. This has been shown by DFT studies to be the favored configuration on the $(10\bar{1}0)$ surface [303]. For every system, the structure of each ligand was equivalent to each other at the beginning of the calculation. It should be noticed that the $(10\bar{1}0)$ surface is invariant under a reflection about a perpendicular $(1\bar{2}10)$ plane containing the Zn binding sites (Zn_A in Fig. 6.4). Additionally, as all investigated adsorbates are achiral, bend molecular configurations with orientations to one or the other direction along the normal to the $(1\bar{2}10)$ plane are equivalent for $\theta = 1$. We chose alternate orientation of the molecules in such a way that, on the same $(10\bar{1}0)$ facet, they look in the same direction whereas the orientation is switched in the neighboring $(10\bar{1}0)$ facets. This in turn implies that, at the $(1\bar{2}10)$ facets, they are either oriented towards each other or looking outward in opposite directions. In this way, every second $(1\bar{2}10)$ facet displays a small *ligand-free* region. It is obviously possible to build up a system with all molecules oriented toward the same direction. However, the chosen model allows us to study two possible scenarios regarding the ligand adsorption while considering a single adduct configuration.

For the optimization of the geometries, periodic DFT calculations have been performed as implemented in VASP. The Kohn-Sham equations were solved at the PBE level of theory. Plane wave basis sets with an energy cutoff of 300 eV as well as the PAW method have been employed. For Brillouin zone integration, k-point meshes were sampled using a $(1 \times 1 \times 4)$ MP grid. During the calculations, every atom was allowed to move till the interatomic forces were

smaller than 10^{-2} eV/Å.

The results concerning the adsorption of the -COOH group on the NW agree in general with those found for the surface adsorption. The molecule binds *via* two asymmetric O-Zn bonds (see Fig. 6.5). The difference between the O₁-Zn and O₂-Zn bond lengths ranges from 0.1 Å to 0.4 Å. This asymmetric bidentate adsorption has been shown to tend to a monodentate one when the system is embedded in an aqueous environment at room temperature [304]. To get insight into the strength of the adsorbate-substrate interaction and compare it with previous results for the surface, we calculated the absorption energy per ligand (Eq. 6.1). The obtained value is -1.31 eV, which compares well with the adsorption energy of the ligand on the nonpolar ZnO surfaces (see Table 6.1).

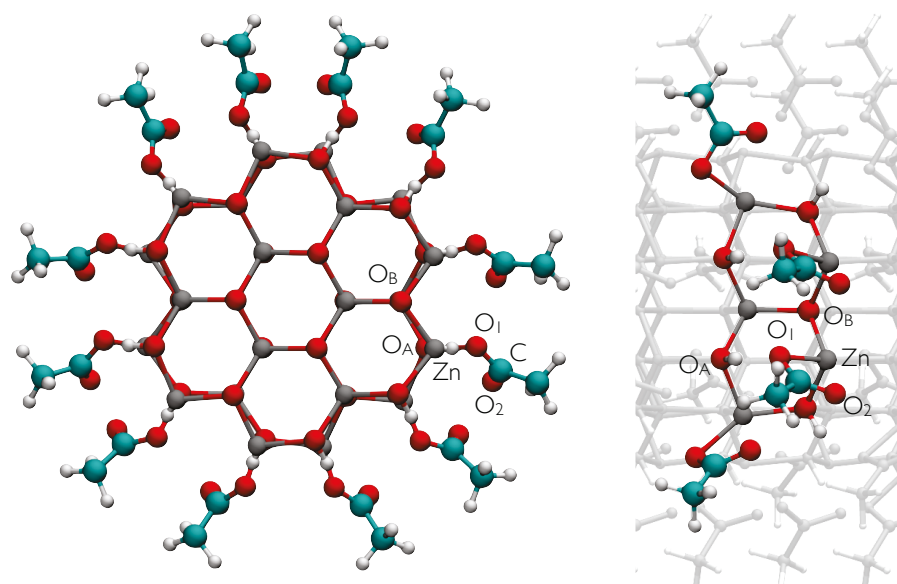


Figure 6.5: Cross-sectional (left) and side (right) views of the optimized structure of the CH₃COOH-modified ZnO nanowire.

The relaxation of the nanowire facets upon adsorption of the -COOH group also resembles that observed for the ZnO surfaces. The tricoordinate Zn atoms relax outwards, thus enlarging the bond length of Zn_A-O_A surface pairs. In this case, the bond length goes from 1.90 Å for the bare nanowire to 2.04-2.12 Å for the modified nanostructure, for a relative elongation of up to 12%. This value is slightly greater than the 9% enlargement found for the two-dimensional model. At the same time, the bond lengths between the fourfold coordinated Zn_B and the O_A atoms in the modified nanowire experience a reduction of around 6% with respect to the bare wire. Hydrogen bonds with one of the -COOH oxygens have bond lengths of 1.66 Å. Previous DFTB calculations for the interaction of CH₃COOH with the (10 $\bar{1}$ 0) ZnO surface yielded a somewhat larger value of 1.74 Å [305]. The C-O bond lengths of the -COOH group vary from 1.31 to 1.27 Å. This is in agreement with the findings for the (10 $\bar{1}$ 0) surface.

The optimized structure of the NW modified with -SH is depicted in Fig. 6.6. The molecular geometry is also in accordance with the structure found for the modification of the nonpolar surfaces. The two nonequivalent configurations of the ligands have been labeled with indexes 1 and 2. The adsorption is dissociative and monodentate with S₁-Zn and S₂-Zn bond lengths

of 2.23 and 2.26 Å, respectively. The corresponding binding energy per adsorbate is -1.18 eV, which is between the values found for the adsorption on the (10 $\bar{1}$ 0) (-1.03 eV) and the (1 $\bar{2}$ 10) (-1.28 eV) surfaces.

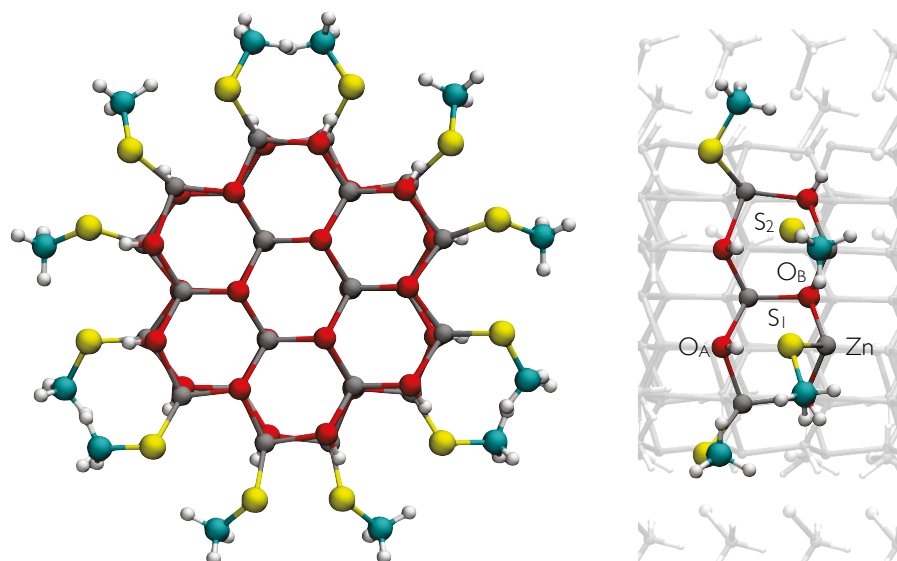


Figure 6.6: Cross-sectional (left) and side (right) views of the optimized structure of the CH₃SH-modified ZnO nanowire.

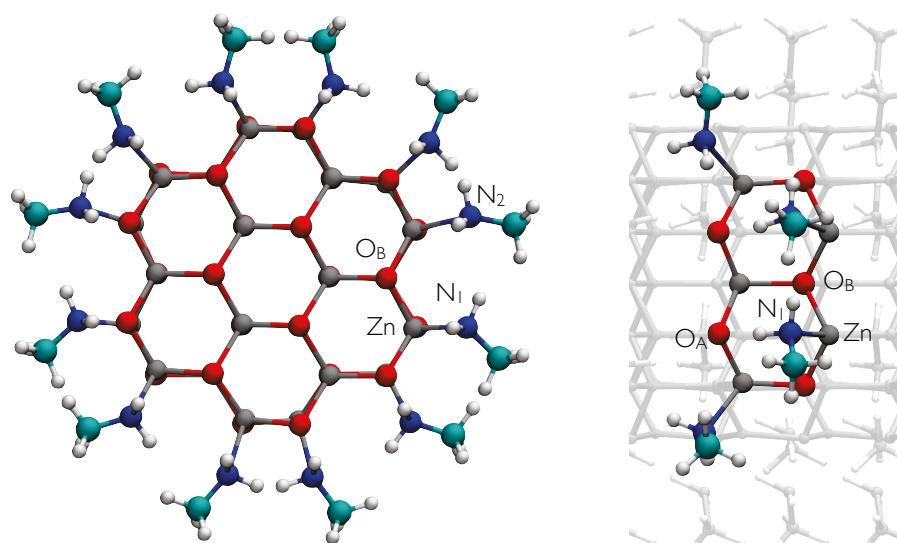


Figure 6.7: Cross-sectional (left) and side (right) views of the optimized structure of the CH₃NH₂-modified ZnO nanowire.

The adsorption energy for the -NH₂ case (0.81 eV) is, in contrast, slightly smaller than that observed for the (10 $\bar{1}$ 0) surface and over 0.3 eV smaller than for the (1 $\bar{2}$ 10) surface. The

optimized structure of the $\text{NH}_2\text{-ZnO}$ system is shown in Fig. 6.7. The adsorbates bind in a nondissociated form with interatomic distances $\text{N}_1\text{-Zn}$ and $\text{N}_2\text{-Zn}$ of about 2.15 and 2.31 Å, respectively. Thus, the N-Zn bond lengths for one of the nonequivalent molecular configurations is in line with the results for the nonpolar surface reported above, whereas, for the second group of ligands, the N-Zn interatomic distance is larger.

Finally, the optimized geometry corresponding to the modification of the NW using MPA is depicted in Fig. 6.8. MPA strongly binds to the nanostructure *via* two symmetric O-Zn bonds with an O-Zn interatomic distance of 1.92 Å. The third oxygen atom of the -PO(OH)_2 group, O_3 , relaxes to a position equidistant from the two hydrogen atoms transferred from the ligand to the surface with an interatomic distance $d_{\text{O}_3 \dots \text{H}} = 1.67$ Å. The adsorption energy per adsorbate amounts in this case to 2.69 eV.

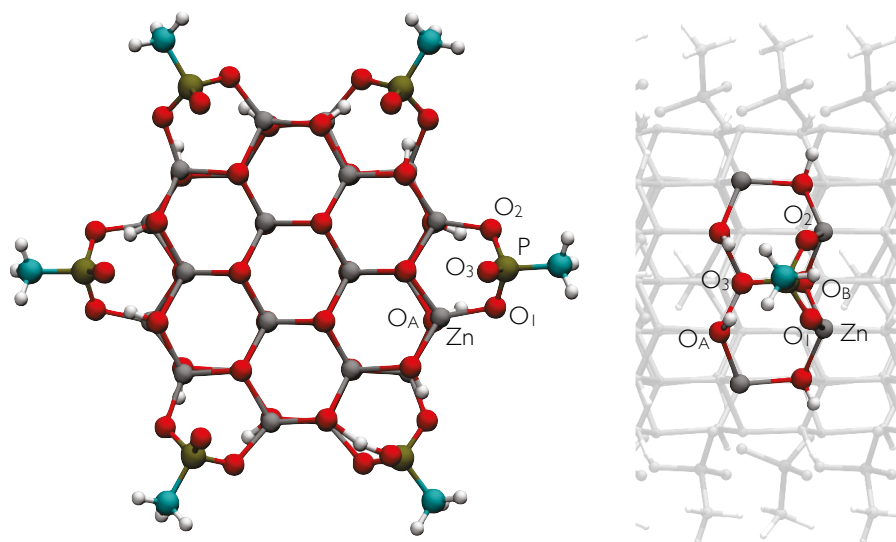


Figure 6.8: Cross-sectional (left) and side (right) views of the optimized structure of the $\text{CH}_3\text{PO(OH)}_2$ -modified ZnO nanowire.

6.3 Glycine Adsorption on $(10\bar{1}0)$ ZnO Surfaces

Thus far we have studied the interaction between monofunctional ligands and nonpolar facets of ZnO. However, in real situations the compound employed for the purpose of surface modification may attach to the substrate through more than one functional group. In this section we investigate the adsorption of a bifunctional linker on the $(10\bar{1}0)$ ZnO surface and how the adsorption mode influences the electronic properties of the complex. We chose glycine ($\text{NH}_2\text{CH}_2\text{COOH}$) due to the availability of two of the most employed anchor groups for ZnO functionalization and its small molecular volume, which minimizes repulsive steric effects.

Glycine adsorption was investigated with DFTB. DFTB has been shown to describe successfully ZnO surfaces and their interaction with small molecules [306]. In our calculations, we considered a tetragonal supercell consisting of a ZnO slab with 16 atomic layers along the $[10\bar{1}0]$ direction and a vacuum region of 20 Å. We define the surface coverage, θ , as the number of glycine

molecules adsorbed per surface unit cell (surface Zn-O pair) and considered coverages of 0.25, 0.5, and 1 by using surface cells with (2×2) , (2×1) , and (1×1) periodicities, respectively. The Brillouin zone integration was performed using MP meshes of $(1 \times 2 \times 2)$ for $\theta = 0.25$ and $(1 \times 4 \times 3)$ for $\theta = 0.5$ and 1. All atoms were allowed to move until the interatomic forces were smaller than 5×10^{-3} eV/Å.

Several molecular orientations were considered during this investigation. The corresponding adsorption energies were calculated using Eq. 6.1. To study the relative thermodynamic stability of the considered surface coverages, we assume that the ZnO surface is in thermodynamic equilibrium with glycine in the gas phase. The variation of the surface energy of the substrate after adsorption of glycine can then be calculated according to

$$\Delta\gamma = \frac{1}{N_A A} (E_T - E_{\text{bare}} - nE_{\text{Gly}}) = \frac{\theta E_{\text{ads}}}{A}, \quad (6.2)$$

where A is the area of the (1×1) surface unit cell and N_A is the number of (1×1) surface unit cells contained in the supercell.

Table 6.2 summarizes the adsorption energies and the surface energy variations for the most stable configurations of the hybrid interface. Our results show that for $\theta = 1$ glycine binds to the surface through the -COOH (-NH₂) group with an adsorption energy of $E_{\text{ads}} = -1.82$ (-1.67) eV. Adsorption through the carboxyl group is, therefore, slightly favored. The corresponding optimized structures are depicted in Fig. 6.9. For the most stable configuration, glycine binds to the substrate in a monodentate mode and dissociatively. Similar investigations on glycine adsorption on Si surfaces found a barrier height for dissociation of only 1 eV [307], suggesting that dissociation is likely to occur at room temperature. One of the carboxylic oxygens, O₁, binds to the surface Zn atom with a bond length of 2.15 Å, whereas the oxygen atom O₂ relaxed to a position equidistant from two neighboring surface Zn atoms at 2.28 Å.

| θ | group | mode | E_{ads} (eV) | $\Delta\gamma$ (eV/Å _{1×1}) | geometry |
|------------------------|------------------------|---|-----------------------|---------------------------------------|--------------------|
| 1 | -COOH | monodentate, anion, dissociated | -1.82 | -1.82 | Fig. 6.9 (top) |
| 1 | -NH ₂ | dissociated | -1.67 | -1.67 | Fig. 6.9 (bottom) |
| 1 | -COOH | monodentate, zwitterion, nondissociated | -0.84 | -0.84 | not shown |
| 0.5 | -COOH/-NH ₂ | bidentate chelating, dissociated | -2.92 | -1.46 | Fig. 6.10 (middle) |
| 0.5 | -COOH/-NH ₂ | monodentate, dissociated | -3.12 | -1.56 | Fig. 6.10 (right) |
| 0.5 | -COOH | bidentate bridging, dissociated | -2.56 | -1.28 | Fig. 6.10 (left) |
| 0.25 | -COOH/-NH ₂ | monodentate, dissociated | -3.05 | -0.76 | Fig. 6.11 (top) |
| 0.25 (V _O) | -COOH/-NH ₂ | monodentate, dissociated | -3.18 | -0.80 | Fig. 6.11 (bottom) |

Table 6.2: DFTB adsorption energies (E_{ads}) and surface energy variations per (1×1) ZnO surface ($\Delta\gamma$) corresponding to the stable binding geometries of glycine on $(10\bar{1}0)$ ZnO.

Adsorption through the -NH₂ group occurs *via* the binding of the nitrogen atom to the metal site. One proton is transferred from the functional group to the surface oxygen site during adsorption as shown in Fig. 6.9 (bottom). It is worth mentioning that a metastable zwitterionic form of glycine on ZnO was only observed for a full coverage, with a relatively small adsorption energy of $E_{\text{ads}} = -0.84$ eV. No stable zwitterionic glycine has either been found on Zn-terminated ZnO polar surfaces [308].

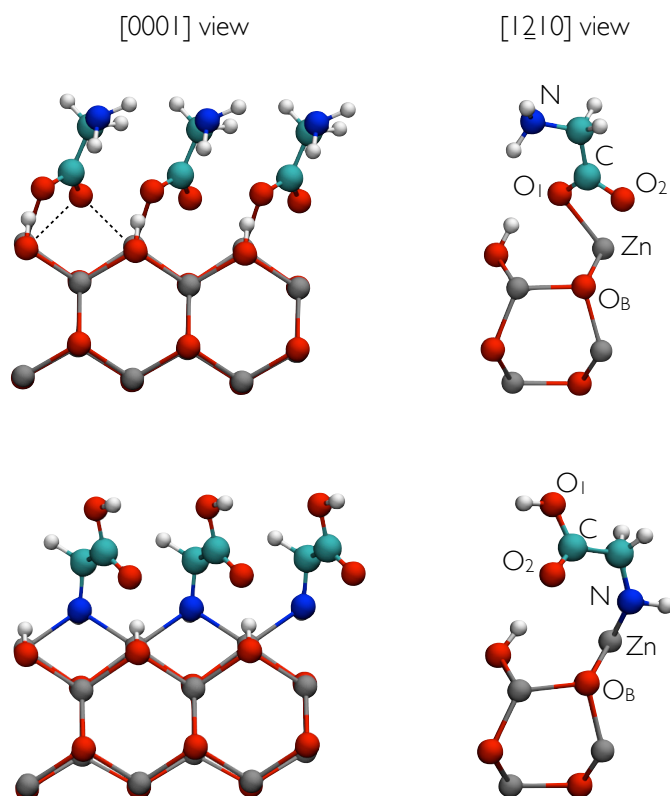


Figure 6.9: Optimized structures of the modified (10 $\bar{1}$ 0) ZnO surface using 1 ML of glycine molecules adsorbed through either the -COOH (top) or the -NH₂ (bottom) groups.

For $\theta = 0.5$, two surface Zn sites per molecule are available, and glycine can therefore adsorb through -COOH in a bidentate bridging configuration. The optimized structure corresponding to this adsorption mode is shown in Fig. 6.10 (left). The bond lengths between the oxygen atoms of the molecule and the surface are $d_{O_1-Zn_1} = 2.03 \text{ \AA}$ and $d_{O_2-Zn_2} = 2.05 \text{ \AA}$. The adsorption energy for this configuration is $E_{\text{ads}} = -2.56 \text{ eV}$. These results are in line with a DFTB investigation where the authors found that acetic acid preferentially attaches to the (10 $\bar{1}$ 0) ZnO surface in a bidentate bridging mode for a 0.5 ML coverage [305]. However, in the case of glycine, a competition between -NH₂ and -COOH groups for attaching to the available binding sites is expected. We found, indeed, that the most stable configurations for the adsorption of glycine involve the attachment of both functional groups. Adsorption in a -COOH bidentate chelating mode occurs through dissociation of the -NH₂ group (Fig. 6.10 middle). The adsorption bond lengths for this case are $d_{N-Zn_1} = 1.95 \text{ \AA}$, $d_{O_1-Zn_2} = 2.19 \text{ \AA}$ and $d_{O_2-Zn_2} = 2.16 \text{ \AA}$, and the adsorption energy is $E_{\text{ads}} = -2.92 \text{ eV}$. Slightly favored ($E_{\text{ads}} = -3.12 \text{ eV}$) is the adsorption in a -COOH monodentate configuration (Fig. 6.10 right). In this case, the -NH₂ group does not dissociate. The bond lengths are $d_{N-Zn_2} = 2.01 \text{ \AA}$ and $d_{O_1-Zn_1} = 1.90 \text{ \AA}$. For each configuration, dissociation of the -COOH group is observed.

The smallest investigated surface coverage is $\theta = 0.25$. For the most stable configuration, the adsorption is produced in a similar manner as for $\theta = 0.5$, that is, the ligand attaches dissociatively through both functional groups in a -COOH monodentate mode (see Fig. 6.11 top). The -NH₂ group binds to the surface Zn₂ site through the nitrogen atom with a bond

length of 2.01 Å, whereas the carboxylic oxygen O_2 adsorbs on a neighboring metal site (Zn_4) with a bond length of 1.99 Å. The corresponding adsorption energy is -3.05 eV. This geometry resembles that found for glycine on polar (0001) ZnO surfaces [308], where the hydrogen of the -COOH group is transferred to the Zn-terminated surface. In contrast, this adsorption mode differs from that found for glycine on TiO_2 (110), where the ligand binds favorably through -COOH in a bidentate bridging configuration for a 0.5 ML coverage [309,310].

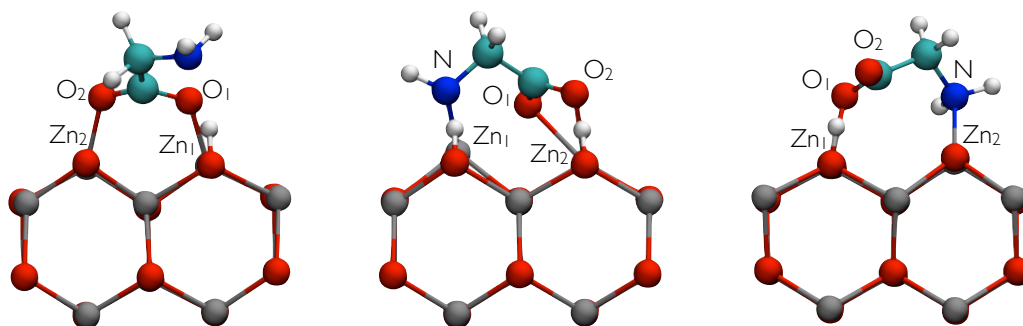


Figure 6.10: Optimized structures of the modified (10 $\bar{1}$ 0) ZnO surface using 0.5 ML of glycine molecules in different binding modes: -COOH bidentate bridging (left), -COOH bidentate chelating with dissociated -NH₂ group (middle) and -COOH monodentate with nondissociated -NH₂ group.

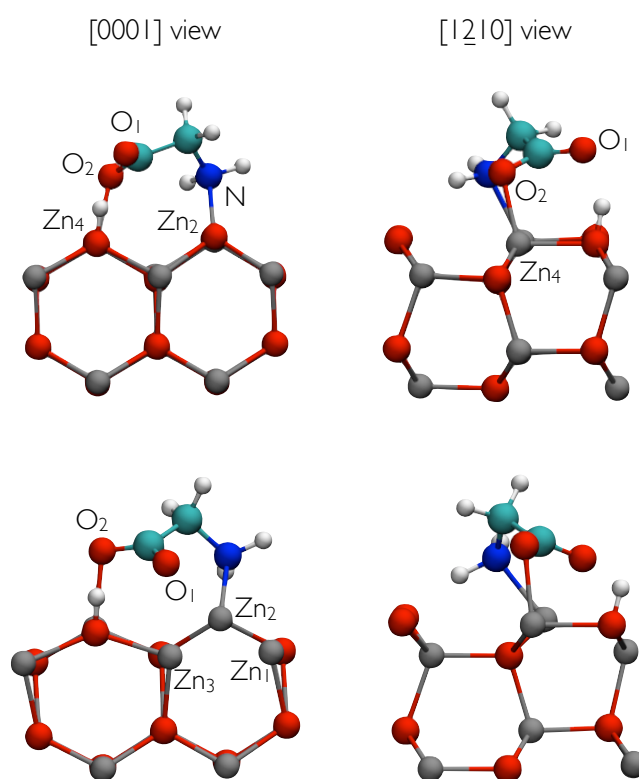


Figure 6.11: Optimized structures of glycine adsorbed on the defect-free (top) and oxygen-reduced (bottom) (10 $\bar{1}$ 0) ZnO surfaces for $\theta = 0.25$.

To analyze the relative thermodynamic stability of the glycine/ZnO interface for different surface coverages, we compare the respective $\Delta\gamma$ values. According to our results, the 1 ML coverage is expected.

Although similar adsorption energies were found for the adsorption of glycine on the ZnO surfaces through either -COOH or -NH₂ groups in high-coverage regimes, the electronic properties of the two modified surfaces are very different. The DOS for the adsorption through -COOH is shown in Fig. 6.12 (middle). Changes with respect to the DOS for the bare surface (Fig. 6.12 top) are observed close to the top of the valence band and the bottom of the conduction band. The states at the VBM have strong projections onto the O_{COOH}-2*p*, surface Zn-3*d*, and N_{NH₂}-2*p* orbitals. For the adsorption through the -NH₂ group, additional levels are inserted close to the VBM, localized mainly at the N-Zn-O₃ bonds (see Fig. 6.12 bottom). In addition, unoccupied intragap levels are also seen, with contributions coming mainly from the -COOH group.

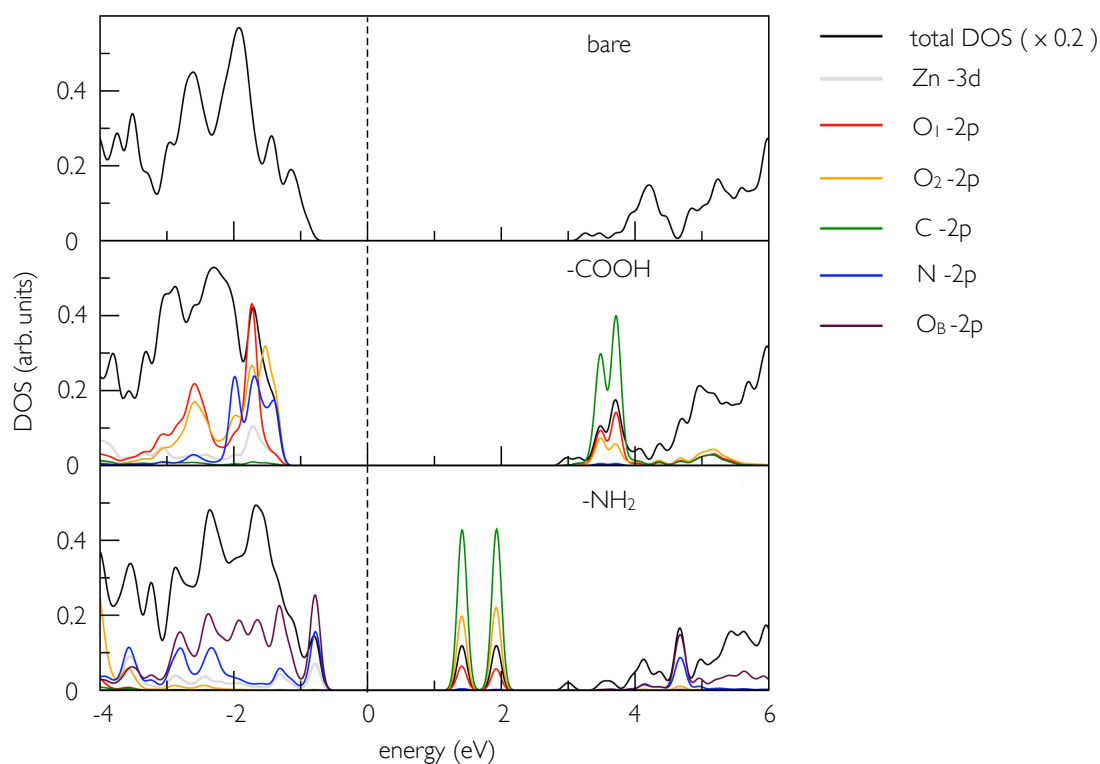


Figure 6.12: Total and projected density of states for the bare (1010) ZnO surface (top) and the modified surface using glycine adsorbed through the -COOH group (middle) and the -NH₂ group (bottom) for $\theta = 1$. The atom notation corresponds to the one employed in Fig. 6.9. The dashed line indicates the Fermi level position.

6.3.1 The effect of surface oxygen vacancies

The successful modification of ZnO surfaces can be hindered by the presence of intrinsic defects and impurities. Surface defects can act as catalysts for adsorption/dissociation of the ligand, thus changing the properties of the nanostructure and affecting the features for device

applications [311–314]. We investigate next the effect of surface oxygen vacancies (V_O) on the adsorption of glycine on the ZnO nonpolar surface. V_O is a common defect in ZnO and has been extensively investigated in bulk materials [315–317] and $(10\bar{1}0)$ surfaces [318]. The oxygen-reduced surface was modeled by removing one surface oxygen per 2×2 surface unit cells. One glycine molecule per oxygen vacancy was considered. The most stable configuration for the adsorption on the defective surface is shown in Fig. 6.11 (bottom). The binding geometry shows some similarities with that for the defect-free surface. The molecule adsorbs through both functional groups, with interatomic distances of $d_{N-Zn_2} = 2.04 \text{ \AA}$, $d_{O_2-Zn_4} = 2.06 \text{ \AA}$, $d_{O_1-Zn_2} = 2.31 \text{ \AA}$, and $d_{O_1-Zn_3} = 2.66 \text{ \AA}$. However, one of the carboxylic oxygens, O_1 , relaxes toward the vacancy site compared to the geometry for the defect-free case. This leads to an energy gain of roughly 0.1 eV, thus revealing a small influence of the defect on the glycine adsorption mode and adsorption strength.

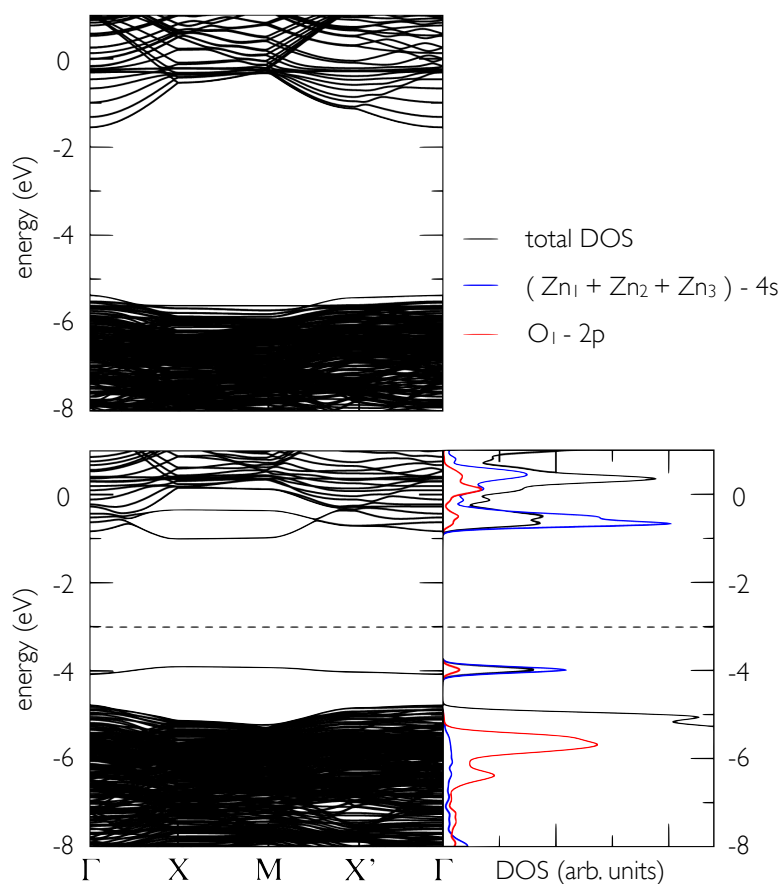


Figure 6.13: Electronic band structure for the 0.25 ML coverage of glycine molecules on the defect-free (top) and oxygen-reduced (bottom) $(10\bar{1}0)$ ZnO surfaces (structures shown in Fig. 6.11). The density of states (DOS) for the defective surface is shown to the right of the corresponding band structure. The blue curve denotes the sum of the projections of the DOS onto the 4s orbitals of atoms Zn_1 , Zn_2 and Zn_3 . The dashed line indicates the Fermi level position.

The densities of states for the glycine adsorption on the defect-free and reduced surfaces for $\theta = 0.25$ are shown in Fig. 6.13. No intragap states appear for the defect-free surface case

(Fig. 6.13 top). However, the adsorption on the defective surface reveals an intragap electronic level with contributions coming mainly from the $4s$ states of atoms Zn_1 , Zn_2 and Zn_3 and the $2p$ states of atom O_1 (Fig. 6.13 bottom).

6.4 Summary

We have investigated the structural properties and energetics of organic/ZnO interfaces for a two-dimensional (nonpolar $(1\bar{2}10)$ surface) and a one-dimensional (nanowire) systems using DFT. In general, similar properties of the complexes were found for both dimensionalities. The adsorption energies of the investigated ligands on ZnO follow the same trend for both the nanowire and the planar structure, being the -COOH-ZnO system the energetically most stable adduct. According to our results, stable organic/ZnO interfaces can be also formed through modification with thiols and phosphonates. In contrast, the interaction between ZnO and alcohols, amines and nitriles is relatively weak.

Furthermore, the adsorption of glycine (which contains both amino and carboxyl functional groups) on the nonpolar $(10\bar{1}0)$ ZnO surface was investigated employing the DFTB method. We found the 1 monolayer coverage to be the most favorable adsorption configuration, with no marked preference concerning the functional group attaching to the substrate. However, the electronic structure of the modified surface is strongly affected when the ligand binds through the $-NH_2$ group. For lower coverages, as new binding sites become available, glycine is expected to bind through both anchor groups. The absolute value of the adsorption energy per ligand is greater for lower coverages than for the fully-covered surface as the molecule can maximize the number of bonds with the substrate, thus leading to an energy gain. The strength of the glycine-ZnO interaction slightly increases when the adsorption takes place at an oxygen-vacancy site. For every studied configuration of the complex, glycine adsorbs dissociatively, where one or two protons are transferred from the adsorbate to the substrate.

Chapter 7

CONCLUDING REMARKS

In the framework of this dissertation, new extensions of the DFTB and TD-DFTB methods were introduced and implemented. The main extension, the so-called onsite correction, constitutes a change in the paradigm of the semiempirical approach. This correction deals with the refinement of one of the main approximations applied in second-order DFTB, namely, the Mulliken approach for the evaluation of two-electron multicenter integrals. This approximation is crucial for the efficient simplification of the method and has been demonstrated to work satisfactorily in many scenarios. However, there is a special case for which this approach becomes critical. In linear response TD-DFTB $\sigma \rightarrow \pi^*$ and $n \rightarrow \pi^*$ excitations are erroneously described as the Mulliken approximation conduces in many occasions to the strict neglect of the corresponding transition charges. We have developed a formalism within which this problem is successfully healed without a drastic repercussion in the complexity and computational demand of the method.

The onsite correction leads to a DFTB scheme where the whole dual electron density matrix is managed self-consistently, unlike the traditional formalism where only its diagonal elements are considered. The binding energies of hydrogen-bonded complexes were shown to be substantially improved within the new scheme. These systems have been acknowledged several times as problematic within the current methodological frame, and an improvement in their description has been pursued. Advances in this regard include a recent third-order energy expansion combined with the insertion of a purely empirical correction for the interaction of hydrogen with neighboring atoms (the so-called DFTB3 method). This extension involves the use of fitted parameters and has been thought to be necessary for the correct characterization of hydrogen bond interaction within DFTB. Our results indicate, however, that the systematic improvement in the description of such interaction is possible through the development of extensions based on fundamental grounds. Generally, a theory based on empiricism is likely to fail in situations differing from those for which the method was originally designed. In this sense, our formalism counts on an essential advantage. We showed in Chapter 3 that the onsite-corrected DFTB approach can equal or even surpass the performance of DFTB3 for the reproduction of hydrogen bond energies of water nanoparticles and small water-containing systems.

The combination of our refinement with a third-order expansion also seems to be promising for the study of hydrogen-bonded complexes. However, this approach does not outperform the sole application of the onsite correction (that is, up to a second-order energy expansion) for the description of large water clusters. This is presumably because there is still room for

improvement within second-order DFTB, and so the inclusion of third order terms do not always necessarily leads to improvements. The further sophistication of the approximation for the evaluation of multicenter integrals is currently under way. Within such scheme, the truncated expansion of the two-electron integrals would enclose terms of the form $(\mu\nu|\kappa\lambda)$, where $\mu, \nu \in A$ and $\kappa, \lambda \in B$ with $A \neq B$. These terms are neglected within the Mulliken approach if at least one of the conditions $\mu \neq \nu$ and $\kappa \neq \lambda$ is met. This future prospect is expected to lead to a further enhanced characterization of hydrogen-bonded complexes. Additionally, a systematic analysis of other ground-state properties such as proton affinities and proton transfer barriers will be accomplished in the future for a more ample assessment of the onsite-corrected DFTB method. The generation of parameters specially designed for the refined formalism constitutes another perspective. An extensive test of its performance for the description of geometries, vibrational frequencies and electronic structures of organic molecules and periodic systems will be accomplished.

Within TD-DFTB, the onsite correction was shown to overcome the inaccurate description of the aforementioned electronic excitations. This was specially illustrated in Chapter 4 for diatomic systems, for which the new formalism is essential to display a qualitatively correct absorption spectrum. The erroneous singlet-triplet degeneracy of $\sigma \rightarrow \pi^*$ and $n \rightarrow \pi^*$ transitions is also corrected within the new scheme. Additionally, during the study of the diatomic species we unveiled a shortcoming of traditional TD-DFTB for the description of $\pi \rightarrow \pi^*$ transitions. This is the incorrect degeneracy of Σ^- and Δ excitation energies, which is also rectified within the proposed scheme. We showed that the onsite correction improves overall upon excitation energies and oscillator strengths. A considerable improvement in the agreement with more sophisticated theoretical methods and experiment in terms of singlet-triplet excitation energies was demonstrated. In this regard, the proposed approach even outperforms TD-DFT at the PBE level and the hybrid schemes PBE0 and CAM-B3LYP. More importantly, this is accomplished at a substantially shorter computational time (1 to 2 orders of magnitude). The use of the corrected TD-DFTB is hence encouraged for the study of singlet-triplet excitations of relatively large systems. The overall accuracy of singlet-singlet excitation energies is in contrast similar to that reached within the original scheme. Aside from the onsite correction, TD-DFTB has been extended here to account for fractional occupancy and spin polarization. This will broaden the applicability of the method. For instance, the simulation of metallic or near-metallic systems at elevated electronic temperature is now possible.

The low computational cost of TD-DFTB makes it especially suitable for the study of photoinduced processes by means of quantum molecular dynamics simulations. In this regard, the effect of the onsite correction on the calculation of energy gradients is under investigation. The inclusion of hybrid functionals within TD-DFTB is also a promising prospect. This may improve the overall accuracy of the method and will allow for new applications. One of those is, for example, the development of an appropriate dressed TD-DFT-based formalism [138, 231] for the description of double-excitations. Additionally, the implementation of range-separated functionals might enhance the description of charge-transfer excitations, which play a fundamental role in several photoreactions. In particular, the description of visible-light activation of TiO_2 and other photocatalysts by complexation with suitable ligands may be improved. The development of a hybrid TD-DFTB formalism is ongoing.

Chapters 5 and 6 were devoted to the application of different density functional approaches to get insight into the interaction of TiO_2 , Al_2O_3 and ZnO with selected compounds. PBE results revealed that ZnO can form stable interfaces with $-\text{COOH}$, $-\text{SH}$ and $-\text{PO}(\text{OH})_2$ anchor groups

in the gas phase. However, many queries still remain concerning the stability of such interfaces in an aqueous environment. Our DFTB findings on glycine adsorption on ZnO suggest that the modification of nonpolar ZnO surfaces using bifunctional linkers needs to be carefully controlled in order to prevent undesired electronic properties of functionalized ZnO nanostructures.

The TD-DFTB approach was employed for the study of some aspects of the photocatalytic activity of TiO₂. The reliability of the chosen methodology was demonstrated by comparison with experimental and first-principle results. We believe that TD-DFTB might indeed become the first-choice method for the investigation of excited-state properties of titania complexes. On the one hand, its efficiency makes it possible to employ models with large dimensions. This combined with the implementation of orbital constraints, allowed the computation of the first 1200 excitation energies and oscillator strengths of systems containing up to 143 atoms in less than one day. This task is unfeasible within an *ab initio* framework. On the other hand, TD-DFTB can accurately describe the structural and electronic properties of titania. In fact, TD-DFTB results are sometimes in better agreement with experiment than full TD-DFT findings themselves due to a fortunate cancellation of errors. The band gaps of the two main TiO₂ polymorphs, rutile and anatase, are excellently given within TD-DFTB, and this constitutes an important ingredient for the accurate description of near band gap excitations of this metal oxide.

The vis-light activation of TiO₂ *via* charge-transfer complexation with NO was demonstrated during the present study. This has been confirmed by experimental measurements conducted in close collaboration within this investigation. In contrast, TiO₂-acetaldehyde complexes were predicted to not absorb visible light. This is also in line with the experimental observation of a vanishing photocatalytic activity of pure TiO₂ samples for the degradation of acetaldehyde under visible illumination. Our results indicate that acetaldehyde may be chosen to test the ability of TiO₂-based photocatalysts to absorb visible light whereas NO would not be a valid choice. Furthermore, the unexpected photocatalytic activity of alumina samples can be explained by formation of CT complexes with NO.

The present study on TiO₂ photocatalysis is only the first step in a promising route of research. The use of the efficient TD-DFTB tool opens a variety of possibilities for the study of more complex systems. The analysis of water coadsorption, as well as the effect of oxygen vacancies or OH groups on the surfaces of titania, constitute some of the future perspectives. This will help in unraveling many unknown aspects of photocatalysis. A very promising outlook of methodological character is the development and implementation of orbital constraints for the calculation of energy gradients. This combined with the parallelization of the TD-DFTB code may eventually make it feasible to run quantum molecular dynamic simulations in the excited state for different TiO₂-pollutant complexes. In this manner, the degradation of the unwanted species could be directly observed in the simulations.

Appendix A

PARAMETERS γ AND W

In spin-unrestricted DFTB, the appearing two-center integrals, Γ (Eq. 3.29), which depend on both the spin-up, ρ_\uparrow , and spin-down, ρ_\downarrow , charge densities are commonly split up into two terms, one depending on the total density, $\rho = \rho_\uparrow + \rho_\downarrow$, and the other on the spin density (or magnetization), $m = \rho_\uparrow - \rho_\downarrow$. In this manner, the method can be easily connected with its spin-restricted version by simply setting the latter integral to zero.

This transformation is done *via* a change of variables from the set $\{\rho_\uparrow, \rho_\downarrow\}$ to $\{\rho, m\}$; thus the XC kernel can be expressed as follows:

$$\frac{\delta^2 E_{xc}[\rho_\uparrow, \rho_\downarrow]}{\delta\rho_\sigma(\mathbf{r})\delta\rho_\tau(\mathbf{r}')} = \frac{\delta^2 E_{xc}[\rho, m]}{\delta\rho(\mathbf{r})\delta\rho(\mathbf{r}')} + \delta_\sigma \frac{\delta^2 E_{xc}[\rho, m]}{\delta m(\mathbf{r})\delta\rho(\mathbf{r}')} + \delta_\tau \frac{\delta^2 E_{xc}[\rho, m]}{\delta\rho(\mathbf{r})\delta m(\mathbf{r}')} + \delta_\sigma \delta_\tau \frac{\delta^2 E_{xc}[\rho, m]}{\delta m(\mathbf{r})\delta m(\mathbf{r}')}, \quad (\text{A.1})$$

where $\delta_\sigma = 2\delta_{\uparrow\sigma} - 1$. By combining the Coulomb kernel with the second derivative of the XC energy with respect to total density [first term in Eq. (A.1)], we obtain the γ functional introduced in the original SCC-DFTB paper [90], whereas the last term is the kernel of the spin constants, W [177]. Thus, the functional Γ can be written as

$$\Gamma_{Al,Bl'}^{\sigma\tau} = \gamma_{Al,Bl'} + \delta_\sigma \delta_\tau W_{Al,Bl'} + 2\delta_\sigma \delta_\tau D_{Al,Bl'}, \quad (\text{A.2})$$

where

$$\begin{aligned} \gamma_{Al,Bl'} &= \left(F_{Al} \left| \frac{1}{|\mathbf{r} - \mathbf{r}'|} + \frac{\delta^2 E_{xc}[\rho, m]}{\delta\rho(\mathbf{r})\delta\rho(\mathbf{r}')} \right|_{\rho_0,0} \right| F_{Bl'} \Big), \\ W_{Al,Bl'} &= \left(F_{Al} \left| \frac{\delta^2 E_{xc}[\rho, m]}{\delta m(\mathbf{r})\delta m(\mathbf{r}')} \right|_{\rho_0,0} \right| F_{Bl'} \Big), \\ D_{Al,Bl'} &= \left(F_{Al} \left| \frac{\delta^2 E_{xc}[\rho, m]}{\delta m(\mathbf{r})\delta\rho(\mathbf{r}')} \right|_{\rho_0,0} \right| F_{Bl'} \Big). \end{aligned} \quad (\text{A.3})$$

The derivatives of the XC functional are evaluated at the total density, ρ_0 , and magnetization, $m = 0$, as the reference system is taken spin-unpolarized. Two-center contributions to W are neglected: $W_{Al,Bl'} = \delta_{AB}W_{Al,l'}$. The parameters D contain the mixed derivative with respect to ρ and m . If spin-orbit interactions are neglected, the XC functional must satisfy $E_{xc}[\rho, m] = E_{xc}[\rho, -m]$ and is therefore an even functional in m . This leads to $D = 0$ and the Γ parameters obtain their final form as in Eq. (3.31).

Appendix B

OBTAINING ORIGINAL DFTB FORMALISM FROM ITS DENSITY MATRIX FORMULATION

The spin-unrestricted Hamiltonian obtained in the original work of Köhler *et al.* [177] can be derived from the formalism presented in section 3.4 by substituting the KS density matrix fluctuation, $\Delta P_{uv}^\tau = n_{u\tau}\delta_{uv} - P_{uv}^{0,\tau}$, and the expression (3.40) for the $\bar{\mathbf{K}}$ matrix in Eq. (4.5):

$$H_{st\sigma} = H_{st\sigma}^0 + \sum_{\tau} \sum_{ACl''} \Gamma_{Al,Cl''}^{\sigma\tau} q_{Al}^{st\sigma} \left(\sum_u n_{u\tau} q_{Cl''}^{uu\tau} - \sum_{uv} P_{uv}^{0,\tau} q_{Cl''}^{uv\tau} \right). \quad (\text{B.1})$$

By using definition (3.38), the sum

$$\begin{aligned} \sum_u n_{u\tau} q_{Cl''}^{uu\tau} &= \sum_u n_{u\tau} \sum_{\kappa \in C,l''} P_{\kappa\kappa}^{uu\tau} \\ &= \sum_u n_{u\tau} \sum_{\kappa \in C,l''} \sum_{\lambda} c_{\kappa u}^\tau c_{\lambda u}^\tau S_{\kappa\lambda} \equiv q_{Cl''}^\tau \end{aligned} \quad (\text{B.2})$$

yields the Mulliken population for the orbitals with quantum number l'' and spin τ at center C , whereas the sum

$$\begin{aligned} \sum_{uv} P_{uv}^{0,\tau} q_{Cl''}^{uv\tau} &= \frac{1}{2} \sum_{uv} P_{uv}^{0,\tau} \sum_{\kappa \in Cl''} \sum_{\lambda} S_{\kappa\lambda} (c_{\kappa u}^\tau c_{\lambda v}^\tau + c_{\kappa v}^\tau c_{\lambda u}^\tau) \\ &= \sum_{\kappa \in Cl''} n_{\kappa\tau}^0 \end{aligned} \quad (\text{B.3})$$

yields the population for the aforementioned orbitals corresponding to the reference system. For the latter sum, the identity, $\sum_{uv} c_{\kappa u}^\tau P_{uv}^{0,\tau} c_{\lambda v}^\tau = n_{\kappa\tau}^0 \delta_{\kappa\lambda}$, was additionally employed. Making use again of definition (3.38) for $q_{Al}^{st\sigma}$ in Eq. (B.1), leads to the following expression for the KS Hamiltonian:

$$H_{st\sigma} = \sum_{\mu\nu} c_{\mu s}^\sigma c_{\nu t}^\sigma H_{\mu\nu\sigma}, \quad (\text{B.4})$$

with

$$H_{\mu\nu\sigma} = H_{\mu\nu\sigma}^0 + \frac{1}{2} S_{\mu\nu} \sum_{\tau} \sum_{Cl''} (\Gamma_{Al,Cl''}^{\sigma\tau} + \Gamma_{Bl',Cl''}^{\sigma\tau}) \Delta q_{Cl''}^\tau. \quad (\text{B.5})$$

In Eq. (B.5), A and l (B and l'') denote, respectively, the center and angular quantum number of AO ϕ_μ (ϕ_ν), and the spin-dependent charge fluctuation, $\Delta q_{Cl''}^\tau = q_{Cl''}^\tau - \sum_{\kappa \in Cl''} n_{\kappa\tau}^0$.

By using Eq. (3.31), the Hamiltonian matrix elements, $H_{\mu\nu\sigma}$, can be finally expressed as

$$\begin{aligned} H_{\mu\nu\sigma} &= H_{\mu\nu\sigma}^0 + \frac{1}{2} S_{\mu\nu} \sum_{Cl''} (\gamma_{Al,Cl''} + \gamma_{Bl',Cl''}) \Delta q_{Cl''} \\ &\quad + \frac{1}{2} \delta_\sigma S_{\mu\nu} \sum_{l''} (W_{Al,l''} \Delta m_{Al''} + W_{Bl',l''} \Delta m_{Bl''}), \end{aligned} \quad (\text{B.6})$$

where $\Delta q_{Cl''} = \Delta q_{Cl''}^\uparrow + \Delta q_{Cl''}^\downarrow$ and $\Delta m_{Cl''} = \Delta q_{Cl''}^\uparrow - \Delta q_{Cl''}^\downarrow$ are the fluctuations of the l -resolved atomic charge and spin populations, respectively.

Appendix C

VERTICAL EXCITATION ENERGIES OF BENCHMARK MOLECULES

C.1 Singlet States

C.1.1 Relative displacement of ω_I with respect to ω_{KS}

We provide in the following tables the singlet-singlet vertical excitation energies (ω_I) for Thiel’s set, obtained with TD-PBE (TZP), traditional (old) and refined TD-DFTB (new). The theoretical best estimates (TBE) [225] as well as some experimental results¹ are additionally given for comparison. ω_{KS} denotes the KS orbital energy difference corresponding to the most dominant single particle transition in the many body wavefunction. The benchmark set has been divided into 4 groups as depicted in Fig. 4.3. All energies are expressed in eV.

| Molecule / Transition | TD-DFT | | | TD-DFTB | | | | | TBE | Exp. |
|--|------------|-------|---------------|-------------------------|--------------------|-------------------------|--------------------|---------------|------|------|
| | ω_I | f_I | ω_{KS} | ω_I^{new} | f_I^{new} | ω_I^{old} | f_I^{old} | ω_{KS} | | |
| Ethene | | | | | | | | | | |
| ¹ B _{1u} ($\pi \rightarrow \pi^*$) | 7.77 | 0.33 | 5.70 | 7.93 | 0.37 | 7.67 | 0.27 | 6.14 | 7.80 | 7.80 |
| Butadiene | | | | | | | | | | |
| ¹ B _u ($\pi \rightarrow \pi^*$) | 5.62 | 0.61 | 3.96 | 5.63 | 0.65 | 5.50 | 0.52 | 4.13 | 6.18 | 5.92 |
| ¹ A _g ($\pi \rightarrow \pi^*$) | 6.30 | 0.00 | 6.31 | 6.41 | 0.00 | 6.39 | 0.00 | 6.02 | 6.55 | |
| Hexatriene | | | | | | | | | | |
| ¹ A _g ($\pi \rightarrow \pi^*$) | 5.07 | 0.00 | 4.90 | 5.04 | 0.00 | 5.04 | 0.00 | 4.78 | 5.09 | 5.21 |
| ¹ B _u ($\pi \rightarrow \pi^*$) | 4.52 | 0.98 | 3.04 | 4.52 | 0.98 | 4.43 | 0.84 | 3.17 | 5.10 | 4.93 |

¹All experimental data employed along this Appendix were taken from the supporting information for Ref. [225] (See references therein).

| Molecule / Transition | TD-DFT | | | TD-DFTB | | | | | TBE | Exp. |
|-----------------------------------|------------|-------|---------------|-------------------------|--------------------|-------------------------|--------------------|---------------|------|------|
| | ω_I | f_I | ω_{KS} | ω_I^{new} | f_I^{new} | ω_I^{old} | f_I^{old} | ω_{KS} | | |
| Octatetraene | | | | | | | | | | |
| $^1A_g(\pi \rightarrow \pi^*)$ | 4.19 | 0.00 | 4.05 | 4.14 | 0.00 | 4.14 | 0.00 | 3.96 | 4.47 | 3.59 |
| $^1B_u(\pi \rightarrow \pi^*)$ | 3.83 | 1.37 | 2.50 | 3.82 | 1.31 | 3.76 | 1.17 | 2.60 | 4.66 | 4.41 |
| Cyclopropene | | | | | | | | | | |
| $^1B_1(\sigma \rightarrow \pi^*)$ | 6.29 | <0.01 | 6.12 | 6.52 | <0.01 | 6.44 | 0.00 | 6.44 | 6.76 | 6.45 |
| $^1B_2(\pi \rightarrow \pi^*)$ | 6.13 | 0.06 | 5.02 | 6.54 | 0.11 | 6.40 | 0.08 | 5.64 | 7.06 | 7.19 |
| Cyclopentadiene | | | | | | | | | | |
| $^1B_2(\pi \rightarrow \pi^*)$ | 4.94 | 0.09 | 3.82 | 4.91 | 0.13 | 4.78 | 0.09 | 4.01 | 5.55 | 5.30 |
| $^1A_1(\pi \rightarrow \pi^*)$ | 6.09 | 0.01 | 5.86 | 6.04 | 0.07 | 6.03 | 0.06 | 5.60 | 6.31 | 6.20 |
| Norbornadiene | | | | | | | | | | |
| $^1A_2(\pi \rightarrow \pi^*)$ | 4.48 | 0.00 | 3.98 | 5.26 | 0.00 | 5.22 | 0.00 | 4.91 | 5.34 | 5.23 |
| $^1B_2(\pi \rightarrow \pi^*)$ | 5.01 | 0.01 | 4.76 | 5.40 | 0.02 | 5.33 | 0.01 | 5.13 | 6.11 | 5.95 |

Table C.1: Singlet-singlet vertical excitation energies compared to energy difference of most dominant single particle transition for Group A.

| Molecule / Transition | TD-DFT | | | TD-DFTB | | | | | TBE | Exp. |
|-----------------------------------|------------|-------|---------------|-------------------------|--------------------|-------------------------|--------------------|---------------|------|------|
| | ω_I | f_I | ω_{KS} | ω_I^{new} | f_I^{new} | ω_I^{old} | f_I^{old} | ω_{KS} | | |
| Benzene | | | | | | | | | | |
| $^1B_{2u}(\pi \rightarrow \pi^*)$ | 5.25 | 0.00 | 5.15 | 5.30 | 0.00 | 5.30 | 0.00 | 5.30 | 5.08 | 4.90 |
| $^1B_{1u}(\pi \rightarrow \pi^*)$ | 6.03 | 0.00 | 5.15 | 5.83 | 0.00 | 5.67 | 0.00 | 5.30 | 6.54 | 6.20 |
| $^1E_{1u}(\pi \rightarrow \pi^*)$ | 6.99 | 1.12 | 5.15 | 6.95 | 1.33 | 6.79 | 0.87 | 5.30 | 7.13 | 6.94 |
| $^1E_{2g}(\pi \rightarrow \pi^*)$ | 8.29 | 0.00 | 7.88 | 7.93 | 0.00 | 7.89 | 0.00 | 7.60 | 8.41 | 7.80 |
| Naphthalene | | | | | | | | | | |
| $^1B_{3u}(\pi \rightarrow \pi^*)$ | 4.23 | <0.01 | 4.18 | 4.23 | 0.01 | 4.23 | 0.01 | 4.06 | 4.24 | 4.00 |
| $^1B_{2u}(\pi \rightarrow \pi^*)$ | 4.08 | 0.05 | 3.41 | 4.08 | 0.08 | 4.01 | 0.05 | 3.50 | 4.77 | 4.45 |
| $^1A_g(\pi \rightarrow \pi^*)$ | 5.86 | 0.00 | 5.73 | 5.89 | 0.00 | 5.87 | 0.00 | 5.84 | 5.87 | 5.52 |
| $^1B_{1g}(\pi \rightarrow \pi^*)$ | 5.04 | 0.00 | 4.99 | 5.12 | 0.00 | 5.11 | 0.00 | 4.91 | 5.99 | 5.22 |
| $^1B_{3u}(\pi \rightarrow \pi^*)$ | 5.75 | 1.16 | 4.15 | 5.72 | 1.23 | 5.63 | 0.91 | 4.43 | 6.06 | 5.63 |
| $^1B_{1g}(\pi \rightarrow \pi^*)$ | 6.20 | 0.00 | 5.08 | 6.19 | 0.00 | 6.06 | 0.00 | 5.54 | 6.47 | |
| $^1B_{2u}(\pi \rightarrow \pi^*)$ | 5.89 | 0.14 | 4.92 | 5.78 | 0.23 | 5.67 | 0.14 | 4.99 | 6.33 | 6.00 |
| $^1A_g(\pi \rightarrow \pi^*)$ | 6.21 | 0.00 | 6.07 | 6.00 | 0.00 | 5.99 | 0.00 | 5.76/6.10 | 6.67 | 6.05 |
| Furan | | | | | | | | | | |
| $^1B_2(\pi \rightarrow \pi^*)$ | 6.13 | 0.16 | 4.82 | 6.21 | 0.18 | 6.06 | 0.12 | 5.17 | 6.32 | 6.06 |
| $^1A_1(\pi \rightarrow \pi^*)$ | 6.39 | <0.01 | 6.06 | 6.53 | 0.01 | 6.49 | <0.01 | 6.15 | 6.57 | |
| $^1A_1(\pi \rightarrow \pi^*)$ | 8.19 | 0.39 | 6.26 | 8.26 | 0.59 | 8.04 | 0.37 | 6.61 | 8.13 | 7.82 |
| Pyrrole | | | | | | | | | | |
| $^1A_1(\pi \rightarrow \pi^*)$ | 6.28 | <0.01 | 5.86 | 6.48 | 0.01 | 6.44 | 0.01 | 6.05 | 6.37 | |
| $^1B_2(\pi \rightarrow \pi^*)$ | 6.37 | 0.17 | 5.09 | 6.54 | 0.17 | 6.39 | 0.11 | 5.49 | 6.57 | 5.98 |
| $^1A_1(\pi \rightarrow \pi^*)$ | 7.88 | 0.41 | 6.16 | 8.09 | 0.57 | 7.88 | 0.36 | 6.60 | 7.91 | 7.54 |

| Molecule / Transition | TD-DFT | | | TD-DFTB | | | | | TBE | Exp. |
|-----------------------------------|------------|-------|---------------|-------------------------|--------------------|-------------------------|--------------------|---------------|------|------|
| | ω_I | f_I | ω_{KS} | ω_I^{new} | f_I^{new} | ω_I^{old} | f_I^{old} | ω_{KS} | | |
| Imidazole | | | | | | | | | | |
| $^1A''(n \rightarrow \pi^*)$ | 5.73 | <0.01 | 5.73 | 6.30 | <0.01 | 6.21 | 0.00 | 6.21 | 6.81 | |
| $^1A'(\pi \rightarrow \pi^*)$ | 6.28 | 0.06 | 5.22 | 6.46 | 0.13 | 6.36 | 0.10 | 5.56 | 6.19 | 6.00 |
| $^1A'(\pi \rightarrow \pi^*)$ | 6.39 | 0.09 | 6.28 | 6.96 | 0.04 | 6.86 | 0.02 | 6.55 | 6.93 | 6.53 |
| Pyridine | | | | | | | | | | |
| $^1B_2(\pi \rightarrow \pi^*)$ | 5.36 | 0.03 | 4.85 | 5.38 | 0.03 | 5.37 | 0.02 | 5.02 | 4.85 | 4.99 |
| $^1B_1(n \rightarrow \pi^*)$ | 4.35 | <0.01 | 4.05 | 4.70 | <0.01 | 4.52 | 0.00 | 4.52 | 4.59 | 4.59 |
| $^1A_2(n \rightarrow \pi^*)$ | 4.44 | 0.00 | 4.41 | 4.84 | 0.00 | 4.81 | 0.00 | 4.81 | 5.11 | 5.43 |
| $^1A_1(\pi \rightarrow \pi^*)$ | 6.23 | 0.01 | 5.21 | 5.98 | 0.02 | 5.82 | 0.01 | 5.31 | 6.26 | 6.38 |
| $^1A_1(\pi \rightarrow \pi^*)$ | 6.54 | <0.01 | 6.49 | 7.20 | 0.63 | 7.02 | 0.41 | 5.59 | 7.18 | 7.22 |
| $^1B_2(\pi \rightarrow \pi^*)$ | 7.12 | 0.23 | 5.80 | 7.14 | 0.58 | 7.01 | 0.40 | 5.88 | 7.27 | |
| Pyrazine | | | | | | | | | | |
| $^1B_{3u}(n \rightarrow \pi^*)$ | 3.55 | <0.01 | 3.24 | 3.91 | <0.01 | 3.72 | 0.00 | 3.72 | 3.95 | 3.83 |
| $^1A_u(n \rightarrow \pi^*)$ | 4.02 | 0.00 | 4.00 | 4.37 | 0.00 | 4.34 | 0.00 | 4.34 | 4.81 | |
| $^1B_{2u}(\pi \rightarrow \pi^*)$ | 5.26 | 0.07 | 4.50 | 5.27 | 0.09 | 5.24 | 0.07 | 4.68 | 4.64 | 4.81 |
| $^1B_{2g}(n \rightarrow \pi^*)$ | 5.09 | 0.00 | 4.72 | 5.81 | 0.00 | 5.53 | 0.00 | 5.53 | 5.56 | 5.46 |
| $^1B_{1g}(n \rightarrow \pi^*)$ | 5.54 | 0.00 | 5.48 | 6.20 | 0.00 | 6.15 | 0.00 | 6.15 | 6.60 | 6.10 |
| $^1B_{1u}(\pi \rightarrow \pi^*)$ | 6.44 | 0.05 | 5.26 | 6.08 | 0.06 | 5.91 | 0.03 | 5.30 | 6.58 | 6.51 |
| $^1B_{2u}(\pi \rightarrow \pi^*)$ | 7.20 | 0.03 | 7.17 | 7.57 | 0.54 | 7.46 | 0.38 | 6.50 | 7.60 | 7.67 |
| $^1B_{1u}(\pi \rightarrow \pi^*)$ | 7.52 | 0.23 | 5.77 | 7.58 | 0.60 | 7.36 | 0.38 | 5.88 | 7.72 | 7.67 |
| Pyrimidine | | | | | | | | | | |
| $^1B_1(n \rightarrow \pi^*)$ | 3.77 | <0.01 | 3.58 | 4.37 | <0.01 | 4.23 | 0.00 | 4.23 | 4.55 | 4.16 |
| $^1A_2(n \rightarrow \pi^*)$ | 3.99 | 0.00 | 3.92 | 4.59 | 0.00 | 4.53 | 0.00 | 4.53 | 4.91 | 4.62 |
| $^1B_2(\pi \rightarrow \pi^*)$ | 5.59 | 0.03 | 5.05 | 5.59 | 0.03 | 5.58 | 0.03 | 5.21 | 5.44 | 5.12 |
| $^1A_1(\pi \rightarrow \pi^*)$ | 6.49 | 0.04 | 5.39 | 6.22 | 0.03 | 6.05 | 0.02 | 5.50 | 6.95 | 6.70 |
| Pyridazine | | | | | | | | | | |
| $^1B_1(n \rightarrow \pi^*)$ | 3.12 | <0.01 | 2.79 | 3.73 | <0.01 | 3.50 | 0.00 | 3.50 | 3.78 | 3.30 |
| $^1A_2(n \rightarrow \pi^*)$ | 3.50 | 0.00 | 3.38 | 4.24 | 0.00 | 4.14 | 0.00 | 4.14 | 4.32 | |
| $^1A_1(\pi \rightarrow \pi^*)$ | 5.46 | 0.02 | 4.92 | 5.37 | 0.03 | 5.36 | 0.02 | 4.96 | 5.18 | 4.90 |
| $^1A_2(n \rightarrow \pi^*)$ | 4.99 | 0.00 | 4.75 | 5.08 | 0.00 | 4.92 | 0.00 | 4.92 | 5.77 | 5.30 |
| Triazine | | | | | | | | | | |
| $^1A''_1(n \rightarrow \pi^*)$ | 3.81 | 0.00 | 3.80 | 4.61 | 0.00 | 4.59 | 0.00 | 4.59 | 4.60 | |
| $^1A''_2(n \rightarrow \pi^*)$ | 4.05 | 0.01 | 3.80 | 4.77 | 0.01 | 4.59 | 0.00 | 4.59 | 4.66 | 4.59 |
| $^1E''(n \rightarrow \pi^*)$ | 3.96 | 0.00 | 3.80 | 4.69 | 0.00 | 4.59 | 0.00 | 4.59 | 4.70 | 3.97 |
| $^1A'_2(\pi \rightarrow \pi^*)$ | 5.95 | 0.00 | 5.85 | 5.96 | 0.00 | 5.96 | 0.00 | 5.96 | 5.79 | 5.70 |
| Tetrazine | | | | | | | | | | |
| $^1B_{3u}(n \rightarrow \pi^*)$ | 1.82 | <0.01 | 1.52 | 2.58 | <0.01 | 2.37 | 0.00 | 2.37 | 2.29 | 2.25 |
| $^1A_u(n \rightarrow \pi^*)$ | 2.82 | 0.00 | 2.71 | 3.75 | 0.00 | 3.68 | 0.00 | 3.68 | 3.51 | 3.4 |
| $^1B_{1g}(n \rightarrow \pi^*)$ | 4.10 | 0.00 | 3.74 | 4.89 | 0.00 | 4.63 | 0.00 | 4.63 | 4.73 | |
| $^1B_{2u}(\pi \rightarrow \pi^*)$ | 5.47 | 0.05 | 4.61 | 5.28 | 0.08 | 5.24 | 0.06 | 4.55 | 4.93 | 5.00 |
| $^1B_{2g}(n \rightarrow \pi^*)$ | 4.77 | 0.00 | 4.60 | 5.25 | 0.00 | 5.08 | 0.00 | 5.08 | 5.20 | |
| $^1A_u(n \rightarrow \pi^*)$ | 4.58 | 0.00 | 4.31 | 4.57 | 0.00 | 4.41 | 0.00 | 4.41 | 5.50 | |

Table C.2: Singlet-singlet vertical excitation energies compared to energy difference of most dominant single particle transition for Group B.

| Molecule / Transition | TD-DFT | | | TD-DFTB | | | | | TBE | Exp. |
|-----------------------------------|------------|-------|---------------|-------------------------|--------------------|-------------------------|--------------------|---------------|------|------|
| | ω_I | f_I | ω_{KS} | ω_I^{new} | f_I^{new} | ω_I^{old} | f_I^{old} | ω_{KS} | | |
| Formaldehyde | | | | | | | | | | |
| $^1A_2(n \rightarrow \pi^*)$ | 3.77 | 0.00 | 3.50 | 4.49 | 0.00 | 4.25 | 0.00 | 4.25 | 3.88 | 3.79 |
| $^1B_1(\sigma \rightarrow \pi^*)$ | 8.78 | <0.01 | 8.19 | 8.69 | <0.01 | 8.34 | 0.00 | 8.34 | 9.10 | |
| $^1A_1(\pi \rightarrow \pi^*)$ | 8.88 | 0.02 | 8.78 | 9.79 | 0.30 | 9.37 | 0.22 | 7.53 | 9.30 | |
| Acetone | | | | | | | | | | |
| $^1A_2(n \rightarrow \pi^*)$ | 4.20 | 0.00 | 3.96 | 4.71 | 0.00 | 4.49 | 0.00 | 4.49 | 4.40 | 4.38 |
| $^1B_1(\sigma \rightarrow \pi^*)$ | 8.14 | <0.01 | 7.86 | 7.83 | 0.01 | 7.71 | 0.01 | 7.68 | 9.10 | |
| $^1A_1(\pi \rightarrow \pi^*)$ | 7.42 | <0.01 | 7.35 | 8.46 | 0.31 | 8.31 | 0.24 | 6.94 | 9.40 | |
| Benzoquinone | | | | | | | | | | |
| $^1A_u(n \rightarrow \pi^*)$ | 2.00 | 0.00 | 1.83 | 2.24 | 0.00 | 2.10 | 0.00 | 2.10 | 2.77 | 2.70 |
| $^1B_{1g}(n \rightarrow \pi^*)$ | 1.87 | 0.00 | 1.69 | 1.79 | 0.00 | 1.67 | 0.00 | 1.67 | 2.76 | 2.70 |
| $^1B_{3g}(\pi \rightarrow \pi^*)$ | 3.37 | 0.00 | 3.06 | 3.78 | 0.00 | 3.74 | 0.00 | 3.56 | 4.26 | 4.40 |
| $^1B_{1u}(\pi \rightarrow \pi^*)$ | 4.49 | 0.23 | 3.15 | 4.46 | 0.33 | 4.38 | 0.26 | 3.18 | 5.28 | 5.40 |
| $^1B_{3u}(n \rightarrow \pi^*)$ | 4.35 | <0.01 | 4.28 | 4.08 | <0.01 | 4.04 | 0.00 | 4.04 | 5.64 | |
| $^1B_{3g}(\pi \rightarrow \pi^*)$ | 6.12 | 0.00 | 5.74 | 5.87 | 0.00 | 5.82 | 0.00 | 5.55 | 6.96 | |
| $^1B_{1u}(\pi \rightarrow \pi^*)$ | 6.82 | 0.37 | 6.50 | 6.43 | 0.19 | 6.37 | 0.14 | 6.04 | 7.92 | 7.30 |
| Formamide | | | | | | | | | | |
| $^1A''(n \rightarrow \pi^*)$ | 5.44 | <0.01 | 5.22 | 5.73 | <0.01 | 5.51 | 0.00 | 5.51 | 5.63 | 5.50 |
| $^1A'(\pi \rightarrow \pi^*)$ | 6.21 | 0.02 | 6.10 | 8.43 | 0.40 | 8.21 | 0.30 | 6.61 | 7.39 | 7.40 |
| Acetamide | | | | | | | | | | |
| $^1A''(n \rightarrow \pi^*)$ | 5.39 | <0.01 | 5.18 | 5.73 | <0.01 | 5.51 | <0.01 | 5.51 | 5.69 | 5.44 |
| $^1A'(\pi \rightarrow \pi^*)$ | 5.75 | 0.03 | 5.71 | 8.23 | 0.32 | 8.03 | 0.24 | 6.55 | 7.27 | 7.40 |
| Propanamide | | | | | | | | | | |
| $^1A''(n \rightarrow \pi^*)$ | 5.41 | <0.01 | 5.21 | 5.70 | <0.01 | 5.49 | <0.01 | 5.48 | 5.72 | 5.44 |
| $^1A'(\pi \rightarrow \pi^*)$ | 5.82 | 0.02 | 5.77 | 8.41 | 0.23 | 8.00 | 0.17 | 6.57 | 7.20 | 7.40 |

Table C.3: Singlet-singlet vertical excitation energies compared to energy difference of most dominant single particle transition for Group C.

| Molecule / Transition | TD-DFT | | | TD-DFTB | | | | | TBE | Exp. |
|-------------------------------|------------|-------|---------------|-------------------------|--------------------|-------------------------|--------------------|---------------|------|------|
| | ω_I | f_I | ω_{KS} | ω_I^{new} | f_I^{new} | ω_I^{old} | f_I^{old} | ω_{KS} | | |
| Cytosine | | | | | | | | | | |
| $^1A'(\pi \rightarrow \pi^*)$ | 4.20 | 0.01 | 3.71 | 4.17 | 0.02 | 4.12 | 0.01 | 3.76 | 4.66 | 4.60 |
| $^1A''(n \rightarrow \pi^*)$ | 3.77 | <0.01 | 3.74 | 3.38 | <0.01 | 3.36 | 0.00 | 3.36 | 4.87 | 5.00 |
| $^1A''(n \rightarrow \pi^*)$ | 4.47 | <0.01 | 4.30 | 4.75 | <0.01 | 4.64 | 0.00 | 4.64 | 5.26 | |
| $^1A'(\pi \rightarrow \pi^*)$ | 4.91 | 0.06 | 4.22 | 5.23 | 0.08 | 5.18 | 0.07 | 4.61 | 5.62 | 5.60 |

| Molecule / Transition | TD-DFT | | | TD-DFTB | | | | | TBE | Exp. |
|-------------------------------|------------|-------|---------------|-------------------------|--------------------|-------------------------|--------------------|---------------|------|------|
| | ω_I | f_I | ω_{KS} | ω_I^{new} | f_I^{new} | ω_I^{old} | f_I^{old} | ω_{KS} | | |
| Thymine | | | | | | | | | | |
| $^1A''(n \rightarrow \pi^*)$ | 4.06 | <0.01 | 3.95 | 3.88 | <0.01 | 3.79 | <0.01 | 3.79 | 4.82 | |
| $^1A'(\pi \rightarrow \pi^*)$ | 4.59 | 0.07 | 3.83 | 4.83 | 0.09 | 4.79 | 0.08 | 4.10 | 5.20 | 4.80 |
| $^1A'(\pi \rightarrow \pi^*)$ | 5.32 | 0.06 | 4.77 | 5.25 | 0.12 | 5.19 | 0.09 | 4.76 | 6.27 | 5.70 |
| $^1A''(n \rightarrow \pi^*)$ | 4.77 | <0.01 | 4.72 | 4.32 | <0.01 | 4.30 | <0.01 | 4.30 | 6.16 | |
| $^1A'(\pi \rightarrow \pi^*)$ | 5.83 | 0.08 | 5.11 | 6.28 | 0.14 | 6.22 | 0.10 | 5.69 | 6.53 | 6.20 |
| Uracil | | | | | | | | | | |
| $^1A''(n \rightarrow \pi^*)$ | 3.95 | <0.01 | 3.85 | 3.78 | <0.01 | 3.70 | 0.00 | 3.70 | 4.80 | 4.38 |
| $^1A'(\pi \rightarrow \pi^*)$ | 4.76 | 0.06 | 4.01 | 4.88 | 0.03 | 4.85 | 0.02 | 4.66 | 5.35 | 5.10 |
| $^1A'(\pi \rightarrow \pi^*)$ | 5.20 | 0.04 | 4.71 | 5.21 | 0.14 | 5.15 | 0.11 | 4.26 | 6.26 | 6.00 |
| $^1A''(n \rightarrow \pi^*)$ | 4.74 | <0.01 | 4.69 | 4.26 | <0.01 | 4.24 | 0.00 | 4.24 | 6.10 | |
| $^1A'(\pi \rightarrow \pi^*)$ | 5.87 | 0.01 | 5.87 | 6.56 | 0.13 | 6.49 | 0.09 | 5.94 | 6.70 | 6.60 |
| $^1A''(n \rightarrow \pi^*)$ | 5.22 | <0.01 | 5.13 | 5.46 | <0.01 | 5.38 | 0.00 | 5.38 | 6.56 | |
| Adenine | | | | | | | | | | |
| $^1A''(n \rightarrow \pi^*)$ | 4.28 | <0.01 | 4.21 | 4.64 | <0.01 | 4.59 | 0.00 | 4.59 | 5.12 | 5.40 |
| $^1A'(\pi \rightarrow \pi^*)$ | 4.57 | 0.12 | 3.86 | 4.83 | 0.22 | 4.77 | 0.18 | 4.11 | 5.25 | 4.63 |
| $^1A'(\pi \rightarrow \pi^*)$ | 5.00 | 0.05 | 4.55 | 5.11 | 0.03 | 5.09 | 0.02 | 4.85 | 5.25 | 4.92 |
| $^1A''(n \rightarrow \pi^*)$ | 5.03 | <0.01 | 4.90 | 5.42 | <0.01 | 5.33 | 0.00 | 5.33 | 5.75 | |

Table C.4: Singlet-singlet vertical excitation energies compared to energy difference of most dominant single particle transition for Group D.

C.1.2 Vertical excitation energies and oscillator strengths

In this section we provide the singlet-singlet vertical excitation energies (ω_I) and oscillator strengths (f_I) for the chosen benchmark set, obtained with traditional (old) and refined TD-DFTB (new). As reference values, we additionally report TD-DFT results using three different exchange-correlation functionals, PBE (TZP), PBE0(TZP) and CAM-B3LYP(6-311G**). Results obtained with TD-DFT (CAM-B3LYP/6-311G**) in the Tamm-Damcoff approximation (TDA) are also given, along with the TBEs and some experimental results. The benchmark set has been divided into 4 groups as depicted in Fig. 4.3. All energies are expressed in eV.

| Molecule / Trans. | TD-DFTB | | | | PBE | | PBE0 | | CAM-B3LYP | | TDA | | TBE | Exp. |
|--|-------------------------|--------------------|-------------------------|--------------------|------------|-------|------------|-------|------------|-------|------------|-------|------|------|
| | ω_I^{new} | f_I^{new} | ω_I^{old} | f_I^{old} | ω_I | f_I | ω_I | f_I | ω_I | f_I | ω_I | f_I | | |
| Ethene | | | | | | | | | | | | | | |
| ${}^1\text{B}_{1u}(\pi \rightarrow \pi^*)$ | 7.93 | 0.37 | 7.67 | 0.27 | 7.77 | 0.33 | 7.79 | 0.37 | 7.97 | 0.38 | 8.61 | 0.59 | 7.80 | 7.80 |
| Butadiene | | | | | | | | | | | | | | |
| ${}^1\text{B}_u(\pi \rightarrow \pi^*)$ | 5.63 | 0.65 | 5.50 | 0.52 | 5.62 | 0.61 | 5.83 | 0.69 | 6.03 | 0.70 | 6.52 | 1.05 | 6.18 | 5.92 |
| ${}^1\text{A}_g(\pi \rightarrow \pi^*)$ | 6.41 | 0.00 | 6.39 | 0.00 | 6.30 | 0.00 | 7.03 | 0.00 | 7.71 | 0.00 | 7.73 | 0.00 | 6.55 | |
| Hexatriene | | | | | | | | | | | | | | |
| ${}^1\text{A}_g(\pi \rightarrow \pi^*)$ | 5.04 | 0.00 | 5.04 | 0.00 | 5.07 | 0.00 | 5.90 | 0.00 | 6.64 | 0.00 | 6.67 | 0.00 | 5.09 | 5.21 |
| ${}^1\text{B}_u(\pi \rightarrow \pi^*)$ | 4.52 | 0.98 | 4.43 | 0.84 | 4.52 | 0.98 | 4.77 | 1.09 | 4.97 | 1.11 | 5.39 | 1.63 | 5.10 | 4.93 |
| Octatetraene | | | | | | | | | | | | | | |
| ${}^1\text{A}_g(\pi \rightarrow \pi^*)$ | 4.14 | 0.00 | 4.14 | 0.00 | 4.19 | 0.00 | 5.04 | 0.00 | 5.83 | 0.00 | 5.86 | 0.00 | 4.47 | 3.59 |
| ${}^1\text{B}_u(\pi \rightarrow \pi^*)$ | 3.82 | 1.31 | 3.76 | 1.17 | 3.83 | 1.37 | 4.09 | 1.50 | 4.31 | 1.53 | 4.67 | 2.23 | 4.66 | 4.41 |
| Cyclopropene | | | | | | | | | | | | | | |
| ${}^1\text{B}_1(\sigma \rightarrow \pi^*)$ | 6.52 | <0.01 | 6.44 | 0.00 | 6.29 | <0.01 | 6.55 | <0.01 | 6.66 | <0.01 | 6.69 | <0.01 | 6.76 | 6.45 |
| ${}^1\text{B}_2(\pi \rightarrow \pi^*)$ | 6.54 | 0.11 | 6.40 | 0.08 | 6.13 | 0.06 | 6.40 | 0.08 | 6.62 | 0.08 | 6.98 | 0.11 | 7.06 | 7.19 |
| Cyclopentadiene | | | | | | | | | | | | | | |
| ${}^1\text{B}_2(\pi \rightarrow \pi^*)$ | 4.91 | 0.13 | 4.78 | 0.09 | 4.94 | 0.09 | 5.11 | 0.09 | 5.22 | 0.09 | 5.62 | 0.14 | 5.55 | 5.30 |
| ${}^1\text{A}_1(\pi \rightarrow \pi^*)$ | 6.04 | 0.07 | 6.03 | 0.06 | 6.09 | 0.01 | 6.69 | 0.01 | 7.07 | 0.02 | 7.09 | 0.02 | 6.31 | 6.20 |
| Norbornadiene | | | | | | | | | | | | | | |
| ${}^1\text{A}_2(\pi \rightarrow \pi^*)$ | 5.26 | 0.00 | 5.22 | 0.00 | 4.48 | 0.00 | 4.91 | 0.00 | 5.21 | 0.00 | 5.41 | 0.00 | 5.34 | 5.23 |
| ${}^1\text{B}_2(\pi \rightarrow \pi^*)$ | 5.40 | 0.02 | 5.33 | 0.01 | 5.01 | 0.01 | 5.66 | 0.01 | 6.11 | 0.03 | 6.17 | 0.02 | 6.11 | 5.95 |
| MSD | | | | | | | | | | | | | | |
| (PBE) | 0.15 | | 0.07 | | | | | | | | | | | |
| (TBE) | -0.37 | | -0.45 | | -0.52 | | -0.09 | | 0.26 | | 0.49 | | | |
| (Exp.) | -0.20 | | -0.26 | | -0.35 | | 0.05 | | 0.34 | | 0.63 | | | |
| RMS | | | | | | | | | | | | | | |
| (PBE) | 0.28 | | 0.25 | | | | | | | | | | | |
| (TBE) | 0.47 | | 0.53 | | 0.62 | | 0.48 | | 0.72 | | 0.75 | | | |
| (Exp.) | 0.39 | | 0.46 | | 0.56 | | 0.56 | | 0.80 | | 0.90 | | | |

Table C.5: Singlet-singlet vertical excitation energies and oscillator strengths for Group A.

| Molecule / Trans. | TD-DFTB | | | | PBE | | PBE0 | | CAM-B3LYP | | TDA | | TBE | Exp. |
|--|-------------------------|--------------------|-------------------------|--------------------|------------|-------|------------|-------|------------|-------|------------|-------|------|------|
| | ω_I^{new} | f_I^{new} | ω_I^{old} | f_I^{old} | ω_I | f_I | ω_I | f_I | ω_I | f_I | ω_I | f_I | | |
| Benzene | | | | | | | | | | | | | | |
| ${}^1\text{B}_{2u}(\pi \rightarrow \pi^*)$ | 5.30 | 0.00 | 5.30 | 0.00 | 5.25 | 0.00 | 5.49 | 0.00 | 5.54 | 0.00 | 5.59 | 0.00 | 5.08 | 4.90 |
| ${}^1\text{B}_{1u}(\pi \rightarrow \pi^*)$ | 5.83 | 0.00 | 5.67 | 0.00 | 6.03 | 0.00 | 6.20 | 0.00 | 6.28 | 0.00 | 6.52 | 0.00 | 6.54 | 6.20 |
| ${}^1\text{E}_{1u}(\pi \rightarrow \pi^*)$ | 6.95 | 1.33 | 6.79 | 0.87 | 6.99 | 1.12 | 7.16 | 1.22 | 7.29 | 1.20 | 7.93 | 1.96 | 7.13 | 6.94 |
| ${}^1\text{E}_{2g}(\pi \rightarrow \pi^*)$ | 7.93 | 0.00 | 7.89 | 0.00 | 8.29 | 0.00 | 9.13 | 0.00 | 9.60 | 0.00 | 9.73 | 0.00 | 8.41 | 7.80 |

| Molecule / Trans. | TD-DFTB | | | | PBE | | PBE0 | | CAM-B3LYP | | TDA | | TBE | Exp. |
|-----------------------------------|-------------------------|--------------------|-------------------------|--------------------|------------|-------|------------|-------|------------|-------|------------|-------|------|------|
| | ω_I^{new} | f_I^{new} | ω_I^{old} | f_I^{old} | ω_I | f_I | ω_I | f_I | ω_I | f_I | ω_I | f_I | | |
| Naphthalene | | | | | | | | | | | | | | |
| $^1B_{3u}(\pi \rightarrow \pi^*)$ | 4.23 | 0.01 | 4.23 | 0.01 | 4.23 | <0.01 | 4.52 | <0.01 | 4.61 | <0.01 | 4.67 | <0.01 | 4.24 | 4.00 |
| $^1B_{2u}(\pi \rightarrow \pi^*)$ | 4.08 | 0.08 | 4.01 | 0.05 | 4.08 | 0.05 | 4.45 | 0.07 | 4.66 | 0.08 | 4.90 | 0.09 | 4.77 | 4.45 |
| $^1A_g(\pi \rightarrow \pi^*)$ | 5.89 | 0.00 | 5.87 | 0.00 | 5.86 | 0.00 | 6.32 | 0.00 | 6.55 | 0.00 | 6.58 | 0.00 | 5.87 | 5.52 |
| $^1B_{1g}(\pi \rightarrow \pi^*)$ | 5.12 | 0.00 | 5.11 | 0.00 | 5.04 | 0.00 | 5.77 | 0.00 | 6.40 | 0.00 | 6.43 | 0.00 | 5.99 | 5.22 |
| $^1B_{3u}(\pi \rightarrow \pi^*)$ | 5.72 | 1.23 | 5.63 | 0.91 | 5.75 | 1.16 | 6.02 | 1.29 | 6.17 | 1.30 | 6.69 | 2.05 | 6.06 | 5.63 |
| $^1B_{1g}(\pi \rightarrow \pi^*)$ | 6.19 | 0.00 | 6.06 | 0.00 | 6.20 | 0.00 | 6.43 | 0.00 | 6.60 | 0.00 | 6.92 | 0.00 | 6.47 | |
| $^1B_{2u}(\pi \rightarrow \pi^*)$ | 5.78 | 0.23 | 5.67 | 0.14 | 5.89 | 0.14 | 6.23 | 0.20 | 6.41 | 0.25 | 6.80 | 0.36 | 6.33 | 6.00 |
| $^1A_g(\pi \rightarrow \pi^*)$ | 6.00 | 0.00 | 5.99 | 0.00 | 6.21 | 0.00 | 7.07 | 0.00 | 7.72 | 0.00 | 7.88 | 0.00 | 6.67 | 6.05 |
| Furan | | | | | | | | | | | | | | |
| $^1B_2(\pi \rightarrow \pi^*)$ | 6.21 | 0.18 | 6.06 | 0.12 | 6.13 | 0.16 | 6.25 | 0.16 | 6.37 | 0.15 | 6.78 | 0.22 | 6.32 | 6.06 |
| $^1A_1(\pi \rightarrow \pi^*)$ | 6.53 | 0.01 | 6.49 | <0.01 | 6.39 | <0.01 | 6.86 | <0.01 | 7.11 | <0.01 | 7.19 | <0.01 | 6.57 | |
| $^1A_1(\pi \rightarrow \pi^*)$ | 8.26 | 0.59 | 8.04 | 0.37 | 8.19 | 0.39 | 8.37 | 0.45 | 8.54 | 0.45 | 9.18 | 0.66 | 8.13 | 7.82 |
| Pyrrole | | | | | | | | | | | | | | |
| $^1A_1(\pi \rightarrow \pi^*)$ | 6.48 | 0.01 | 6.44 | 0.01 | 6.28 | <0.01 | 6.68 | <0.01 | 6.90 | <0.01 | 6.99 | <0.01 | 6.37 | |
| $^1B_2(\pi \rightarrow \pi^*)$ | 6.54 | 0.17 | 6.39 | 0.11 | 6.37 | 0.17 | 6.51 | 0.18 | 6.63 | 0.16 | 7.01 | 0.21 | 6.57 | 5.98 |
| $^1A_1(\pi \rightarrow \pi^*)$ | 8.09 | 0.57 | 7.88 | 0.36 | 7.88 | 0.41 | 8.07 | 0.46 | 8.28 | 0.46 | 8.88 | 0.70 | 7.91 | 7.54 |
| Imidazole | | | | | | | | | | | | | | |
| $^1A''(n \rightarrow \pi^*)$ | 6.30 | <0.01 | 6.21 | 0.00 | 5.73 | <0.01 | 6.32 | <0.01 | 6.54 | <0.01 | 6.55 | <0.01 | 6.81 | |
| $^1A'(\pi \rightarrow \pi^*)$ | 6.46 | 0.13 | 6.36 | 0.10 | 6.28 | 0.06 | 6.57 | 0.15 | 6.72 | 0.15 | 7.03 | 0.18 | 6.19 | 6.00 |
| $^1A'(\pi \rightarrow \pi^*)$ | 6.96 | 0.04 | 6.86 | 0.02 | 6.39 | 0.09 | 7.18 | 0.03 | 7.33 | 0.02 | 7.50 | 0.05 | 6.93 | 6.53 |
| Pyridine | | | | | | | | | | | | | | |
| $^1B_2(\pi \rightarrow \pi^*)$ | 5.38 | 0.03 | 5.37 | 0.02 | 5.36 | 0.03 | 5.58 | 0.04 | 5.61 | 0.04 | 5.71 | 0.03 | 4.85 | 4.99 |
| $^1B_1(n \rightarrow \pi^*)$ | 4.70 | <0.01 | 4.52 | 0.00 | 4.35 | <0.01 | 4.87 | <0.01 | 5.07 | <0.01 | 5.13 | <0.01 | 4.59 | 4.59 |
| $^1A_2(n \rightarrow \pi^*)$ | 4.84 | 0.00 | 4.81 | 0.00 | 4.44 | 0.00 | 5.23 | 0.00 | 5.48 | 0.00 | 5.49 | 0.00 | 5.11 | 5.43 |
| $^1A_1(\pi \rightarrow \pi^*)$ | 5.98 | 0.02 | 5.82 | 0.01 | 6.23 | 0.01 | 6.41 | 0.02 | 6.48 | 0.02 | 6.74 | 0.02 | 6.26 | 6.38 |
| $^1A_1(\pi \rightarrow \pi^*)$ | 7.20 | 0.63 | 7.02 | 0.41 | 6.54 | <0.01 | 7.43 | 0.48 | 7.55 | 0.49 | 8.11 | 0.48 | 7.18 | 7.22 |
| $^1B_2(\pi \rightarrow \pi^*)$ | 7.14 | 0.58 | 7.01 | 0.40 | 7.12 | 0.23 | 7.40 | 0.47 | 7.52 | 0.48 | 8.07 | 0.78 | 7.27 | |
| Pyrazine | | | | | | | | | | | | | | |
| $^1B_{3u}(n \rightarrow \pi^*)$ | 3.91 | <0.01 | 3.72 | 0.00 | 3.55 | <0.01 | 4.00 | 0.01 | 4.19 | <0.01 | 4.26 | <0.01 | 3.95 | 3.83 |
| $^1A_u(n \rightarrow \pi^*)$ | 4.37 | 0.00 | 4.34 | 0.00 | 4.02 | 0.00 | 4.78 | 0.00 | 5.03 | 0.00 | 5.04 | 0.00 | 4.81 | |
| $^1B_{2u}(\pi \rightarrow \pi^*)$ | 5.27 | 0.09 | 5.24 | 0.07 | 5.26 | 0.07 | 5.44 | 0.10 | 5.46 | 0.09 | 5.63 | 0.11 | 4.64 | 4.81 |
| $^1B_{2g}(n \rightarrow \pi^*)$ | 5.81 | 0.00 | 5.53 | 0.00 | 5.09 | 0.00 | 5.66 | 0.00 | 5.82 | 0.00 | 5.91 | 0.00 | 5.56 | 5.46 |
| $^1B_{1g}(n \rightarrow \pi^*)$ | 6.20 | 0.00 | 6.15 | 0.00 | 5.54 | 0.00 | 6.58 | 0.00 | 6.88 | 0.00 | 6.89 | 0.00 | 6.60 | 6.10 |
| $^1B_{1u}(\pi \rightarrow \pi^*)$ | 6.08 | 0.06 | 5.91 | 0.03 | 6.44 | 0.05 | 6.60 | 0.06 | 6.65 | 0.07 | 6.95 | 0.08 | 6.58 | 6.51 |
| $^1B_{2u}(\pi \rightarrow \pi^*)$ | 7.57 | 0.54 | 7.46 | 0.38 | 7.20 | 0.03 | 7.91 | 0.30 | 8.00 | 0.35 | 8.45 | 0.50 | 7.60 | 7.67 |
| $^1B_{1u}(\pi \rightarrow \pi^*)$ | 7.58 | 0.60 | 7.36 | 0.38 | 7.52 | 0.23 | 7.79 | 0.38 | 7.90 | 0.36 | 8.54 | 0.55 | 7.72 | 7.67 |
| Pyrimidine | | | | | | | | | | | | | | |
| $^1B_1(n \rightarrow \pi^*)$ | 4.37 | <0.01 | 4.23 | 0.00 | 3.77 | <0.01 | 4.34 | 0.01 | 4.55 | <0.01 | 4.60 | <0.01 | 4.55 | 4.16 |
| $^1A_2(n \rightarrow \pi^*)$ | 4.59 | 0.00 | 4.53 | 0.00 | 3.99 | 0.00 | 4.70 | 0.00 | 4.91 | 0.00 | 4.94 | 0.00 | 4.91 | 4.62 |
| $^1B_2(\pi \rightarrow \pi^*)$ | 5.59 | 0.03 | 5.58 | 0.03 | 5.59 | 0.03 | 5.83 | 0.04 | 5.85 | 0.03 | 5.95 | 0.03 | 5.44 | 5.12 |
| $^1A_1(\pi \rightarrow \pi^*)$ | 6.22 | 0.03 | 6.05 | 0.02 | 6.49 | 0.04 | 6.69 | 0.04 | 6.76 | 0.04 | 7.05 | 0.05 | 6.95 | 6.70 |
| Pyridazine | | | | | | | | | | | | | | |
| $^1B_1(n \rightarrow \pi^*)$ | 3.73 | <0.01 | 3.50 | 0.00 | 3.12 | <0.01 | 3.66 | 0.01 | 3.82 | <0.01 | 3.91 | <0.01 | 3.78 | 3.30 |
| $^1A_2(n \rightarrow \pi^*)$ | 4.24 | 0.00 | 4.14 | 0.00 | 3.50 | 0.00 | 4.30 | 0.00 | 4.55 | 0.00 | 4.58 | 0.00 | 4.32 | |
| $^1A_1(\pi \rightarrow \pi^*)$ | 5.37 | 0.03 | 5.36 | 0.02 | 5.46 | 0.02 | 5.70 | 0.02 | 5.71 | 0.02 | 5.81 | 0.02 | 5.18 | 4.90 |
| $^1A_2(n \rightarrow \pi^*)$ | 5.08 | 0.00 | 4.92 | 0.00 | 4.99 | 0.00 | 5.53 | 0.00 | 5.74 | 0.00 | 5.78 | 0.00 | 5.77 | 5.30 |
| Triazine | | | | | | | | | | | | | | |
| $^1A''_1(n \rightarrow \pi^*)$ | 4.61 | 0.00 | 4.59 | 0.00 | 3.81 | 0.00 | 4.56 | 0.00 | 4.75 | 0.00 | 4.77 | 0.00 | 4.60 | |
| $^1A''_2(n \rightarrow \pi^*)$ | 4.77 | 0.01 | 4.59 | 0.00 | 4.05 | 0.01 | 4.63 | 0.02 | 4.85 | 0.02 | 4.90 | 0.02 | 4.66 | 4.59 |
| $^1E''(n \rightarrow \pi^*)$ | 4.69 | 0.00 | 4.59 | 0.00 | 3.96 | 0.00 | 4.63 | 0.00 | 4.84 | 0.00 | 4.87 | 0.00 | 4.70 | 3.97 |
| $^1A'_2(\pi \rightarrow \pi^*)$ | 5.96 | 0.00 | 5.96 | 0.00 | 5.95 | 0.00 | 6.24 | 0.00 | 6.25 | 0.00 | 6.30 | 0.00 | 5.79 | 5.70 |

| Molecule / Trans. | TD-DFTB | | | | PBE | | PBE0 | | CAM-B3LYP | | TDA | | TBE | Exp. |
|-----------------------------------|-------------------------|--------------------|-------------------------|--------------------|------------|-------|------------|-------|------------|-------|------------|-------|------|------|
| | ω_I^{new} | f_I^{new} | ω_I^{old} | f_I^{old} | ω_I | f_I | ω_I | f_I | ω_I | f_I | ω_I | f_I | | |
| Tetrazine | | | | | | | | | | | | | | |
| $^1B_{3u}(n \rightarrow \pi^*)$ | 2.58 | <0.01 | 2.37 | 0.00 | 1.82 | <0.01 | 2.28 | 0.01 | 2.44 | <0.01 | 2.54 | <0.01 | 2.29 | 2.25 |
| $^1A_u(n \rightarrow \pi^*)$ | 3.75 | 0.00 | 3.68 | 0.00 | 2.82 | 0.00 | 3.61 | 0.00 | 3.86 | 0.00 | 3.90 | 0.00 | 3.51 | 3.4 |
| $^1B_{1g}(n \rightarrow \pi^*)$ | 4.89 | 0.00 | 4.63 | 0.00 | 4.10 | 0.00 | 4.86 | 0.00 | 5.01 | 0.00 | 5.12 | 0.00 | 4.73 | |
| $^1B_{2u}(\pi \rightarrow \pi^*)$ | 5.28 | 0.08 | 5.24 | 0.06 | 5.47 | 0.05 | 5.66 | 0.07 | 5.63 | 0.06 | 5.83 | 0.07 | 4.93 | 5.00 |
| $^1B_{2g}(n \rightarrow \pi^*)$ | 5.25 | 0.00 | 5.08 | 0.00 | 4.77 | 0.00 | 5.40 | 0.00 | 5.57 | 0.00 | 5.62 | 0.00 | 5.20 | |
| $^1A_u(n \rightarrow \pi^*)$ | 4.57 | 0.00 | 4.41 | 0.00 | 4.58 | 0.00 | 5.13 | 0.00 | 5.32 | 0.00 | 5.38 | 0.00 | 5.50 | |
| MSD | | | | | | | | | | | | | | |
| (PBE) | 0.23 | | 0.12 | | | | | | | | | | | |
| (TBE) | 0.12 | | -0.23 | | -0.35 | | 0.12 | | 0.28 | | 0.48 | | | |
| (Exp.) | 0.13 | | 0.02 | | -0.06 | | 0.38 | | 0.44 | | 0.76 | | | |
| RMS | | | | | | | | | | | | | | |
| (PBE) | 0.41 | | 0.36 | | | | | | | | | | | |
| (TBE) | 0.37 | | 0.43 | | 0.54 | | 0.31 | | 0.41 | | 0.59 | | | |
| (Exp.) | 0.35 | | 0.34 | | 0.39 | | 0.49 | | 0.59 | | 0.85 | | | |

Table C.6: Singlet-singlet vertical excitation energies and oscillator strengths for Group B.

| Molecule / Trans. | TD-DFTB | | | | PBE | | PBE0 | | CAM-B3LYP | | TDA | | TBE | Exp. |
|-----------------------------------|-------------------------|--------------------|-------------------------|--------------------|------------|-------|------------|-------|------------|-------|------------|-------|------|------|
| | ω_I^{new} | f_I^{new} | ω_I^{old} | f_I^{old} | ω_I | f_I | ω_I | f_I | ω_I | f_I | ω_I | f_I | | |
| Formaldehyde | | | | | | | | | | | | | | |
| $^1A_2(n \rightarrow \pi^*)$ | 4.49 | 0.00 | 4.25 | 0.00 | 3.77 | 0.00 | 3.87 | 0.00 | 3.88 | 0.00 | 3.91 | 0.00 | 3.88 | 3.79 |
| $^1B_1(\sigma \rightarrow \pi^*)$ | 8.69 | <0.01 | 8.34 | 0.00 | 8.78 | <0.01 | 8.96 | <0.01 | 9.01 | <0.01 | 9.10 | <0.01 | 9.10 | |
| $^1A_1(\pi \rightarrow \pi^*)$ | 9.79 | 0.30 | 9.37 | 0.22 | 8.88 | 0.02 | 9.35 | 0.03 | 9.37 | <0.01 | 9.57 | <0.01 | 9.30 | |
| Acetone | | | | | | | | | | | | | | |
| $^1A_2(n \rightarrow \pi^*)$ | 4.71 | 0.00 | 4.49 | 0.00 | 4.20 | 0.00 | 4.36 | 0.00 | 4.38 | 0.00 | 4.41 | 0.00 | 4.40 | 4.38 |
| $^1B_1(\sigma \rightarrow \pi^*)$ | 7.83 | 0.01 | 7.71 | 0.01 | 8.14 | <0.01 | 8.69 | <0.01 | 8.87 | <0.01 | 8.93 | <0.01 | 9.10 | |
| $^1A_1(\pi \rightarrow \pi^*)$ | 8.46 | 0.31 | 8.31 | 0.24 | 7.42 | <0.01 | 8.51 | 0.03 | 8.80 | 0.06 | 8.91 | 0.03 | 9.40 | |
| Benzoquinone | | | | | | | | | | | | | | |
| $^1A_u(n \rightarrow \pi^*)$ | 2.24 | 0.00 | 2.10 | 0.00 | 2.00 | 0.00 | 2.65 | 0.00 | 2.97 | 0.00 | 3.00 | 0.00 | 2.77 | 2.70 |
| $^1B_{1g}(n \rightarrow \pi^*)$ | 1.79 | 0.00 | 1.67 | 0.00 | 1.87 | 0.00 | 2.48 | 0.00 | 2.80 | 0.00 | 2.84 | 0.00 | 2.76 | 2.70 |
| $^1B_{3g}(\pi \rightarrow \pi^*)$ | 3.78 | 0.00 | 3.74 | 0.00 | 3.37 | 0.00 | 3.84 | 0.00 | 4.15 | 0.00 | 4.29 | 0.00 | 4.26 | 4.40 |
| $^1B_{1u}(\pi \rightarrow \pi^*)$ | 4.46 | 0.33 | 4.38 | 0.26 | 4.49 | 0.23 | 4.93 | 0.35 | 5.24 | 0.41 | 5.60 | 0.49 | 5.28 | 5.40 |
| $^1B_{3u}(n \rightarrow \pi^*)$ | 4.08 | <0.01 | 4.04 | 0.00 | 4.35 | <0.01 | 5.62 | <0.01 | 6.19 | <0.01 | 6.21 | <0.01 | 5.64 | |
| $^1B_{3g}(\pi \rightarrow \pi^*)$ | 5.87 | 0.00 | 5.82 | 0.00 | 6.12 | 0.00 | 6.77 | 0.00 | 7.10 | 0.00 | 7.23 | 0.00 | 6.96 | |
| $^1B_{1u}(\pi \rightarrow \pi^*)$ | 6.43 | 0.19 | 6.37 | 0.14 | 6.82 | 0.37 | 7.40 | 0.57 | 7.72 | 0.54 | 8.23 | 1.03 | 7.92 | 7.30 |
| Formamide | | | | | | | | | | | | | | |
| $^1A''(n \rightarrow \pi^*)$ | 5.73 | <0.01 | 5.51 | 0.00 | 5.44 | <0.01 | 5.59 | <0.01 | 5.61 | <0.01 | 5.64 | <0.01 | 5.63 | 5.50 |
| $^1A'(\pi \rightarrow \pi^*)$ | 8.43 | 0.40 | 8.21 | 0.30 | 6.21 | 0.02 | 7.28 | <0.01 | 7.56 | <0.01 | 7.65 | <0.01 | 7.39 | 7.40 |
| Acetamide | | | | | | | | | | | | | | |
| $^1A''(n \rightarrow \pi^*)$ | 5.73 | <0.01 | 5.51 | <0.01 | 5.39 | <0.01 | 5.62 | <0.01 | 5.66 | <0.01 | 5.68 | <0.01 | 5.69 | 5.44 |
| $^1A'(\pi \rightarrow \pi^*)$ | 8.23 | 0.32 | 8.03 | 0.24 | 5.75 | 0.03 | 7.02 | 0.02 | 7.45 | 0.03 | 7.46 | 0.03 | 7.27 | 7.40 |
| Propanamide | | | | | | | | | | | | | | |
| $^1A''(n \rightarrow \pi^*)$ | 5.70 | <0.01 | 5.49 | <0.01 | 5.41 | <0.01 | 5.65 | <0.01 | 5.71 | <0.01 | 5.73 | <0.01 | 5.72 | 5.44 |
| $^1A'(\pi \rightarrow \pi^*)$ | 8.41 | 0.23 | 8.00 | 0.17 | 5.82 | 0.02 | 7.07 | 0.02 | 7.51 | 0.02 | 7.54 | 0.02 | 7.20 | 7.40 |
| MSD | | | | | | | | | | | | | | |
| (PBE) | 0.56 | | 0.37 | | | | | | | | | | | |
| (TBE) | -0.25 | | -0.44 | | -0.81 | | -0.21 | | 0.02 | | 0.12 | | | |
| (Exp.) | 0.07 | | -0.08 | | -0.67 | | -0.11 | | 0.07 | | 0.21 | | | |
| RMS | | | | | | | | | | | | | | |
| (PBE) | 1.06 | | 0.93 | | | | | | | | | | | |
| (TBE) | 0.88 | | 0.88 | | 0.96 | | 0.31 | | 0.23 | | 0.25 | | | |
| (Exp.) | 0.70 | | 0.64 | | 0.88 | | 0.27 | | 0.17 | | 0.31 | | | |

Table C.7: Singlet-singlet vertical excitation energies and oscillator strengths for Group C.

| Molecule / Trans. | TD-DFTB | | | | PBE | | PBE0 | | CAM-B3LYP | | TDA | | TBE | Exp. |
|------------------------------------|-------------------------|--------------------|-------------------------|--------------------|------------|-------|------------|-------|------------|-------|------------|-------|------|------|
| | ω_I^{new} | f_I^{new} | ω_I^{old} | f_I^{old} | ω_I | f_I | ω_I | f_I | ω_I | f_I | ω_I | f_I | | |
| Cytosine | | | | | | | | | | | | | | |
| $^1A'$ ($\pi \rightarrow \pi^*$) | 4.17 | 0.02 | 4.12 | 0.01 | 4.20 | 0.01 | 4.77 | 0.04 | 5.01 | 0.06 | 5.20 | 0.07 | 4.66 | 4.60 |
| $^1A''$ ($n \rightarrow \pi^*$) | 3.38 | <0.01 | 3.36 | 0.00 | 3.77 | <0.01 | 4.92 | <0.01 | 5.27 | <0.01 | 5.29 | <0.01 | 4.87 | 5.00 |
| $^1A''$ ($n \rightarrow \pi^*$) | 4.75 | <0.01 | 4.64 | 0.00 | 4.47 | <0.01 | 5.32 | <0.01 | 5.88 | <0.01 | 5.90 | <0.01 | 5.26 | |
| $^1A'$ ($\pi \rightarrow \pi^*$) | 5.23 | 0.08 | 5.18 | 0.07 | 4.91 | 0.06 | 5.57 | 0.10 | 5.95 | 0.12 | 6.14 | 0.12 | 5.62 | 5.60 |
| Thymine | | | | | | | | | | | | | | |
| $^1A''$ ($n \rightarrow \pi^*$) | 3.88 | <0.01 | 3.79 | <0.01 | 4.06 | <0.01 | 4.79 | <0.01 | 5.05 | <0.01 | 5.07 | <0.01 | 4.82 | |
| $^1A'$ ($\pi \rightarrow \pi^*$) | 4.83 | 0.09 | 4.79 | 0.08 | 4.59 | 0.07 | 5.11 | 0.15 | 5.33 | 0.18 | 5.59 | 0.22 | 5.20 | 4.80 |
| $^1A'$ ($\pi \rightarrow \pi^*$) | 5.25 | 0.12 | 5.19 | 0.09 | 5.32 | 0.06 | 6.16 | 0.07 | 6.65 | 0.07 | 6.81 | 0.12 | 6.27 | 5.70 |
| $^1A''$ ($n \rightarrow \pi^*$) | 4.32 | <0.01 | 4.30 | <0.01 | 4.77 | <0.01 | 6.02 | <0.01 | 6.39 | <0.01 | 6.40 | <0.01 | 6.16 | |
| $^1A'$ ($\pi \rightarrow \pi^*$) | 6.28 | 0.14 | 6.22 | 0.10 | 5.83 | 0.08 | 6.46 | 0.16 | 6.82 | 0.18 | 7.00 | 0.19 | 6.53 | 6.20 |
| Uracil | | | | | | | | | | | | | | |
| $^1A''$ ($n \rightarrow \pi^*$) | 3.78 | <0.01 | 3.70 | 0.00 | 3.95 | <0.01 | 4.73 | <0.01 | 4.99 | <0.01 | 5.02 | <0.01 | 4.80 | 4.38 |
| $^1A'$ ($\pi \rightarrow \pi^*$) | 4.88 | 0.03 | 4.85 | 0.02 | 4.76 | 0.06 | 5.30 | 0.14 | 5.50 | 0.18 | 5.75 | 0.21 | 5.35 | 5.10 |
| $^1A'$ ($\pi \rightarrow \pi^*$) | 5.21 | 0.14 | 5.15 | 0.11 | 5.20 | 0.04 | 6.06 | 0.04 | 6.56 | 0.04 | 6.70 | 0.06 | 6.26 | 6.00 |
| $^1A''$ ($n \rightarrow \pi^*$) | 4.26 | <0.01 | 4.24 | 0.00 | 4.74 | <0.01 | 5.94 | 0.00 | 6.30 | <0.01 | 6.32 | <0.01 | 6.10 | |
| $^1A'$ ($\pi \rightarrow \pi^*$) | 6.56 | 0.13 | 6.49 | 0.09 | 5.87 | 0.01 | 6.66 | 0.13 | 7.04 | 0.14 | 7.22 | 0.17 | 6.70 | 6.60 |
| $^1A''$ ($n \rightarrow \pi^*$) | 5.46 | <0.01 | 5.38 | 0.00 | 5.22 | <0.01 | 6.36 | 0.00 | 6.82 | <0.01 | 6.82 | <0.01 | 6.56 | |
| Adenine | | | | | | | | | | | | | | |
| $^1A''$ ($n \rightarrow \pi^*$) | 4.64 | <0.01 | 4.59 | 0.00 | 4.28 | <0.01 | 5.10 | <0.01 | 5.37 | <0.01 | 5.40 | <0.01 | 5.12 | 5.40 |
| $^1A'$ ($\pi \rightarrow \pi^*$) | 4.83 | 0.22 | 4.77 | 0.18 | 4.57 | 0.12 | 5.13 | 0.22 | 5.39 | 0.25 | 5.55 | 0.06 | 5.25 | 4.63 |
| $^1A'$ ($\pi \rightarrow \pi^*$) | 5.11 | 0.03 | 5.09 | 0.02 | 5.00 | 0.05 | 5.38 | 0.05 | 5.50 | 0.04 | 5.67 | 0.29 | 5.25 | 4.92 |
| $^1A''$ ($n \rightarrow \pi^*$) | 5.42 | <0.01 | 5.33 | 0.00 | 5.03 | <0.01 | 5.73 | <0.01 | 5.98 | <0.01 | 6.01 | <0.01 | 5.75 | |
| MSD | | | | | | | | | | | | | | |
| (PBE) | 0.09 | | 0.03 | | | | | | | | | | | |
| (TBE) | -0.75 | | -0.81 | | -0.84 | | -0.06 | | 0.28 | | 0.39 | | | |
| (Exp.) | -0.37 | | -0.29 | | -0.51 | | 0.18 | | 0.34 | | 0.65 | | | |
| RMS | | | | | | | | | | | | | | |
| (PBE) | 0.32 | | 0.30 | | | | | | | | | | | |
| (TBE) | 0.91 | | 0.96 | | 0.89 | | 0.11 | | 0.30 | | 0.41 | | | |
| (Exp.) | 0.61 | | 0.64 | | 0.63 | | 0.30 | | 0.45 | | 0.70 | | | |

Table C.8: Singlet-singlet vertical excitation energies and oscillator strengths for Group D.

C.2 Triplet States

C.2.1 Relative displacement of ω_I with respect to ω_{KS}

In this section we provide the singlet-triplet vertical excitation energies (ω_I) for the chosen benchmark set, obtained with TD-PBE (TZP), traditional (old) and refined TD-DFTB (new). The TBEs as well as some experimental results are additionally given for comparison. ω_{KS} denotes the KS orbital energy difference corresponding to the most dominant single particle transition in the many body wavefunction. The benchmark set has been divided into groups A, B and C as depicted in Fig. 4.3. All energies are expressed in eV.

| Molecule / Transition | TD-DFT | | TD-DFTB | | | TBE | Exp. |
|-------------------------------------|------------|---------------|-------------------------|-------------------------|---------------|------|------|
| | ω_I | ω_{KS} | ω_I^{new} | ω_I^{old} | ω_{KS} | | |
| Ethene | | | | | | | |
| ${}^3B_{1u}(\pi \rightarrow \pi^*)$ | 4.24 | 5.70 | 4.51 | 5.32 | 6.14 | 4.50 | 4.60 |
| Butadiene | | | | | | | |
| ${}^3B_u(\pi \rightarrow \pi^*)$ | 2.95 | 3.96 | 3.09 | 3.64 | 4.13 | 3.20 | 3.22 |
| ${}^3A_g(\pi \rightarrow \pi^*)$ | 5.03 | 6.19 | 4.99 | 5.57 | 6.02 | 5.08 | 4.91 |
| Hexatriene | | | | | | | |
| ${}^3A_g(\pi \rightarrow \pi^*)$ | 4.05 | 4.90 | 4.00 | 4.46 | 4.78 | 4.15 | 4.11 |
| ${}^3B_u(\pi \rightarrow \pi^*)$ | 2.27 | 3.04 | 2.39 | 2.82 | 3.17 | 2.40 | 2.61 |
| Octatetraene | | | | | | | |
| ${}^3A_g(\pi \rightarrow \pi^*)$ | 3.36 | 4.05 | 3.32 | 3.71 | 3.96 | 3.55 | 3.55 |
| ${}^3B_u(\pi \rightarrow \pi^*)$ | 1.86 | 2.50 | 1.97 | 2.33 | 2.60 | 2.20 | 2.10 |
| Cyclopropene | | | | | | | |
| ${}^3B_1(\sigma \rightarrow \pi^*)$ | 5.80 | 6.12 | 6.24 | 6.44 | 6.44 | 6.62 | |
| ${}^3B_2(\pi \rightarrow \pi^*)$ | 3.81 | 5.02 | 4.39 | 5.04 | 5.64 | 4.34 | 4.16 |
| Cyclopentadiene | | | | | | | |
| ${}^3B_2(\pi \rightarrow \pi^*)$ | 2.90 | 3.82 | 3.07 | 3.58 | 4.01 | 3.25 | 3.10 |
| ${}^3A_1(\pi \rightarrow \pi^*)$ | 4.89 | 5.86 | 4.83 | 5.28 | 5.60 | 5.09 | |
| Norbornadiene | | | | | | | |
| ${}^3A_2(\pi \rightarrow \pi^*)$ | 3.17 | 3.98 | 3.93 | 4.52 | 4.91 | 3.72 | 3.47 |
| ${}^3B_2(\pi \rightarrow \pi^*)$ | 3.78 | 4.76 | 4.09 | 4.68 | 5.13 | 4.16 | 3.90 |

Table C.9: Singlet-triplet vertical excitation energies compared to energy difference of most dominant single particle transition for Group A.

| Molecule / Transition | TD-DFT | | TD-DFTB | | | TBE | Exp. |
|--|------------|---------------|-------------------------|-------------------------|---------------|------|------|
| | ω_I | ω_{KS} | ω_I^{new} | ω_I^{old} | ω_{KS} | | |
| Benzene | | | | | | | |
| ${}^3\text{B}_{2u}(\pi \rightarrow \pi^*)$ | 4.96 | 5.15 | 5.30 | 5.30 | 5.30 | 5.88 | 5.60 |
| ${}^3\text{B}_{1u}(\pi \rightarrow \pi^*)$ | 4.01 | 5.15 | 4.11 | 4.71 | 5.30 | 4.15 | 3.94 |
| ${}^3\text{E}_{1u}(\pi \rightarrow \pi^*)$ | 4.63 | 5.15 | 4.82 | 5.06 | 5.30 | 4.86 | 4.76 |
| ${}^3\text{E}_{2g}(\pi \rightarrow \pi^*)$ | 7.17 | 7.88 | 6.90 | 7.27 | 7.60 | 7.51 | |
| Naphthalene | | | | | | | |
| ${}^3\text{B}_{3u}(\pi \rightarrow \pi^*)$ | 3.83 | 4.15 | 3.87 | 3.98 | 4.06 | 4.18 | |
| ${}^3\text{B}_{2u}(\pi \rightarrow \pi^*)$ | 2.81 | 3.41 | 2.91 | 3.24 | 3.50 | 3.11 | |
| ${}^3\text{A}_g(\pi \rightarrow \pi^*)$ | 5.28 | 5.73 | 5.23 | 5.54 | 5.76 | 5.52 | |
| ${}^3\text{B}_{1g}(\pi \rightarrow \pi^*)$ | 4.24 | 4.99 | 4.29 | 4.65 | 4.91 | 4.47 | |
| ${}^3\text{B}_{3u}(\pi \rightarrow \pi^*)$ | 4.04 | 4.18 | 4.34 | 4.38 | 4.43 | 5.11 | |
| ${}^3\text{B}_{1g}(\pi \rightarrow \pi^*)$ | 5.01 | 5.08 | 5.33 | 5.40 | 5.54 | 6.48 | |
| ${}^3\text{B}_{2u}(\pi \rightarrow \pi^*)$ | 4.35 | 4.92 | 4.43 | 4.71 | 4.99 | 4.64 | |
| ${}^3\text{A}_g(\pi \rightarrow \pi^*)$ | 5.61 | 6.07 | 5.60 | 5.74 | 5.84 | 6.47 | |
| ${}^3\text{B}_{1g}(\pi \rightarrow \pi^*)$ | 6.33 | 6.84 | 6.20 | 6.47 | 6.69 | 6.76 | |
| ${}^3\text{A}_g(\pi \rightarrow \pi^*)$ | 5.68 | 5.85 | 6.00 | 6.03 | 6.10 | 6.79 | |
| Furan | | | | | | | |
| ${}^3\text{B}_2(\pi \rightarrow \pi^*)$ | 3.91 | 4.82 | 4.30 | 4.76 | 5.17 | 4.17 | 4.02 |
| ${}^3\text{A}_1(\pi \rightarrow \pi^*)$ | 5.29 | 6.06 | 5.52 | 5.90 | 6.15 | 5.48 | 5.22 |
| Pyrrole | | | | | | | |
| ${}^3\text{A}_1(\pi \rightarrow \pi^*)$ | 5.28 | 5.86 | 5.55 | 5.83 | 6.05 | 5.51 | 5.10 |
| ${}^3\text{B}_2(\pi \rightarrow \pi^*)$ | 4.24 | 5.09 | 4.64 | 5.08 | 5.49 | 4.48 | 4.21 |
| Imidazole | | | | | | | |
| ${}^3\text{A}''(n \rightarrow \pi^*)$ | 5.51 | 5.77 | 6.06 | 6.21 | 6.21 | 6.37 | |
| ${}^3\text{A}'(\pi \rightarrow \pi^*)$ | 4.39 | 5.22 | 4.75 | 5.18 | 5.56 | 4.69 | |
| ${}^3\text{A}'(\pi \rightarrow \pi^*)$ | 5.44 | 6.18 | 5.82 | 6.19 | 6.55 | 5.79 | |
| ${}^3\text{A}'(\pi \rightarrow \pi^*)$ | 5.94 | 6.51 | 6.20 | 6.42 | 6.64 | 6.55 | |
| Pyridine | | | | | | | |
| ${}^3\text{B}_2(\pi \rightarrow \pi^*)$ | 4.45 | 4.85 | 4.70 | 4.88 | 5.02 | 4.64 | 4.84 |
| ${}^3\text{B}_1(n \rightarrow \pi^*)$ | 3.68 | 4.05 | 4.25 | 4.52 | 4.52 | 4.25 | |
| ${}^3\text{A}_2(n \rightarrow \pi^*)$ | 4.30 | 4.41 | 4.73 | 4.81 | 4.81 | 5.28 | |
| ${}^3\text{A}_1(\pi \rightarrow \pi^*)$ | 4.13 | 5.21 | 4.25 | 4.83 | 5.31 | 4.06 | 4.10 |
| ${}^3\text{A}_1(\pi \rightarrow \pi^*)$ | 4.80 | 5.44 | 4.99 | 5.26 | 5.59 | 4.91 | |
| ${}^3\text{B}_2(\pi \rightarrow \pi^*)$ | 5.48 | 5.80 | 5.70 | 5.78 | 5.88 | 6.08 | |
| Tetrazine | | | | | | | |
| ${}^3\text{B}_{3u}(n \rightarrow \pi^*)$ | 1.08 | 1.52 | 2.07 | 2.37 | 2.37 | 1.89 | 1.69 |
| ${}^3\text{A}_u(n \rightarrow \pi^*)$ | 2.48 | 2.71 | 3.53 | 3.68 | 3.68 | 3.52 | 2.90 |
| ${}^3\text{B}_{1g}(n \rightarrow \pi^*)$ | 3.30 | 3.74 | 4.31 | 4.63 | 4.63 | 4.21 | 3.60 |
| ${}^3\text{B}_{1u}(n \rightarrow \pi^*)$ | 4.32 | 5.57 | 4.26 | 4.85 | 5.32 | 4.54 | |
| ${}^3\text{B}_{2u}(\pi \rightarrow \pi^*)$ | 4.14 | 4.61 | 4.20 | 4.39 | 4.55 | 4.93 | |
| ${}^3\text{B}_{2g}(n \rightarrow \pi^*)$ | 4.17 | 4.60 | 4.74 | 5.08 | 5.08 | 5.03 | |
| ${}^3\text{A}_u(n \rightarrow \pi^*)$ | 3.98 | 4.31 | 4.20 | 4.41 | 4.41 | 4.33 | |
| ${}^3\text{B}_{1u}(n \rightarrow \pi^*)$ | 5.15 | 5.80 | 5.24 | 5.52 | 5.86 | 5.38 | |

Table C.10: Singlet-triplet vertical excitation energies compared to energy difference of most dominant single particle transition for Group B.

| Molecule / Transition | TD-DFT | | TD-DFTB | | | TBE | Exp. |
|-------------------------------------|------------|---------------|-------------------------|-------------------------|---------------|------|------|
| | ω_I | ω_{KS} | ω_I^{new} | ω_I^{old} | ω_{KS} | | |
| Formaldehyde | | | | | | | |
| ${}^3A_2(n \rightarrow \pi^*)$ | 3.01 | 3.50 | 3.90 | 4.25 | 4.25 | 3.50 | 3.50 |
| ${}^3A_1(\pi \rightarrow \pi^*)$ | 5.56 | 7.24 | 5.94 | 6.74 | 7.53 | 5.87 | 5.82 |
| Acetone | | | | | | | |
| ${}^3A_2(n \rightarrow \pi^*)$ | 3.55 | 3.96 | 4.16 | 4.49 | 4.49 | 4.05 | 4.16 |
| ${}^3A_1(\pi \rightarrow \pi^*)$ | 5.63 | 6.87 | 5.82 | 6.41 | 6.94 | 6.03 | 5.88 |
| Benzoquinone | | | | | | | |
| ${}^3A_u(n \rightarrow \pi^*)$ | 1.54 | 1.83 | 1.87 | 2.10 | 2.10 | 2.62 | 2.32 |
| ${}^3B_{1g}(n \rightarrow \pi^*)$ | 1.41 | 1.69 | 1.46 | 1.67 | 1.67 | 2.51 | 2.28 |
| ${}^3B_{3g}(\pi \rightarrow \pi^*)$ | 2.63 | 3.06 | 3.08 | 3.36 | 3.56 | 3.41 | |
| ${}^3B_{1u}(\pi \rightarrow \pi^*)$ | 2.46 | 3.15 | 2.55 | 2.91 | 3.18 | 2.96 | |
| Formamide | | | | | | | |
| ${}^3A''(n \rightarrow \pi^*)$ | 4.85 | 5.22 | 5.20 | 5.51 | 5.51 | 5.36 | 5.30 |
| ${}^3A'(\pi \rightarrow \pi^*)$ | 5.21 | 5.99 | 5.88 | 6.26 | 6.61 | 5.74 | |
| Acetamide | | | | | | | |
| ${}^3A''(n \rightarrow \pi^*)$ | 4.84 | 5.18 | 5.21 | 5.51 | 5.51 | 5.42 | |
| ${}^3A'(\pi \rightarrow \pi^*)$ | 5.27 | 5.96 | 5.84 | 6.21 | 6.55 | 5.88 | |
| Propanamide | | | | | | | |
| ${}^3A''(n \rightarrow \pi^*)$ | 4.87 | 5.21 | 5.18 | 5.48 | 5.48 | 5.45 | |
| ${}^3A'(\pi \rightarrow \pi^*)$ | 5.28 | 5.95 | 5.86 | 6.23 | 6.57 | 5.90 | |

Table C.11: Singlet-triplet vertical excitation energies compared to energy difference of most dominant single particle transition for Group C.

C.2.2 Vertical excitation energies

In this section we provide the singlet-triplet vertical excitation energies (ω_I) for the chosen benchmark set, obtained with traditional (old), refined TD-DFTB (new) and TD-DFT at three different levels (PBE/TZP, PBE0/TZP and CAM-B3LYP/6-311G**). Results obtained with TD-DFT (CAM-B3LYP/6-311G**) in the TDA are also given, along with the TBEs and some experimental findings. The benchmark set has been divided into groups A, B and C as depicted in Fig. 4.3. All energies are expressed in eV.

| Molecule / Trans. | TD-DFTB | | PBE | PBE0 | CAM-B3LYP | TDA | TBE | Exp. |
|--|-------------------------|-------------------------|-------|-------|-----------|-------|------|------|
| | ω_I^{new} | ω_I^{old} | | | | | | |
| Ethene | | | | | | | | |
| ${}^3\text{B}_{1u}(\pi \rightarrow \pi^*)$ | 4.51 | 5.32 | 4.24 | 3.82 | 3.90 | 4.36 | 4.50 | 4.60 |
| Butadiene | | | | | | | | |
| ${}^3\text{B}_u(\pi \rightarrow \pi^*)$ | 3.09 | 3.64 | 2.95 | 2.56 | 2.60 | 3.15 | 3.20 | 3.22 |
| ${}^3\text{A}_g(\pi \rightarrow \pi^*)$ | 4.99 | 5.57 | 5.03 | 4.71 | 4.75 | 5.05 | 5.08 | 4.91 |
| Hexatriene | | | | | | | | |
| ${}^3\text{A}_g(\pi \rightarrow \pi^*)$ | 4.00 | 4.46 | 4.05 | 3.78 | 3.80 | 4.15 | 4.15 | 4.11 |
| ${}^3\text{B}_u(\pi \rightarrow \pi^*)$ | 2.39 | 2.82 | 2.27 | 1.89 | 1.86 | 2.51 | 2.40 | 2.61 |
| Octatetraene | | | | | | | | |
| ${}^3\text{A}_g(\pi \rightarrow \pi^*)$ | 3.32 | 3.71 | 3.36 | 3.10 | 3.10 | 3.49 | 3.55 | 3.55 |
| ${}^3\text{B}_u(\pi \rightarrow \pi^*)$ | 1.97 | 2.33 | 1.86 | 1.47 | 1.39 | 2.12 | 2.20 | 2.10 |
| Cyclopropene | | | | | | | | |
| ${}^3\text{B}_1(\sigma \rightarrow \pi^*)$ | 6.24 | 6.44 | 5.80 | 6.04 | 6.18 | 6.22 | 6.62 | |
| ${}^3\text{B}_2(\pi \rightarrow \pi^*)$ | 4.39 | 5.04 | 3.81 | 3.53 | 3.64 | 4.07 | 4.34 | 4.16 |
| Cyclopentadiene | | | | | | | | |
| ${}^3\text{B}_2(\pi \rightarrow \pi^*)$ | 3.07 | 3.58 | 2.90 | 2.56 | 2.60 | 3.06 | 3.25 | 3.10 |
| ${}^3\text{A}_1(\pi \rightarrow \pi^*)$ | 4.83 | 5.28 | 4.89 | 4.63 | 4.67 | 4.95 | 5.09 | |
| Norbornadiene | | | | | | | | |
| ${}^3\text{A}_2(\pi \rightarrow \pi^*)$ | 3.93 | 4.52 | 3.17 | 2.94 | 3.05 | 3.45 | 3.72 | 3.47 |
| ${}^3\text{B}_2(\pi \rightarrow \pi^*)$ | 4.09 | 4.68 | 3.78 | 3.44 | 3.50 | 3.96 | 4.16 | 3.90 |
| MSD | | | | | | | | |
| (PBE) | 0.21 | 0.71 | | | | | | |
| (TBE) | -0.11 | 0.39 | -0.32 | -0.60 | -0.56 | -0.13 | | |
| (Exp.) | 0.00 | 0.54 | -0.21 | -0.54 | -0.50 | -0.03 | | |
| RMS | | | | | | | | |
| (PBE) | 0.32 | 0.78 | | | | | | |
| (TBE) | 0.18 | 0.48 | 0.38 | 0.62 | 0.57 | 0.19 | | |
| (Exp.) | 0.21 | 0.61 | 0.25 | 0.56 | 0.53 | 0.10 | | |

Table C.12: Singlet-triplet vertical excitation energies for Group A.

| Molecule / Trans. | TD-DFTB | | PBE | PBE0 | CAM-B3LYP | TDA | TBE | Exp. |
|--|-------------------------|-------------------------|------|------|-----------|------|------|------|
| | ω_I^{new} | ω_I^{old} | | | | | | |
| Benzene | | | | | | | | |
| ${}^3\text{B}_{2u}(\pi \rightarrow \pi^*)$ | 5.30 | 5.30 | 4.96 | 5.14 | 5.16 | 5.25 | 5.88 | 5.60 |
| ${}^3\text{B}_{1u}(\pi \rightarrow \pi^*)$ | 4.11 | 4.71 | 4.01 | 3.59 | 3.55 | 4.12 | 4.15 | 3.94 |
| ${}^3\text{E}_{1u}(\pi \rightarrow \pi^*)$ | 4.82 | 5.06 | 4.63 | 4.71 | 4.80 | 4.86 | 4.86 | 4.76 |
| ${}^3\text{E}_{2g}(\pi \rightarrow \pi^*)$ | 6.90 | 7.27 | 7.17 | 7.34 | 7.44 | 7.45 | 7.51 | |
| Naphthalene | | | | | | | | |
| ${}^3\text{B}_{3u}(\pi \rightarrow \pi^*)$ | 3.87 | 3.98 | 3.83 | 3.96 | 4.07 | 4.14 | 4.18 | |
| ${}^3\text{B}_{2u}(\pi \rightarrow \pi^*)$ | 2.91 | 3.24 | 2.81 | 2.55 | 2.50 | 3.03 | 3.11 | |
| ${}^3\text{A}_g(\pi \rightarrow \pi^*)$ | 5.23 | 5.54 | 5.28 | 5.32 | 5.39 | 5.48 | 5.52 | |
| ${}^3\text{B}_{1g}(\pi \rightarrow \pi^*)$ | 4.29 | 4.65 | 4.24 | 4.09 | 4.12 | 4.40 | 4.47 | |
| ${}^3\text{B}_{3u}(\pi \rightarrow \pi^*)$ | 4.34 | 4.38 | 4.04 | 4.27 | 4.32 | 4.42 | 5.11 | |
| ${}^3\text{B}_{1g}(\pi \rightarrow \pi^*)$ | 5.33 | 5.40 | 5.01 | 5.74 | 6.38 | 6.39 | 6.48 | |
| ${}^3\text{B}_{2u}(\pi \rightarrow \pi^*)$ | 4.43 | 4.71 | 4.35 | 4.40 | 4.50 | 4.64 | 4.64 | |
| ${}^3\text{A}_g(\pi \rightarrow \pi^*)$ | 5.60 | 5.74 | 5.61 | 6.05 | 6.26 | 6.31 | 6.47 | |
| ${}^3\text{B}_{1g}(\pi \rightarrow \pi^*)$ | 6.20 | 6.47 | 6.33 | 6.60 | 6.84 | 6.93 | 6.76 | |
| ${}^3\text{A}_g(\pi \rightarrow \pi^*)$ | 6.00 | 6.03 | 5.68 | 6.17 | 6.69 | 6.78 | 6.79 | |
| Furan | | | | | | | | |
| ${}^3\text{B}_2(\pi \rightarrow \pi^*)$ | 4.30 | 4.76 | 3.91 | 3.59 | 3.60 | 3.99 | 4.17 | 4.02 |
| ${}^3\text{A}_1(\pi \rightarrow \pi^*)$ | 5.52 | 5.90 | 5.29 | 5.17 | 5.21 | 5.37 | 5.48 | 5.22 |
| Pyrrole | | | | | | | | |
| ${}^3\text{A}_1(\pi \rightarrow \pi^*)$ | 5.55 | 5.83 | 5.28 | 5.26 | 5.31 | 5.42 | 5.51 | 5.10 |
| ${}^3\text{B}_2(\pi \rightarrow \pi^*)$ | 4.64 | 5.08 | 4.24 | 3.98 | 3.97 | 4.32 | 4.48 | 4.21 |
| Imidazole | | | | | | | | |
| ${}^3\text{A}''(n \rightarrow \pi^*)$ | 6.06 | 6.21 | 5.51 | 5.89 | 5.99 | 6.06 | 6.37 | |
| ${}^3\text{A}'(\pi \rightarrow \pi^*)$ | 4.75 | 5.18 | 4.39 | 4.16 | 4.17 | 4.50 | 4.69 | |
| ${}^3\text{A}'(\pi \rightarrow \pi^*)$ | 5.82 | 6.19 | 5.44 | 5.42 | 5.52 | 5.67 | 5.79 | |
| ${}^3\text{A}'(\pi \rightarrow \pi^*)$ | 6.20 | 6.42 | 5.94 | 5.99 | 6.04 | 6.20 | 6.55 | |
| Pyridine | | | | | | | | |
| ${}^3\text{B}_2(\pi \rightarrow \pi^*)$ | 4.70 | 4.88 | 4.45 | 4.52 | 4.57 | 4.64 | 4.64 | 4.84 |
| ${}^3\text{B}_1(n \rightarrow \pi^*)$ | 4.25 | 4.52 | 3.68 | 4.05 | 4.24 | 4.31 | 4.25 | |
| ${}^3\text{A}_2(n \rightarrow \pi^*)$ | 4.73 | 4.81 | 4.30 | 5.06 | 5.32 | 5.35 | 5.28 | |
| ${}^3\text{A}_1(\pi \rightarrow \pi^*)$ | 4.25 | 4.83 | 4.13 | 3.70 | 3.67 | 4.24 | 4.06 | 4.10 |
| ${}^3\text{A}_1(\pi \rightarrow \pi^*)$ | 4.99 | 5.26 | 4.80 | 4.85 | 4.93 | 5.00 | 4.91 | |
| ${}^3\text{B}_2(\pi \rightarrow \pi^*)$ | 5.70 | 5.78 | 5.48 | 5.68 | 5.73 | 5.80 | 6.08 | |

| Molecule / Trans. | TD-DFTB | | PBE | PBE0 | CAM-B3LYP | TDA | TBE | Exp. |
|--|-------------------------|-------------------------|-------|-------|-----------|-------|------|------|
| | ω_I^{new} | ω_I^{old} | | | | | | |
| Tetrazine | | | | | | | | |
| ${}^3\text{B}_{3u}(n \rightarrow \pi^*)$ | 2.07 | 2.37 | 1.08 | 1.38 | 1.56 | 1.69 | 1.89 | 1.69 |
| ${}^3\text{A}_u(n \rightarrow \pi^*)$ | 3.53 | 3.68 | 2.48 | 3.14 | 3.39 | 3.45 | 3.52 | 2.90 |
| ${}^3\text{B}_{1g}(n \rightarrow \pi^*)$ | 4.31 | 4.63 | 3.30 | 3.66 | 3.78 | 3.89 | 4.21 | 3.60 |
| ${}^3\text{B}_{1u}(n \rightarrow \pi^*)$ | 4.26 | 4.85 | 4.32 | 3.61 | 3.54 | 4.28 | 4.54 | |
| ${}^3\text{B}_{2u}(\pi \rightarrow \pi^*)$ | 4.20 | 4.39 | 4.14 | 4.05 | 4.02 | 4.15 | 4.93 | |
| ${}^3\text{B}_{2g}(n \rightarrow \pi^*)$ | 4.74 | 5.08 | 4.17 | 4.50 | 4.68 | 4.77 | 5.03 | |
| ${}^3\text{A}_u(n \rightarrow \pi^*)$ | 4.20 | 4.41 | 3.98 | 4.47 | 4.69 | 4.76 | 4.33 | |
| ${}^3\text{B}_{1u}(n \rightarrow \pi^*)$ | 5.24 | 5.52 | 5.15 | 5.25 | 5.32 | 5.38 | 5.38 | |
| MSD | | | | | | | | |
| (PBE) | 0.28 | 0.55 | | | | | | |
| (TBE) | -0.24 | 0.03 | -0.52 | -0.41 | -0.30 | -0.13 | | |
| (Exp.) | 0.26 | 0.59 | -0.19 | -0.18 | -0.12 | 0.11 | | |
| RMS | | | | | | | | |
| (PBE) | 0.41 | 0.63 | | | | | | |
| (TBE) | 0.41 | 0.45 | 0.63 | 0.48 | 0.42 | 0.26 | | |
| (Exp.) | 0.38 | 0.69 | 0.33 | 0.29 | 0.31 | 0.25 | | |

Table C.13: Singlet-triplet vertical excitation energies for Group B.

| Molecule / Trans. | TD-DFTB | | PBE | PBE0 | CAM-B3LYP | TDA | TBE | Exp. |
|-------------------------------------|-------------------------|-------------------------|-------|-------|-----------|-------|------|------|
| | ω_I^{new} | ω_I^{old} | | | | | | |
| Formaldehyde | | | | | | | | |
| ${}^3A_2(n \rightarrow \pi^*)$ | 3.90 | 4.25 | 3.01 | 3.07 | 3.10 | 3.18 | 3.50 | 3.50 |
| ${}^3A_1(\pi \rightarrow \pi^*)$ | 5.94 | 6.74 | 5.56 | 4.97 | 5.08 | 5.58 | 5.87 | 5.82 |
| Acetone | | | | | | | | |
| ${}^3A_2(n \rightarrow \pi^*)$ | 4.16 | 4.49 | 3.55 | 3.66 | 3.70 | 3.77 | 4.05 | 4.16 |
| ${}^3A_1(\pi \rightarrow \pi^*)$ | 5.82 | 6.41 | 5.63 | 5.23 | 5.32 | 5.73 | 6.03 | 5.88 |
| Benzoquinone | | | | | | | | |
| ${}^3A_u(n \rightarrow \pi^*)$ | 1.87 | 2.10 | 1.54 | 2.07 | 2.38 | 2.45 | 2.62 | 2.32 |
| ${}^3B_{1g}(n \rightarrow \pi^*)$ | 1.46 | 1.67 | 1.41 | 1.92 | 2.24 | 2.30 | 2.51 | 2.28 |
| ${}^3B_{3g}(\pi \rightarrow \pi^*)$ | 3.08 | 3.36 | 2.63 | 2.60 | 2.72 | 3.03 | 3.41 | |
| ${}^3B_{1u}(\pi \rightarrow \pi^*)$ | 2.55 | 2.91 | 2.46 | 2.01 | 2.03 | 2.70 | 2.96 | |
| Formamide | | | | | | | | |
| ${}^3A''(n \rightarrow \pi^*)$ | 5.20 | 5.51 | 4.85 | 4.95 | 5.00 | 5.07 | 5.36 | 5.30 |
| ${}^3A'(\pi \rightarrow \pi^*)$ | 5.88 | 6.26 | 5.21 | 5.09 | 5.12 | 5.39 | 5.74 | |
| Acetamide | | | | | | | | |
| ${}^3A''(n \rightarrow \pi^*)$ | 5.21 | 5.51 | 4.84 | 5.01 | 5.08 | 5.14 | 5.42 | |
| ${}^3A'(\pi \rightarrow \pi^*)$ | 5.84 | 6.21 | 5.27 | 5.23 | 5.27 | 5.52 | 5.88 | |
| Propanamide | | | | | | | | |
| ${}^3A''(n \rightarrow \pi^*)$ | 5.18 | 5.48 | 4.87 | 5.05 | 5.14 | 5.20 | 5.45 | |
| ${}^3A'(\pi \rightarrow \pi^*)$ | 5.86 | 6.23 | 5.28 | 5.26 | 5.31 | 5.55 | 5.90 | |
| MSD | | | | | | | | |
| (PBE) | 0.42 | 0.79 | | | | | | |
| (TBE) | -0.20 | 0.17 | -0.61 | -0.61 | -0.52 | -0.29 | | |
| (Exp.) | -0.13 | 0.27 | -0.53 | -0.48 | -0.35 | -0.17 | | |
| RMS | | | | | | | | |
| (PBE) | 0.47 | 0.83 | | | | | | |
| (TBE) | 0.41 | 0.47 | 0.67 | 0.64 | 0.56 | 0.30 | | |
| (Exp.) | 0.39 | 0.57 | 0.57 | 0.52 | 0.44 | 0.24 | | |

Table C.14: Singlet-triplet vertical excitation energies for Group C.

Bibliography

- [1] V. E. Henrich and P. A. Cox. *The surface science of metal oxides*. Cambridge University Press, Cambridge, 1994.
- [2] G. A. Somorjai. *Introduction to surface chemistry and catalysis*. John Wiley & Sons, New York, 1994.
- [3] P. V. Kamat. Photochemistry on nonreactive and reactive (semiconductor) surfaces. *Chem. Rev.*, 93:267–300, 1993.
- [4] M. A. Fox and M. T. Dulay. Heterogeneous photocatalysis. *Chem. Rev.*, 93:341–357, 1993.
- [5] M. R. Hoffmann, S. T. Martin, W. Choi, and D. W. Bahnemann. Environmental applications of semiconductor photocatalysis. *Chem. Rev.*, 95:69–96, 1995.
- [6] M. Kaneko and I. Okura. *Photocatalysis: science and technology*. Springer-Verlag Berlin, 2002.
- [7] X.-Q. Gong and A. Selloni. Reactivity of anatase TiO₂ nanoparticles: The role of the minority (001) surface. *J. Phys. Chem. B*, 109(42):19560–19562, 2005.
- [8] A. C. Stern, R. W. Boubel, D. B. Tuner, and D. L. Fox. *Fundamentals of Air Pollution*. Academic Press: Orlando, FL, 1984.
- [9] C. N. Rusu and J. T. Yates. Photochemistry of NO chemisorbed on TiO₂(110) and TiO₂ powders. *J. Phys. Chem. B*, 104:1729–1737, 2000.
- [10] S. Suzuki, T. Tsuneda, and K. Hirao. A theoretical investigation on photocatalytic oxidation on the TiO₂ surface. *J. Chem. Phys.*, 136:024706, 2012.
- [11] V. H. Houlding and M. Gratzel. Photochemical hydrogen generation by visible light. sensitization of titanium dioxide particles by surface complexation with 8-hydroxyquinoline. *J. Am. Chem. Soc.*, 105(17):5695–5696, 1983.
- [12] G. Zhang, G. Kim, and W. Choi. Visible light driven photocatalysis mediated via ligand-to-metal charge transfer (LMCT): an alternative approach to solar activation of titania. *Energy Environ. Sci.*, 7:954–966, 2014.
- [13] Y. Cho, H. Kyung, and W. Choi. Visible light activity of TiO₂ for the photoreduction of CCl₄ and Cr(vi) in the presence of nonionic surfactant (Brij). *Appl. Catal. B: Environ.*, 52(1):23–32, 2004.

- [14] Y. S. Seo, C. Lee, K. H. Lee, and K. B. Yoon. 1:1 and 2:1 charge-transfer complexes between aromatic hydrocarbons and dry titanium dioxide. *Angew. Chem. Int. Ed.*, 44:910–913, 2005.
- [15] A. Ramakrishnan, S. Neubert, B. Mei, J. Strunk, L. Wang, M. Bledowski, M. Muhler, and R. Beranek. Enhanced performance of surface-modified TiO₂ photocatalysts prepared via a visible-light photosynthetic route. *Chem. Commun.*, 48:8556–8558, 2012.
- [16] X. Lu, A. Linsebigler, and J. T. Yates. Ti³⁺ defect sites on TiO₂(110): Production and chemical detection of active sites. *J. Phys. Chem.*, 98:11733, 1994.
- [17] N. K. Pande and A. T. Bell. A study of the interactions of NO with Rh/TiO₂ and TiO₂-promoted Rh/TiO₂. *J. Catal.*, 97:137, 1986.
- [18] D. C. Sorescu and J. T. Yates (Jr). First principles calculations of the adsorption properties of CO and NO on the defective TiO₂(110) surface. *J. Phys. Chem. B*, 106:6184–6199, 2002.
- [19] T. J. Dines, C. H. Rochester, and A. M. Ward. Infrared and Raman study of the adsorption of NH₃, pyridine, NO and NO₂ on anatase. *J. Chem. Soc. Faraday Trans.*, 87:643, 1991.
- [20] A. Markovits, B. Mguig, M. Calatayud, and C. Minot. Spin localization for NO adsorption on surface O atoms of metal oxides. *Catal. Today*, 113:201–207, 2006.
- [21] D. C. Sorescu, C. N. Rusu, and J. T. Yates (Jr). Adsorption of NO on the TiO₂(110) surface: An experimental and theoretical study. *J. Phys. Chem. B*, 104:4408–4417, 2000.
- [22] J. A. Rodriguez, T. Jirsak, G. Liu, J. Hrbek, J. Dvorak, and A. Maiti. Chemistry of NO₂ on oxide surfaces: Formation of NO₃ on TiO₂(110) and NO₂-O vacancy interactions. *J. Am. Chem. Soc.*, 123:9597–9605, 2001.
- [23] J. Li, L. Wu, and Y. Zhang. Theoretical study of adsorbed-decomposition of NO, CO and CH₂O on a TiO₂(110) (1 x 1) defect surface. *Chem. Phys. Letters*, 342:249–258, 2001.
- [24] J. Oviedo and J. F. Sanz. N₂O decomposition on TiO₂ (110) from dynamic first-principles calculations. *J. Phys. Chem. B*, 109:16223–16226, 2005.
- [25] M. A. Henderson, J. Szanyi, and C. H. F. Peden. Conversion of N₂O to N₂ on TiO₂ (110). *Catal. Today*, 85:251–266, 2003.
- [26] S. Budavari, editor. *The Merck Index. An Encyclopedia of Chemicals, Drugs, and Biologicals*. Merck and Co. Inc., Rahway, NJ, 1989.
- [27] *International Agency for research on cancer (IARC), IARC monographs on the evaluations of carcinogenic risk to humans (Vol. 71, 1999)*.
- [28] B. I. Stefanov, Z. Topalian, C. G. Granqvist, and L. Österlund. Acetaldehyde adsorption and condensation on anatase TiO₂: Influence of acetaldehyde dimerization. *J. Mol. Catal. A: Chem.*, 381:77–88, 2014.

- [29] J. J. Plata, V. Collico, A. M. Márquez, and J. F. Sanz. Analysis of the origin of lateral interactions in the adsorption of small organic molecules on oxide surfaces. *Theor. Chem. Acc.*, 132:1311, 2013.
- [30] Z. L. Wang. *ZnO bulk, Thin Films and Nanostructures*. Elsevier, Oxford, 2006.
- [31] Z. L. Wang. Nanostructures of zinc oxide. *Mater. Today*, 7(6):26–33, 2004.
- [32] C. Lao, Y. Ci, C. P. Wong, and Z. L. Wang. Enhancing the electrical and optoelectronic performance of nanobelt devices by molecular surface functionalization. *Nano Lett.*, 7:1323, 2007.
- [33] J. H. He, C. H. Ho, and C. Y. Chen. Polymer functionalized ZnO nanobelts as oxygen sensors with a significant response enhancement. *Nanotechnology*, 20:065503, 2009.
- [34] L. Peng, J. Zhai, D. Wang, Y. Zhang, Q. Zhao, P. Wang, S. Pang, Z. Fan, and T. Xie. The enhancement of oxygen sensitivity of ZnO macropore film by functionalizing with azo pigment. *Photochem. Photobiol. Sci.*, (8):875–880, 2009.
- [35] J. Zhou, Y. Gu, Y. Hu, W. Mai, P.-H. Yeh, G. Bao, A. K. Sood, D. L. Polla, and Z. L. Wang. Gigantic enhancement in response and reset time of ZnO UV nanosensor by utilizing Schottky contact and surface functionalization. *Appl. Phys. Lett.*, 94:191103, 2009.
- [36] J. H. He, Yen H. Lin, M. E. McConney, V. V. Tsukruk, and Z. L. Wang. Enhancing UV photoconductivity of ZnO nanobelt by polyacrylonitrile functionalization. *J. Appl. Phys.*, 102:084303, 2007.
- [37] R. Yakimova, G. Steinhoff, R.M. Pectoral Jr., C. Vahlberg, V. Khranovskyy, G.R. Yazdi, K. Uvdal, and A. Lloyd Spetz. Novel material concepts of transducers for chemical and biosensors. *Biosens. Bioelectron.*, 22:2780–2785, 2007.
- [38] L. G. Bach, Md. R. Islam, Y. H. Kim, S. D. Seo, C. Park, H. G. Kim, and K. T. Lim. A facile route towards the synthesis of polystyrene/zinc oxide nanocomposites. *J. Nanosci. Nanotechnol.*, 13(1):694–697, 2013.
- [39] G. Jayalakshmi, N. Gopalakrishnan, and T. Balasubramanian. Activation of room temperature ferromagnetism in ZnO films by surface functionalization with thiol and amine. *J. Alloys Compd.*, 551:667–671, 2013.
- [40] G. Jayalakshmi, S. Sriraman Narayanan, and T. Balasubramanian. Activation and deactivation of room temperature ferromagnetism in ZnO films. *Functional Materials Letters*, 5:1250044, 2012.
- [41] S.-Z. Deng, H.-M. Fan, M. Wang, M.-R. Zheng, J.-B. Yi, R.-Q. Wu, H.-R. Tan, C.-H. Sow, J. Ding, Y.-P. Feng, and K.-P. Loh. Thiol-capped ZnO nanowire/nanotube arrays with tunable magnetic properties at room temperature. *ACS Nano*, 4(1):495–505, 2010.
- [42] Y. K. Gao, F. Traeger, O. Shekhah, H. Idriss, and C. Wöll. Probing the interaction of the amino acid alanine with the surface of ZnO (10-10). *J. Colloid Interface Sci*, 338:16–21, 2009.

- [43] G. Jayalakshmi, K. Saravanan, and T. Balasubramanian. Impact of thiol and amine functionalization on photoluminescence properties of ZnO films. *J. Lumin.*, 140:21–25, 2013.
- [44] G. Jayalakshmi and T. Balasubramanian. Enhancing mechanism for room temperature ferromagnetism in ZnO films on amine functionalization. *J. Mater. Sci.-Mater. Electron.*, 24:2928–2933, 2013.
- [45] O. Taratula, E. Galoppini, D. Wang, D. Chu, Z. Zhang, H. Chen, G. Saraf, and Y. Lu. Binding studies of molecular linkers to ZnO and MgZnO nanotip films. *J. Phys. Chem. B*, 110:6506, 2006.
- [46] S. Kuehn, S. Friede, S. Sadofev, S. Blumstengel, F. Henneberger, and T. Elsaesser. Surface excitons on a ZnO (000-1) thin film. *Appl. Phys. Lett.*, 103(19):191909, 2013.
- [47] Y. Cao, E. Galoppini, P. I. Reyes, and Y. Lu. Functionalization of nanostructured ZnO films by copper-free click reaction. *Langmuir*, 29(25):7768–7775, 2013.
- [48] K. Yao, L. Chen, Y. Chen, F. Li, and P. Wang. Interfacial nanostructuring of ZnO nanoparticles by fullerene surface functionalization for annealing-free hybrid bulk heterojunction solar cells. *J. Phys. Chem. C*, 116(5):3486–3491, 2012.
- [49] S. K. Hau, Y.-J. Cheng, H.-L. Yip, Y. Zhang, H. Ma, and A. K.-Y. Jen. Effect of chemical modification of fullerene-based self-assembled monolayers on the performance of inverted polymer solar cells. *ACS Appl. Mater. Inter.*, 2(7):1892–1902, 2010.
- [50] X. Tian, J. Xu, and W. Xie. Controllable modulation of the electronic structure of ZnO (10-10) surface by carboxylic acids. *J. Phys. Chem. C*, 114:3973–3980, 2010.
- [51] A. Lenz, L. Selegård, F. Söderlind, A. Larsson, P. O. Holtz, K. Uvdal, L. Ojamae, and P.-O. Käll. ZnO nanoparticles functionalized with organic acids: An experimental and quantum-chemical study. *J. Phys. Chem. C*, 113(40):17332–17341, 2009.
- [52] O. Taratula, E. Galoppini, R. Mendelsohn, P. I. Reyes, Z. Zhang, Z. Duan, J. Zhong, and Y. Lu. Stepwise functionalization of ZnO nanotips with DNA. *Langmuir*, 25(4):2107–2113, 2009.
- [53] A. Gupta, B. C. Kim, E. Edwards, C. Brantley, and P. Ruffin. Functionalization of ZnO nanowires for potential p-nitrophenol sensing applications. *Adv. Mat. Res.*, 567:228–231, 2012.
- [54] C. L. Perkins. Molecular anchors for self-assembled monolayers on ZnO: A direct comparison of the thiol and phosphonic acid moieties. *J. Phys. Chem. C*, 113:18276–18286, 2009.
- [55] K. Ogata, T. Hama, K. Hama, K. Koike, S. Sasa, M. Inoue, and M. Yano. Characterization of alkanethiol/ZnO structures by X-ray photoelectron spectroscopy. *Appl. Surf. Sci.*, 241:146–149, 2005.
- [56] P. W. Sadik, S. J. Pearton, D.P. Norton, E. Lambers, and F. Ren. Functionalizing Zn- and O-terminated ZnO with thiols. *J. Appl. Phys.*, 101(10):104514, 2007.

- [57] J. Chen, R. E. Ruther, Y. Tan, L. M. Bishop, and R. J. Hamers. Molecular adsorption on ZnO(10-10) single-crystal surfaces: Morphology and charge transfer. *Langmuir*, 28:10437–10445, 2012.
- [58] J. Singh, J. Im, E. J. Watters, J. E. Whitten, J. W. Soares, and D. M. Steeves. Thiol dosing of ZnO single crystals and nanorods: Surface chemistry and photoluminescence. *Surf. Sci.*, 609:183–189, 2013.
- [59] K. Ogata, K. Koike, S. Sasa, M. Inoue, and M. Yano. X-ray photoelectron spectroscopy characterization of aminosilane anchored to ZnO nanorod arrays grown by an aqueous solution method with microwave-assisted heating. *J. Vac. Sci. Technol. B*, 27:1834, 2009.
- [60] C. G. Allen, D. J. Baker, J. M. Albin, H. E. Oertli, D. T. Gillaspie, D. C. Olson, T. E. Furtak, and R. T. Collins. Surface modification of ZnO using triethoxysilane-based molecules. *Langmuir*, 24:13393, 2008.
- [61] J. A. Soares, J. E. Whitten, D. W. Oblas, and D. M. Steeves. Novel photoluminescence properties of surface-modified nanocrystalline zinc oxide: Toward a reactive scaffold. *Langmuir*, 24:371–374, 2008.
- [62] G. J. Ehlert and H. A. Sodano. Zinc oxide nanowire interphase for enhanced interfacial strength in lightweight polymer fiber composites. *ACS Appl. Mater. Inter.*, 1(8):1827–1833, 2009.
- [63] M. Head-Gordon, R. J. Rico, M. Oumi, and T. J. Lee. A doubles correction to electronic excited states from configuration interaction in the space of single substitutions. *Chem. Phys. Lett.*, 219(1–2):21–29, 1994.
- [64] I. Shavitt. The history and evolution of configuration interaction. *Mol. Phys.*, 94(1):3–17, 1998.
- [65] D. Maurice and M. Head-Gordon. Analytical second derivatives for excited electronic states using the single excitation configuration interaction method: theory and application to benzo[a]pyrene and chalcone. *Mol. Phys.*, 96(10):1533–1541, 1999.
- [66] Chr. Møller and M. S. Plesset. Note on an approximation treatment for many-electron systems. *Phys. Rev.*, 46:618–622, 1934.
- [67] R. Krishnan and J. A. Pople. Approximate fourth-order perturbation theory of the electron correlation energy. *Int. J. Quant. Chem.*, 14:91–100, 2004.
- [68] G. D. Purvis and R. J. Bartlett. A full coupled-cluster singles and doubles model: The inclusion of disconnected triples. *J. Chem. Phys.*, 76(4):1910–1918, 1982.
- [69] K. Raghavachari, G. W. Trucks, J. A. Pople, and M. Head-Gordon. A fifth-order perturbation comparison of electron correlation theories. *Chem. Phys. Lett.*, 157(6):479–483, 1989.
- [70] J. A. Pople, M. HeadGordon, D. J. Fox, K. Raghavachari, and L. A. Curtiss. Gaussian1 theory: A general procedure for prediction of molecular energies. *J. Chem. Phys.*, 90(10):5622–5629, 1989.

- [71] L. A. Curtiss, K. Raghavachari, G. W. Trucks, and J. A. Pople. Gaussian2 theory for molecular energies of first and second-row compounds. *J. Chem. Phys.*, 94(11):7221–7230, 1991.
- [72] L. A. Curtiss, K. Raghavachari, P. C. Redfern, V. Rassolov, and J. A. Pople. Gaussian-3 (G3) theory for molecules containing first and second-row atoms. *J. Chem. Phys.*, 109(18):7764–7776, 1998.
- [73] E. Runge and E. K. U. Gross. Density-functional theory for time-dependent systems. *Phys. Rev. Lett.*, 52(12):997–1000, 1984.
- [74] M. E. Casida and M. Huix-Rotllant. Progress in time-dependent density-functional theory. *Annu. Rev. Phys. Chem.*, 63:287–323, 2012.
- [75] K. Burke. Perspective on density functional theory. *J. Chem. Phys.*, 136:150901, 2012.
- [76] C.A. Ullrich. *Time-Dependent Density-Functional Theory: Concepts and Applications*. Oxford University Press, USA, 2012.
- [77] D. Jacquemin, V. Wathelet, E. A. Perpète, and C. Adamo. Extensive TD-DFT benchmark: Singlet-excited states of organic molecules. *J. Chem. Theory Comput.*, 5(9):2420–2435, 2009.
- [78] D. Jacquemin, E. A. Perpète, I. Ciofini, and C. Adamo. Assessment of functionals for TD-DFT calculations of singlet-triplet transitions. *J. Chem. Theory Comput.*, 6(5):1532–1537, 2010.
- [79] D. Jacquemin, E. A. Perpète, I. Ciofini, C. Adamo, R. Valero, Y. Zhao, and D. G. Truhlar. On the performances of the M06 family of density functionals for electronic excitation energies. *J. Chem. Theory Comput.*, 6(7):2071–2085, 2010.
- [80] E. Hückel. Quantentheoretische Beiträge zum Benzolproblem. *ZS. f. Phys.*, 70:204–286, 1931.
- [81] E. Hückel. Quantentheoretische Beiträge zum Benzolproblem. *ZS. f. Phys.*, 72:310–337, 1931.
- [82] E. Hückel. Quantentheoretische Beiträge zum Problem der aromatischen und ungesättigten Verbindungen. III. *ZS. f. Phys.*, 76:628–648, 1932.
- [83] E. Hückel. Die freien Radikale der organischen Chemie. *ZS. f. Phys.*, 83:632–668, 1933.
- [84] R. C. Bingham, M. J. S. Dewar, and D. H. Lo. Ground states of molecules. XXV. MINDO/3. improved version of the MINDO semiempirical SCF-MO method. *J. Am. Chem. Soc.*, 97(6):1285–1293, 1975.
- [85] M. J. S. Dewar, E. G. Zoebisch, E. F. Healy, and J. J. P. Stewart. AM1: a new general purpose quantum mechanical molecular model. *J. Am. Chem. Soc.*, 107(13):3902–3909, 1985.
- [86] J. J. P. Stewart. Optimization of parameters for semiempirical methods I. method. *J. Comput. Chem.*, 10(2):209–220, 1989.

- [87] J. J .P. Stewart. Optimization of parameters for semiempirical methods II. applications. *J. Comput. Chem.*, 10(2):221–264, 1989.
- [88] J. J .P. Stewart. Optimization of parameters for semiempirical methods. III Extension of PM3 to Be, Mg, Zn, Ga, Ge, As, Se, Cd, In, Sn, Sb, Te, Hg, Tl, Pb, and Bi. *J. Comput. Chem.*, 12(3):320–341, 1991.
- [89] D. Porezag, T. Frauenheim, T. Köhler, G. Seifert, and R. Kaschner. Construction of tight-binding-like potentials on the basis of density-functional theory: Application to carbon. *Phys. Rev. B*, 51(19):12947–12957, 1995.
- [90] M. Elstner, D. Porezag, G. Jungnickel, J. Elsner, M. Haugk, T. Frauenheim, S. Suhai, and G. Seifert. Self-consistent-charge density-functional tight-binding method for simulations of complex materials properties. *Phys. Rev. B*, 58(11):7260–7268, 1998.
- [91] T. A. Niehaus, S. Suhai, F. Della Sala, P. Lugli, M. Elstner, G. Seifert, and T. Frauenheim. Tight-binding approach to time-dependent density-functional response theory. *Phys. Rev. B*, 63(8):085108, 2001.
- [92] R. G. Parr and W. Yang. *Density-functional theory of atoms and molecules*. Oxford University Press, New York, 1989.
- [93] C.A. Ullrich. *Time-dependent Density Functional Theory: Concept and Applications*. Oxford University Press, New York, 2012.
- [94] L. H. Thomas. The calculation of atomic fields. *Proc. Camb. Phil. Soc.*, 23:542–548, 1927.
- [95] E. Fermi. Un metodo statistice per la determinazione di alcune proprieta dell’atomo. *Rend. Accad. Nazl. Lincei*, 6:602–607, 1927.
- [96] E. H. Lieb. Thomas-Fermi theory revisited. *Phys. Rev. Lett.*, 31:681–683, 1973.
- [97] E. H. Lieb. The Thomas-Fermi theory of atoms, molecules and solids. *Adv. in Math*, 23:22–116, 1977.
- [98] E. H. Lieb. Thomas-Fermi and related theories of atoms and molecules. *Rev. Mod. Phys.*, 53:603–641, 1981.
- [99] P. Hohenberg and W. Kohn. Inhomogeneous electron gas. *Phys. Rev.*, 136(3B):B864, 1964.
- [100] M. Levy. Electron densities in search of Hamiltonians. *Phys. Rev. A*, 26:1200, 1982.
- [101] E. H. Lieb. Density functionals for coulomb systems. *Int. J. Quantum Chem.*, 24:243–277, 1983.
- [102] P. A. M. Dirac. Note on exchange phenomena in the Thomas atom. *Proc. Cambridge Philos. Soc.*, 26:376–85, 1930.
- [103] C. F. von Weizsäcker. Zur theorie der kernmassen. *Z. Physik*, 96:431–458, 1935.

- [104] W. Kohn and L.J. Sham. Self-consistent equations including exchange and correlation effects. *Phys. Rev.*, 140:A1133, 1965.
- [105] D. M. Ceperley and B. J. Alder. Ground state of the electron gas by a stochastic method. *Phys. Rev. Lett.*, 45:566–569, Aug 1980.
- [106] S. H. Vosko, L. Wilk, and M. Nusair. Accurate spin-dependent electron liquid correlation energies for local spin density calculations: a critical analysis. *Can. J Phys.*, 58:1200–1211, 1980.
- [107] J. P. Perdew and A. Zunger. Self-interaction correction to density-functional approximations for many-electron systems. *Phys. Rev. B*, 23:5048–5079, 1981.
- [108] L. A. Cole and J. P. Perdew. Calculated electron affinities of the elements. *Phys. Rev. A*, 25:1265–1271, 1982.
- [109] J. P. Perdew and Y. Wang. Accurate and simple analytic representation of the electron-gas correlation energy. *Phys. Rev. B*, 45:13244–13249, 1992.
- [110] G. L. Oliver and J. P. Perdew. Spin-density gradient expansion for the kinetic energy. *Phys. Rev. A*, 20:397–403, 1979.
- [111] U. von Barth and L. Hedin. A local exchange-correlation potential for the spin polarized case. *J. Phys. C: Solid State Phys.*, 5:1629–1642, 1972.
- [112] J. P. Perdew. Accurate density functional for the energy: Real-space cutoff of the gradient expansion for the exchange hole. *Phys. Rev. Lett.*, 55:1665–1668, 1985.
- [113] J. P. Perdew and Y. Wang. Accurate and simple density functional for the electronic exchange energy: Generalized gradient approximation. *Phys. Rev. B*, 33:8800–8802, 1986.
- [114] A. D. Becke. Density-functional exchange-energy approximation with correct asymptotic behavior. *Phys. Rev. A*, 38(6):3098–3100, 1988.
- [115] J. P. Perdew, J. A. Chevary, S. H. Vosko, K. A. Jackson, M. R. Pederson, D. J. Singh, and C. Fiolhais. Atoms, molecules, solids, and surfaces: Applications of the generalized gradient approximation for exchange and correlation. *Phys. Rev. B*, 46:6671–6687, 1992.
- [116] C. Lee, W. Yang, and R. G. Parr. Development of the colle-salvetti correlation-energy formula into a functional of the electron density. *Phys. Rev. B*, 37:785–789, 1988.
- [117] J.P. Perdew, K. Burke, and M. Ernzerhof. Generalized gradient approximation made simple. *Phys. Rev. Lett.*, 77(18):3865–3868, 1996.
- [118] J. P. Perdew, K. Burke, and M. Ernzerhof. Generalized gradient approximation made simple [Phys. Rev. Lett. 77, 3865 (1996)]. *Phys. Rev. Lett.*, 78:1396–1396, 1997.
- [119] A. D. Becke. A new mixing of Hartree–Fock and local density-functional theories. *J. Chem. Phys.*, 98:1372–1377, 1993.
- [120] A. D. Becke. Density-functional thermochemistry. III. the role of exact exchange. *J. Chem. Phys.*, 98:5648–5652, 1993.

- [121] A. D. Becke. Density-functional thermochemistry. IV. a new dynamical correlation functional and implications for exact-exchange mixing. *J. Chem. Phys.*, 104(3):1040–1046, 1996.
- [122] J. P. Perdew, M. Ernzerhof, and K. Burke. Rationale for mixing exact exchange with density functional approximations. *J. Chem. Phys.*, 105(22):9982–9985, 1996.
- [123] C. Adamo and V. Barone. Toward reliable density functional methods without adjustable parameters: The PBE0 model. *J. Chem. Phys.*, 110(13):6158–6170, 1999.
- [124] M. Ernzerhof and G. E. Scuseria. Assessment of the Perdew–Burke–Ernzerhof exchange–correlation functional. *J. Chem. Phys.*, 110(11):5029–5036, 1999.
- [125] J. Paier, M. Marsman, K. Hummer, G. Kresse, I. C. Gerber, and J. G. Ángyán. Screened hybrid density functionals applied to solids. *J. Chem. Phys.*, 124:154709, 2006.
- [126] J. Heyd, G.E. Scuseria, and M. Ernzerhof. Hybrid functionals based on a screened Coulomb potential. *J. Chem. Phys.*, 118:8207, 2003.
- [127] J. Heyd, G.E. Scuseria, and M. Ernzerhof. Erratum: “hybrid functionals based on a screened Coulomb potential” [*J. Chem. Phys.* 118, 8207 (2003)]. *J. Chem. Phys.*, 124(21):9906, 2006.
- [128] T. Yanai, D. P Tew, and N. C Handy. A new hybrid exchange–correlation functional using the Coulomb-attenuating method (CAM-B3LYP). *Chem. Phys. Lett.*, 393(1–3):51–57, 2004.
- [129] Y. Tawada, T. Tsuneda, S. Yanagisawa, T. Yanai, and K. Hirao. A long-range-corrected time-dependent density functional theory. *J. Chem. Phys.*, 120:8425, 2004.
- [130] E. Rudberg, P. Salek, T. Helgaker, and H. Ågren. Calculations of two-photon charge-transfer excitations using Coulomb-attenuated density-functional theory. *J. Chem. Phys.*, 123:184108, 2005.
- [131] M. J. G. Peach, T. Helgaker, P. Salek, T. W. Keal, O. B. Lutnaes, D. J. Tozer, and N. C. Handy. Assessment of a Coulomb-attenuated exchange–correlation energy functional. *Phys. Chem. Chem. Phys.*, 8:558–562, 2006.
- [132] R. Kobayashi and R. D. Amos. The application of CAM-B3LYP to the charge-transfer band problem of the zincbacteriochlorin–bacteriochlorin complex. *Chem. Phys. Lett.*, 420:106–109, 2006.
- [133] S. Chakravarty, M. B. Fogel, and W. Kohn. Dynamic response of inhomogeneous Fermi systems. *Phys. Rev. Lett.*, 43:775–778, 1979.
- [134] L. J. Bartolotti. Time-dependent extension of the Hohenberg–Kohn–Levy energy-density functional. *Phys. Rev. A*, 24:1661–1667, 1981.
- [135] B. M. Deb and S. K. Ghosh. Schrödinger fluid dynamics of many-electron systems in a time-dependent density-functional framework. *J. Chem. Phys.*, 77(1):342–348, 1982.

- [136] A. Dreuw, J. L. Weisman, and M. Head-Gordon. Long-range charge-transfer excited states in time-dependent density functional theory require non-local exchange. *J. Chem. Phys.*, 119:2943, 2003.
- [137] A. Heßelmann, A. Ipatov, and A. Görling. Charge-transfer excitation energies with a time-dependent density-functional method suitable for orbital-dependent exchange-correlation kernels. *Phys. Rev. A*, 80:012507, 2009.
- [138] N. T. Maitra, F. Zhang, R. J. Cave, and K. Burke. Double excitations within time-dependent density functional theory linear response. *J. Chem. Phys.*, 120(13):5932–5937, 2004.
- [139] R. J. Cave, F. Zhang, N. T. Maitra, and K. Burke. A dressed TDDFT treatment of the 2Ag states of butadiene and hexatriene. *Chem. Phys. Lett.*, 389(1-3):39–42, 2004.
- [140] B. G. Levine, C. Ko, J. Quenneville, and T. J. Martínez. Conical intersections and double excitations in time-dependent density functional theory. *Mol. Phys.*, 104:1039–1051, 2007.
- [141] F. Cordova, L. J. Doriol, A. Ipatov, M. E. Casida, C. Filippi, and A. Vela. Troubleshooting time-dependent density-functional theory for photochemical applications: Oxirane. *J. Chem. Phys.*, 127:164111, 2007.
- [142] S. K. Ghosh and A. K. Dhara. Density-functional theory of many-electron systems subjected to time-dependent electric and magnetic fields. *Phys. Rev. A*, 38:1149–1158, 1988.
- [143] M. E. Casida. *Recent Advances in Density Functional Methods, Part I*, chapter Time-dependent Density Functional Response Theory for Molecules, pages 155–192. World Scientific, 1995.
- [144] M. Petersilka, U. J. Gossmann, and E. K. U. Gross. Excitation energies from time-dependent density-functional theory. *Phys. Rev. Lett.*, 76:1212–1215, 1996.
- [145] M. Petersilka, E. K. U. Gross, and K. Burke. Excitation energies from time-dependent density functional theory using exact and approximate functionals. *Int. J. Quantum Chem.*, 80:534, 2000.
- [146] I. Vasiliev, S. Ögüt, and J. R. Chelikowsky. Ab initio excitation spectra and collective electronic response in atoms and clusters. *Phys. Rev. Lett.*, 82(9):1919–1922, 1999.
- [147] I. Vasiliev, S. Ögüt, and J. R. Chelikowsky. First-principles density-functional calculations for optical spectra of clusters and nanocrystals. *Phys. Rev. B*, 65:115416, 2002.
- [148] H. Appel, E. K. U. Gross, and K. Burke. Double-pole approximation in time-dependent density functional theory. *J. Quant. Chem.*, 106:2840–2847, 2006.
- [149] R. G. Gordon and Y. S. Kim. Theory for the forces between closed-shell atoms and molecules. *J. Chem. Phys.*, 56(6):3122–3133, 1972.
- [150] W. A. Harrison. *Pseudopotentials in the theory of metals*. Benjamin, New York, 1966.
- [151] J. C. Slater and G. F. Koster. Simplified LCAO method for the periodic potential problem. *Phys. Rev.*, 94:1498–1524, 1954.

- [152] D. J. Chadi. Atomic and electronic structures of reconstructed Si(100) surfaces. *Phys. Rev. Lett.*, 43:43–47, 1979.
- [153] W. A. Harrison. Overlap interactions and bonding in ionic solids. *Phys. Rev. B*, 34:2787–2793, 1986.
- [154] J.-M. Jancu, R. Scholz, F. Beltram, and F. Bassani. Empirical spd^s* tight-binding calculation for cubic semiconductors: General method and material parameters. *Phys. Rev. B*, 57:6493–6507, 1998.
- [155] C. Z. Wang, K. M. Ho, and C. T. Chan. Tight-binding molecular-dynamics study of amorphous carbon. *Phys. Rev. Lett.*, 70:611–614, 1993.
- [156] M. Hashimoto, Y. Ishida, S. Wakayama, R. Yamamoto, M. Doyama, and T. Fujiwara. Atomistic studies of grain boundary segregation in Fe-P and Fe-B alloys-II. electronic structure and intergranular embrittlement. *Acta Metall.*, 32(1):13–20, 1984.
- [157] C. M. Sayers. Impurity promoted intergranular fracture. *Philosophical Magazine Part B*, 50(5):635–640, 1984.
- [158] M. Menon and K. R. Subbaswamy. Nonorthogonal tight-binding molecular-dynamics scheme for silicon with improved transferability. *Phys. Rev. B*, 55:9231–9234, 1997.
- [159] O. K. Andersen and O. Jepsen. Explicit, first-principles tight-binding theory. *Phys. Rev. Lett.*, 53:2571–2574, 1984.
- [160] E. Artacho and F. Ynduráin. Nonparametrized tight-binding method for local and extended defects in homopolar semiconductors. *Phys. Rev. B*, 44:6169–6187, 1991.
- [161] J. Harris. Simplified method for calculating the energy of weakly interacting fragments. *Phys. Rev. B*, 31:1770–1779, 1985.
- [162] W. M. C. Foulkes and R. Haydock. Tight-binding models and density-functional theory. *Phys. Rev. B*, 39:12520–12536, 1989.
- [163] G. Seifert, H. Eschrig, and W. Bieger. Eine approximative Variante des LCAO-X_α Verfahrens. *Z. Phys. Chem. (Leipzig)*, 267:529, 1986.
- [164] D. Porezag. *Development of ab-initio and approximate density functional methods and their application to complex fullerene systems*. PhD thesis, Fakultät für Naturwissenschaften, Technischen Universität Chemnitz-Zwickau, 1997.
- [165] M. Wahiduzzaman, A. F. Oliveira, P. Philippsen, L. Zhechkov, E. van Lenthe, H. A. Witek, and T. Heine. DFTB parameters for the periodic table: Part 1, electronic structure. *J. Chem. Theory Comput.*, 9(9):4006–4017, 2013.
- [166] H. A. Witek, C. Kohler, T. Frauenheim, K. Morokuma, and M. Elstner. Relativistic parametrization of the self-consistent-charge density-functional tight-binding method. 1. atomic wave functions and energies. *J. Phys. Chem. A*, 111:5712–5719, 2007.
- [167] J. Junquera, Ó. Paz, D. Sánchez-Portal, and E. Artacho. Numerical atomic orbitals for linear-scaling calculations. *Phys. Rev. B*, 64:235111, 2001.

- [168] M. Elstner. *Weiterentwicklung quantenmechanischer Rechenverfahren für organische Moleküle und Polymere*. PhD thesis, Universität Gesamthochschule Paderborn, 1998.
- [169] B. Grundkötter-Stock. *Density Functional based Tight Binding parameters for boron and sublattice symmetry broken adatom adsorption on graphene*. PhD thesis, University of Bremen, 2013.
- [170] T. Frauenheim, F. Weich, T. Köhler, S. Uhlmann, D. Porezag, and G. Seifert. Density-functional-based construction of transferable nonorthogonal tight-binding potentials for Si and SiH. *Phys. Rev. B*, 52:11492, 1995.
- [171] P. Sitch, T. Frauenheim, and R. Jones. A density functional tight-binding approach for modelling Ge and GeH structures. *J. Phys.: Condens. Matter*, 8:6873, 1996.
- [172] J. Widany, F. Weich, T. Köhler, D. Porezag, and T. Frauenheim. Dynamic properties and structure formation of boron and carbon nitrides. *Diamond Relat. Mater.*, 5:1031, 1996.
- [173] F. Weich, J. Widany, and T. Frauenheim. Paracyanogenlike structures in high-density amorphous carbon nitride. *Phys. Rev. Lett.*, 78:3326, 1997.
- [174] R. Gutierrez, T. Frauenheim, T. Köhler, and G. Seifert. Stability of silicon carbide structures: from clusters to solid surfaces. *J. Mater. Chem.*, 6:1657, 1996.
- [175] R. Kaschner, T. Frauenheim, T. Köhler, and G. Seifert. A density-functional-based tight-binding scheme for the study of silicon-oxygen compounds. *J. Comp. Aided Mat. Design*, 4:53, 1997.
- [176] M. Haugk, J. Elsner, and T. Frauenheim. A density-functional based tight-binding approach to GaAs surface reconstructions. *J. Phys.: Condens. Matter*, 9:7305, 1997.
- [177] C. Köhler, G. Seifert, U. Gerstmann, M. Elstner, H. Overhof, and T. Frauenheim. Approximate density-functional calculations of spin densities in large molecular systems and complex solids. *Phys. Chem. Chem. Phys.*, 3(23):5109–5114, 2001.
- [178] M. J. Han, T. Ozaki, and J. Yu. O(N) LDA+U electronic structure calculation method based on the nonorthogonal pseudoatomic orbital basis. *Phys. Rev. B*, 73:045110, 2006.
- [179] T. Frauenheim, G. Seifert, M. Elstner, T. Niehaus, C. Kohler, M. Amkreutz, M. Sternberg, Z. Hajnal, A. Di Carlo, and S. Suhai. Atomistic simulations of complex materials: ground-state and excited-state properties. *J. Phys.: Condens. Matter*, 14(11):3015–3047, 2002.
- [180] B. N. Cox, M. A. Coulthard, and P. Lloyd. A calculation of the Coulomb correlation energy, U, for transition metals in Hubbard’s model. *J. Phys. F: Met. Phys.*, 4:807–820, 1974.
- [181] M. Elstner, K. Jalkanen, M. Knapp-Mohammady, T. Frauenheim, and S. Suhai. DFT studies on helix formation in N-acetyl-(L-alanyl)n-N-methylamide for n=1-20. *Chem. Phys.*, 256:15–27, 2000.

- [182] M. Elstner, T. Frauenheim, E. Kaxiras, G. Seifert, and S. Suhai. A self-consistent charge density-functional based tight-binding scheme for large biomolecules. *Phys. Status Solidi B*, 217(1):357–376, 2000.
- [183] M. Haugk, J. Elsner, T. Frauenheim, G. Seifert, and M. Sternberg. Structures, energetics and electronic properties of complex III-V semiconductor systems. *Phys. Status Solidi B*, 217(1):473–511, 2000.
- [184] T. Frauenheim, G. Seifert, M. Elstner, Z. Hajnal, G. Jungnickel, D. Porezag, S. Suhai, and R. Scholz. A self-consistent charge density-functional based tight-binding method for predictive materials simulations in physics, chemistry and biology. *Phys. Status Solidi B*, 217(1):41–62, 2000.
- [185] B. Hourahine, S. Sanna, B. Aradi, C. Köhler, T. A. Niehaus, and Th. Frauenheim. Self-interaction and strong correlation in DFTB. *J. Phys. Chem. A*, 111:5671, 2007.
- [186] S. Sanna, B. Hourahine, T. Gallauner, and T. Frauenheim. An efficient LDA+U based tight binding approach. *J. Phys. Chem. A*, 111:5665–5670, 2007.
- [187] M. Elstner, P. Hobza, T. Frauenheim, S. Suhai, and E. Kaxiras. Hydrogen bonding and stacking interactions of nucleic acid base pairs: A density-functional-theory based treatment. *J. Chem. Phys.*, 114:5149, 2001.
- [188] L. Zhechkov, T. Heine, S. Patchkovskii, G. Seifert, and H. A. Duarte. An efficient a posteriori treatment for dispersion interaction in density-functional-based tight binding. *J. Chem. Theory Comput.*, 1(5):841–847, 2005.
- [189] G. M. Seabra, R. C. Walker, M. Elstner, D. A. Case, and A. E. Roitberg. Implementation of the SCC-DFTB method for hybrid QM/MM simulations within the Amber Molecular Dynamics package. *J. Phys. Chem. A*, 111:5655–5664, 2007.
- [190] H. L. Woodcock, M. Hodoscek, and B. R. Brooks. Exploring SCC-DFTB paths for mapping QM/MM reaction mechanisms. *J. Phys. Chem. A*, 111:5720–5728, 2007.
- [191] M. Elstner. The SCC-DFTB method and its application to biological systems. *Theo. Chem. Acc.*, 116:316–325, 2006.
- [192] Y. Yang, H. Yu, D. York, Q. Cui, and M. Elstner. Extension of the self-consistent-charge density-functional tight-binding method: Third-order expansion of the density functional theory total energy and introduction of a modified effective Coulomb interaction. *J. Phys. Chem. A*, 111(42):10861–10873, 2007.
- [193] M. Gaus, Q. Cui, and M. Elstner. DFTB3: Extension of the self-consistent-charge density-functional tight-binding method (SCC-DFTB). *J. Chem. Theory Comput.*, 7(4):931–948, 2011.
- [194] M. Gaus, A. Goez, and M. Elstner. Parametrization and benchmark of DFTB3 for organic molecules. *J. Chem. Theory Comput.*, 9(1):338–354, 2013.
- [195] Z. Bodrog and B. Aradi. Possible improvements to the self-consistent-charges density-functional tight-binding method within the second order. *Phys. Status Solidi B*, 249:259–269, 2012.

- [196] J. A. Pople, D. L. Beveridge, and P. A. Dobosh. Approximate self-consistent molecular-orbital theory. V. Intermediate neglect of differential overlap. *J. Chem. Phys.*, 47:2026–2033, 1967.
- [197] J. A. Pople, D. P. Santry, and G. A. Segal. Approximate self-consistent molecular orbital theory. I. Invariant procedures. *J. Chem. Phys.*, 43:S129–s135, 1965.
- [198] K. Rüdénberg. On the three- and four-center integrals in molecular quantum mechanics. *J. Chem. Phys.*, 19:1433–1434, 1951.
- [199] H. P. Figeys, P. Geerlings, and C. Van Alsenoy. Rotational invariance of INDO theories including d-orbitals into the basis set. *Int. J. Quantum Chem.*, 11(5):705–713, 1977.
- [200] A. Domínguez, B. Aradi, T. Frauenheim, V. Lutsker, and T. A. Niehaus. Extensions of the time-dependent density functional based tight-binding approach. *J. Chem. Theory Comput.*, 9(11):4901–4914, 2013.
- [201] B. Aradi, B. Hourahine, and T. Frauenheim. DFTB+, a sparse matrix-based implementation of the DFTB method. *J. Phys. Chem. A*, 111(26):5678–5684, 2007.
- [202] C. M. Maupin, B. Aradi, and G. A. Voth. The self-consistent charge density functional tight binding method applied to liquid water and the hydrated excess proton: Benchmark simulations. *J. Phys. Chem. B*, 114(20):6922–6931, 2010.
- [203] H. R. Leverentz, H. W. Qi, and D. G. Truhlar. Assessing the accuracy of density functional and semiempirical wave function methods for water nanoparticles: Comparing binding and relative energies of (H₂O)₁₆ and (H₂O)₁₇ to CCSD(T) results. *J. Chem. Theory Comput.*, 9(2):995–1006, 2013.
- [204] T. H. Choi, R. Liang, C. M. Maupin, and G. A. Voth. Application of the SCC-DFTB method to hydroxide water clusters and aqueous hydroxide solutions. *J. Phys. Chem. B*, 117(17):5165–5179, 2013.
- [205] R. Liang, J. M. J. Swanson, and G. A. Voth. Benchmark study of the SCC-DFTB approach for a biomolecular proton channel. *J. Chem. Theory Comput.*, 10(1):451–462, 2014.
- [206] A. G. Baboul, L. A. Curtiss, P. C. Redfern, and K. Raghavachari. Gaussian-3 theory using density functional geometries and zero-point energies. *J. Chem. Phys.*, 110(16):7650–7657, 1999.
- [207] S. Yoo, E. Aprà, X. C. Zeng, and S. S. Xantheas. High-level ab initio electronic structure calculations of water clusters (H₂O)₁₆ and (H₂O)₁₇: A new global minimum for (H₂O)₁₆. *Phys. Chem. Lett.*, 1(20):3122–3127, 2010.
- [208] D. Heringer, T. A. Niehaus, M. Wanko, and T. Frauenheim. Analytical excited state forces for the time-dependent density-functional tight-binding method. *J. Comp. Chem.*, 28(16):2589–2601, 2007.
- [209] C. Y. Yam, S. Yokojima, and G. H. Chen. Linear-scaling time-dependent density functional theory. *Phys. Rev. B*, 68:153105, 2003.

- [210] T. A. Niehaus, D. Heringer, B. Torralva, and T. Frauenheim. Importance of electronic self-consistency in the TDDFT based treatment of nonadiabatic molecular dynamics. *Eur. Phys. J. D*, 35(3):467–477, 2005.
- [211] R. Mitric, U. Werner, M. Wohlgemuth, G. Seifert, and V. Bonacic-Koutecký. Nonadiabatic dynamics within time-dependent density functional tight binding method. *J. Phys. Chem. A*, 113:12700–12705, 2009.
- [212] J. Jakowski, S. Irle, and K. Morokuma. Time-dependent quantum dynamical simulations of C2 condensation under extreme conditions. *Phys. Chem. Chem. Phys.*, 14:6273–6279, 2012.
- [213] Y. Wang, C.-Y. Yam, Th. Frauenheim, G.H. Chen, and T.A. Niehaus. An efficient method for quantum transport simulations in the time domain. *Chem. Phys.*, 391(1):69–77, 2011.
- [214] T. A. Niehaus. Approximate time-dependent density functional theory. *J. Mol. Struct.: THEOCHEM*, 914:38–49, 2009.
- [215] T.A. Niehaus and F. Della Sala. Range separated functionals in the density functional based tight-binding method: Formalism. *Phys. Status Solidi B*, 249:237–244, 2012.
- [216] M. E. Casida. Review: Time-dependent density-functional theory for molecules and molecular solids. *J. Mol. Struct.: THEOCHEM*, 914:3–18, 2009.
- [217] A. Ipatov, F. Cordova, L. J. Doriol, and M. E. Casida. Excited-state spin-contamination in time-dependent density-functional theory for molecules with open-shell ground states. *J. Mol. Struct.: THEOCHEM*, 914:60–73, 2009.
- [218] TURBOMOLE V6.4 2012, a development of University of Karlsruhe and Forschungszentrum Karlsruhe GmbH, 1989-2007, TURBOMOLE GmbH, since 2007; available from <http://www.turbomole.com> (accessed may 30, 2013).
- [219] J. Oddershede, N. E. Gruener, and G. H. F. Diercksen. Comparison between equation of motion and polarization propagator calculations. *Chem. Phys.*, 97:303–310, 1985.
- [220] P. H. Krupenie. The spectrum of molecular oxygen. *J. Phys. Chem. Ref. Data*, 1(2):423–534, 1972.
- [221] N. J. Turro, V. Ramamurthy, and J. C. Scaiano. *Principles of Molecular Photochemistry: An introduction.*, pages 195–196. University Science Books, first edition, 2009.
- [222] T. Grabo, M. Petersilka, and E. K. U. Gross. Molecular excitation energies from time-dependent density functional theory. *J. Mol. Struct.: THEOCHEM*, 501-502:353–367, 2000.
- [223] R. Bauernschmitt and R. Ahlrichs. Treatment of electronic excitations within the adiabatic approximation of time dependent density functional theory. *Chem. Phys. Lett.*, 256:454–464, 1996.
- [224] A. Hesselmann and A. Goerling. Blindness of the exact density response function to certain types of electronic excitations. *Phys. Rev. Lett.*, 102:233003, 2009.

- [225] M. Schreiber, M.R. Silva-Junior, S.P.A. Sauer, and W. Thiel. Benchmarks for electronically excited states: CASPT2, CC2, CCSD, and CC3. *J. Chem. Phys.*, 128:134110, 2008.
- [226] R. Peverati and D. G. Truhlar. Performance of the M11 and M11-L density functionals for calculations of electronic excitation energies by adiabatic time-dependent density functional theory. *Phys. Chem. Chem. Phys.*, 14:11363–11370, 2012.
- [227] L. Goerigk, J. Moellmann, and S. Grimme. Computation of accurate excitation energies for large organic molecules with double-hybrid density functionals. *Phys. Chem. Chem. Phys.*, 11:4611–4620, 2009.
- [228] N. Mardirossian, J. A. Parkhill, and M. Head-Gordon. Benchmark results for empirical post-GGA functionals: Difficult exchange problems and independent tests. *Phys. Chem. Chem. Phys.*, 13:19325–19337, 2011.
- [229] F. Della Sala and E. Fabiano. Accurate singlet and triplet excitation energies using the localized Hartree–Fock Kohn–Sham potential. *Chem. Phys.*, 391(1):19–26, 2011.
- [230] M. R. Silva-Junior, M. Schreiber, S. P. A. Sauer, and W. Thiel. Benchmarks for electronically excited states: Time-dependent density functional theory and density functional theory based multireference configuration interaction. *J. Chem. Phys.*, 129(10):104103, 2008.
- [231] M. Huix-Rotllant, A. Ipatov, A. Rubio, and M. E. Casida. Assessment of dressed time-dependent density-functional theory for the low-lying valence states of 28 organic chromophores. *Chem. Phys.*, 391(1):120–129, 2011.
- [232] F. Trani, G. Scalmani, G. Zheng, I. Carnimeo, M.J. Frisch, and V. Barone. Time dependent density functional tight binding: New formulation and benchmark of excited states. *J. Chem. Theory Comput.*, 7:3304–3313, 2011.
- [233] M. J. G. Peach, P. Benfield, Helgaker T., and D. J. Tozer. Excitation energies in density functional theory: An evaluation and a diagnostic test. *J. Chem. Phys.*, 128:044118, 2008.
- [234] M. Caricato, G. W. Trucks, M. J. Frisch, and K. B. Wiberg. Electronic transition energies: A study of the performance of a large range of single reference density functional and wave function methods on valence and Rydberg states compared to experiment. *J. Chem. Theory Comput.*, 6(2):370–383, 2010.
- [235] C. A. Barboza, P. A. M. Vazquez, D. Mac-Leod Carey, and R. Arratia-Perez. A TD-DFT basis set and density functional assessment for the calculation of electronic excitation energies of fluorene. *Int. J. Quantum Chem.*, 112:3434–3438, 2012.
- [236] N. H. List, J. M. Olsen, T. Rocha-Rinza, O. Christiansen, and J. Kongsted. Performance of popular XC-functionals for the description of excitation energies in GFP-like chromophore models. *Int. J. Quantum Chem.*, 112:789–800, 2012.
- [237] A. Dreuw and M. Head-Gordon. Single-reference ab initio methods for the calculation of excited states of large molecules. *Chem. Rev.*, 105(11):4009–4037, 2005.

- [238] S. Hirata and M. Head-Gordon. Time-dependent density functional theory within the Tamm–Dancoff approximation. *Chem. Phys. Lett.*, 314(3–4):291–299, 1999.
- [239] M. E. Casida, F. Gutierrez, J. G. Guan, F. X. Gadea, D. Salahub, and J. P. Daudey. Charge-transfer correction for improved time-dependent local density approximation excited-state potential energy curves: Analysis within the two-level model with illustration for H-2 and LiH. *J. Chem. Phys.*, 113(17):7062–7071, 2000.
- [240] M. J. G. Peach, M. J. Williamson, and D. J. Tozer. Influence of triplet instabilities in TDDFT. *J. Chem. Theory Comput.*, 7(11):3578–3585, 2011.
- [241] M. J. G. Peach and D. J. Tozer. Overcoming low orbital overlap and triplet instability problems in TDDFT. *J. Phys. Chem. A*, 116(39):9783–9789, 2012.
- [242] J. S. Sears, T. Koerzdoerfer, C.-R. Zhang, and J.-L. Bredas. Communication: Orbital instabilities and triplet states from time-dependent density functional theory and long-range corrected functionals. *J. Chem. Phys.*, 135(15):151103, 2011.
- [243] M. Valiev, E.J. Bylaska, N. Govind, K. Kowalski, T.P. Straatsma, H.J.J. Van Dam, D. Wang, J. Nieplocha, E. Apra, T.L. Windus, and W.A. de Jong. NWChem: A comprehensive and scalable open-source solution for large scale molecular simulations. *Comput. Phys. Commun.*, 181(9):1477–1489, 2010.
- [244] M. E. Foster and B. M. Wong. Nonempirically tuned range-separated DFT accurately predicts both fundamental and excitation gaps in DNA and RNA nucleobases. *J. Chem. Theory Comput.*, 8:2682–2687, 2012.
- [245] M. Miura, Y. Aoki, and B. Champagne. Assessment of time-dependent density functional schemes for computing the oscillator strengths of benzene, phenol, aniline, and fluorobenzene. *J. Chem. Phys.*, 127(8):084103, 2007.
- [246] M. Caricato, G. W. Trucks, M. J. Frisch, and K. B. Wiberg. Oscillator strengths: How does TD-DFT compare to EOM-CCSD? *J. Chem. Theory Comput.*, 7:456–466, 2011.
- [247] P. G. Szalay, T. Watson, A. Perera, V. F. Lotrich, and R. J. Bartlett. Benchmark studies on the building blocks of DNA. 1. superiority of coupled cluster methods in describing the excited states of nucleobases in the franck–condon region. *J. Phys. Chem. A*, 116(25):6702–6710, 2012.
- [248] J. F. Stanton and R. J. Bartlett. The equation of motion coupled-cluster method. A systematic biorthogonal approach to molecular excitation energies, transition probabilities, and excited state properties. *J. Chem. Phys.*, 98(9):7029–7039, 1993.
- [249] R. J. Bartlett and M. Musiał. Coupled-cluster theory in quantum chemistry. *Rev. Mod. Phys.*, 79:291–352, 2007.
- [250] N. A. Besley. Calculation of the electronic spectra of molecules in solution and on surfaces. *Chem. Phys. Lett.*, 390:124–129, 2004.
- [251] H. Appel, E. K. U. Gross, and K. Burke. Excitations in time-dependent density-functional theory. *Phys. Rev. Lett.*, 90:043005, 2003.

- [252] C. Lun Pang, R. Lindsay, and G. Thornton. Chemical reactions on rutile TiO₂(110). *Chem. Soc. Rev.*, 37:2328–2353, 2008.
- [253] D. Zhang, G. Li, H. Wang, K. M. Chan, and J. C. Yu. Biocompatible anatase single-crystal photocatalysts with tunable percentage of reactive facets. *Cryst. Growth Des.*, 10(3):1130–1137, 2010.
- [254] A. Feldhoff, C. Mendive, T. Bredow, and D. Bahnemann. Direct measurement of size, three-dimensional shape, and specific surface area of anatase nanocrystals. *ChemPhysChem*, 8(6):805–809, 2007.
- [255] X. Wang, B. Huang, Z. Wang, X. Qin, X. Zhang, Y. Dai, and M.-H. Whangbo. Synthesis of anatase TiO₂ tubular structures microcrystallites with a high percentage of 001 facets by a simple one-step hydrothermal template process. *Chem. Eur. J.*, 16:7106–7109, 2010.
- [256] Z. Wang, K. Lv, G. Wang, K. Deng, and D. Tang. Study on the shape control and photocatalytic activity of high-energy anatase titania. *Appl. Catal. B: Environ.*, 100(1–2):378–385, 2010.
- [257] A. Vittadini, A. Selloni, F. P. Rotzinger, and M. Grätzel. Structure and energetics of water adsorbed at TiO₂ anatase (101) and (001) surfaces. *Phys. Rev. Lett.*, 81:2954–2957, 1998.
- [258] Y.-F. Li, Z.-P. Liu, L. Liu, and W. Gao. Mechanism and activity of photocatalytic oxygen evolution on titania anatase in aqueous surroundings. *J. Am. Chem. Soc.*, 132(37):13008–13015, 2010.
- [259] H. G. Yang, C. H. Sun, S. Z. Qiao, J. Zou, G. Liu, S. C. Smith, H. M. Cheng, and G. Q. Lu. Anatase TiO₂ single crystals with a large percentage of reactive facets. *Nature*, 453:638–641, 2008.
- [260] H. G. Yang, G. Liu, S. Z. Qiao, C. H. Sun, Y. G. Jin, S. C. Smith, J. Zou, H. M. Cheng, and G. Q. Lu. Solvothermal synthesis and photoreactivity of anatase TiO₂ nanosheets with dominant {001} facets. *J. Am. Chem. Soc.*, 131(11):4078–4083, 2009.
- [261] M. V. Sofianou. Study of TiO₂ anatase nano and microstructures with dominant {001} facets for NO oxidation. *Environ. Sci. Pollut. R.*, 19:3719–3726, 2012.
- [262] G. Dolgonos, B. Aradi, N. H. Moreira, and T. Frauenheim. An improved self-consistent-charge density-functional tight-binding (SCC-DFTB) set of parameters for simulation of bulk and molecular systems involving titanium. *J. Chem. Theory Comput.*, 6(1):266–278, 2010.
- [263] G. Kresse and J. Hafner. Ab initio molecular dynamics for liquid metals. *Phys. Rev. B*, 47:558–561, 1993.
- [264] G. Kresse and J. Hafner. Ab initio molecular-dynamics simulation of the liquid-metal–amorphous-semiconductor transition in germanium. *Phys. Rev. B*, 49:14251–14269, 1994.
- [265] G. Kresse and J. Furthmüller. Efficiency of ab-initio total energy calculations for metals and semiconductors using a plane-wave basis set. *Comp. Mater. Sci.*, 6(1):15–50, 1996.

- [266] G. Kresse and J. Furthmüller. Efficient iterative schemes for ab initio total-energy calculations using a plane-wave basis set. *Phys. Rev. B*, 54:11169–11186, 1996.
- [267] P. E. Blöchl. Projector augmented-wave method. *Phys. Rev. B*, 50:17953–17979, 1994.
- [268] G. Kresse and D. Joubert. From ultrasoft pseudopotentials to the projector augmented-wave method. *Phys. Rev. B*, 59:1758–1775, 1999.
- [269] H. J. Monkhorst and J. D. Pack. Special points for Brillouin-zone integrations. *Phys. Rev. B*, 13:5188–5192, 1976.
- [270] J. D. Pack and H. J. Monkhorst. "special points for Brillouin-zone integrations"-a reply. *Phys. Rev. B*, 16:1748–1749, 1977.
- [271] J. K. Burdett, T. Hughbanks, G. J. Miller, J. W. Richardson, and J. V. Smith. Structural-electronic relationships in inorganic solids: powder neutron diffraction studies of the rutile and anatase polymorphs of titanium dioxide at 15 and 295 K. *J. Am. Chem. Soc.*, 109(12):3639–3646, 1987.
- [272] H. Tang, F. Lévy, H. Berger, and P. E. Schmid. Urbach tail of anatase TiO₂. *Phys. Rev. B*, 52:7771–7774, 1995.
- [273] F. Labat, P. Baranek, C. Domain, C. Minot, and C. Adamo. Density functional theory analysis of the structural and electronic properties of TiO₂ rutile and anatase polytypes: Performances of different exchange-correlation functionals. *J. Chem. Phys.*, 126(15):154703, 2007.
- [274] K. Yang, Y. Dai, and B. Huang. Understanding photocatalytic activity of S- and P-doped TiO₂ under visible light from first-principles. *J. Phys. Chem. C*, 111(51):18985–18994, 2007.
- [275] M. M. Islam, T. Bredow, and A. Gerson. Electronic properties of oxygen-deficient and aluminum-doped rutile TiO₂ from first principles. *Phys. Rev. B*, 76:045217, 2007.
- [276] L. Kernazhitsky, V. Shymanovska, T. Gavrillko, V. Naumov, L. Fedorenko, V. Kshnyakin, and J. Baran. Room temperature photoluminescence of anatase and rutile TiO₂ powders. *J. Lumin.*, 146:199–204, 2014.
- [277] D. J. Tozer, R. D. Amos, N. C. Handy, B. O. Roos, and L. Serrano-Andrés. Does density functional theory contribute to the understanding of excited states of unsaturated organic compounds? *Mol. Phys.*, 97(7):859–868, 1999.
- [278] D. J. Tozer. Relationship between long-range charge-transfer excitation energy error and integer discontinuity in Kohn–Sham theory. *J. Chem. Phys.*, 119(24):12697–12699, 2003.
- [279] B. Mguig, M. Calatayud, and C. Minot. Theoretical investigation of NO oxidation over TiO₂-anatase. *Surf. Rev. Lett.*, 10:175–182, 2003.
- [280] J. Ahn and J.W. Rabalais. Composition and structure of the Al₂O₃(0001)-(1 x 1) surface. *Surf. Sci.*, 388(1–3):121–131, 1997.

- [281] P. Guénard, G. Renaud, A. Barbier, and M. Gautier-Soyer. Determination of the α -Al₂O₃(0001) surface relaxation and termination by measurements of crystal truncation rods. *Surf. Rev. Lett.*, 05(01):321–324, 1998.
- [282] T. Suzuki, S. Hishita, K. Oyoshi, and R. Souda. Structure of α -Al₂O₃(0001) surface and Ti deposited on α -Al₂O₃(0001) substrate: CAICISS and RHEED study. *Surf. Sci.*, 437(3):289–298, 1999.
- [283] I. Batyrev, A. Alavi, and M. W. Finnis. Ab initio calculations on the Al₂O₃(0001) surface. *Faraday Discuss.*, 114:33–43, 1999.
- [284] X.-G. Wang, A. Chaka, and M. Scheffler. Effect of the environment on α -Al₂O₃ (0001) surface structures. *Phys. Rev. Lett.*, 84:3650–3653, 2000.
- [285] I. G. Batyrev, A. Alavi, and M. W. Finnis. Equilibrium and adhesion of Nb/sapphire: The effect of oxygen partial pressure. *Phys. Rev. B*, 62:4698–4706, 2000.
- [286] R. Meyer, Q. Ge, J. Lockemeyer, R. Yeates, M. Lemanski, D. Reinalda, and M. Neurock. An ab initio analysis of adsorption and diffusion of silver atoms on alumina surfaces. *Surf. Sci.*, 601(1):134–145, 2007.
- [287] M. A. Nygren, D. H. Gay, C. Richard, and A. Catlow. Hydroxylation of the surface of the corundum basal plane. *Surf. Sci.*, 380(1):113–123, 1997.
- [288] K. C. Hass, W. F. Schneider, A. Curioni, and W. Andreoni. The chemistry of water on alumina surfaces: Reaction dynamics from first principles. *Science*, 282(5387):265–268, 1998.
- [289] R. Di Felice and J. E. Northrup. Theory of the clean and hydrogenated Al₂O₃(0001)-(1 x 1) surfaces. *Phys. Rev. B*, 60:R16287–R16290, 1999.
- [290] Z. Lodziana and J. K. Nørskov. Adsorption of Cu and Pd on α -Al₂O₃(0001) surfaces with different stoichiometries. *J. Chem. Phys.*, 115(24):11261–11267, 2001.
- [291] A. Marmier and S. C. Parker. Ab initio morphology and surface thermodynamics of α -Al₂O₃. *Phys. Rev. B*, 69:115409, 2004.
- [292] P. Liu, T. Kendelewicz, G. E. Brown Jr., E. J. Nelson, and S. A. Chambers. Reaction of water vapor with α -Al₂O₃(0001) and α -Fe₂O₃(0001) surfaces: synchrotron X-ray photoemission studies and thermodynamic calculations. *Surf. Sci.*, 417(1):53–65, 1998.
- [293] A. Hellman and H. Grönbeck. First-principles studies of NO_x chemistry on Agn/ α -Al₂O₃. *J. Phys. Chem. C*, 113:3674–3682, 2009.
- [294] C. Verdozzi, D. R. Jennison, P. A. Schultz, and M. P. Sears. Sapphire (0001) surface, clean and with d-metal overlayers. *Phys. Rev. Lett.*, 82:799–802, 1999.
- [295] C. Ruberto, Y. Yourdshahyan, and B. I. Lundqvist. Surface properties of metastable alumina: A comparative study of κ - and α -Al₂O₃. *Phys. Rev. B*, 67:195412, 2003.
- [296] C. Wöll. The chemistry and physics of zinc oxide surfaces. *Prog. Surf. Sci.*, 82:55–120, 2007.

- [297] J. M. Soler, E. Artacho, J. D. Gale, A. Garcia, J. Junquera, P. Ordejón, and D. Sánchez-Poral. The SIESTA method for ab initio order-N materials simulation. *J. Phys.: Condens. Matter*, 14:2745–2779, 2002.
- [298] N. Troullier and J. L. Martins. Efficient pseudopotentials for plane-wave calculations. *Phys. Rev. B*, 43:1993–2006, 1991.
- [299] N. H. Moreira, A. Dominguez, T. Frauenheim, and A. L. da Rosa. On the stabilization mechanisms of organic functional groups on ZnO surfaces. *Phys. Chem. Chem, Phys.*, 14:15445–15451, 2012.
- [300] B. Xiang, P. Wang, X. Zhang, S. A. Dayeh, D. P. R. Aplin, C. Soci, D. Yu, and D. Wang. Rational synthesis of p-type zinc oxide nanowire arrays using simple chemical vapor deposition. *Nano Lett.*, 7:323, 2007.
- [301] C. H. Liu, W. C. Yiu, F. C. K. Au, J. X. Ding, C. S. Lee, and S. T. Lee. Electrical properties of zinc oxide nanowires and intramolecular p-n junctions. *Appl. Phys. Lett.*, 83:3168, 2003.
- [302] W. Fan, H. Xu, A. L. Rosa, Th. Frauenheim, and R. Q. Zhang. First-principles calculations of reconstructed [0001] ZnO nanowires. *Phys. Rev. B*, 76:073302, 2007.
- [303] X. Q. Shi, H. Xu, M. A. Van Hove, N. H. Moreira, A. L. Rosa, and T. Frauenheim. Substrate mediated stabilization of methylphosphonic acid on ZnO non-polar surfaces. *Surf. Sci.*, 606(3–4):289–292, 2012.
- [304] A. Dominguez, S. grosse Holthaus, S. Köppen, T. Frauenheim, and A. L. da Rosa. The role of water co-adsorption on the modification of ZnO nanowires using acetic acid. *Phys. Chem. Chem. Phys.*, 2014. DOI: 10.1039/c4cp00667d.
- [305] N. H. Moreira, A. L. da Rosa, and T. Frauenheim. Covalent functionalization of ZnO surfaces: A density functional tight binding study. *Appl. Phys. Lett.*, 94:193109, 2009.
- [306] N. H. Moreira, G. Dolgonos, B. Aradi, A. L. da Rosa, and T. Frauenheim. Toward an accurate density-functional tight-binding description of zinc-containing compounds. *J. Chem. Theory Comput*, 5:605–614, 2009.
- [307] A. C. Ferraz and R. Miotto. Glycine adsorption on silicon (001). *Braz. J. Phys.*, 36(2A):309–312, 2006.
- [308] S. Irrera, D. Costa, and P. Marcus. DFT periodic study of adsorption of glycine on the (0001) surface of zinc terminated ZnO. *J. Mol. Struct.: THEOCHEM*, 903:49–58, 2009.
- [309] R. Tonner. Adsorption of proline and glycine on the TiO₂(110) surface: A density functional theory study. *ChemPhysChem*, 11:1053, 2010.
- [310] T. J. Lerotholi, E. A. Kröger, M. J. Knight, W. Unterberger, K. Hogan, D. C. Jackson, C. L. Lamont, and D. P. Woodruff. Adsorption structure of glycine on TiO₂(110): A photoelectron diffraction determination. *Surf. Sci.*, 603:2305–2311, 2009.
- [311] M. H. Huang, S. Mao, H. Feick, H. Yan, Y. Wu, H. Kind, E. Weber, R. Russo, and P. Yang. Room-temperature ultraviolet nanowire nanolasers. *Science*, 292:1897, 2001.

- [312] X. Q. Meng, D. Z. Shen, J. Y. Zhang, D. X. Zhao, Y. M. Lu, L. Dong, Z. Z. Zhang, Y. C. Liu, and X. W. Fan. The structural and optical properties of ZnO nanorod arrays. *Sol. State Commun.*, 135:179, 2005.
- [313] H. T. Ng, B. Chen, J. Li, J. Han, M. M. J. Wu, S. X. Li, and E. E. Haller. Optical properties of single-crystalline ZnO nanowires on m-sapphire. *Appl. Phys. Lett.*, 82:2023, 2003.
- [314] X. Liu, X. Wu, H. Cao, and R. P. H. Chang. Growth mechanism and properties of ZnO nanorods synthesized by plasma-enhanced chemical vapor deposition. *J. Appl. Phys.*, 95:3141, 2004.
- [315] A. Janotti and C. G. Van de Walle. Native point defects in ZnO. *Phys. Rev. B*, 76(16):165202, 2007.
- [316] F. Oba, A. Togo, I. Tanaka, J. Paier, and G. Kresse. Defect energetics in ZnO: A hybrid Hartree-Fock density functional study. *Phys. Rev. B*, 77(24):245202, 2008.
- [317] S. Lany and A. Zunger. Many-body GW calculation of the oxygen vacancy in ZnO. *Phys. Rev. B*, 81(11):113201, 2010.
- [318] J. D. Prades, A. Cicera, and J. R. Morante. Ab initio calculations of NO₂ and SO₂ chemisorption onto non-polar ZnO surfaces. *Sens. Actuators B: Chem.*, 142:179–184, 2009.